Dissertation

submitted to the

Combined Faculties of the Natural Sciences and Mathematics

of the Ruperto-Carola-University of Heidelberg, Germany

for the degree of

Doctor of Natural Sciences

Put forward by

Felix Müller

born in Neu-Ulm

Oral examination on December 5, 2013

Jet production measurements at the ATLAS experiment

Referees: Prof. Dr. Hans-Christian Schultz-Coulon
Prof. Dr. Norbert Herrmann

Abstract

Jet production is the dominant process at high transverse momentum in proton-proton collisions at the Large Hadron Collider and allows for a precise test of the strong interaction and the structure of the proton. The inclusive jet cross-section has been measured with the ATLAS detector at two centre-of-mass energies of $\sqrt{s} = 2.76\,\text{TeV}$ and $\sqrt{s} = 7\,\text{TeV}$. The datasets correspond to an integrated luminosity of $0.20\,\text{pb}^{-1}$ and $37\,\text{pb}^{-1}$, respectively. Based on jets that are identified using the anti-k_t algorithm with two radius parameters of 0.4 and 0.6, the double-differential inclusive jet cross-section is presented as a function of the jet transverse momentum p_T and seven ranges of the jet rapidity y. The measurement comprised the calibration of the luminosity detectors for $\sqrt{s} = 2.76\,\text{TeV}$, where an uncertainty of 2.7% has been achieved. The ratio of the cross-section measurements is determined as a function of transverse momentum as well as the dimensionless quantity $x_\text{T} = 2p_\text{T}/\sqrt{s}$. The systematic uncertainties on the ratio is significantly reduced due to the cancellation of correlated uncertainties in the two measurements. Results are compared to predictions from perturbative QCD calculations at next-to-leading order precision corrected for non-perturbative effects, and predictions from parton shower Monte Carlo simulations with next-to-leading order matrix elements. Several PDF sets, parton shower tunes and Monte Carlo simulations are compared. In addition, the jet cross-section data are analysed within a framework of next-to-leading order perturbative QCD calculations to determine the parton distribution functions of the proton, together with data from HERA.

Zusammenfassung

Jetproduktion ist der dominierende Prozess bei Proton-Proton-Kollisionen am Large Hadron Collider und ermöglicht präzise Untersuchungen der starken Wechselwirkung und der Struktur des Protons. In der vorliegenden Arbeit wird die Bestimmung des inklusiven Jet-Wirkungsquerschnittes mit Hilfe des ATLAS-Detektors bei zwei verschiedenen Schwerpunktsenergien von $\sqrt{s} = 2{,}76\,\text{TeV}$ und $\sqrt{s} = 7\,\text{TeV}$ vorgestellt. Jets sind hierbei mittels des anti-k_t-Algorithmus definiert. Der Wirkungsquerschnitt wird als Funktion des Transversalimpulses in sieben Rapiditätsbereichen und für Radiusparameter von 0.4 und 0.6 gemessen. Der Quotient der Wirkungsquerschnitte bei verschiedenen Schwerpunktsenergien als Funktion des Transversalimpulses oder der dimensionslosen Größe $x_\text{T} = 2p_\text{T}/\sqrt{s}$ bildet darüber hinaus einen noch präziseren Test, da sich dabei die korrelierten Komponenten der Unsicherheiten aus beiden Messungen aufheben. Die Messungen beruhen auf Datensätzen von $0{,}20\,\text{pb}^{-1}$ beziehungsweise $37\,\text{pb}^{-1}$ und schließen die erstmalige Kalibrierung der Luminositätsdetektoren bei $\sqrt{s} = 2{,}76\,\text{TeV}$ ein, bei der eine Unsicherheit von 2.7% erreicht wird. Die Ergebnisse werden mit Vorhersagen aus Störungsrechnungen der Quantenchromodynamik zweiter Ordnung verglichen. Nicht-perturbative Effekte werden hierbei entweder mittels Korrekturfaktoren oder durch direkte Kombination der Matrixelementberechnung mit Monte-Carlo-Simulationen berücksichtigt. Außerdem wird eine Bestimmung der Partonverteilungsfunktionen des Protons mit den ATLAS-Jetdaten und Daten von HERA innerhalb einer perturbativen QCD-Rechnung vorgestellt.

Contents

Introduction

Particle jets are collimated sprays of hadrons and the dominant product of proton-proton collisions at the Large Hadron Collider. In the theory of the strong interaction, *Quantum Chromodynamics*, they can be understood as the result of a hard scatter of the fundamental constituents of the protons, quarks and gluons. Since quarks and gluons cannot exist freely in this theory, they are subject to a fragmentation process, which leads to the creation of a large number of stable hadrons forming a jet in the direction of the original scatter.

Jets are the main tool to probe the hard interaction. However, they represent an inclusive observable of several processes, as just described. To be able to draw conclusions on the fundamental processes of Quantum Chromodynamics, comparisons between theory predictions and experimental data have to be performed. The calculation of the predictions consists of two parts. The strong interaction at high energies can be approximated by perturbative calculations. Non-perturbative effects such as the fragmentation and forming of hadrons in the final state are accounted for by using phenomenological models that are tuned to data.

The topic of this thesis is the measurement of the inclusive jet cross-section with the ATLAS experiment in proton-proton collision data at the centre-of-mass energies $\sqrt{s} = 7\,\text{TeV}$ and $\sqrt{s} = 2.76\,\text{TeV}$, corresponding to an integrated luminosity of $\mathcal{L} = 37.3\,\text{pb}^{-1}$ and $\mathcal{L} = 0.20\,\text{pb}^{-1}$, respectively. This measurement is a universal test of the hard interaction, combining all possible processes for jet production in one observable, and one of the first precision measurement to be performed at the LHC due to the small statistical uncertainty. The challenges of the measurement consist in the jet calibration and the systematic uncertainties thereof. The inclusive jet cross-section is determined as function of the transverse momentum and the rapidity of the jets. The different aspects of QCD are probed by comparison of data with a series of theory predictions using different distribution functions of the quarks and gluons inside the proton, and various parton shower Monte Carlo simulations that describe the fragmentation process.

Measuring at two different centre-of-mass energies offers the additional possibility to analyse the scaling behaviour of the cross-section. This is particularly interesting from the experimental side due to the large correlations of the uncertainties between measurements at the same detector. Since correlated uncertainties cancel in the ratio of the two cross-section, the systematic uncertainty can be reduced substantially with respect to the measurement at one centre-of-mass energy only. Exploiting the correlation between the measurements, the data is tested for its sensitivity to the structure of the proton.

Overview

This thesis provides a comprehensive description of the inclusive jet cross-section measurements at two centre-of-mass energies, $\sqrt{s} = 2.76\,\text{TeV}$ and $\sqrt{s} = 7\,\text{TeV}$, and the ratio thereof. The theoretical framework for jet production at a hadron collider and the definition of particle jets as the main observable

is given in Section 1. In Section 2, the employed theoretical predictions and their uncertainties are presented. The Large Hadron Collider and the ATLAS detector are introduced in Section 3, including the luminosity devices, whose calibration with respect to the $\sqrt{s} = 2.76\,\text{TeV}$ dataset is described in Section 4. Section 5 is dedicated to the jet reconstruction, the calibration of the jet energy scale, and the jet selection criteria, which are revised particularly for the $\sqrt{s} = 2.76\,\text{TeV}$ dataset. The measurements of the inclusive jet cross-section at $\sqrt{s} = 7\,\text{TeV}$ and $\sqrt{s} = 2.76\,\text{TeV}$ are presented in detail in Section 6 and 7, consisting of the data selection, the unfolding procedure, the determination of the systematic uncertainties, and the comparison of the result to different theory predictions. Both measurements are combined in the jet cross-section ratio, which takes into account the correlations of the systematic uncertainties for both, theory predictions and experimental data, as presented in Section 8. The potential of the combined data is probed in a fit of the parton distribution functions.

Author's contributions

The work presented in this thesis as been carried out within the ATLAS collaboration and comprises three analyses: the measurement of the inclusive jet cross-section at $\sqrt{s} = 2.76\,\text{TeV}$ [1] and $\sqrt{s} = 7\,\text{TeV}$ [2], and the determination of the luminosity at $\sqrt{s} = 2.76\,\text{TeV}$ [3]. Due to the complexity of modern high-energy particle physics experiments, these studies have been performed in a combined effort of a small group of people. Nevertheless, the author has made essential contributions in many aspects of the analyses, as indicated in the following.

As to the theory predictions, the author performed the large-scale production of samples using the event generator Powheg, employing different configuration with respect to the interfaced parton shower Monte Carlo simulation, the tune and the production modes, including a generic study of the matching between Powheg and the parton shower simulation and the validation against a reference sample. In particular, he investigated several approaches to suppress spurious events with large weights, which have been verified with the authors of Powheg and resulted in a new release [4].

The contributions from the author to the jet cross-section measurement at $\sqrt{s} = 7\,\text{TeV}$ comprise the complete data chain as a cross-check, including the combined central and forward region, which had been merged from two separate analyses. Furthermore, the author determined the luminosity and performed extensive data verification studies with respect to the influence of the vertex position of the collision and the stability of the jet yield under pile-up conditions.

In the course of the jet cross-section measurement at $\sqrt{s} = 2.76\,\text{TeV}$, the luminosity calibration of the corresponding dataset has been performed. The author contributed to this effort with the determination of the bunch charge and the systematic uncertainties thereof, which is an essential input to calibration procedure in the van-der-Meer scan. In addition, he studied the long-term stability of the different algorithms and helped to select the reference system for the luminosity measurement.

In the jet cross-section measurement at $\sqrt{s} = 2.76\,\text{TeV}$, the author has been one of the two main analysers and editors of the corresponding paper. His contributions comprise the event selection on basis of the detector status, verification and refinement of the trigger scheme due to potential inefficiencies, determination of the luminosity and extensive data verification studies. The latter consists in detailed comparisons of data and Monte Carlo simulation, the analysis of the jet yield in pile-up conditions and checks of the jet energy scale. He revised the jet selection that had been tested for a centre-of-mass energy of $\sqrt{s} = 7\,\text{TeV}$ only, and studied the source and impact of jets with large energy fractions in a poorly instrumented detector region. As a result, this type of jets was excluded in both data and the Monte Carlo simulation, as well as in the measurement at $\sqrt{s} = 7\,\text{TeV}$ for ratio.

CHAPTER 1

Jet production at a hadron collider

The first experimental evidence for *particle jets* was found in 1975 at the electron-positron (ep) storage ring SPEAR [7], observing collimated sprays of hadrons with high transverse momenta in opposite directions. The fact that the hadrons had not been distributed isotropically, as predicted by competing models, but in a back-to-back configuration, was interpreted as the result of a quark-antiquark pair production, where jets emerge from the complicated fragmentation process of the quarks due to the nature of the strong force. Beside quarks, jets can also originate from gluons, the second fundamental constituent that is interacting via the strong force. Indirect evidence for gluons and gluonic jets was presented by the PLUTO collaboration at the e^+e^- collider DORIS [8], confirmed later in direct measurements at the e^+e^- collider PETRA [9–12]. Figure 1.1 shows the representation of a collision event from the PLUTO experiment at the PETRA collider as cross-sectional view of the detector. Clearly, the reconstructed particle tracks are separated into three distinct regions. The process was interpreted as $e^+e^- \to q\bar{q}g$, i.e. a quark-antiquark production in combination with the emission of a hard gluon, each of which results in a jet of particles.

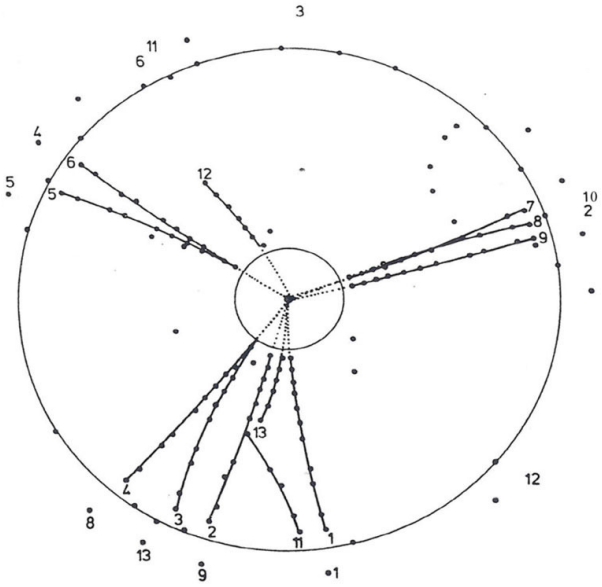

Figure 1.1: Evident three-jet event from PLUTO, interpreted as a $e^+e^- \to q\bar{q}g$ process [5, 6].

It is a fundamental finding that the quarks or gluons that are produced at the small distances of the strong interaction can be mapped on the jets of hadrons at a scale that can be observed experimentally. As a consequence, angular and energy distributions of jets are the major tools to probe the strong interaction described by the theory of *Quantum Chromodynamics* (QCD).

In this chapter, a brief review of the essential features of the strong interaction is given, leading to a sound picture of jet production events in a hadron collider. A detailed description of QCD including the derivation of the stated formulae can be found elsewhere [13, 14].

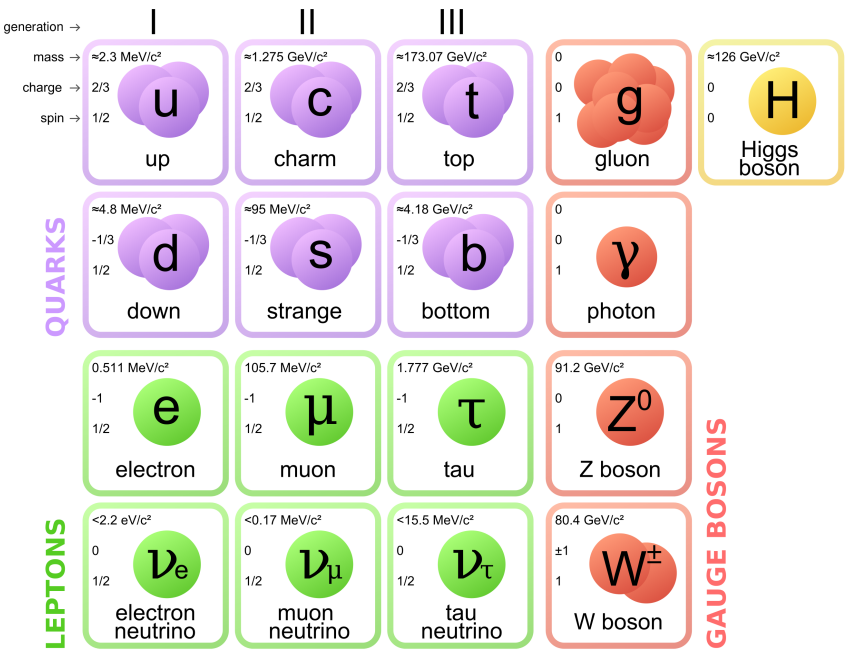

Figure 1.2: The fundamental constituents of the Standard model of Particles Physics and their properties. Shown are six quarks, six leptons, four gauge bosons and the Higgs boson, including their masses, charges and spins. The masses of the fermions and gauge bosons are taken from the Particle Data Group [15]; the Higgs mass is the average of the measurements of a particle compatible with the Higgs boson at ATLAS [16] and CMS [17]. Particles that exist in different colour or electric charge are indicated by multiple circles. The corresponding antiparticles to the fermions are not shown. Figure adapted from [18].

The outline of the chapter is as follows. A brief summary of the Standard Model of particle physics is given in Section 1.1. The characteristics of the strong interactions are explained in Section 1.2, in preparation for the comprehensive description of a proton-proton collision events in Section 1.3. Finally, the definition of particle jets and the inclusive jet cross-section are given in Sections 1.4 and 1.5.

1.1 The Standard Model of particle physics

The Standard Model of particle physics (SM) describes the elementary particles and their interactions. It is a relativistic quantum field theory of the electromagnetic, the weak and the strong force, based on the symmetry group $SU(3)_C \times SU(2)_L \times U(1)_Y$. Gravitation is not included. The SM consists of four gauge bosons as mediators of the forces, 12 elementary spin-½ fermions, namely six leptons and six quark flavours, and the Higgs boson, which assigns mass to the particles. To each of the fermions, an antiparticle with opposite charges exists. An overview of the constituents of the SM is shown in Figure 1.2.

Leptons can interact via the electromagnetic and the weak force. They may be grouped into left-handed electroweak SU(2) doublets consisting of a massive lepton and a massless neutrino. Three generations of are known to date: the electron (e), the muon (μ), the tau (τ) and the corresponding neutrinos, ν_e, ν_μ, ν_τ. Only the neutrinos and the lightest massive lepton, the electron, are stable, whereas the muon and tau decay via the weak force. Electron, muon and tau carry an electric charge of -1 in units of the elementary charge. The neutrinos are electrically neutral and thus only interact weakly. Observations of neutrino oscillations [19] indicate that the mass of the neutrinos is non-zero.

Quarks are subject to the electromagnetic, the weak and the strong force. They exist in six different flavours, namely up (u), down (d), strange (s), charm (c), bottom (b) and top (t), given in increasing order of mass. It ranges from a few MeV/c^2 for the light quarks d, u to about 170 GeV/c^2 for the top quark. Quarks carry an electric charge of either $-1/3$ elementary charges (d, s, b) or $+2/3$ (u, c, t), and a colour charge, which is attributed in the framework of Quantum Chromodynamics (QCD), describing the strong interaction. Only colour-neutral objects can exist freely, hence quarks form compound, colour-less

objects: the hadrons. The concept of colour within QCD will be elaborated on in Section 1.2.

The force carriers in the SM are spin-1 gauge bosons, obtained from the local $SU(3)_C \times SU(2)_L \times U(1)_Y$ gauge symmetry that defines the SM. The electroweak symmetry group $SU(2)_L \times U(1)_Y$ generates the mediator of the electromagnetic force, the photon (γ), and the mediators of the weak force, the $W^{\pm}$ and Z bosons. The propagator of the strong force is the gluon (g), generated by the colour gauge group $SU(3)_C$. Gluons carry colour and anticolour, giving rise to eight gluons of the resulting colour octet. Hence, they can interact with themselves. An overview of the interaction between the particles of the SM is given in Figure 1.3.

The mass of the fermions and the gauge bosons is acquired by means of the so-called Higgs mechanism. The mechanism is a spontaneous symmetry breaking of the $SU(2)_L \times U(1)_Y$ group. The Higgs mechanism gives rise to the existence of a massive particle, the so-called Higgs boson. It is uncharged, carries spin-0 and couples to the mass of particles, including self-coupling. The original formulation of the SM had not considered the masses of particles. The Higgs mechanism was introduced particularly to explain why the photon is massless while the $W^{\pm}$ and Z bosons are very heavy. There are strong indications that the boson discovered recently at the LHC [16, 17] is the SM Higgs boson, showing its properties regarding spin, mass, charge, parity, and a uniform coupling to mass in its decay modes.

1.2 Quantum Chromodynamics

The strong interaction of coloured objects, i.e. quarks and gluons, is described within the framework of Quantum Chromodynamics (QCD). Two properties are characteristic of QCD, namely *confinement* and *asymptotic freedom*. Confinement relates to the phenomenon that coloured objects do not exist freely. The colour confinement hypothesis of QCD explains this observation by the nature of the strong force between two coloured particles, which, unlike the electromagnetic interactions, does diminish as they are separated, but increases linearly with the distance. As a consequence an infinite amount of energy would be required to fully separate two coloured objects. In contrast to this, asymptotic freedom denotes the property of QCD that with increasing energies, or decreasing distances, the strength of the strong force is reduced, and quarks asymptotically act as free particles. The two properties can be understood from the nature of the gluon self-interaction, as outlined in the following.

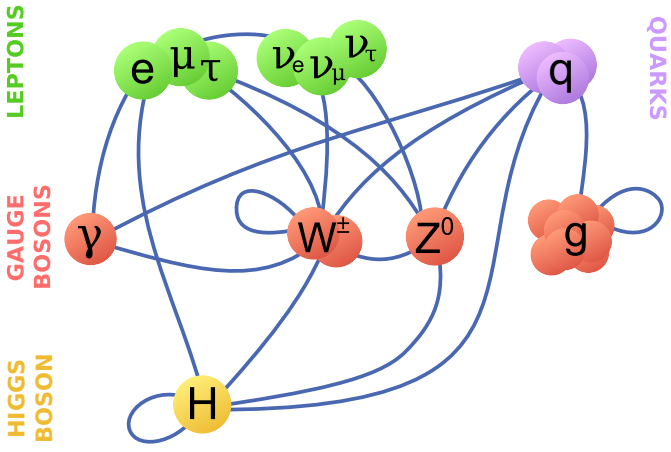

Figure 1.3: Overview of interactions in the Standard Model of particle physics. Particles that interact with each other are connected with a *solid line*. Figure adapted from [20].

QCD is a non-abelian gauge theory based on the $SU(3)_C$ symmetry group. Its Lagrangian is given by

$$\mathcal{L}_{\text{QCD}} = \sum_{q}^{n_f} \overline{\psi}_{q,a}(i\gamma^\mu \partial_\mu \delta_{ab} - g_S \gamma^\mu t^C_{ab} \mathcal{A}^C_\mu - m_q \delta_{ab})\psi_{q,b} - \frac{1}{4} F^A_{\mu\nu} F^{\mu\nu}_A, \tag{1.1}$$

where the summation runs over the six different quark flavours q, and repeated indices are summed over according to the Einstein summation convention. The Dirac matrices γ^μ are used as orthogonal basis vectors for the contravariant vectors in the 4-dimensional Minkowski space. The $\psi_{q,a}$ is the quark-field spinor of a quark with mass m_q and the colour index $a = [1, N_c = 3]$, where N_c is the number of colours. Quarks are called the *fundamental representation* of the $SU(3)_C$ colour group.

In contrast, gluons are called the *adjoint representation* of the $SU(3)_C$ colour group, derived from the gluon fields $\mathcal{A}^C$ with $C = [1, N_c^2 - 1 = 8]$. The eight 3×3 matrices $SU(3)_C$ are the generators of the $SU(3)_C$, responsible for the colour exchange in the quark-gluon interaction. The QCD coupling constant g_S is related to the strong coupling α_S via $\alpha_S = g_S^2/4\pi$. The gluonic field tensor $F^A_{\mu\nu}$ is derived from the structure constants of the $SU(3)_C$, f_{ABC}, as

$$F^A_{\mu\nu} = \partial_\mu \mathcal{A}^A_\nu - \partial_\mu \mathcal{A}^A_\mu - g_S f_{ABC} \mathcal{A}^B_\mu \mathcal{A}^C_\nu. \tag{1.2}$$

The last term in Equation 1.2 describes the gluon self-interaction in QCD and leads to triple and quartic gluon vertices. In terms of Feynman diagrams, the Lagrangian can be expressed by the following, simplified graphical representation:

$\mathcal{L}_{\text{QCD}} \approx$ 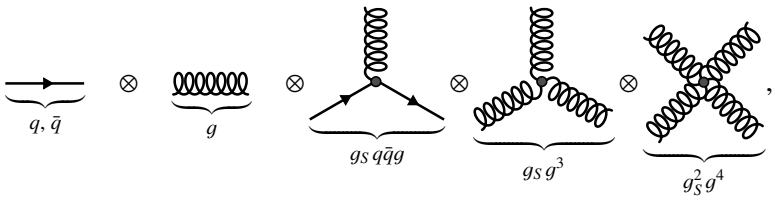

, (1.3)

where $q\bar{q}$ correspond to quarks, g to the gluons, and g_S is the QCD coupling constant, as before. The matrix element of the transitions between initial and final state is obtained using the Feynman rules [13]. The cross-section of a particular final state, e.g. a process $q\bar{q} \to q\bar{q}$, is given by the sum of all possible combinations, including higher-order loop corrections. It is the last two terms in Equation 1.3 that give rise to the increased complexity of QCD compared to the electromagnetic interaction in quantum electrodynamics (QED), and characterise the nature of the strong force.

1.2.1 Asymptotic freedom and colour confinement

Higher-order loop corrections in the calculation of a process introduce ultra-violet (UV) divergencies from the fact that gluons create infinitely high momenta. Being a quantum field theory, these divergencies are treated in QCD with the concepts of *renormalisation* and *regularisation*. In the regularisation procedure, the infinities are absorbed in counterterms, which allows to express the divergencies in a well-defined manner. Thus, the non-physical divergencies may be separated from the physical process by introducing a *renormalisation scale* μ_R, at which the non-physical corrections become large. Here, the physical scale to which μ_R relates to is the scale of the interaction, Q^2. Generally, the impact of the non-physical corrections is expected to decrease with increasing accuracy of the calculation, i.e. the number of included higher-order diagrams.

As a consequence of the renormalisation procedure, a scale dependence is introduced to the strong

coupling constant α_S: the coupling is not limited to a single vertex like qqg, but includes an infinite amount of loop corrections. Accordingly, α_S becomes a function of the scale Q^2 at which it is evaluated. In the one-loop approximation, i.e. the first order of perturbation theory, the strong coupling constant α_S is obtained as

$$\alpha_S(Q^2) = \frac{\alpha_S(\mu_R^2)}{1 + \beta_0\, \alpha_S(\mu_R^2)\, \ln(Q^2/\mu_R^2)}. \tag{1.4}$$

The coefficient β_0 is the first term in the β function of the strong coupling constant [21, 22], which expresses the dependence of α_S on the energy. β_0 evaluates to

$$\beta_0 = \frac{11N_c - 2n_f}{12\pi}. \tag{1.5}$$

where N_c is the number of colours, and n_f the number of quark flavours accessible at the scale Q^2. Since the N_c term dominates against the n_f term, β_0 has a positive sign. In other words, the corrections from gluon loop diagrams exceed the contributions from $q\bar{q}$ loops. As a result, $\alpha_S(Q^2)$ in Equation 1.4 becomes asymptotically weaker for increasing energies and decreasing distances. This is the aforementioned *asymptotic freedom* of quarks and gluons in the limit of high energies and short distances. The effect of the *running coupling* of the strong interaction $\alpha_S(Q^2)$ can by understood analogous to the *screening* of charges in QED due to virtual electron-positron loops in the vacuum. In the vicinity of an electric charge, the virtual electron-positron charges effectively polarise the vacuum, which diminishes the electric field at a finite distance. Hence, the coupling is modified: it appears weaker at large distances, and stronger at small distances. However, the effect is opposite in QCD. While $q\bar{q}$ pairs behave similarly to the electron-positron pairs, thus screening the colour charge, the gluon-gluon loops enhance the field, as they carry colour charge themselves. The occurring self-interaction of the gluon in virtual gluon-loops thus increases the colour charge, and α_S appears stronger at large distances. At short distances in contrast, i.e. inside the surrounding gluonic colour contribution, the bare strong force is not as strong. At sufficiently high values of Q^2, $\alpha_S(Q^2)$ becomes small enough to perform calculations in a perturbative approach. A common choice is $Q^2 > 1\,\mathrm{GeV}^2$.

Although it does not strictly follow from the theory of QCD, the self-interacting nature of gluons can also serve as an explanation for the phenomenon of *colour confinement*. When two colour-charged objects that form a colourless state together are separated, a colour field is created between them, consisting of gluons mediating the strong interaction. Due to the self-attraction of gluons, the field forms a narrow tube, having a diameter in the order of 1 fm. Thus, the force mediated by this tube is independent of the distance, while the energy stored in the colour field increases linearly with the distance between the two particles. At some point, it becomes energetically favourable to create a new $q\bar{q}$ pair from the vacuum instead of further increasing the field energy. The process of creating new $q\bar{q}$ pairs only stops when the produced particles form colour-neutral final states, e.g. with the initial-state particles.

1.2.2 The parton model and evolution equations

As a consequence of asymptotic freedom, the constituents of the proton act as quasi-free particles. Hence, deep inelastic scattering (DIS) of protons can be explained by an elastic scattering of point-like particles, given that the involved energies are sufficiently high. This interpretation was first introduced in the *parton model* [23, 24] and lead to the improved parton model in the framework of QCD. Since proton-proton (pp) collisions hold the complexity of two composite objects, the parton model may be introduced using DIS of electron-proton (ep) collisions [14].

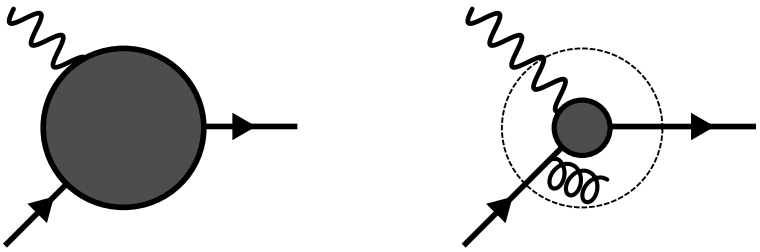

(a) $Q^2 = Q_0^2$ (b) $Q^2 > Q_0^2$

Figure 1.4: Deep inelastic scattering (DIS) in electron-proton collisions at a transverse momentum squared of Q^2. Adapted from [25].

Without further knowledge about the internal structure of the proton, the differential cross-section for DIS in a collisions of an electron and a proton with the four-momenta p_e and p_p, respectively, is given in the high energy limit, $Q^2 \gg m_p^2 y^2$, by

$$\frac{d^2\sigma}{dx\,dQ^2} = \frac{4\pi\alpha^2}{Q^4}\left[(1-y)\,\frac{F_2(x,Q^2)}{x} + y^2 F_1(x,Q^2)\right]. \tag{1.6}$$

Here, F_1 and F_2 are the pure magnetic and electromagnetic *structure functions* of the proton, respectively. The structure functions are a convenient way to express the incalculable internal, compound structure. They are parametrised in terms of the squared momentum transfer between a quark and the electron, $Q^2 = -q^2$, and the momentum fraction x of the proton momentum carried by the scattered parton. The fraction of the lepton energy transferred to the proton rest frame, y, is given by $y = \frac{p_p \cdot q}{p_p \cdot p_e}$.

In the simple quark-parton model, the DIS cross-section is interpreted as the sum of the elastic cross-section of the electron with each of the point-like partons. It results in the cross-section

$$\frac{d\sigma}{dQ^2} = \frac{4\pi\alpha^2}{xQ^4}\sum_q^{n_f}\int_0^1 d\xi\, q(\xi)\, e_q^2\,\frac{x}{2}\left[1+(1-y)^2\right]\delta(x-\xi), \tag{1.7}$$

where $q(\xi)$ denotes the probability to find a quark q in the proton with a fraction ξ of the total proton momentum. $q(\xi)$ is also called *parton distribution function* (PDF). Comparing Equations 1.6 and 1.7 yields

$$F_2 = 2xF_1 = \sum_q^{n_f} e_q^2\, xq(x), \tag{1.8}$$

The first term in Equation 1.8 is the Callan-Gross relation, which is a direct consequence of quarks having spin-½. The second term predicts that in the DIS limit, $Q^2 \to \infty$, the content of the proton only depends on the momentum fraction x of the parton, but not on the absolute energy of the collision. This property is called *Bjorken scaling*. However, $F_1(x, Q^2)$ and $F_2(x, Q^2)$ have been found to obey the Bjorken scaling only approximately at $x \approx 0.1$, but to violate scaling for lower and higher x [15].

The *scale violations* of the structure function in the proton can be explained within the framework of QCD by the additional processes of the partons inside the proton. At first order in α_S, these are gluon radiation, $q \to qg$, gluon splitting, $g \to gg$, and quark pair production, $g \to qq$. The violation of the Bjorken scaling in DIS of ep collisions can be understood as depicted in Figure 1.4: a photon which

interacts with a quark at a certain momentum transfer squared Q_0^2 probes the proton content at distances proportional to $1/Q_0^2$. The photon-quark interaction appears to be point-like, as shown in Figure 1.4a. Probing the same quark at a scale $Q^2 > Q_0^2$ increases the spatial resolution of the probing photon and allows to detect for instance a possible gluon radiation that might not have been visible before, as shown in Figure 1.4b. Hence, while the photon at Q_0 has seen a quark with transverse momentum fraction of x before, the photon at Q^2 effectively interacts with a quark with a fraction of $x - z$, where z is the momentum fraction carried away by the gluon. As a consequence, the cross-section depends on Q^2.

Given the contributions from additional gluon and quark emissions due to the asymptotic freedom of the strong coupling, the content of the proton is divided between *valence quarks*, *sea quarks* and gluons. Valence quarks determine the outer properties of the proton in terms of the quantum numbers. Being composed of two up quarks and one down quark, its charge is $+1e$. Sea quarks are $q\bar{q}$ pairs which are generated from gluons in quantum fluctuations of the vacuum. The generation of gluons and sea

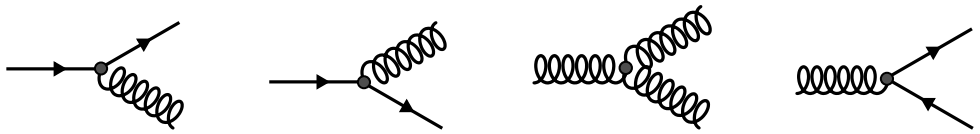

(a) $P_{q\leftarrow q}(z)$ (b) $P_{g\leftarrow q}(z)$ (c) $P_{g\leftarrow g}(z)$ (d) $P_{q\leftarrow g}(z)$

Figure 1.5: Feynman diagrams of the splitting functions $P_{j\leftarrow i}(z)$ at the lowest order of perturbative QCD. Each splitting function expresses the probability that a parton of type i transforms to a parton of type j. Here, the outgoing parton j is represented by the upper branch, carrying the fraction z of the momentum of the incoming parton i.

quarks can be described to first order with so-called splitting functions $P_{j\leftarrow i}(z)$. Each splitting function gives the probability that a parton of type i emits a quark or gluon, transforming it to a parton of type j, as shown in Figure 1.5. Four different transformations exist at lowest order, namely $P_{q\leftarrow q}(z)$, $P_{g\leftarrow q}(z)$, $P_{g\leftarrow g}(z)$, and $P_{q\leftarrow g}(z)$. The variable z denotes the momentum fraction carried away by the outgoing parton. Hence, for a given cross-section σ_n in the parton evolution after n splittings, the cross-section σ_{n+1} after the subsequent splitting can be calculated as

$$\sigma_{i+1} = \int \sigma_i \frac{dp_i^2}{p_i^2} dz \frac{\alpha_S}{2\pi} P_{j\leftarrow i}(z), \tag{1.9}$$

where p_i is the four-momentum of the incoming parton.

Using this result, the parton densities can be expressed in terms of x and Q^2 as

$$\frac{dq_i(x,Q^2)}{d\ln(Q^2)} = \frac{\alpha_S}{2\pi} \int_x^1 \left(q_i\left(z,Q^2\right) P_{q\leftarrow q}\left(\frac{x}{z}\right) + g\left(z,Q^2\right) P_{q\leftarrow g}\left(\frac{x}{z}\right)\right) \frac{dz}{z} \tag{1.10}$$

$$\frac{dg(x,Q^2)}{d\ln(Q^2)} = \frac{\alpha_S}{2\pi} \int_x^1 \left(\sum_i q_i\left(z,Q^2\right) P_{g\leftarrow q}\left(\frac{x}{z}\right) + g\left(z,Q^2\right) P_{g\leftarrow g}\left(\frac{x}{z}\right)\right) \frac{dz}{z}. \tag{1.11}$$

Equation 1.10 and 1.11 are the QCD evolution equations of parton densities, also called *DGLAP* equations [26–28]. The first equation describes the transformation of the quark densities $q_i(x,Q^2)$ with Q^2 due to gluon emission and gluon splitting. The second equation describes the transformation of the gluon density $g(x,Q^2)$ due to additional gluons radiated by quarks or gluons. The DGLAP equations in the presented form are evaluated at leading order and assume massless partons. Hence, they only apply to the light quarks u, d, and s.

1.2.3 QCD factorisation

At higher orders, the parton density evolution becomes a combination of subsequent $1 \to 2$ processes of quark splittings and gluon emissions, as described by the DGLAP equations and splitting functions. The process can be illustrated as follows:

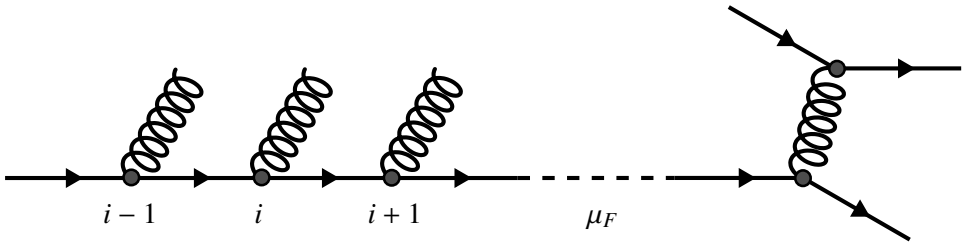

(1.12)

The incoming quark experiences a parton evolution, radiating gluons along its way. Each gluon carries away a transverse momentum $k^2_{\mathrm{T},i}$ in an interaction at order $\alpha_\mathrm{S}\log(Q^2)$, before the altered quark eventually enters the hard parton-photon interaction depicted on the right. Hence, two different types of calculations are generally present: the collinear parton splitting or soft gluon emission in the $1 \to 2$ process before the parton collision on the one hand; and the hard $2 \to 2$ scattering process on the other hand. It is an essential concept of the QCD framework that these two categories, namely the long-distance, universal, soft and collinear contributions, and the short-distance, process-specific perturbative hard scattering, can be separated. This concept is known as *factorisation theorem* [29].

For the interaction of two protons A, B with the momenta p_A and p_B, respectively, the cross-section can be written as the convolution of the parton distribution functions q_a, q_b and the hard scattering cross-section $\hat{\sigma}_{ab\to cd}$:

$$\mathrm{d}\sigma(p_A, p_B, Q^2) = \sum_{a,b} \int_{x_a,x_b=0}^{1} dx_a dx_b \underbrace{q_a\left(x_a, \mu_F^2\right) q_b\left(x_b, \mu_F^2\right)}_{\text{PDFs}} \times \underbrace{\mathrm{d}\hat{\sigma}_{ab\to cd}\left(p_a, p_b, \alpha_\mathrm{S}(\mu_R^2), Q^2/\mu_F^2, Q^2/\mu_R^2\right)}_{\text{hard scatter}}. \tag{1.13}$$

Here, $p_a = x_a p_A$ and $p_b = x_b p_B$ are the initial momenta of parton a and b, and μ_F and μ_R are the factorisation and renormalisation scales, respectively. The renormalisation scale μ_R was introduced to treat UV divergencies in the perturbative approximation of the strong coupling. The factorisation scale μ_F absorbs the collinear divergencies of QCD into physical quantities in a similar way, which can be interpreted as defining a boundary between the soft and hard terms here. Both, μ_F and μ_R are not know a priori. A common choice for deep inelastic scattering is $\mu_F^2 = \mu_R^2 = Q^2$. In principle, the cross-section σ should be independent of the factorisation and renormalisation scales. Indeed, this is the case when σ is calculated to all orders in α_S. However, due to the necessary approximations in both the non-perturbative and perturbative contributions, this is usually not possible and results in an uncertainty on the theory calculation.

1.3 Proton-proton collisions: the full picture

The concepts introduced in the preceding sections allow to describe the complete process of a proton-proton collision as illustrated in Figure 1.6. The process starts on the left hand side with two partons from the colliding protons, mostly gluons at the energies considered in the following. These initial-

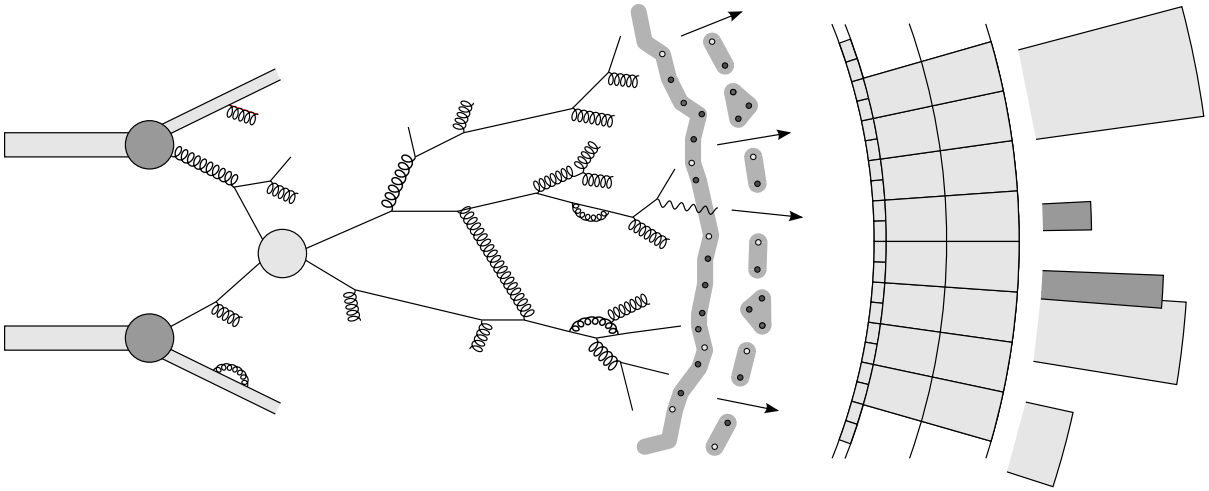

Figure 1.6: Illustration of the hard interaction of two partons from the incoming protons and the subsequent parton shower, hadronisation and reconstruction of the outgoing particles.

state particles first undergo a parton evolution in subsequent parton splittings and additional radiations, so-called *initial-state radiation* (ISR), before they interact at a high momentum scale. Essentially, any fundamental particle of the SM can be produced in the hard interaction, namely quarks, leptons, gauge bosons or the Higgs boson, but also new particles from theories beyond the Standard Model (BSM). However, the QCD processes are expected to dominate, i.e. the outgoing partons are usually quarks and gluons. The products evolve further through subsequent splittings and emissions analogous to the parton evolution in the initial state. This so-called *final-state radiation* (FSR) leads to the formation of a *parton shower*. As the parton shower develops, the scale of the interaction decreases, while the strong coupling increases, respectively. This ultimately triggers the process of hadronisation, in which the partons form colourless states. Some of the generated hadrons are not stable and decay further. The final decay products are measured in the detector, as depicted on the right hand side of Figure 1.6. Not shown are additional interactions from the remaining constituents of the proton, the so-called *underlying event*.

1.3.1 Kinematics of the collision

In the high energy limit, the two incoming protons A, B with four-momenta p_A, p_B collide at a centre-of-mass energy of

$$\sqrt{s} = p_A + p_B. \tag{1.14}$$

The colliding partons a, b inside the protons, however, only carry a momentum fraction x_a, x_b, according to the parton distribution functions as explained in Section 1.2.2. Since x_a and x_b usually differ, the centre-of-mass frame of the parton-parton interaction is boosted along the beam direction. Thus it is convenient to define variables that transform easily under the longitudinal boosts: the *rapidity* y, the azimuthal angle ϕ, and the transverse momentum p_{T}. For a given four-momentum of a parton $p^\mu = (E, p_x, p_y, p_z)$, the rapidity with respect to a beam along the z axis is defined as

$$y = \frac{1}{2} \ln\left(\frac{E + p_z}{E - p_z}\right). \tag{1.15}$$

The rapidity is additive under Lorentz transformation in z direction and rapidity differences $\Delta y = y_2 - y_1$ are boost invariant. In the limit of massless partons, $m \to 0$, the rapidity transforms into the *pseudo-rapidity* η, given as

$$\eta = -\ln \tan\left(\frac{\theta}{2}\right). \tag{1.16}$$

Here, θ is the polar angle between the momentum vector of the parton and the beam axis. The pseudo-rapidity is useful from the experimental point of view, since it provides a fixed angle that can be measured directly in the detector. Further useful numerical quantities in the interaction of two partons are

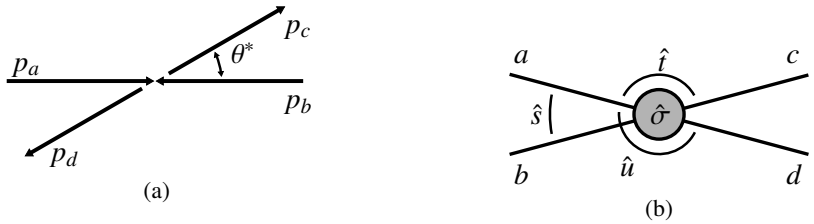

Figure 1.7: Two body parton-parton kinematics: (a) definition of the scattering angle $\theta*$ in the centre-of-mass frame (b) definition of the Mandelstam variables $\hat{s}$ and $\hat{t}$. Adapted from [14].

the *Mandelstam* variables. Figure 1.7a shows the kinematics in the scattering of two partons $ab \to cd$ with the scattering angle θ^* in the centre-of-mass frame. The Mandelstam variables encode the energy, momenta, and angles of the partons of the scattering process in a Lorentz-invariant way, according to

$$\hat{s} = (p_a + p_b)^2 \tag{1.17}$$

$$\hat{t} = (p_a - p_c)^2 = -\frac{\hat{s}}{2}(1 - \cos\theta^*) \tag{1.18}$$

$$\hat{u} = (p_a - p_d)^2 = -\frac{\hat{s}}{2}(1 + \cos\theta^*). \tag{1.19}$$

The definition of $\hat{s}$, $\hat{t}$ and $\hat{u}$ is also depicted in Figure 1.7b. Using energy and longitudinal momentum conservation, the momentum fractions x_a, x_b can be expressed in terms of the rapidities of the outgoing partons c and d and the dimensionless quantity $x_\mathrm{T} = 2p_\mathrm{T}/\sqrt{s}$ as

$$x_a = \frac{x_\mathrm{T}}{2}\left(e^{y_c} + e^{y_d}\right) \tag{1.20}$$

$$x_b = \frac{x_\mathrm{T}}{2}\left(e^{-y_c} + e^{-y_d}\right). \tag{1.21}$$

1.3.2 Hard interaction

The calculation of the hard interaction profits from the asymptotic freedom in QCD, which allows the short-distance cross-section in Equation 1.13 to be calculated in a perturbative series at fixed order of the strong coupling. Using the Mandelstam variables given in Equations 1.17 to 1.19, the parton-parton cross-section of a subprocess [14] contributing to the total cross-section can be written as

$$d\hat{\sigma} = \frac{1}{16\pi^2\hat{s}}\overline{\sum}|\mathcal{M}|^2\,\frac{d^3p_c}{E_c}\,\delta(\hat{s} + \hat{t} + \hat{u}). \tag{1.22}$$

process	$\overline{\sum}\lvert\mathcal{M}\rvert^2/(4\pi\alpha_S)^2$	diagrams
$qq' \to qq'$	$\frac{4}{9}\frac{s^2+u^2}{t^2}$	(a)
$q\bar{q}' \to q\bar{q}'$	$\frac{4}{9}\frac{s^2+u^2}{t^2}$	(a)
$qq \to qq$	$\frac{4}{9}\left(\frac{s^2+u^2}{t^2}+\frac{s^2+t^2}{u^2}\right)-\frac{8}{27}\frac{s^2}{ut}$	(a),(b)
$q\bar{q} \to q'\bar{q}'$	$\frac{4}{9}\frac{t^2+u^2}{s^2}$	(c)
$q\bar{q} \to q\bar{q}$	$\frac{4}{9}\left(\frac{s^2+u^2}{t^2}+\frac{t^2+u^2}{s^2}\right)-\frac{8}{27}\frac{u^2}{st}$	(a),(c)
$q\bar{q} \to gg$	$\frac{32}{27}\frac{u^2+t^2}{ut}-\frac{8}{3}\frac{u^2+t^2}{s^2}$	(d),(e),(f)
$gg \to q\bar{q}$	$\frac{1}{6}\frac{u^2+t^2}{ut}-\frac{3}{8}\frac{u^2+t^2}{s^2}$	(d),(e),(f)*
$qg \to qg$	$-\frac{4}{9}\frac{u^2+s^2}{us}+\frac{u^2+s^2}{t^2}$	(g),(h),(i)
$gg \to gg$	$\frac{9}{2}\left(3-\frac{ut}{s^2}-\frac{us}{t^2}-\frac{st}{u^2}\right)$	(j),(k),(l)

Table 1.1: The invariant matrix elements squared $\overline{\sum}\lvert\mathcal{M}\rvert^2$ for $2 \to 2$ scattering processes in QCD at lowest order for massless partons. The colour and spin indices are averaged over the initial states, and summed over the final states. The corresponding diagrams for each process are given in Figure 1.8. Diagrams marked with * are reversed [13, 14, 30].

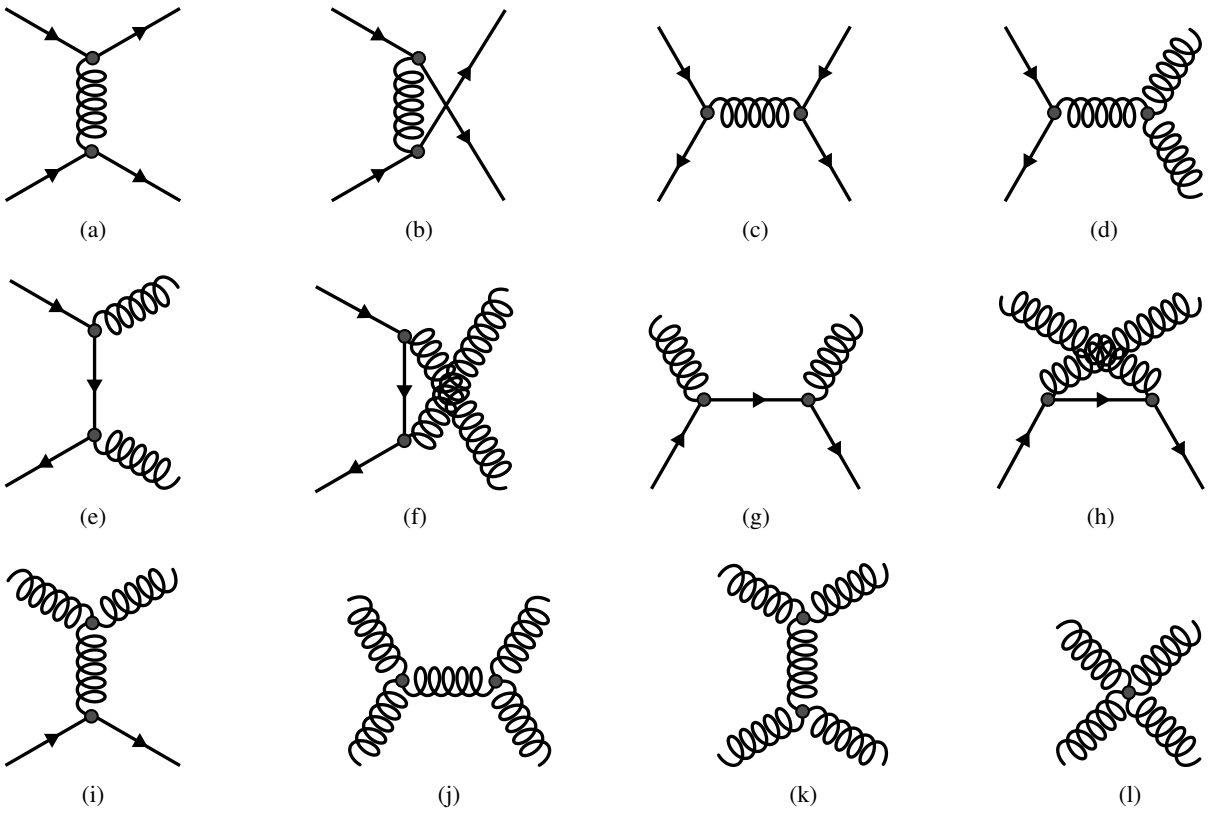

Figure 1.8: Leading-order QCD diagrams for quark and gluon scattering. Diagrams adapted from [14].

Here, p_c and E_c are the momentum and energy of the scattered parton c, and $\overline{\sum}|\mathcal{M}|^2$ denotes the invariant matrix element squared of the $2 \to 2$ subprocess. The matrix elements for all $2 \to 2$ subprocesses in QCD at leading order (LO) for massless partons are given in Table 1.1, and the corresponding diagrams are shown in Figure 1.8. The last term in Equation 1.22, $\delta(\hat{s}+\hat{t}+\hat{u}$, accounts for energy and momentum conservation.

Higher-order terms in the perturbative series of α_S generally diminish the sensitivity to the renormalisation and factorisation scale and thus are more predictive. However, due to the self-interacting nature of the strong coupling, the number of diagrams that contribute to the cross-section increases rapidly with higher orders, so that the current precision of the theory calculation does not exceed next-to-leading order (NLO) for QCD scattering processes. The NLO terms in α_S comprise two different types of corrections. On one hand, the cross-section of the $2 \to 2$ is modified by additional terms from virtual quantum loops. Accordingly, these terms are denoted as *virtual corrections*. On the other hand, the initial- and final-state partons may emit additional gluons or split into $q\bar{q}$ pairs, resulting in a $2 \to 3$ process. Since these terms correspond to the production of a real parton in the final state, they are called *real corrections*. A few diagrams that correspond to these subprocesses are shown in Figure 1.9.

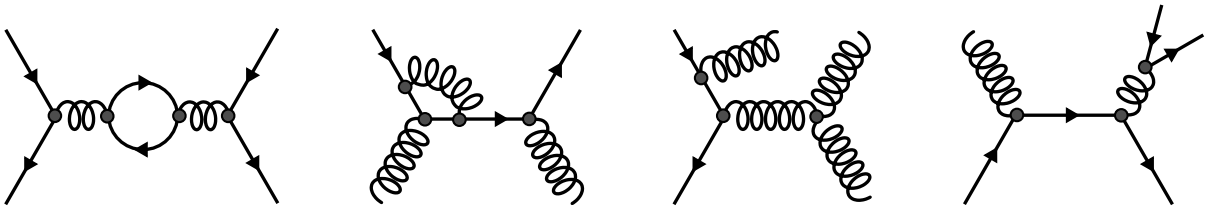

(a) (b) (c) (d)

Figure 1.9: Examples of next-to-leading-order QCD diagrams for quark and gluon interactions: (a), (b) virtual contributions (c), (d) real contributions.

1.3.3 Parton showers from initial and final state radiation

The final state of the hard subprocess usually comprises two partons that move a way from each other with large transverse momentum p_T. Due to colour confinement, these partons cannot exist freely. Instead, the increasing energy in the colour field between them enhances the probability of parton splittings and additional radiation. It leads to a fragmentation process, in which the initial partons successively lose energy by creating $q\bar{q}$ pairs and emitting gluons. The developing parton shower results in a high multiplicity of final-state partons.

In terms of the hard subprocess, the successive collinear parton splittings and soft gluon emissions in the fragmentation represent higher-order corrections. They are described by the splitting functions $P_{j\leftarrow i}(z)$ and the DGLAP parton evolution functions as given in Equations 1.10 and 1.11. As it is not possible to calculate the corrections exactly, the parton evolution is approximated by the dominant contributions in orders of α_S.

The parton splitting functions describe only the collinear-enhanced parton splittings and emissions, corresponding to the real terms in the NLO corrections of the hard interaction. To obtain a coherent description of the parton shower development at fixed order in the strong coupling, the virtual terms from quantum loop effects have to be taken into account as well. They are included in the *Sudakov form factors* $\Delta_i(Q_{i-1}, Q_i)$, which interpret the parton evolution from a probabilistic point of view. They give the probability of a parton i to evolve from a scale Q_i to Q_{i-1} without an additional branching into any

of the partons j. Hence, virtual contributions are incorporated in the possibility not to branch, while the real contributions are represented by the splitting itself. The Sudakov form factor is given by

$$\Delta_i(Q_{i-1}, Q_i) = \exp\left(-\sum_j \int_{Q_0}^{Q} \frac{dQ}{Q} \int_0^1 dz \, \frac{\alpha_S}{2\pi} P_{j\leftarrow i}(z)\right). \tag{1.23}$$

The generation of the parton shower is performed as follows. First, the interval $[\hat{Q}^2, Q_0^2]$ is divided into n subintervals $[Q_i^2, Q_{i-1}^2]$, where $\hat{Q}$ is a initial scale given by the hard process, and Q_0 is the cut-off scale at which further emissions cannot be resolved. In each subinterval $[Q_i^2, Q_{i-1}^2]$, the probability $\Delta_i(q, q_0)$ that no branching occurs is calculated according to Equation 1.23. The procedure is repeated for each branch j until the cut-off scale Q_0 is reached eventually. An example of a parton shower evolution in the probabilistic approach is depicted in Figure 1.10.

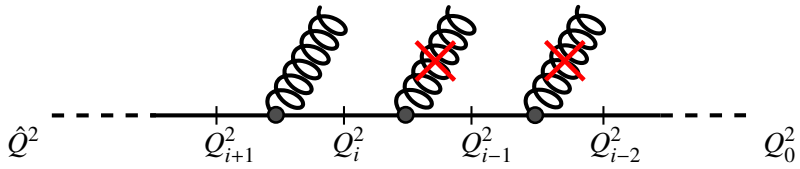

Figure 1.10: Illustration of the parton shower evolution in the probabilistic approach using the Sudakov form factor $\Delta_i(Q_{i-1}, Q_i)$. Branchings which are vetoed in this example according to $\Delta_i(Q_{i-1}, Q_i)$ are marked with a *red cross*.

Two different types of parton showers occur in proton-proton collisions. A parton shower from *final-state radiation* (FSR) develops subsequent to the hard interaction and evolves from the scale of the hard interaction, $\hat{Q}$, to the cut-off scale Q_0, as described above. However, parton showers can also be triggered from initial-state radiation (ISR), prior to the hard interaction. Here, the interaction scale $\hat{Q}$ of the hard process marks the end of the parton shower evolution. Instead of developing the shower from a large to a small scale, additional parton splittings and gluon emissions of the incoming parton are added in reverse order, starting from the scale of the hard process $\hat{Q}$. In the *backward evolution*, the energy of the incoming parton is increased in each reaction until the kinematic constraint of the pp collision, $x_a x_b \, s = \hat{s}$, is reached. Here, x_a, x_b are the momentum fractions of the colliding partons, and s and $\hat{s}$ are the centre-of- mass energies squared of the protons and partons, respectively. Since the backward evolution modifies the scale of the initial parton, it also alters the probability to find a parton with such scale in the proton given by the PDF $q(x, Q^2)$. Hence, the probability of the initial parton to avoid any splitting in the interval $[Q_{i+1}, Q_i]$ has to be changed accordingly:

$$\Delta_i'(Q_{i+1}, Q_i) = \Delta_i(Q_{i+1}, Q_i) \frac{q(x, Q_{i+1})}{q(x, Q_i}). \tag{1.24}$$

Usually, the parton evolution is not expressed in terms of Q^2, but the transverse momentum, p_T, or the opening angle of the outgoing particle, starting from the highest p_T and largest angles, respectively.

1.3.4 Hadronisation

Due to the steady decrease of the interaction scale in the parton shower development, the perturbative calculation of the strong coupling becomes invalid at some point, and the shower evolution enters a non-perturbative phase, in which the coloured particles form colour-neutral final states. To date, no theory exist to calculate this phase of hadronisation, being one of the least understood processes in QCD.

Instead, models based on general features of QCD are used. The two most prominent are the *Lund-string model* [31] and the *cluster model* [32]. Both models are based on the notion that the potential energy between two separating coloured object increases linearly with the distance, while the force between them stays constant. Once the energy stored in the field becomes large enough, new $q\bar{q}$ pairs are produced from the vacuum. This interpretation is borrowed from the confinement of coloured objects due to the self-attraction of gluons, as described in Section 1.2.1. Differences between the models arise from the overall formation of colour-neutral bound states.

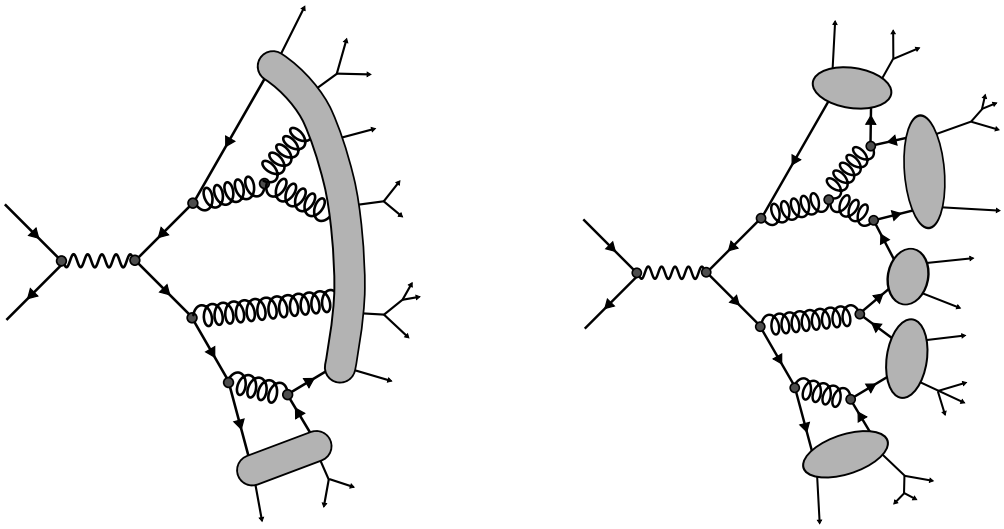

(a) string model (b) cluster model

Figure 1.11: Illustration of the hadronisation process in parton showers using (a) the Lund-string model and (b) the cluster model. The parton shower is initiated from a $q\bar{q}$ pair.

String model The hadronisation in the Lund-string model is illustrated in Figure 1.11a, showing a parton shower initiated from a $q\bar{q}$ pair. This model is based on the assumption that each parton has a unique colour partner, connected by a string segment. It is depicted here by the grey band, which connects the quarks in the final-state of the parton shower. Since the quarks have been produced from a colour-neutral photon, the string between the initial $q\bar{q}$ pair is colour-neutral by construction. Subsequent $q\bar{q}$ splittings during the parton shower break the strings, but preserve the colour neutrality of each string requiring that the connected $q\bar{q}$ pairs have opposite colour. The colour-neutral final-state hadrons, shown by the small arrows on the right, are achieved using the same mechanism of $q\bar{q}$ splittings, until all energy stored in the string is consumed eventually. Additional gluons in between the two colour partners are understood in the large-n limit, i.e. due to their large number, they do not alter the colour connection. Instead, they produce a kink in the string, which results in an increased hadron production in direction of the gluons due to the higher energy of the stretched field.

Cluster model The cluster model makes use of the *pre-confinement* property of QCD [33]. It says that at evolution scales well below the scale of the initial interaction, partons can be grouped locally in colour-neutral clusters independently of the hard process type and scale. In a first step, all gluons in the final-state of the parton shower are forced to split further into $q\bar{q}$ pairs to reach a scale below a cut-off Q_0, as shown in Figure 1.11b. Subsequently, clusters are formed from quarks and antiquarks to colour-neutral states of so-called *proto-hadrons*. The production of final-state hadrons is analogous to the last step in the string model described above.

1.4 Jet definition

The description of pp collisions in Section 1.3 consists of three different levels in the evolution of the interaction: the *parton level*, comprising the final-state partons from the hard interaction; a spray of hadrons at *particle level*, formed in the hadronisation process; and the *detector level*, at which the hadrons become accessible experimentally. Ideally, the measurement of the produced hadrons at the detector level provides an access to the original partons in the hard interaction and the parton shower in order to probe the features of QCD. However, the characteristics of QCD changes drastically among the different levels, namely from few partons at the hard interaction to a high multiplicity of final state hadrons at particle level. The observable to achieve a correspondence between the different levels in the parton evolution are *particle jets*. The concept of jets is motivated by the experimental finding that each hard parton from the interaction results in a collimated, localised spray of hadrons. This spray of hadrons is clustered in a well-defined manner using a jet algorithm. As a consequence, the definition of a jet is not unique, but depends on the choice of the algorithm.

In general, jet algorithms can be grouped in two classes, namely *cone* and *sequential algorithms* [34]. Cone algorithms are based on the intuitive idea to find geometric regions in which the energy of the objects inside is maximal, i.e. cone around a hard final-state hadron. The algorithm used throughout this work is the anti-k_t algorithm [35], which falls into the class of the sequential algorithms and is a special case of the generalised k_T algorithm [35]. It is based on the idea of a reversed parton shower evolution, performing an iterative, pair-wise clustering of the elementary final-state objects to larger objects with increased momentum. Eventually, the final jet corresponds to the reconstructed hard partons, from which the shower originated.

The jet definition consists of a distance measure and a recombination scheme. The former defines at which distance two objects belong to the same jet, i.e. which of the soft and collinear splittings in the fragmentation should be resolved, and which are merged to an inclusive observable. The recombination scheme on the other hand determines how to merge two objects. In the anti-k_t algorithm, the distance measure d_{ij} between two objects i, j is combination of a geometrical component and the transverse momenta of the objects, according to

$$d_{ij} = \min\left(\frac{1}{p^2_{\mathrm{T},i}}, \frac{1}{p^2_{\mathrm{T},j}}\right)\frac{\Delta R^2_{ij}}{R^2} \qquad \text{and} \tag{1.25}$$

$$d_{iB} = \frac{1}{p^2_{\mathrm{T},i}}, \tag{1.26}$$

where

$$\Delta R^2_{ij} = (y_i - y_j)^2 + (\phi_i - \phi_j)^2. \tag{1.27}$$

The first part on the right side of Equation 1.25 selects the object with the largest transverse momentum, while the second part introduces the geometrical distance ΔR_{ij}, determined from the azimuthal angle ϕ and the rapidity y given by Equation 1.27. Equation 1.26 sets the exit condition for the sequential algorithm, which is executed as follows. First, the distance measures d_{ij} and d_{iB} are calculated for all combinations of the objects i, j, and the minimum value among d_{ij} and d_{iB} is retained as d_min. If d_min is obtained from d_{ij}, the objects i and j are combined adding their four-vectors. If d_min corresponds to d_{iB}, the object i is added to the list of final jets. The sequence is repeated until all objects are clustered into final jets.

The main characteristics of the jets defined by the anti-k_t algorithm are its cone-like geometrical shape

and the fact that objects are clustered around the hardest objects in the collision event. Furthermore, the anti-k_t algorithm is both infrared and collinear safe and shows small sensitivity to non-perturbative effects in the fragmentation and hadronisation [34]. It can be applied at parton, particle and detector level, using partons, final-state hadrons or reconstructed objects in the detector as input objects, respectively. Hence, it is well-suited for high energy proton-proton collisions.

1.5 Inclusive jet cross-section

Given the factorisation theorem of soft and hard contributions in Equation 1.13, the cross-section of the hard scattering subprocess $ab \to cd$ in Equation 1.22, and a jet algorithm that is fully efficient, i.e. the particle-level jets correspond to the final-state partons at parton level, $p^{\mu}_{\text{jet}} = p^{\mu}_{\text{parton}}$, the prediction for the inclusive jet cross-section in pp collisions at LO QCD results in

$$\frac{Ed^3\sigma}{d^3p} = \frac{1}{16\pi^2 s} \sum_{\substack{a,b,\\c,d}} \iint_{x_a,x_b} \frac{dx_a}{x_a}\frac{dx_b}{x_b}\, q_a\left(x_a,\mu_F^2\right)\, q_b\left(x_b,\mu_F^2\right) \times \overline{\sum} |\mathcal{M}_{ab\to cd}|^2 \, \frac{1}{1+\delta_{cd}} \delta(\hat{s}+\hat{t}+\hat{u}). \quad (1.28)$$

The first sum, $\sum_{a,b,c,d}$, runs over all combinations of quarks, antiquarks and gluons in the process $ab \to cd$ of the hard scattering, which is calculated from the matrix element $\overline{\sum}|\mathcal{M}_{ab\to cd}|^2$. In the latter, the initial spins are averaged, while final spins are summed. The factor $1/(1+\delta_{cd})$ accounts for cases with identical partons in the final state. The kinematics of the hard scatterings is expressed in terms of the Mandelstam variables $\hat{s}$, $\hat{t}$ and $\hat{u}$, given in Equations 1.17 to 1.19.

The cross-section of the hard process is folded with the parton distribution functions of the proton, $q_a(x_a,\mu_F^2)$, $q_b(x_b,\mu_F^2)$. x_a and x_b are the momentum fractions of the incoming partons, which are calculated according to Equations 1.20 and 1.21, and integrated over in the interval $[0,1]$. They relate to the centre-of-mass energy of the protons and partons, $\sqrt{s}$ and $\sqrt{\hat{s}}$ respectively, by $x_a x_b\, s = \hat{s}$. μ_F in the proton PDF is the factorisation scale. The renormalisation scale, μ_R, does not appear in Equation 1.28, since the hard interaction is given in the LO approximation in α_S.

Comparison of the theoretical prediction with the experimental data is usually done in the distribution of the jet transverse momentum, p_T, and the jet rapidity, y. The inclusive cross-section in Equation 1.28 can be transformed to the double-differential inclusive jet cross-section according to

$$\frac{Ed^3\sigma}{d^3p} = \frac{d^3\sigma}{d^2p_T dy} \longrightarrow \frac{1}{2\pi p_T}\frac{d^2\sigma}{dp_T dy}, \quad (1.29)$$

using the relation $\frac{dy}{dp_z} = \frac{1}{E}$ and $p_x^2 + p_y^2 = p_T^2$ in the second expression, and an integration over the azimuthal angle in the third expression of Equation 1.29.

Experimentally, the double-differential inclusive jet cross-section is determined in fixed bins of the rapidity and the transverse momentum, as the number of jets in each bin, $N_{\text{jet}}(|y|, p_T)$, divided by the integrated luminosity $\mathcal{L}$:

$$\sigma(|y|, p_T) = \frac{N_{\text{jet}}(|y|, p_T)}{\mathcal{L}}. \quad (1.30)$$

The luminosity is a machine parameter of the particle collider given by the intensity and geometry of the beam. It expresses the ability to produce particle collisions and has the dimensions $1/area$. The double-differential inclusive jet cross-section given in Equation 1.30 is the primary observable in this work.

CHAPTER 2

Theoretical predictions

As shown in the previous section, a particle collision consists of a series of complex subprocesses that are too complicated to be described as a whole. Instead, it is factorised into a number of components, which can be summarised as follows. First, the initial partons from the proton are determined by means of a PDF. Second, the matrix element of the hard interaction is calculated using the perturbative QCD formulation. Third, the parton shower is evolved on basis of a probabilistic approach. Fourth, the process of hadronisation and subsequent decay into stable particles is modelled. Moreover, additional processes from the underlying event or overlapping collisions have to be described as well.

This factorisation is not perfect, and a consistent combination of these processes is only obtained easily when calculations at leading order in the strong coupling are employed, while ambiguities can arise at higher orders. Hence, the available event generators form two distinct groups. The first consists of event generators that calculate the cross-section at high precision, usually at NLO or above, but only include the parton-level subprocesses without parton shower and other non-perturbative effects. Since this type is expected to be more accurate regarding the actual cross-section, it is used as the baseline for the comparison with the experimental data. The second type of event generators are simulations on a event-by-event basis to study the complete interaction from the hard scattering of partons up to the reconstruction of stable particles in the detector. This allows to study the kinematic distributions of the event, to calibrate the energy of the jets, to assess resolution effects, and the impact of different running conditions of the accelerator. In this type of predictions, the precision of the cross-section is not as important; rather the shape of the kinematic distribution has to be described well in order to obtain a good understanding of the detector. In addition, these predictions can be used to derive corrections to the NLO parton-level cross-section for non-perturbative effects.

The structure of this chapter is as follows. First, event generators capable of simulating the complete interaction at LO precision are presented in Section 2.1. The calculation of the matrix element of the hard interaction at NLO precision and how this parton-level cross-section is evolved to the particle level is shown in Section 2.2. A similar approach to reach NLO precision using k-factors is presented in Section 2.3. In Section 2.4, a possibility to interface the NLO matrix element calculation directly to a parton shower simulation is shown.

2.1 General-purpose event generators

The Monte Carlo event generators considered here are so-called *general-purpose event generators*, as they are able to simulate the complete collision in full detail to the level of individual stable particles. Typically, they include e^+e^-, ep, pp and $p\overline{p}$ collisions and a large selection of hard-scattering processes, but also model all effects that the in- and outgoing particle are subject to as well as additional interactions in the underlying event. As output, they do not provide the cross-section in its integrated form, but the simulated events with the complete particle content and their four-vectors. Thus, the cross-section as well as all kinematic distribution are obtained from binning the events into the according histograms. In addition, the simulated events can be interfaced to detector simulations, which are normally not included in the Monte Carlo generator itself.

As described before, no enclosed, homogeneous formulation exists for the complete process of the hard interaction, parton shower, hadronisation and underlying event. Instead, the complete process is divided into subprocesses, which are implemented using dedicated models. Monte Carlo generators often include several options for each subprocess, but to obtain a consistent overall description, some general choices have to be made, e.g. with respect to the ordering of the parton shower emissions. Hence, principal differences between the generators arise, and which choice is suited best depends on the process under study and is not clear a priori. Two Monte Carlo generators are employed in the course of this work, namely the programs Pythia [36] and Herwig [37]. They are described in Sections 2.1.1 and 2.1.2 in more detail.

The main application of the general-purpose event generators in the course of this work concerns the following tasks: determination of non-perturbative corrections to evolve perturbative QCD matrix element calculations at NLO from parton level to particle level; input to the detector simulation to obtain the bin migration between particle- and detector-level distribution due to resolution effects; determination of the jet energy calibration of the detector; consistency checks with kinematic distribution in data.

2.1.1 Pythia

The Monte Carlo simulation Pythia is a general-purpose event generator as described above. It employs a matrix element calculation of the $2 \to 2$ process at LO precision, a p_T-ordered parton shower in the LL approximation [38], and an underlying event simulation with multiple interactions. The hadronisation is performed according to the Lund-string model, described in Section 1.3.4.

Pythia is used in two versions, Pythia 6 [36] and Pythia 8 [39]. Apart from the different underlying programming language, Pythia 8 employs an improved modelling of the diffractive processes. For reasons of stability, Pythia 6.425 is used primarily.

2.1.2 Herwig

The event generator Herwig [37] has a similar scope like Pythia. It also uses a matrix element calculation of the $2 \to 2$ process at LO precision, but employs an angular-ordered parton shower [40] and a cluster model for the hadronisation. The latter is described in Section 1.3.4. Two major releases of Herwig are used, differing in the simulation of the underlying event. Herwig 6 assigns this task to the add-on generator Jimmy [41], but it does not contain a simulation of multiple parton interaction. Herwig++ [42] includes a native underlying event simulation using an eikonal multiple parton-parton scattering model [43].

PDF set reference	MRST 2007 [44]	MSTW 2008 [45]	CTEQ 6L1 [46]	CT 10 [47]	NNPDF 2.1 [48, 49]	HERAPDF 1.5 [50]	ABM 11 [51]
accuracy	LO*	NLO	LO	NLO	NLO	NLO	NLO
HERA DIS	yes	yes	yes	yes	yes	no	yes
fixed target DIS	yes	yes	yes	yes	yes	no	yes
fixed target DY	yes	yes	yes	yes	yes	no	yes
Tevatron W, Z	yes	yes	yes	yes	some	no	some
Tevatron jets	yes	yes	yes	yes	yes	no	yes
LHC W, Z + jets	no	no	no	no	no	no	no
α_S (NLO)	0.120	0.120	0.118	0.118	0.119	0.1176	0.1179
HF scheme	RTGMVF	RTGMVF	SACOT GMVFN	SACOT GMVFN	FONLL GMVFN	RTGMVFN	BMSN FFNS

Table 2.1: Overview of selected PDF sets, including the accuracy of the perturbative QCD calculations that is used, the input datasets, the employed heavy flavour (HF) scheme, and the value used for the strong coupling constant $\alpha_S(Z)$. The term LO* indicates a modified PDF fit at LO precision using a relaxed momentum sum rule and a NLO definition of α_S [44].

2.1.3 PDF sets

The framework of perturbative QCD allows to describe the Q^2 evolution of the parton distribution inside the proton. However, it does not predict the x dependence. Hence, the shape of the PDF at a given scale $Q^2 = Q_0^2$ is parametrised in an initial analytical form, where $\frac{2}{0}$ has to be large enough that the perturbative series in α_S is valid. The parton distributions are evolved to larger scales using the DGLAP formalism. Since the DGLAP equations only apply to light quarks, heavy quarks have to be treated separately via massive NLO calculations. Several so-called *heavy flavour* (HF) schemes exist, such as the ZMVFNS[1] scheme [52] or the *ACOT*[2] scheme [53]. The parameters are determined from experimental data across a large region of phase space in x and Q^2. Typically, the fit contains 20 parameters including the strong coupling α_S, and 2000 data points from fixed target and collision experiments.

Hence, a PDF *set* is defined primarily by the choice of the functional form for the PDF and the HF scheme, as well as the data that is used in the global fit of the parameters and contains the parton distribution functions of the quark flavours and the gluon as function of x and Q^2. An overview of the employed PDF sets is given in Table 2.1.

2.1.4 Tunes for Monte Carlo generators

Since exact descriptions of initial- and final-state radiation, hadronisation, or underlying event are not available, approximations in the Monte Carlo models are required, e.g. by introducing cut-off parameters to avoid regimes where the calculation is divergent or for computational reasons. The parameters used for a given Monte Carlo generator are combined in sets, so-called *tunes*. They typically comprise several hundred settings, but the physics processes are defined by only a few dominating parameters, e.g. the value of the strong coupling α_S in the perturbative domain, or the parameters of the fragmentation function in the non-perturbative domain.

Tunes are derived from a selection of datasets under dedicated running conditions that allow to probe different aspects of the event generator. The tuning comprises the following subprocesses, given in the order at which they are typically performed [55]: final-state radiation and hadronisation; initial-

[1] ZMVFNS - *zero mass variable-flavour number scheme*.
[2] ACOT - Initials of the authors *Aivazis, Collins, Olness, and Tung*.

generator	tune
Pythia 6.4.25	AUET2B [46] CTEQ6L1 AMBT2B [46] CTEQ6L1 AUET2 [54] LO** AUET2B [46] LO** Perugia 2011 [55] Perugia 2010 [55] AMBT1 (MC10) [56]
Pythia 8.1.50 [39]	tune 4C [46]
Herwig++ 2.5.1 [42]	UE7000-2 [46]

Table 2.2: Monte Carlo generators and parton shower tunes used for the determination of the non-perturbative correction factors.

state radiation and *primordial* k_T[3]; underlying event, beam remnants and colour reconnection; energy scaling. However, depending on the tuning procedure and included data, tunes generally possess a certain characteristic, i.e. they focus on the modelling of perturbative or non-perturbative processes. This indicates that the models are not universal enough to account for each scenario alike. On the same lines, the tuning depends on the used PDF set, since the QCD factorisation of short and long range effects may not be perfect in the full event picture. Table 2.2 lists a selection of tunes that are used in this thesis. Since each event generator employs different parametrisations, tunes are not interchangeable, but often the same procedure is employed for several generators in parallel.

2.1.5 Detector simulation

The ATLAS simulation framework [57] simulates the interaction of the particle content from the Monte Carlo event generator with the material inside the detector. This includes the measurement of the particle showers with the given detector technology and the signal processing chain as in the read-out electronics of the detector. A high precision of the detector simulation is essential in the understanding of the observables of the measurement, since the detection of every particle is affected by the calibration of the detector and resolution effects. The reprocessing of the simulation data is performed using the same reconstruction software as for experimental data.

As the main component of the framework, the GEANT4 software toolkit is employed [58]. It consists of a collection of various models to implement interactions of hadrons and leptons with the nuclei in the detector material. The configuration of the models in GEANT4 is defined in so-called *physics lists*. ATLAS uses the `QGSP_BERT` list, which was validated in test beam studies [59, 60].

2.2 Prediction using perturbative QCD at NLO precision

The LO approximation provides the basic features of the hard interaction in a $2 \to 2$ process. However, higher-order corrections in α_S modify the cross-section and the event topology through virtual loop corrections and real emissions. To obtain a prediction at high precision, those corrections have to be taken into account. The approach of the NLO calculation discussed here follows the presentation in [61].

The cross-section of the hard interaction at NLO precision is obtained from the contributions of the

[3] Primordial k_T denotes the transverse momentum of the initial-state partons.

LO and the NLO diagrams,

$$\sigma = \sigma^{\mathrm{LO}} + \sigma^{\mathrm{NLO}}. \tag{2.1}$$

Here, σ^{LO} and σ^{NLO} are the fully exclusive cross-sections: σ^{LO} contains all LO diagrams of the $2 \to 2$ process, while σ^{NLO} contains the virtual-loop contributions to the $2 \to 2$ process and the real emissions with three final-states particles in the $2 \to 3$ diagram.

The cross-section is obtained by integrating over the corresponding phase space of the final-state particles. For the LO term in Equation 2.1, it follows

$$\sigma^{\mathrm{LO}} = \int_m d\sigma^{\mathrm{LO}}, \tag{2.2}$$

where m is the number of partons in the final state, i.e. $m = 2$. The phase space integration for σ^{LO} is finite and can be calculated analytically as well as numerically. The NLO term in Equation 2.1 consists of two separate integrals for the virtual loop corrections and the real emission:

$$\sigma^{\mathrm{NLO}} = \int_{m+1} d\sigma^{\mathrm{R}} + \int_m d\sigma^{\mathrm{V}}. \tag{2.3}$$

While the sum of the two integrals is finite, the separate integration is not. Different types of singularities arise in the calculation. Infrared divergencies are present in the contributions from the real emissions. The virtual loop corrections contain both infrared and ultraviolet divergencies. Ultraviolet singularities can be resolved in field theory using the concepts of regularisation and renormalisation. For the remaining soft and collinear divergencies in $d\sigma^{\mathrm{R}}$, $d\sigma^{\mathrm{V}}$ of Equation 2.3, the integrals differ in phase space by the one additional parton of the real emission, preventing the numerical integration in the vicinity of the poles of the divergencies. Several methods exist to solve this issue. The used calculation is based on the *dipole subtraction method* [61].

The general idea of the subtraction method is to introduce an additional term $d\sigma^{\mathrm{A}}$ that exhibits the same poles as $d\sigma^{\mathrm{R}}$. Hence, $d\sigma^{\mathrm{A}}$ acts as local counterterm for $d\sigma^{\mathrm{R}}$, and Equation 2.3 can be rewritten as

$$\sigma^{\mathrm{NLO}} = \int_{m+1} \left[d\sigma^{\mathrm{R}} - d\sigma^{\mathrm{A}} \right] + \int_{m+1} d\sigma^{\mathrm{A}} + \int_m d\sigma^{\mathrm{V}}. \tag{2.4}$$

Given a proper approximation of the poles in $d\sigma^{\mathrm{R}}$ by $d\sigma^{\mathrm{A}}$, the integration of the first term on the right hand side of Equation 2.4 is finite, and the remaining divergencies are associated with the last two terms. To be able to combine the two integrations and explicitly cancel the poles in the numerical integration of $d\sigma^{\mathrm{A}}$ and $d\sigma^{\mathrm{V}}$, $d\sigma^{\mathrm{A}}$ is chosen such that the integration over the one-parton subspace can be performed analytically. It follows

$$\sigma^{\mathrm{NLO}} = \int_{m+1} \left[d\sigma^{\mathrm{R}} - d\sigma^{\mathrm{A}} \right] + \int_m \left[d\sigma^{\mathrm{V}} + \int_1 d\sigma^{\mathrm{A}} \right]. \tag{2.5}$$

Both integrals in Equation 2.5 are finite and provide the cross-sections for the real emission and virtual loop contributions separately. The actual form of $d\sigma^{\mathrm{A}}$ used here is the so-called *dipole factorisation formulae* [61].

2.2.1 The NLOJET++ program

The parton-level cross-sections are obtained in a perturbative QCD calculation at NLO precision using the NLOJET++ 4.1.2 [62] program. It implements the dipole subtraction method as described above with a small modification to improve the stability of the numerical calculation by introducing an additional phase space cut. Following a recommendation from the authors of NLOJET++, the factorisation scale, μ_F, and renormalisation scale, μ_R, are chosen for each event as the maximum jet p_T separately in each rapidity bin, i.e. $\mu_F = \mu_R = \mu = p_\mathrm{T}^{max}(y)$. Hence, if jets are present in different rapidity bins, several scales are used within the same event. The prediction is determined for a variety of NLO PDF sets, which are described in Section 2.1.3. The CT 10 PDF set is used as baseline. In order to have a consistent calculation regarding the strong coupling, the value for α_S is chosen in agreement with value used in the PDF set.

2.2.2 Systematic uncertainties

The uncertainties on the theory prediction in the NLO perturbative QCD framework arise from the uncertainty on the renormalisation and factorisation scale, the PDF set and the strong coupling constant. To enable a fast calculation, NLOJET++ is interfaced to the APPLGRID framework [63], which allows the a posteriori variation of the scale, PDF set, and α_S. APPLGRID is based on the QCD factorisation shown in Section 1.2.3 and stores the perturbative coefficients of the QCD calculation, the hard scatter $\hat{\sigma}_{ab\to cd}$, in a look-up table.

Scale choice

The uncertainty on the scale choice is assessed by varying the factorisation scale and the renormalisation scale by a factors f_{μ_F} and f_{μ_R} with respect to the original choice in the calculation. Hence $\mu_R = f_{\mu_R} \cdot p_\mathrm{T}^\mathrm{max}$ and $\mu_F = f_{\mu_F} \cdot p_\mathrm{T}^\mathrm{max}$. A scan over the range $[0.1, 5.0]$ for both factors f_{μ_F} and f_{μ_R} independently, is shown in Figure 2.1 for anti-k_t jets with $R = 0.4$ and $\sqrt{s} = 2.76\,\mathrm{TeV}$ in several regions of phase space. Scale factors above unity result in moderate changes of the cross-section with respect to the nominal choice, while scale factors below unity have a more substantial impact [64]. In general, the effect of scale variations is more pronounced at large p_T. Common factors for the scale variation are factors of two. The considered combinations are

$$(f_{\mu_R}, f_{\mu_F}) = (0.5, 0.5),\ (0.5, 1.0),\ (1.0, 0.5), \tag{2.6}$$

$$(1.0, 2.0),\ (2.0, 1.0),\ (2.0, 2.0). \tag{2.7}$$

The extreme combinations $(0.5, 2)$ and $(2, 0.5)$ are excluded due to large logarithmic factors in the theory calculation. The envelope of the resulting variations is taken as the scale uncertainty. Its size is found to be generally within $d\sigma/\sigma = ^{+5}_{-10}$ %, apart from the region of large transverse momentum and rapidity, where it reaches up to $d\sigma/\sigma = ^{+5}_{-35}$ %. Furthermore, an alternative choice for the factorisation and renormalisation scale is tested, where the scales are set to the maximum jet p_T in the event, $\mu_F = \mu_R = \mu = p_\mathrm{T}^{max}$, regardless of the rapidity of the jet. Since the maximum jet p_T is always larger or equal than the maximum jet p_T in a particular rapidity bin, and since the impact of a larger scale is found to be small, the difference with respect to the default choice is small. It ranges within $d\sigma/\sigma = ^{+0}_{-10}$ %, except for the very forward region where it is $d\sigma/\sigma = ^{+0}_{-15}$ %. Hence, the alternative choice is generally covered by the scale variations described above [64].

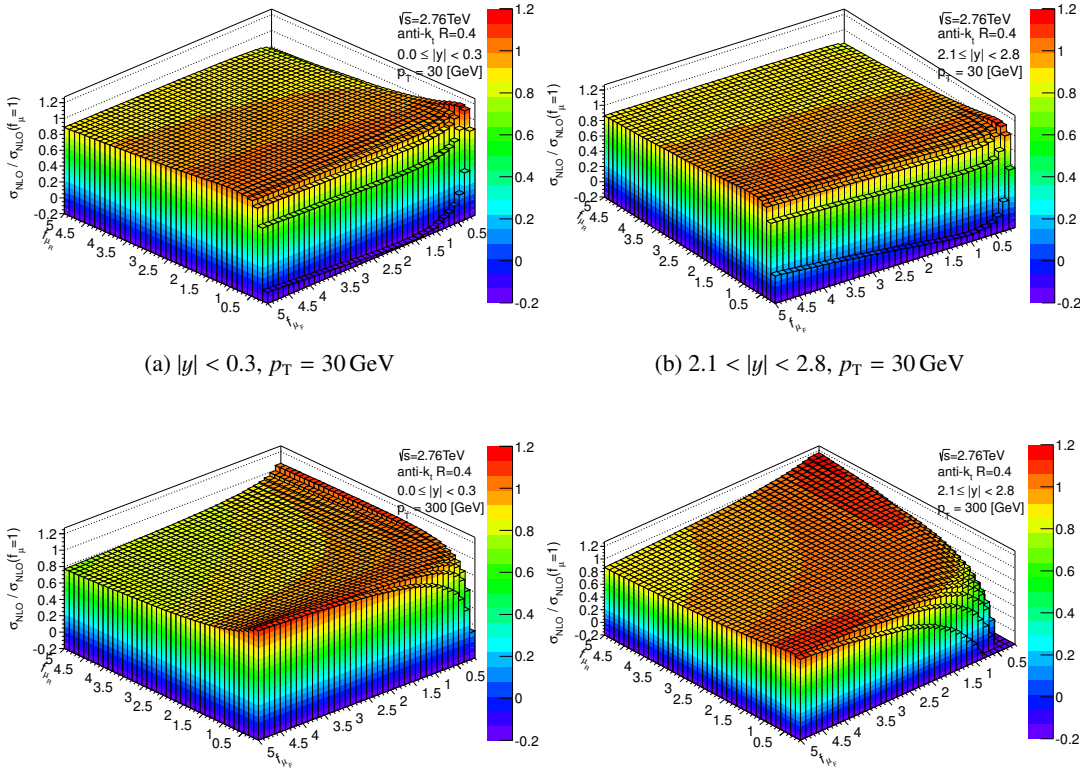

(a) $|y| < 0.3$, $p_{\mathrm{T}} = 30\,\mathrm{GeV}$

(b) $2.1 < |y| < 2.8$, $p_{\mathrm{T}} = 30\,\mathrm{GeV}$

(c) $|y| < 0.3$, $p_{\mathrm{T}} = 300\,\mathrm{GeV}$

(d) $2.1 < |y| < 2.8$, $p_{\mathrm{T}} = 300\,\mathrm{GeV}$

Figure 2.1: Comparison of the parton-level cross-section obtained from the NLO perturbative QCD calculation under variation of the factorisation and renormalisation scale, μ_F and μ_R, respectively, for several regions in p_{T} and $|y|$. The prediction is obtained with NLOJET++ and the CT 10 PDF set for anti-k_t jets with $R = 0.4$. The default scale choice is $\mu_F = \mu_R = \mu = p_{\mathrm{T}}^{max}(y)$. Variations are obtained applying the factors f_{μ_F} and f_{μ_R} to μ_F and μ_R, respectively [64].

Parton distribution functions and strong coupling

The uncertainty due to the imperfect knowledge of the PDF is evaluated according to the prescription of each PDF set and the PDF4LHC recommendations [65]. It is defined at 68% confidence level.

The prescription of the CTEQ group [66] is used to determine the uncertainty due to the available measurement accuracy of α_{S}. The cross-section is calculated using a series of PDF sets, which are derived for various fixed α_{S} values, within a 68% confidence level.

The combined relative systematic uncertainty on the parton-level cross-section obtained from the NLO perturbative QCD calculation with NLOJET++ and the CT 10 PDF set is presented in Figure 2.2 for a centre-of-mass energy of $\sqrt{s} = 2.76\,\mathrm{TeV}$. It is shown for anti-$k_t$ jets with $R = 0.6$ as a function of the p_{T} in three representative rapidity ranges. The uncertainty due to the scale is the dominating component on the lower bound of the total uncertainty in all rapidity bins. The upper bound is mainly driven by the uncertainty due to the PDF at high p_{T}, and the strong coupling at low p_{T}. The total size is within $^{+5\%}_{-10\%}$ for small p_{T} and $|y|$, but increases substantially towards large p_{T} and $|y|$. As shown in Figure A.1 of the appendix, The uncertainties for anti-k_t jets with $R = 0.4$ are very similar, except of the forward region where the contribution of the scale choice are larger by a factor of two.

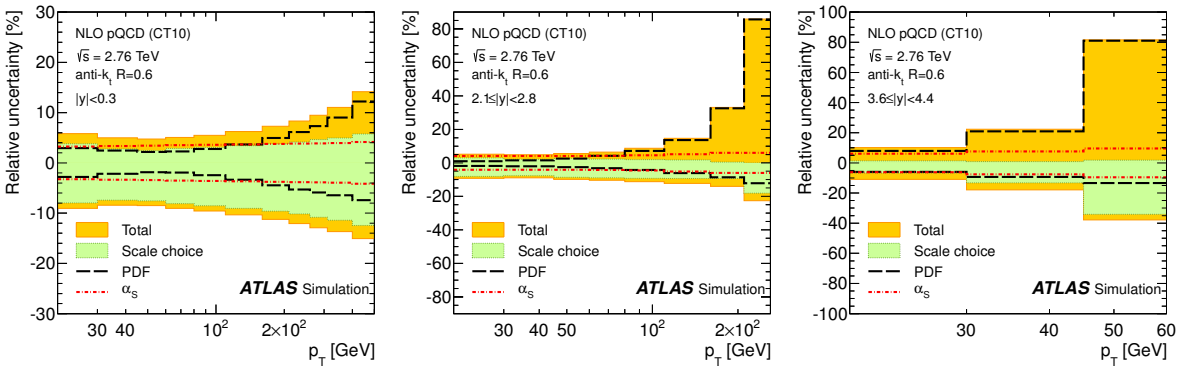

(a) (b) (c)

Figure 2.2: Theoretical uncertainty of the perturbative QCD calculation for the inclusive jet cross-section at $\sqrt{s} = 2.76\,\text{TeV}$ as function of p_T, in three representative rapidity bins [1]. The contributions from the factorisation and renormalisation scale, the PDF and the strong coupling constant α_S is shown separately. Jets are defined using the anti-k_t algorithm with $R = 0.6$.

2.2.3 Non-perturbative corrections

The perturbative QCD calculation described above provides the parton-level cross-section of the interaction at NLO precision. To obtain a prediction at particle-level, a correction for initial and final state radiation, the underlying event and multiple deep-inelastic scatterings in the same interaction has to be applied. The approach used here to derive these corrections is based on the assumption that the main event topology is given by the hard interaction, and the aforementioned non-perturbative effects can be considered as corrections to the matrix element calculation. A clear example is the parton shower, which mostly carries the momentum of the outgoing parton, but not all the momentum is contained in the jet reconstruction at particle level due to out-of-cone effects. The energy loss can be addressed with a correction factor obtained from simulation. This particular effect is competing with contributions of the underlying events and multiple interactions, which may overlap with the parton shower of the outgoing partons and add additional energy to it. Jets with a small radius parameter are expected to suffer more from out-of-cone effects, but are influenced less by the underlying event. A large radius parameter ensures a better coverage of the parton shower, but is prone to collect more energy from other particles in the event. Thus the value of the correction for anti-k_t jets with a radius parameter of $R = 0.6$ is expected to be larger than the one for $R = 0.4$, but the actual size of the correction results from a complex interplay of several effects.

The procedure to determine the correction for non-perturbative effects is based on Monte Carlo event generators that are able to describe the particle-level cross-section. Correction factors are derived from the bin-wise ratio of the cross-sections with and without non-perturbative effects, $c_\text{np}(y, p_\text{T})$,

$$\frac{\sigma(y, p_\text{T})_\text{particle}}{\sigma(y, p_\text{T})_\text{parton}} \approx \frac{\sigma(y, p_\text{T})^\text{LO}_\text{np on}}{\sigma(y, p_\text{T})^\text{LO}_\text{np off}} = c_\text{np}(y, p_\text{T}). \tag{2.8}$$

Non-perturbative (np) effects comprise the parton shower, the hadronisation and the underlying event. Multiple interactions superimposing the event under study have not been included in accordance with running conditions in the corresponding data taking phase for this analysis. The factors $c_\text{np}(y, p_\text{T})$ used to propagate the parton-level calculation at NLO precision is obtained from NLOJET++ to particle-level.

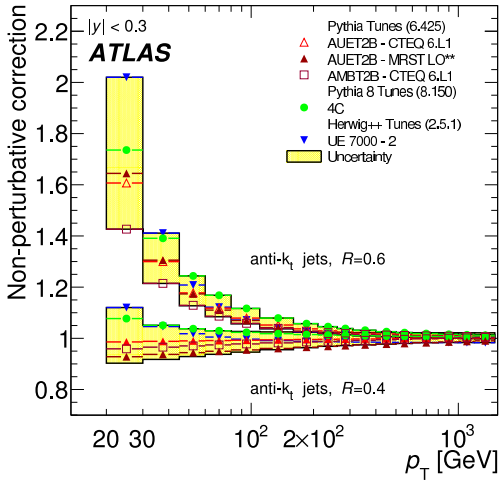

Figure 2.3: Non-perturbative correction factors for anti-k_t jets with $R = 0.4$ (*lower band*) and $R = 0.6$ (*upper band*) in the central rapidity region. The nominal correction is obtained from Pythia 6.425 with the Auet 2b tune (*hollow triangles*). The systematic uncertainties are obtained from the differences between various Monte Carlo simulations and parton shower tunes. For reasons of visibility, only a subset of the considered tunes is shown. [2]

Each bin of the cross-section $\sigma(y, p_T)|^{\text{NLO}}_{\text{parton}}$ is multiplied with the corresponding correction $c_{\text{np}}(y, p_T)$, so that

$$\sigma(y, p_T)^{\text{NLO}}_{\text{particle}} \approx c_{\text{np}}(y, p_T) \cdot \sigma(y, p_T)^{\text{NLO}}_{\text{parton}}. \tag{2.9}$$

Since different models exist for each of the processes integrated in the complete event generation, the size of the non-perturbative correction factors is sensitive to the Monte Carlo simulation used and the parton shower tunes therein. Hence, the differences between the models is considered as the dominating systematic uncertainty for $c_{\text{np}}(y, p_T)$.

A selection of different tunes and Monte Carlo generators is listed in Table 2.2. The variety among tunes is covered using the Pythia 6 event generator, whereas Pythia 8 and Herwig++ are used to assess differences between models. Pythia 6.425 with the Auet 2b tune and the Cteq 6l1 PDF set is used as the default. The uncertainty on the non-perturbative corrections is derived from the envelope of the correction factors obtained for the other tunes.

Figure 2.3 shows the non-perturbative correction factors $c_{\text{np}}(y, p_T)$ for anti-k_t jets with $R = 0.4$ and $R = 0.6$ in the central rapidity region and $\sqrt{s} = 7$ TeV. For jets with large transverse momenta, $c_{\text{np}}(y, p_T)$ is close to unity for both radius parameters, due to the fact that non-perturbative effects are generally soft. As expected, the value of $c_{\text{np}}(y, p_T)$ is consistently larger for $R = 0.6$ than for $R = 0.4$. For $R = 0.6$ $c_{\text{np}}(y, p_T)$ reaches up to 1.6 for the nominal simulation, while the correction factor for $R = 0.4$ is close to unity across the whole p_T range. Apparently, the different non-perturbative effects balance for the latter. The difference between tunes and models is sizeable at low p_T and results in an uncertainty of up to 20%. Thus, it exceeds the uncertainty of the perturbative QCD calculation in that region. At large p_T, the uncertainty is below 2% and thus negligible. At larger rapidity, the non-perturbative correction factors have a similar shape, but they are reduced in size, as listed in Table A.1 in the appendix.

The non-perturbative correction factors for $\sqrt{s} = 2.76$ TeV are presented in Figure 2.4. As before, $c_{\text{np}}(y, p_T)$ is found to be about 60% larger for $R = 0.6$ than for $R = 0.4$, but the correction factors for $R = 0.4$ is at about 0.9 for low p_T. Table A.1 also lists the correction factors in other regions of phase space.

Criticism to the approach using a perturbative QCD matrix element calculation NLO with non-perturbative corrections from a Monte Carlo simulation at LO without further modification arises from the fact that the mixture of different precisions can lead to inconsistencies in the calculation. In this

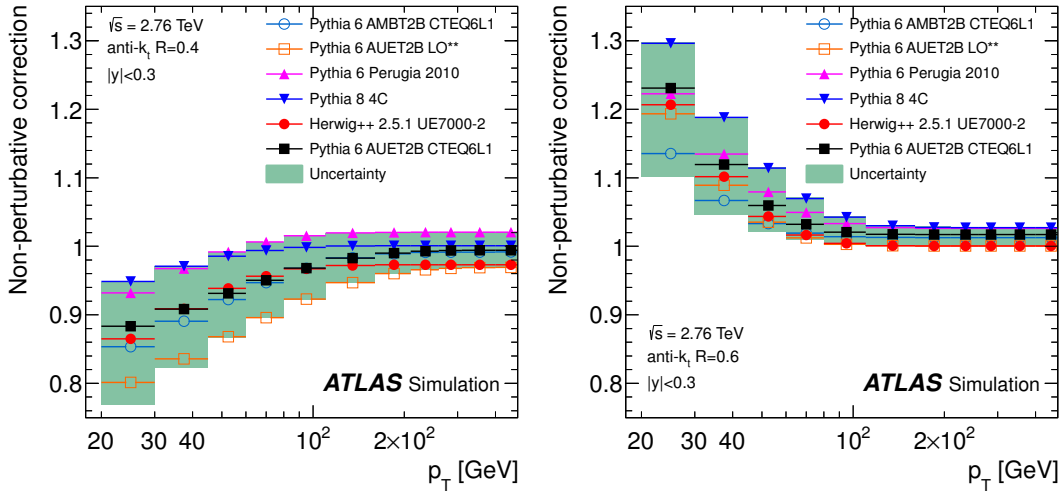

(a) Anti-k_t jets with $R = 0.4$

(b) Anti-k_t jets with $R = 0.6$

Figure 2.4: Non-perturbative correction factors for anti-k_t jets with $R = 0.4$ (a) and $R = 0.6$ (b), respectively, in the rapidity region $|y| < 0.3$ for $\sqrt{s} = 2.76\,\text{TeV}$. The nominal correction is obtained from Pythia 6.425 using the Auet 2b tune and the Cteq 6l1 PDF set. The systematic uncertainties are obtained from the differences between various Monte Carlo simulations and parton shower tunes. For reasons of visibility, only a subset of the considered tunes is shown. [1]

particular case, the inconsistency is a double counting of the first branching of the outgoing particle. The NLO calculation explicitly includes the $2 \to 3$ process via the real emission diagrams, while in the LO matrix element this branching is handled by ISR and FSR, and carefully tuned. Hence, the correction factor $c_{\text{np}}(y, p_{\text{T}})$ in Equation 2.8 also contains a portion of the LO to NLO difference of the matrix element.

Nevertheless, the use of NLO matrix element with the corresponding NLO PDF sets is strongly favourable, since it exhibits a much better agreement with data, showing that high precision in the calculation is needed. In Section 2.4, an approach to avoid this kind of double counting is described.

2.2.4 Electroweak correction

Usually, corrections from electroweak contributions are negligible in QCD processes at hadron colliders, since they are suppressed by the smaller coupling $\alpha < \alpha_{\text{S}}$. However, at very high momentum transfers of about 1 TeV, i.e. $Q^2 \gg m_W$, these corrections may become important due to *Sudakov logarithms* [67], which appear from the virtual exchange of soft or collinear massive weak gauge bosons [68, 69]. Calculations of these weak radiative corrections to dijet production at hadron colliders became available recently for pp collisions at $\sqrt{s} = 7\,\text{TeV}$ [70]. The effect was found to be $O(10\%)$ at $p_{\text{T}} > 1\,\text{TeV}$, and negligible at small p_{T}. However, electroweak corrections are not included in the theory predictions, since the analysis at $\sqrt{s} = 7\,\text{TeV}$ had already been completed at that time. No studies have been performed for $\sqrt{s} = 2.76\,\text{TeV}$, but the impact is expected to be similar or smaller than for $\sqrt{s} = 7\,\text{TeV}$.

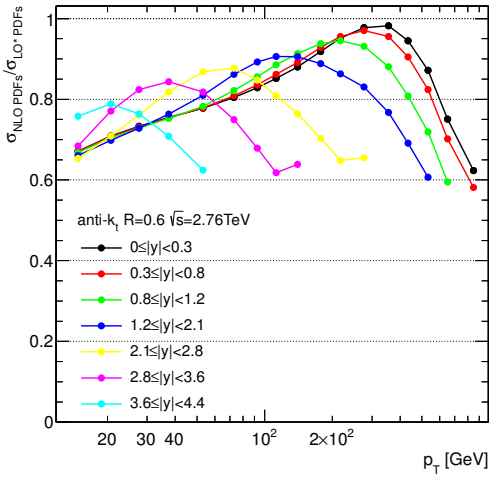

Figure 2.5: k-factors for a correction of the PDF set from LO to NLO accuracy, determined from the bin-wise ratio of parton-level cross-section at LO precision with two different PDF sets, namely the MSTW 2008 NLO PDF and the MRST 2007 LO* PDF. The correction factors are shown for anti-k_t jets with $R = 0.6$ at $\sqrt{s} = 2.76\,\text{TeV}$ in separate bins of rapidity. [64]

2.3 Reweighting from LO to NLO: the *k*-factor approach

In this approach, the LO precision of the Monte Carlo simulation is improved to NLO by a reweighting procedure using a so-called *k-factor*, where k depends on the transverse momentum and the rapidity of the jet. It is determined from the bin-wise ratio of the inclusive jet cross-section at parton-level, calculated using a NLO matrix element, $\sigma(y, p_\text{T})^\text{NLO}_\text{parton}$ and a LO matrix element $\sigma(y, p_\text{T})^\text{LO}_\text{parton}$ with the corresponding NLO and LO PDF set, respectively:

$$k(y, p_\text{T}) = \frac{\sigma(y, p_\text{T})^\text{NLO}_\text{parton}}{\sigma(y, p_\text{T})^\text{LO}_\text{parton}}. \tag{2.10}$$

The k-factor corrected particle-level cross-section is obtained by

$$\sigma(y, p_\text{T})^\text{NLO}_\text{particle} \approx k(y, p_\text{T}) \cdot \sigma(y, p_\text{T})^\text{LO}_\text{particle}, \tag{2.11}$$

where $\sigma(y, p_\text{T})^\text{LO}_\text{particle}$ is the particle-level cross-section from the LO Monte Carlo simulation.

The particle-level cross-section using the k-factor approach in Equation 2.11 is identical to a calculation of the matrix element at NLO with non-perturbative corrections as given in Equation 2.9. The advantage of the k-factor approach is that it can be applied to the particle-level and detector-level cross-sections alike[4]. On the other hand, the k-factor correction only improves the final cross-section distribution. It does not improve the event topology, where a NLO matrix element calculation is still expected to produce a more accurate result. Furthermore, mixing a NLO matrix element calculation with a LO parton shower formulation leads to inconsistencies, as already discussed in Section 2.2.3. Therefore, the reweighted Monte Carlo simulation with the k-factor approach should only be used to investigate effects, where the dominant feature is the detector simulation, and the influence of the event simulation is minor.

In this analysis, the k-factor corrected cross-section is used to study detector effects and to propa-

[4] A general ambiguities arise from the fact that it is not always possible to determine the corresponding rapidity and transverse momentum at parton-level for a given particle-level or detector-level jet when applying the k-factor $k(y, p_\text{T})$. In general, the values at particle level give a reasonable result. For jets at detector level that cannot be matched unambiguously to a particle-level jet, the values at detector level are used for the best result.

gate the measured detector-level cross-sections to particle level. The procedure is slightly modified as follows. The matrix element in Equation 2.10 is calculated at LO in both numerator and denominator, and only the PDF is reweighted from LO to NLO. To limit the inconsistency with the parton shower simulation, NLOJET++ is used at LO precision to determine the k-factors. The according PDF sets are the MSTW 2008 NLO PDF [45] and the MRST 2007 LO* PDF [44]. The result is shown in Figure 2.5 for anti-k_t jets with $R = 0.6$ at $\sqrt{s} = 2.76\,\text{TeV}$, as function of the parton p_T, in separate bins of rapidity. The correction factors range from 0.6 to about 1.0, and hence is comparable in size with the non-perturbative corrections shown in Figure 2.4. The results for $R = 0.4$ are identical, since the two final state partons of the LO calculations always correspond to two distinct jets, regardless the size of the radius parameter R. The results for $\sqrt{s} = 7\,\text{TeV}$ are similar.

2.4 NLO matrix element interfaced to a LO parton shower

As shown in Section 2.1, the general-purpose Monte Carlo generators can provide a coherent description of the hard interaction and the parton shower, and thus predict a particle-level cross-sections, i.e. a cross-section where non-perturbative effects of QCD are included. Since the calculation of both the perturbative and non-perturbative processes becomes very complex for higher orders, these generators are usually based on calculations at LO precision in α_S for the matrix element, and LL precision for the emissions in the parton shower. Although this approximation has shown a satisfying agreement with the data in the past, it has principle shortcomings: a LO calculation of the matrix element generally provides only the correct order of magnitude and shows a large dependency on the factorisation and renormalisation scale. Moreover, the kinematic distribution of the third hardest jet is expected to be more accurate if described by the NLO perturbative QCD calculation of the matrix element instead of the parton shower. Hence, a NLO precision of the matrix element calculation is strongly favoured.

Two possibilities to obtain a particle-level cross-section at NLO have been presented in Sections 2.2.3 and 2.3, namely the matrix element calculation in perturbative QCD at NLO precision with bin-wise correction factors for non-perturbative effects, and the k-factor approach where the Monte Carlo simulation with a LO matrix element is reweighted to NLO precision using a per-jet correction. Both methods exhibit an incorrect treatment in the so-called *matching* between the matrix element and the parton shower. This inconsistency is related to the term for the real emissions, σ^R, in Equation 2.3, which corresponds to the $2 \to 3$ diagrams at Born-level, i.e. diagrams without any virtual loops. The diagrams account for the first additional branching of in- or outgoing particles in the event. However, the Monte Carlo generator with a LO matrix element includes the first branching in the LL approximation of the parton shower, as indicated by the following graphical representation:

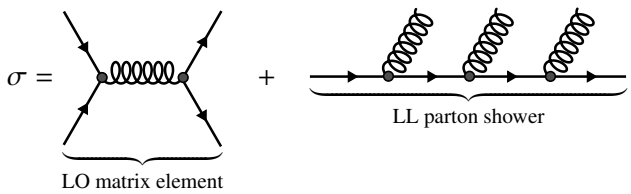

(2.12)

The left side corresponds to the parton-level cross-section at LO precision, σ^LO. The right side represents the emissions from the evolution of the parton shower. While this approach is consistent for a matrix element calculation at LO, it results in a double counting of the first emission when the term for

the real emission, σ^{R}, of the NLO matrix element calculation is interfaced to the same parton shower:

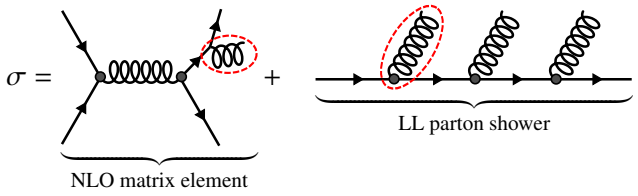

(2.13)

Several methods to resolve this ambiguity in the matching between matrix element and parton shower exist [71–74]. Here, the approach of the Powheg method [72] is presented.

2.4.1 The Powheg formalism

The idea of the Powheg approach is to establish a clean interface between the NLO matrix element calculation and the LO parton shower Monte Carlo in order to avoid the double counting described above. The procedure is as follows. First, the $2 \rightarrow 2$ process is calculated at NLO, i.e. including all NLO diagrams of the virtual corrections, of which two examples are shown in Figures 1.9a and 1.9b. Then, one additional branching is added to one of the initial-state or final-state partons of these diagrams. To generate this emission, Powheg employs a modified Sudakov form factor in analogy to the corresponding calculation in the parton shower simulation, with the difference that it provides a NLO accuracy in α_{S} to achieve an exact NLO matrix element calculation. Hence, the additional branching represents either the real emission of the NLO correction in the case of a $2 \rightarrow 2$ process at LO, as shown for two examples in Figures 1.9c and 1.9d. Or it can be seen as the first emission in the parton shower evolution for a $2 \rightarrow 2$ process at NLO, as shown for two examples in Figures 2.6a and 2.6b. In any case, the result is a $2 \rightarrow 3$ process with a clean interface to the parton shower simulation. By assigning the ambiguous

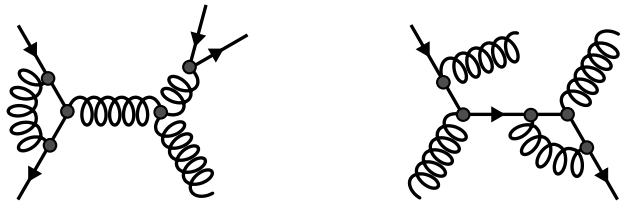

Figure 2.6: Examples of next-to-next-to-leading-order QCD diagrams for quark and gluon interactions.

first branching always to the matrix element calculation, Powheg allows to resolve the double counting between the matrix element calculation and the parton shower. The Powheg method implies that this first emission is the hardest in the event, but it can be shown that this assumption is physical and without loss of generality [72] for both, angle-ordered and p_{T}-ordered parton shower calculations. Accordingly, the parton shower simulation must be able to veto any emission that is harder than the first emission generated by Powheg. However, all generators that agree with the *Generic User Process Interface for Event Generators* [75] have to fulfil this requirement.

The formalism to generate the hardest emission in the Powheg approach follows the equation

$$d\sigma = d\sigma^{\mathrm{B}}(\phi_v) d\phi_v \left[\Delta^{\mathrm{R}}(\phi_v, 0) + \Delta^{\mathrm{R}}(\phi_v, p_{\mathrm{T}}) \frac{d\sigma^{\mathrm{R}}(\phi_v, \phi_r)}{d\sigma^{\mathrm{LO}}(\phi_v)} \theta(k_{\mathrm{T}} - p_{\mathrm{T}}) d\phi_r \right]. \tag{2.14}$$

Here, $d\sigma^{\mathrm{B}}$ is the differential cross-section used to generate the $2 \to 2$ process,

$$d\sigma^{\mathrm{B}}(\phi_v) = d\sigma^{\mathrm{LO}}(\phi_v) + d\sigma^{\mathrm{V}}(\phi_v) + \int_r d\sigma^{\mathrm{R}}(\phi_v, \phi_r) d\phi_r. \tag{2.15}$$

In both equations, $\sigma^{\mathrm{R}}(\phi_v, \phi_r)$ denotes the contributions from the real terms of the NLO diagrams, and $\sigma^{\mathrm{LO}}(\phi_v)$ represents the LO terms. The phase space is written as $d\phi = d\phi_v d\phi_r$, where $d\phi_v$ denotes the phase space of the $2 \to 2$ process, and $d\phi_r$ the one of the real emissions of the NLO contributions. Δ^{R} is the Powheg Sudakov form factor at NLO precision, defined as

$$\Delta^{\mathrm{R}}(\phi_i, p_{\mathrm{T}}^{\mathrm{min}}) = \exp\left[- \int_r d\phi_r \frac{d\sigma^{\mathrm{R}}(\phi_v, \phi_r)}{d\sigma^{\mathrm{LO}}(\phi_v)} \, \theta(k_{\mathrm{T}}(\phi_r) - p_{\mathrm{T}}^{\mathrm{min}}) \right], \tag{2.16}$$

which obeys the DGLAP Equation 1.10 and 1.11, and gives the probability that no parton splitting occurs. The transverse momentum of the emitted particle with respect to the emitting one is given as $k_{\mathrm{T}}(\phi_r)$, and θ is the angle between them. The lower cut-off on the transverse momentum, $p_{\mathrm{T}}^{\mathrm{min}}$, is introduced to suppress non-physical values of α_{S} and in the PDF [76].

Separating the first emission from the parton shower and assigning it to the matrix element calculation introduces an additional scale in the parton shower description, the so-called *matching scale*. Powheg defines it as the hardest emission in the event by transverse momentum of the branching, $k_{\mathrm{T}}(\phi_r)$. For a p_{T}-ordered parton shower generator like Pythia, this choice is natural and can be implemented straight forward. Angular-ordered parton shower generators like Herwig provide a p_{T}-veto mechanism that discards all jets with $p_{\mathrm{T}} > k_{\mathrm{T}}$, and introduce a so-called *vetoed truncated shower* [72] to deal with the fact that the hardest emission may not be the first in angular-ordered parton showers, as required by the Powheg formalism.

2.4.2 Event weighting and fluctuations in observables

The inclusive jet cross-section is a steeply falling function for increasing transverse momentum, being roughly proportional to p_{T}^{-5}. Thus, it is difficult to cover the phase space at large p_{T} with a satisfying number of entries when uniform weights are used in the event generation. Monte Carlo simulations usually address this problem by producing several independent samples in a defined kinematic range of the phase space, e.g. by the Born k_{T} of the $2 \to 2$ process. These samples are then recombined to populate the full phase space using event weights according to the cross-section of the individual sample to populate the full phase space. Powheg offers a different approach, which provides a homogeneous samples with individually weighted events. The event generation is distributed according to the differential jet cross-section multiplied with a suppression factor S, defined as

$$S(k_{\mathrm{T}}) = \left(\frac{k_{\mathrm{T}}^2}{k_{\mathrm{T}}^2 + k_{\mathrm{T,supp}}^2} \right)^3 . \tag{2.17}$$

Here, k_{T} is the transverse momentum of the final-state partons at Born level. $k_{\mathrm{T,supp}}$ is the so-called *Born suppression factor*. The behaviour of $S(k_{\mathrm{T}})$ is such that the event production is largely suppressed at low transverse momentum, while for larger transverse momenta the spectrum is uniformly populated up to the value of approximately $k_{\mathrm{T,supp}}$. To each generated event, an individual weight $1/S(k_{\mathrm{T}})$ is assigned. Accordingly to the behaviour of $S(k_{\mathrm{T}})$, weights at $k_{\mathrm{T}} > k_{\mathrm{T,supp}}$ are close to unity, while weights at small k_{T} are large.

Problems with the weighting scheme arise in combination with certain event topologies in the Powheg

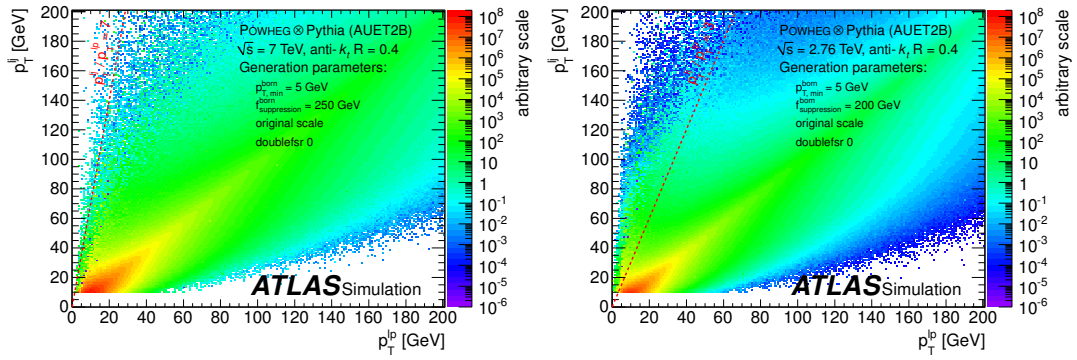

(a) $\sqrt{s} = 7\,\text{TeV}$, original scale

(b) $\sqrt{s} = 2.76\,\text{TeV}$, original scale

Figure 2.7: Matching of the transverse momenta of the leading parton from POWHEG, $p_{\text{T}}^{l}p$, and the leading jet after the parton shower, $p_{\text{T}}^{l}j$, in a sample using weighted events. POWHEG is interfaced to PYTHIA with the AUET 2B tune to simulate the parton shower, and the anti-k_t algorithm with a radius parameter of $R = 0.4$ is used. The default configuration from POWHEG is applied with a generation parameter of $k_{\text{T,supp}} = 200\,\text{GeV}$ and $k_{\text{T,supp}} = 250\,\text{GeV}$ for $\sqrt{s} = 2.76\,\text{TeV}$ and $\sqrt{s} = 7\,\text{TeV}$, respectively. The *dotted line* indicates the event cut $p_{\text{T}}^{lj}/p_{\text{T}}^{lp} > \kappa$.

event generation. These events contain jets at particle-level with very large values of the transverse momenta, although the partons themselves only carry a relatively low p_{T}. Furthermore, these jets have been found to be mostly uncorrelated with the initial partons in rapidity and azimuthal angle. This suggests that these high p_{T} jets originate from additional radiations in the parton shower, despite the fact that the hardest branching in the POWHEG formalism has to be generated in the matrix element calculation.

The reason is a much larger matching scale than the maximum p_{T} of the partons, so that the subsequent radiative emissions in the parton shower is allowed to produce jets with large p_{T}. The effect can be visualised in Figures 2.7b and 2.7a, showing the distribution of the transverse momentum of the leading parton, p_{T}^{lp} versus the transverse momentum of the leading jet, p_{T}^{lj} for a centre-of-mass energy of $\sqrt{s} = 2.76\,\text{TeV}$ and $\sqrt{s} = 7\,\text{TeV}$, respectively. Although most events are found in the region $p_{\text{T}}^{lp} = p_{\text{T}}^{lj}$ as expected, a clear side band at $p_{\text{T}}^{lp} \approx 10\,\text{GeV}$ is present. Here, events with small p_{T} of the leading parton migrate to large p_{T} of the leading jet. The jets in this region are found to be produced primarily from initial state radiation, as shown in the distribution of p_{T}^{lp} versus p_{T}^{lj} of Figures 2.8a and 2.8b. In the latter, ISR was explicitly switched off in the parton shower simulation, resulting in an effective suppression of the migration.

The problem that arises from the large matching scale and the corresponding migration is twofold. First, the migration suggests that the ordering of subsequent emissions is not perfect, thus indicating a potential double counting. The second issue concerns the weighting scheme. Since the underlying Born k_{T} of these events is small, they carry very large weights according to Equation 2.17. Due to the migration described above, these heavy-weighted events cause distortions in the final jet spectrum. Being very rare in comparison to the majority of events, those distortion can not be smoothed by increasing the number of events in the sample.

This effect was first observed in the measurement of the jet cross-section at ATLAS [2], and addressed by the authors of POWHEG [4] in the course of the study presented below. Four different approaches to suppress the fluctuations in the final observables have been investigated, as described in the following.

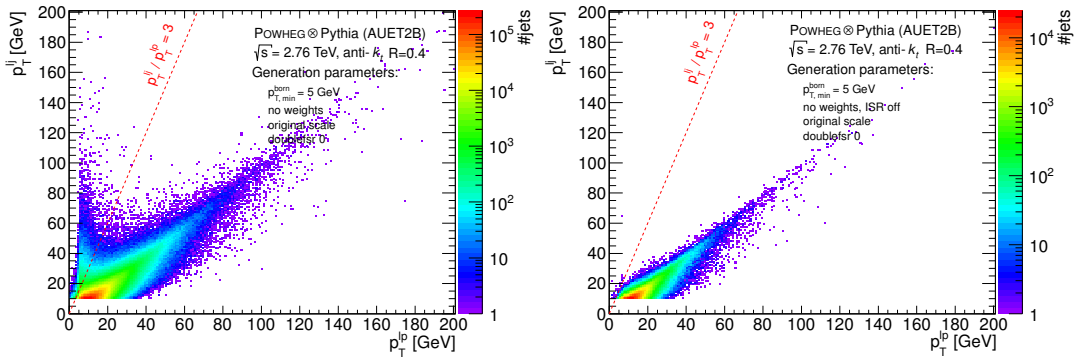

(a) $\sqrt{s} = 2.76\,\text{TeV}$, no weights (b) $\sqrt{s} = 2.76\,\text{TeV}$, no weights, ISR off

Figure 2.8: Matching of the transverse momenta of the leading parton from POWHEG, p_{T}^{lp}, and the leading jet after the parton shower, p_{T}^{lj}, in a sample with unweighted events. POWHEG is interfaced to PYTHIA with the AUET 2B tune to simulate the parton shower in two configurations: (a) with and (b) without the simulation of ISR. The anti-k_t algorithm with a radius parameter of $R = 0.4$ is used. The sample is produced using unweighted events with a generation cut of $k_{\text{T, min}}^{Born} = 5\,\text{GeV}$. The *dotted line* indicates the event cut $p_{\text{T}}^{lj}/p_{\text{T}}^{lp} > \kappa$.

Event cut approach

Since the event topologies are expected to be rare, the fluctuations can be suppressed by removing events that fulfil

$$p_{\text{T}}^{lj}/p_{\text{T}}^{lp} > \kappa. \tag{2.18}$$

This approach was developed in the jet cross-section measurement at $\sqrt{s} = 7\,\text{TeV}$ [2]. The parameter κ was chosen to be 7, being the largest value before spikes in the final observables reappear. The corresponding distribution is shown in Figure 2.7a. The event cut approach was found to introduce only a negligible bias. However, not all fluctuations are removed using $\kappa = 7$ in the POWHEG event sample at $\sqrt{s} = 2.76\,\text{TeV}$, and the parameter must be relaxed to $\kappa = 3$, as shown in Figure 2.7b. This removes a considerable fraction of events, corresponding to almost 10% of the cross-section in the range of $30\,\text{GeV} < p_{\text{T}} < 80\,\text{GeV}$ for the central rapidity region, $|y| < 0.3$. Figure 2.9a shows the comparison of the prediction for the inclusive jet cross-section at $\sqrt{s} = 2.76\,\text{TeV}$ as a function of p_{T} in the rapidity range $|y| < 0.3$ for anti-k_t jets with $R = 0.4$ for several values of κ. $\kappa = 3$ is used as reference, since it shows no fluctuations. A difference of up to 10% between $\kappa = 3$ and $\kappa = 7$ is observed. The predictions for $\kappa = 7$ and $\kappa = \infty$, i.e. without the event cut, are at the same level for the bins where no fluctuations are present. This is a sign that only a small bias is introduced by the event cut. In the rapidity range of $0.3 < |y| < 0.8$, shown in Figure 2.9b, also the prediction with $\kappa = 7$ suffers from large fluctuations.

Unweighted event sample

To diminish the impact of the migration of the events with very large weights from low p_{T}^{lp} to large p_{T}^{lj}, samples with unweighted events can be produced. In order to cover the complete phase space, the sample is split in slices of p_{T}^{lj} in conjunction with a generation cut on $k_{\text{T}}^{\text{Born}}$. Figure 2.10 shows the boundary definition of the jet sample in the plane of p_{T}^{lp} and p_{T}^{lj} for a sample with unweighted events, $p_{\text{T}}^{\text{Born}} = 5$ GeV. Although the reach in p_{T} is limited, it is obvious that a considerable fraction of events

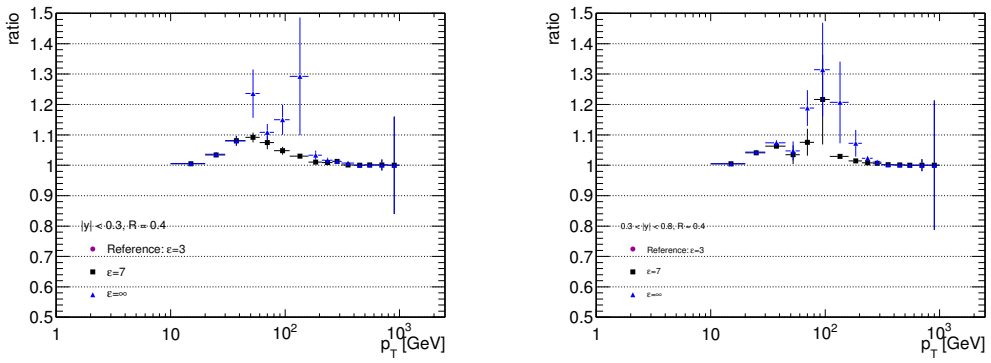

(a) $|y| < 0.3$ (b) $0.3 < |y| < 0.8$

Figure 2.9: Comparison of the prediction of the inclusive jet cross-section at $\sqrt{s} = 2.76\,\text{TeV}$ as a function of p_T for anti-k_t jets with $R = 0.4$ using Powheg with Pythia and the Auet 2b tune for several values of κ. As reference, a value of $\kappa = 3$ is used.

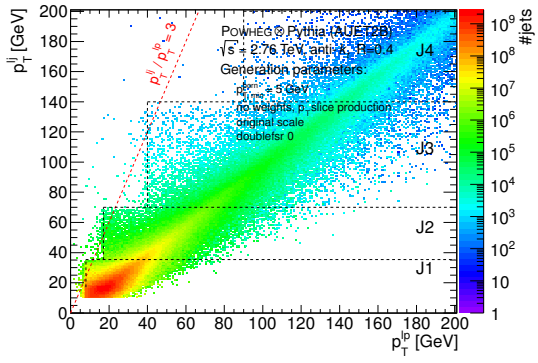

Figure 2.10: Matching of the transverse momenta of the leading parton from Powheg, $p_\text{T}^l p$, and the leading jet after the parton shower, $p_\text{T}^l j$, in a combined sample from a p_T-sliced production. Powheg is interfaced to Pythia with the Auet 2b tune to simulate the parton shower. The anti-k_t algorithm with a radius parameter of $R = 0.4$ is used. The sample is composed of several subsamples in defined p_T ranges of the particle-level jets of [17, 35] (J1), [35, 70] (J2), [70, 140] (J3), [140, 280] (J4), [280, 560] (J5) in GeV. The *dotted lines* indicate the boundaries of the subsamples and the event cut [2] $p_\text{T}^{lj}/p_\text{T}^{lp} > \kappa$.

is present at low p_T^{lp} and large p_T^{lj}. Hence, the generation cut for the jet slices effectively corresponds to the event cut approach, and is expected to introduce a similar bias. However, it should be noted that Figure 2.10 might be misleading with respect to the size of the expected bias. The region at very low p_T^{lp}, i.e. at low p_T^Born, is problematic since the Born cross-section for the production of light partons diverges. Powheg avoids this by allowing negative weights in combination with the Born suppression factor for the weighted event generation. Thus, the large number of migrating events in the sample without weights may not be physical.

Matching scale modification

To avoid fluctuations in the final observables after the showering process, the original matching scale provided by Powheg can be modified [77]. A new matching scale, the minimum transverse momentum between the final-state partons with respect to each other in the centre-of-mass frame and with respect to the beam axis in the lab frame is assigned. This matching scale choice is particularly suited for the p_T-ordered parton shower scheme as applied in Pythia and avoids any migrations from low p_T^{lp} to large p_T^{lj}, as shown in Figures 2.11a and 2.11b. The resulting cross-section is reduced by about 10%. The different matching scale choice can be justified by the fact that it does not spoil the NLO accuracy and the leading logarithmic accuracy of the program, but rather exploits the uncertainty associated to shower effects at subleading level [4].

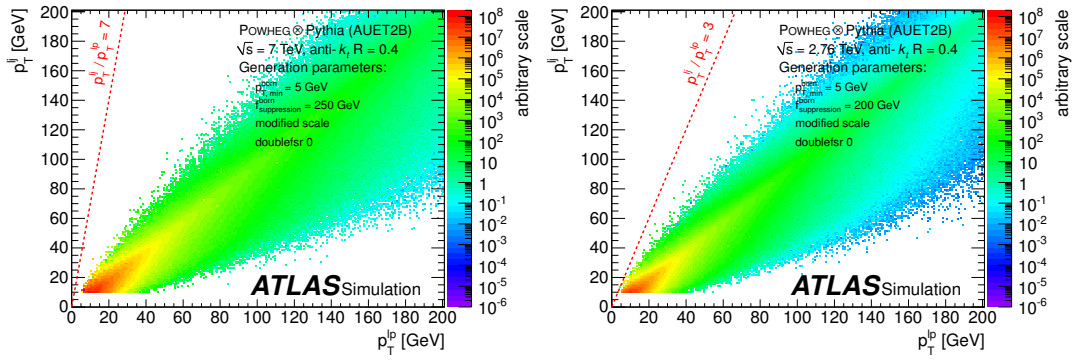

(a) $\sqrt{s} = 7\,\text{TeV}$, modified matching scale (b) $\sqrt{s} = 2.76\,\text{TeV}$, modified matching scale

Figure 2.11: Matching of the transverse momenta of the leading parton from Powheg, $p_{\text{T}}^{l}p$, and the leading jet after the parton shower, $p_{\text{T}}^{l}j$, in a sample using weighted events with a modified matching scale. Powheg is interfaced to Pythia with the Auet 2b tune to simulate the parton shower, and the anti-k_t algorithm with a radius parameter of $R = 0.4$ is used. The default configuration from Powheg is applied with a generation parameter of $k_{\text{T,supp}} = 200\,\text{GeV}$ and $k_{\text{T,supp}} = 250\,\text{GeV}$ for $\sqrt{s} = 2.76\,\text{TeV}$ and $\sqrt{s} = 7\,\text{TeV}$, respectively. The *dotted line* indicates the event cut [2] $p_{\text{T}}^{lj}/p_{\text{T}}^{lp} > \kappa$.

Improved suppression

Very recently, the authors of the Powheg Box dijet generator have addressed the issue with the spikes in the final observables in a dedicated note [4] and a new version of the generator. They identified the event topologies leading to the large weights with rare events from gluon emissions $q \to qg$ and gluon splittings $g \to q\bar{q}$. By default, the Powheg Box does not include the corresponding configurations $q \to gq$ and $g \to \bar{q}q$, which is problematic in this very suppressed region of phase space. The latest revision 2169 of the software offers a switch `doublefsr=1` to include these processes for an improved handling of the suppression. Details may be found in [4]. Figures 2.12a and 2.12b show that using the option `doublefsr=1` any migrations from low p_{T}^{lp} to high p_{T}^{lj} are effectively avoid, and the distribution is homogeneous, i.e. without spikes.

2.4.3 Comparison

Figure 2.13 shows the comparison of the theory predictions for the inclusive jet cross-section from Powheg for different matching scale choices in a ratio to the prediction using the nominal original scale with `doublefsr=1`, separately for two centre-of-mass energies $\sqrt{s} = 2.76\,\text{TeV}$ and $\sqrt{s} = 7\,\text{TeV}$, and two rapidity bins. The used parton shower Monte Carlo simulation is Pythia with the tune Auet 2b. The radius parameter for the anti-k_t jets is $R = 0.4$, but similar results have been found for $R = 0.6$.

At $\sqrt{s} = 2.76\,\text{TeV}$ in the central region, shown in Figure 2.13a, the difference from the scale variation using a scale factor is in the order of $d\sigma/\sigma = ^{+25}_{-0}$ % at $p_{\text{T}} = 20\,\text{GeV}$, and within $d\sigma/\sigma = ^{+5}_{-0}$ % at $p_{\text{T}} = 400\,\text{GeV}$. At $2.1 < |y| < 2.8$, shown in Figure 2.13b, it is $d\sigma/\sigma = ^{+25}_{-0}$ % ($d\sigma/\sigma = ^{+10}_{-10}$ %) at low (high) p_{T}. At $\sqrt{s} = 7\,\text{TeV}$, the difference is larger at low p_{T}, and of similar size in the high p_{T} region, as shown in Figures 2.13c and 2.13d. The central value of the sample using the modified matching scale results in a up to 10% lower cross-section at low p_{T} for the central value, but agrees within a few percent at larger p_{T}. In general, it shows a good agreement with the nominal prediction in the forward region for both centre-of-mass energies. Also shown is the prediction using the event cut to suppress spikes in the final distributions. It differs by about 10% in the range of $20\,\text{GeV} < p_{\text{T}} < 100\,\text{GeV}$ at both

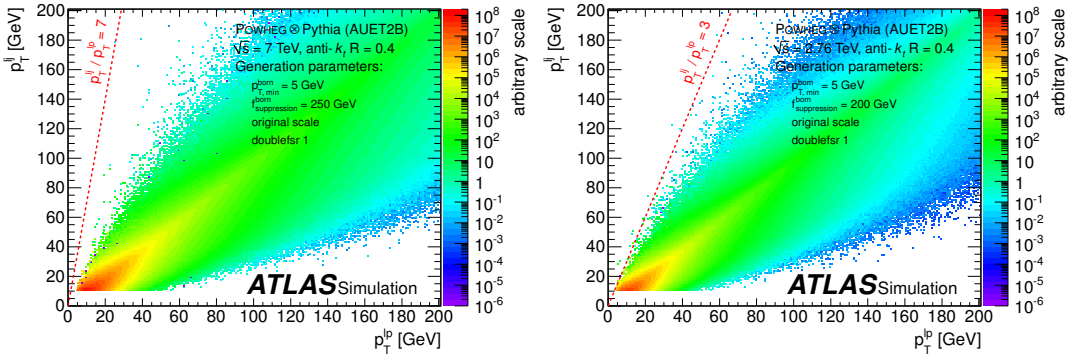

(a) $\sqrt{s} = 7\,\text{TeV}$, `doublefsr=1` (b) $\sqrt{s} = 2.76\,\text{TeV}$, `doublefsr=1`

Figure 2.12: Matching of the transverse momenta of the leading parton from POWHEG, $p_{\mathrm{T}}^{l}p$, and the leading jet after the parton shower, $p_{\mathrm{T}}^{l}j$, in a sample using weighted events and the `doublefsr=1` option. POWHEG is interfaced to PYTHIA with the AUET 2B tune to simulate the parton shower, and the anti-k_t algorithm with a radius parameter of $R = 0.4$ is used. The default configuration from POWHEG is applied with a generation parameter of $k_{\mathrm{T,supp}} = 200\,\text{GeV}$ and $k_{\mathrm{T,supp}} = 250\,\text{GeV}$ for $\sqrt{s} = 2.76\,\text{TeV}$ and $\sqrt{s} = 7\,\text{TeV}$, respectively. The *dotted line* indicates the event cut [2] $p_{\mathrm{T}}^{lj}/p_{\mathrm{T}}^{lp} > \kappa$.

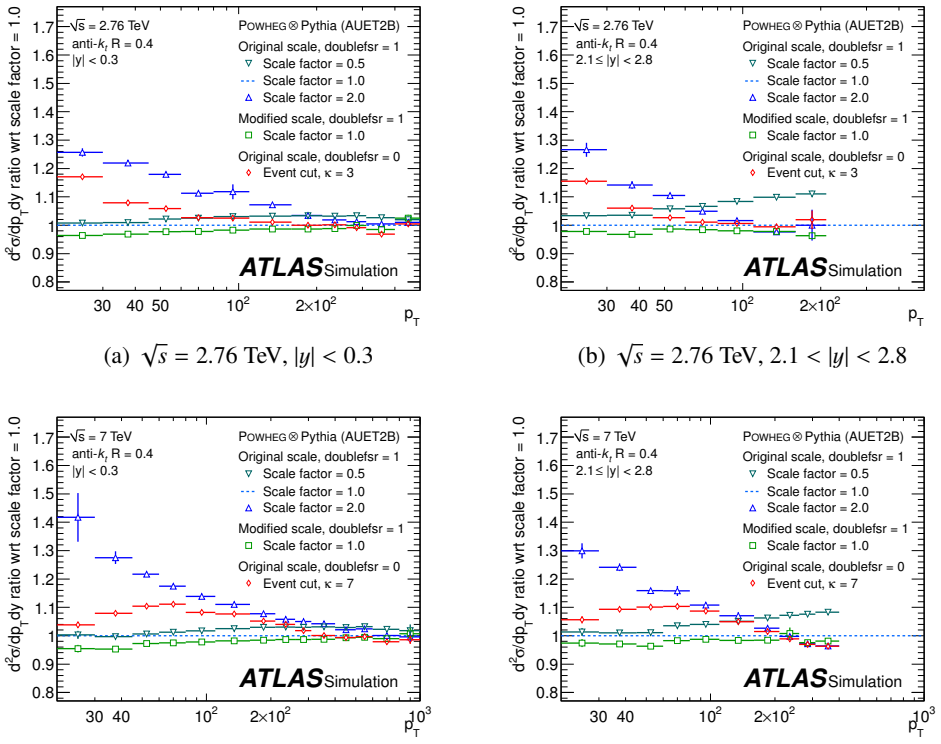

(a) $\sqrt{s} = 2.76\,\text{TeV}$, $|y| < 0.3$ (b) $\sqrt{s} = 2.76\,\text{TeV}$, $2.1 < |y| < 2.8$

(c) $\sqrt{s} = 7\,\text{TeV}$, $|y| < 0.3$ (d) $\sqrt{s} = 7\,\text{TeV}$, $2.1 < |y| < 2.8$

Figure 2.13: Comparison of the predictions for the inclusive jet cross-section from POWHEG for different matching scale choices in a ratio to the prediction using the nominal original scale with *doublefsr=1*, separately for two centre-of-mass energies and two rapidity bins. The used parton shower Monte Carlo simulation is PYTHIA with the tune AUET 2B. The jet algorithm is anti-k_t with a radius parameter of $R = 0.4$. Also shown is the prediction using an event cut to suppress spikes in the final distributions [2]. Results for $R = 0.6$ are very similar.

centre-of-mass energies with respect to the nominal prediction, but is contained within the variation of the matching scale choice.

Since the event generation with `doublefsr=1` naturally avoids any problems with rare event topologies and the associated large matching scale, and since it is the solution recommended by the authors of the Powheg Box dijet generator, it is used for the nominal prediction from NLO matrix elements with parton shower Monte Carlo. The configurations used for the event generation are listed in Tables A.4 and A.5 in the appendix.

2.4.4 Systematic uncertainty

As shown above, an additional uncertainty arises in the Powheg approach from the different approaches to calculate the matching scale, μ_M. The sensitivity of the result on the matching scale is studied by varying μ_M with a scale factor f_{μ_M}. The result is shown in Figure 2.14 for anti-k_t jets with $R = 0.4$ at $\sqrt{s} = 2.76$ TeV and $\sqrt{s} = 7$ TeV for several representative regions in y-p_{T} space. The nominal Powheg sample with `doublefsr=1` and the original matching scale, $f_{\mu_M} = 1$, is used as reference. At low p_{T}, a local minimum in the cross-section is found for a scale factor of about 0.8. In the high p_{T} forward region, shown in Figures 2.14b and 2.14d, the minimum is found at larger values than 1.0. In any case, a scale factor of 1.0 is very close to the minimal cross-section in the prediction. Consequently, the uncertainty on the matching scale choice is assessed by varying the matching scale by the factors 0.5, 1.0 (nominal) and 2.0. The uncertainty is taken from the envelope of this variation.

Unlike Nlojet++ with Applgrid, the Powheg program does not offer a framework to vary the PDF set, the strong coupling α_{S}, and the factorisation and renormalisation scales, μ_F and μ_R, respectively. Therefore, the determination of the corresponding uncertainties is computationally intensive and could not be carried out within this work. However, they are expected to be of similar size than in the pure calculation at NLO precision provided by Nlojet++.

2.5 Summary of theory predictions

A comparison of the different approaches to obtain a theory predictions at NLO precision is presented in Figure 2.15. Is shows the inclusive jet cross-section at $\sqrt{s} = 2.76$ TeV using jets with a radius parameter of $R = 0.6$ in the rapidity range $|y| < 0.3$ from Nlojet++ with non-perturbative correction applied, Powheg with Pythia and the Auet 2b tune, and Pythia with the Auet 2b tune in the k-factor approach. The uncertainty on the prediction from Powheg corresponds to the matching scale uncertainty only, obtained as the envelope from variations by factors of 0.5 and 2.0, while the prediction from Nlojet++ includes the uncertainty due the scales μ_R and μ_F, the PDF set, α_{S}, and the parton shower tunes. The central values of Nlojet++ and Powheg show reasonable agreement, with differences being smaller than 10%. However, since the uncertainties given for Nlojet++ are expected to be highly correlated with those from Powheg, and since the uncertainty due to the matching scale is small at high p_{T}, the difference is not fully covered. The larger difference of up to 35% of the prediction from Pythia with respect to the others on the other hand can be attributed to the fact that Pythia inherently is a LO calculation. The k-factor procedure applied here only accounts for the PDF part of the calculation, while the matrix element is not included in the correction. Hence, the comparison confirms that the procedure cannot be expected to produce a accurate result and should be used primarily for validation studies of detector effects only.

Consequently, the prediction from Nlojet++ with the CT 10 PDF set and non-perturbative corrections from Pythia with the Auet 2b tune is used as the default for the comparison to experimental data

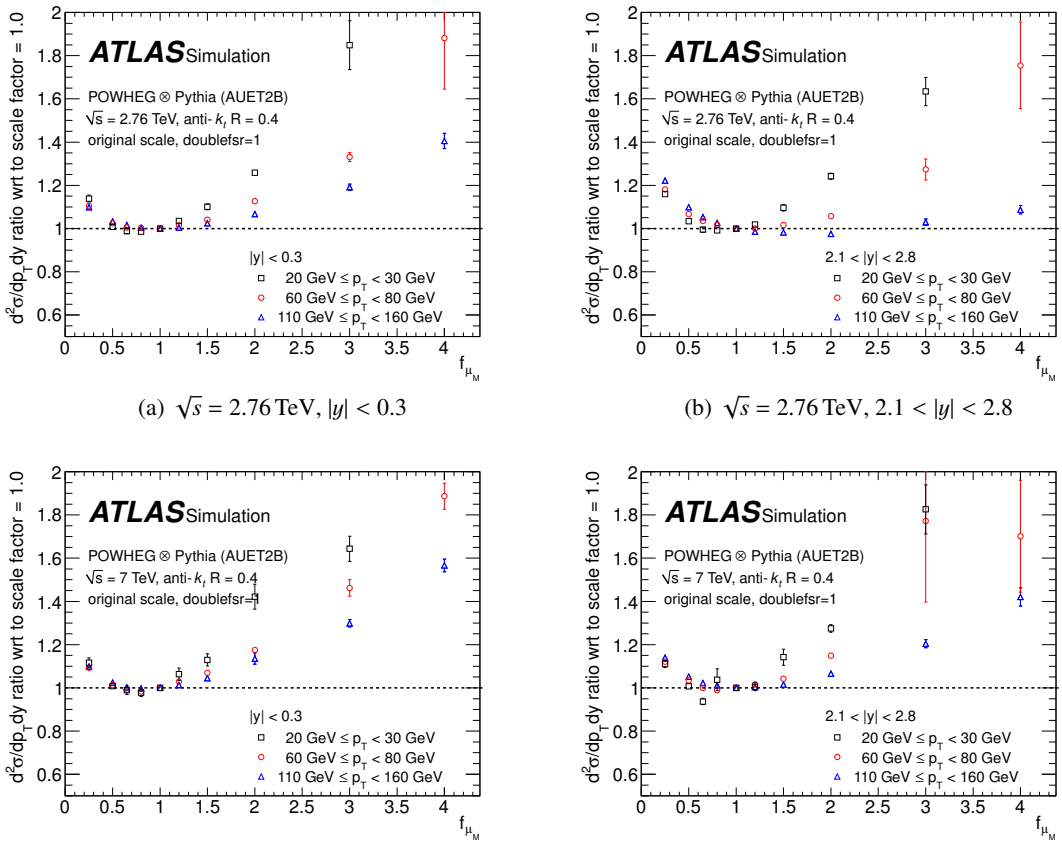

(a) $\sqrt{s} = 2.76\,\text{TeV}$, $|y| < 0.3$

(b) $\sqrt{s} = 2.76\,\text{TeV}$, $2.1 < |y| < 2.8$

(c) $\sqrt{s} = 7\,\text{TeV}$, $|y| < 0.3$

(d) $\sqrt{s} = 7\,\text{TeV}$, $2.1 < |y| < 2.8$, $\sqrt{s} = 7\,\text{TeV}$

Figure 2.14: Variation of the matching scale, μ_M, using the scale factor f_{mu_M}, shown for anti-k_t jets with $R = 0.4$ at several regions: (a) $|y| < 0.3$, $\sqrt{s} = 2.76\,\text{TeV}$, (b) $2.1 < |y| < 2.8$, $\sqrt{s} = 2.76\,\text{TeV}$, (c) $|y| < 0.3$, $\sqrt{s} = 7\,\text{TeV}$, and (d) $2.1 < |y| < 2.8$, $\sqrt{s} = 7\,\text{TeV}$. The nominal POWHEG sample with `doublefsr=1` and the original matching scale, $f_{mu_M} = 1$, is used as reference. The parton shower is simulated using PYTHIA with the AUET 2B tune.

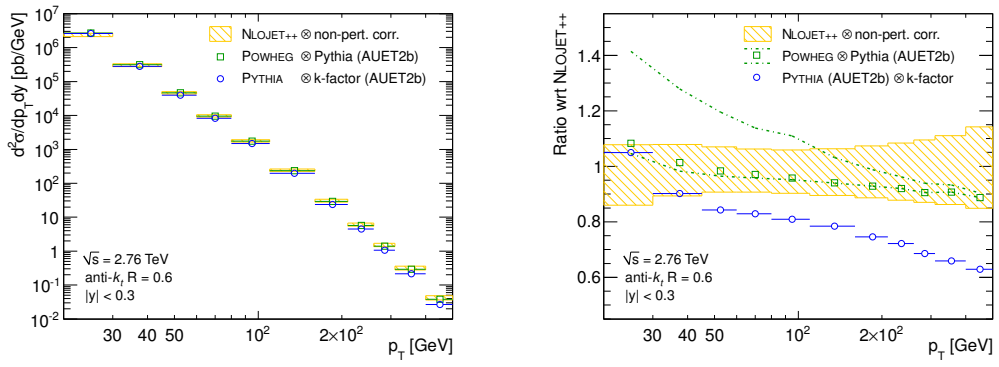

(a) (b)

Figure 2.15: Comparison of different NLO theory predictions using jets with $R = 0.6$ in the rapidity range $|y| < 0.3$ for (a) the inclusive jet cross-section and (b) in a ratio with respect to the prediction from NLOJET++. The prediction from NLOJET++ includes the uncertainty due the scales μ_R and μ_F, the PDF set, and α_S. The uncertainty on the prediction from POWHEG corresponds to the matching scale uncertainty only, obtained as the envelope from variations by factors of 0.5 and 2.0. For the predictions from PYTHIA only the statistical uncertainty is shown.

throughout this thesis, since it is expected to provide an accurate cross-section calculation, and includes the full evaluation of the systematic uncertainties due to the scales μ_R and μ_F, the PDF set, α_S, and the parton shower tunes. Nevertheless, data is also compared to predictions from POWHEG, since its novel approach offers a coherent treatment of ambiguities between NLO matrix elements and LO parton shower, and thus might become the preferred one in the future.

CHAPTER 3

The ATLAS experiment

The first proposal for the *ATLAS experiment*[1] in its current form was made in 1994. It emerged from the combination of two detector studies with similar outlines, EAGLE [78] and ASCOT [79], which were merged into a single, general-purpose detector. In 1999, the design of the ATLAS detector was finalised with the publication of the technical design report [80, 81] and the construction of the different components started. Due to the complexity and large number of subsystems, the detector was built in a collaborative effort of 138 institutions from all over the world. The assembly of the subsystems in the experimental cavern started in 2003 and reached completion in 2008. Today, the ATLAS collaboration is formed by about 3000 physicists from 175 institutions in 38 countries.

The ATLAS experiment is located at the *Large Hadron Collider* (LHC), a particle accelerator built to collide protons or heavy ions at a centre-of-mass energy up to 14 TeV. The LHC is part of CERN[2], the European laboratory for particle physics. Founded in 1954, CERN hosted a series of high energy particle physics colliders and their experiments, such as the Proton Synchrotron (PS) at which the weak neutral currents were discovered, or the Super Proton Synchrotron (SPS) where the W and Z bosons were discovered. Many of the accelerators are still operational and form the pre-acceleration chain for the particles before injected into the LHC, as shown in Figure 3.1.

[1] ATLAS - *A toroidal LHC apparatus*.
[2] CERN - *European organisation for nuclear research*, Geneva, Switzerland.

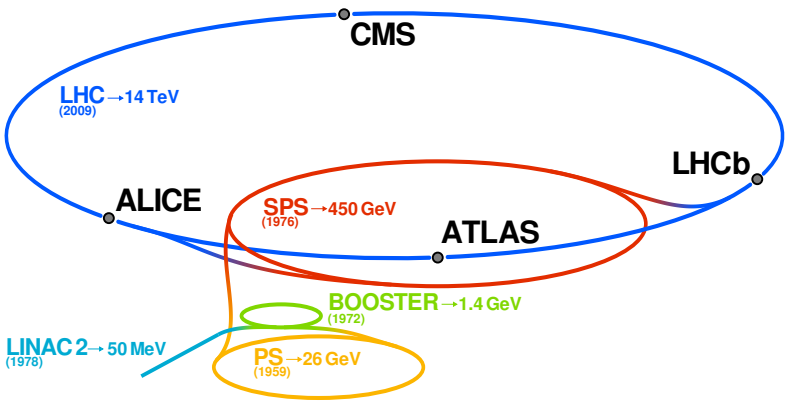

Figure 3.1: The accelerator complex at CERN and the four main experiments at the LHC, namely ATLAS, LHCb, CMS and ALICE. The pre-accelerator chain consists of the linear accelerator LINAC2, the booster, the Proton Synchrotron (PS) and the Super Proton Synchrotron (SPS), until protons are injected in the Large Hadron Collider (LHC) ring. Also shown are the final beam energies of each pre-accelerator and the year of first operation.

The LHC is the replacement of the Large Electron Positron collider (LEP), which was used to perform precision measurements of electroweak physics. However, circular electron-positron colliders are limited in the maximal energy they can achieve because of synchrotron radiation. The proton-proton collisions at the LHC allow both high centre-of-mass energies and high interaction rates, making them a perfect discovery machine for new particles and phenomena beyond the Standard Model of particle physics up to the TeV range.

The physics program of the ATLAS experiment [81] covers both, precision measurements of the fundamental parameters of the SM, and searches for new phenomena beyond the SM. However, the most important objectives of the physics program are the discovery and the study of the Higgs boson, the only particle of the SM that had been predicted, but not yet observed experimentally at the conceptional phase of ATLAS. Hence, the experiment is required to cover a very broad spectrum of possible processes over a large energy range. In addition, it has to cope with a high interaction rate, since the cross-sections for the production of the Higgs boson and new particles in BSM theories are usually very small compared to the total cross-section of inelastic pp collisions. The resulting design principles for the detector are as follows:

Tracking The tracking system must provide a high granularity and position resolution to be able to resolve the vertices and high momentum tracks from overlapping collision events in the same bunch crossing, as well as exceptional radiation hardness due to the required proximity to the interaction point. Furthermore, it must provide good performance of secondary vertex detection for studies of b-quarks or τ-leptons, e.g. in the decay channels of the Higgs boson, $H \to bb$ and $H \to \tau\tau$.

Calorimeter A calorimeter with good energy resolution of photons and electrons, as well as τ-leptons and jets, is essential. Benchmark processes for the energy measurement are the Higgs decays into photons, electrons, b-quarks or τ-leptons, searches for new heavy gauge bosons or quark compositeness using highly energetic electrons and jets, as well as QCD precision measurements such as the inclusive jet cross-section. As for the tracking system, a fine segmentation is necessary for a good position resolution, separation of close-by particles and for particle identification. Furthermore, the calorimeter must provide full coverage of the solid angle to be able to reconstruct neutrinos from the *missing energy* in the event, and to detect forward jets from the Higgs production mechanism of vector boson fusion.

Muon spectrometer A separate muon spectrometer at a large distance to the interaction points is required to perform the identification and precision measurements of muons over a large momentum range, such as muon final states in the Higgs decay $H \to ZZ^* \to 4\mu$.

The outline of this chapter is as follows. After the introduction to the LHC in Section 3.1, the ATLAS detector is described in detail in Section 3.2, including the inner detector, the calorimeter, the muon spectrometer and the luminosity detectors. The ATLAS trigger system is outlined in Section 3.3.

3.1 Large Hadron Collider

The Large Hadron Collider is located in a circular tunnel with a circumference of 27 km about 100 m below ground level. It hosts four main experiments. ATLAS and CMS[3] are general-purpose experiments, dedicated to the discovery of the Higgs boson, precision measurements of SM parameters and search for

[3] CMS - *Compact muon solenoid.*

new phenomena beyond the SM. The ALICE[4] experiment is specialised on the investigation of heavy ion collisions, where a new state of matter, the quark-gluon plasma, is expected to be generated. The LHCb[5] experiment is designed to measure the parameters of CP violation in rare decays of b quarks and hence explain the asymmetry of matter and anti-matter in the universe. In addition, there are two smaller experiments for very specialised research, the TOTEM[6] and LHCf[7] experiments, dedicated to processes at small scattering angles.

The physics program of the LHC comprises collisions of protons, heavy ions, and proton-ion collisions. However, most of the operation is dedicated to pp collisions. The data used in this analysis are pp collision data at $\sqrt{s} = 7\,\text{TeV}$ in the data taking period from 2010, corresponding to an integrated luminosity of $\mathcal{L}_{\text{del}} = 48.1\,\text{pb}^{-1}$, and pp collisions at $\sqrt{s} = 2.76\,\text{TeV}$ from March 2011, corresponding to $\mathcal{L}_{\text{del}} = 230\,\text{nb}^{-1}$. The given numbers refer to the integrated luminosities delivered by the LHC; the actually recorded data by the experiment may differ.

Before injection into the LHC and ramping to the final energy, the protons are pre-accelerated using the existing accelerator infrastructure at CERN. The proton source is a duoplasmatron, at which proton ions are extracted from hydrogen gas. The initial acceleration to an energy of 50 MeV is performed by the linear accelerator LINAC2. Subsequently, the protons are boosted to 1.4 GeV to increase the bunch density before inserting them into the Proton Synchrotron. Here, the energy is increased to 25 GeV. The last acceleration stage prior to the LHC is the Super Proton Synchrotron, where the protons are accelerated to an energy of 450 GeV. The typical turnaround time between two fills of the LHC is 2 h, and one fill lasts for about 12 h until the intensity of the beam is substantially reduced by pp collisions, beam-gas interactions and defocusing of the beam. The accelerator chain is depicted in Figure 3.1.

As a consequence of the cavity-based acceleration principle of all accelerators in the pre-accelerator chain, a proton bunch structure is introduced. Typically, each bunch consists of about $n_p = 10^{11}$ protons. Bunches have a minimal separation of 25 ns and are grouped in *bunch trains* of about 100 bunches before injection into the LHC. At full intensity, the proton beam in the LHC consists of 2808 colliding bunches. The acceleration from 450 GeV to the final energy in the LHC is performed separately for the two counter-rotating beam lines using eight superconducting radio frequency (RF) cavities each. The accelerating field has an effective strength of 2 MV/m and oscillates with a frequency of 400 MHz. In a ring with a circumference of $d = 27\,\text{km}$, 35640 bunch positions, so-called *buckets*, are possible. To retain a bunch crossing frequency of $f = 40.08\,\text{MHz}$ at the experiments, maximally every tenth bucket is filled. Due to limitations from the injection and extraction, the maximal number of filled bunches is 2808, as stated above.

In contrast to the e^+e^- collider LEP, the limiting factor for the centre-of-mass energy at the LHC is not the synchrotron radiation, i.e. the accelerating capabilities, but the required bending power to keep the protons in the ring. For that purpose, 1232 superconductive dipole magnets are installed at the LHC, designed to operate at a maximal magnetic field of 8.4 T. Liquid Helium in a superfluid state is used to sustain a temperature of 1.9 K. The two beam pipes are housed in the same cryostat for compactness.

At the four interaction points of the experiments, the beam lines intersect under strong focusing of the beam. The nominal beam parameters for the ATLAS experiment are a crossing angle of $\varphi = 200\,\mu\text{rad}$ and a beam width of $\sigma_x = \sigma_y = 16\,\mu\text{m}$. From these machine parameters, the instantaneous luminosity

[4] ALICE - *A large ion collider experiment*.
[5] LHCb - *Large hadron collider beauty*.
[6] TOTEM - *Total elastic and diffractive cross-section measurement*.
[7] LHCf - *Large hadron collider forward*.

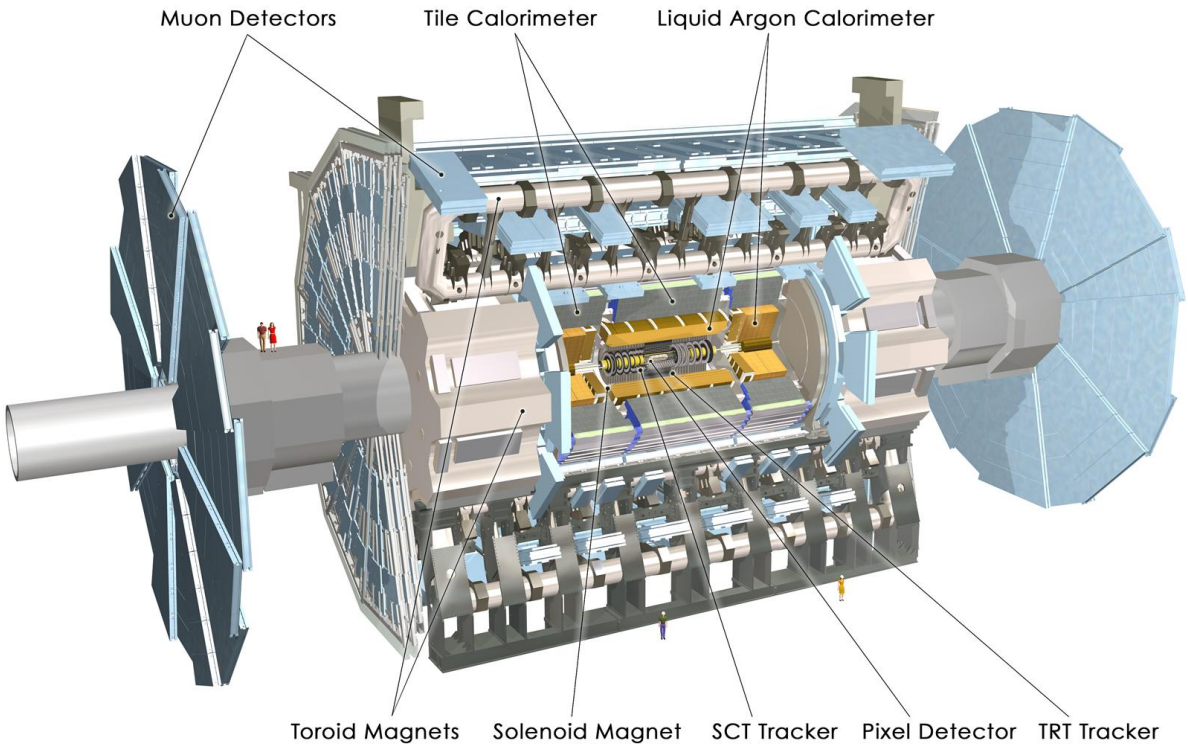

Figure 3.2: Layout of the ATLAS detector, including the inner detector, the calorimeter, the muon detectors, and the magnet system [82].

of a collider ring can be defined as

$$\mathcal{L}_{\text{inst}} = \frac{n_c f_r \cdot n_a n_b}{2\pi \Sigma_x \Sigma_y}. \tag{3.1}$$

Here, n_a and n_b are the number of protons in the colliding beams a and b, and n_c is the number of colliding bunches. The revolution frequency f_r is given by $f_r = d/c = 11.2\,\text{kHz}$, where d is the circumference of the ring, and c is the speed of light. The product $\Sigma_x \Sigma_y$ characterises the horizontal and vertical convolution of the two beams, i.e. the cross-section area. At full intensity, the LHC is designed to reach an instantaneous luminosity of about $10^{34}\ 1/cm^2 s$.

3.2 The ATLAS detector

The ATLAS detector consists of three main systems. From inside out, those are: the inner detector that tracks particles to obtain their momenta; the calorimeter to stop the particles and measure their energy; and the muon spectrometer that determines the momenta of the highly penetrating muons. To be able to reconstruct the strictly weakly-interacting neutrinos, ATLAS follows the design principle of a hermetic 4π detector. The layout of the ATLAS detector is shown in Figure 3.2. The appearance is dominated by the large magnet system, which is an essential part for the momentum measurement in the inner detector and the muon spectrometer. In total, the ATLAS detector has a length of 46 m and a diameter of 25 m. The overall weight amounts to 7000 t.

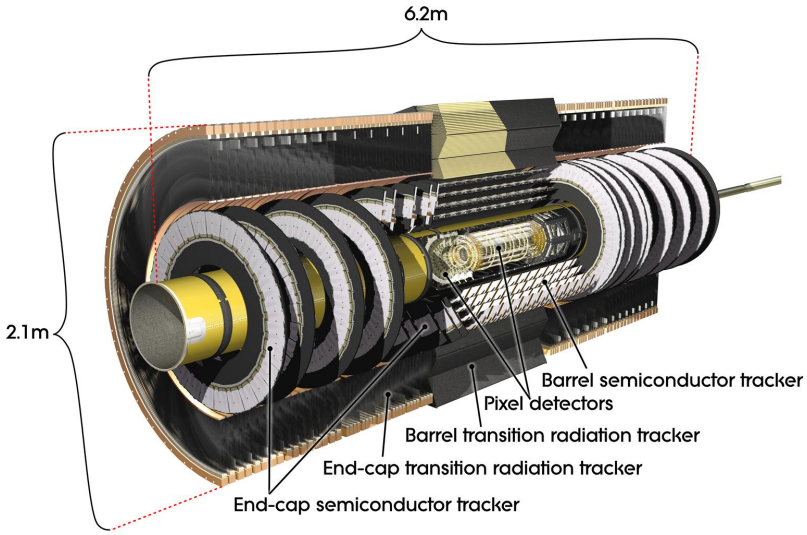

Figure 3.3: Layout of the inner detector, housing the vertex detection, tracking system and particle identification. The pixel detector is located closest to the interaction point, followed by the semiconductor tracker and the transition radiation tracker. At small pseudo-rapidity, the detectors are arranged in a cylindrical shape, while for larger pseudo-rapidity, a disc geometry is used. [83].

The ATLAS reference system is an orthogonal, right-handed coordinate system, where the origin is the nominal interaction point in the centre of the detector. The z-axis is defined by the direction of the beam line. The x-axis points to the centre of the LHC ring, and the y-axis points upward. The azimuthal angle ϕ specifies the angle in the plane orthogonal to the beam axis, while the polar angle θ is given with respect to the beam axis. The transverse component of the momentum p is denoted as $p_{\mathrm{T}} = \sqrt{p_x^2 + p_y^2}$. Alike, the *transverse energy*, E_{T}, is the projection of the energy E on the x-y plane, $E_{\mathrm{T}} = E \cos\theta$. The rapidity is given as $y = \frac{1}{2} \ln\left[(E + p_z)/(E - p_z)\right]$. In the high-energy limit, it can be approximated by the pseudo-rapidity, $\eta = -\ln\tan\left[\theta/2\right]$.

3.2.1 Magnet system

The magnet configuration of the ATLAS detector consists of an inner and outer magnet system with different field configuration. The thin, superconducting solenoid magnet of the inner magnet system has a diameter of 2.4 m and a length of 5.3 m. It provides a 2 T magnetic field parallel to the beam axis for the measurement of particle momenta in the tracking system of the inner detector. The outer magnet system consists of a barrel and two end-cap air-core toroid magnets. Its total length is 25.3 m and it has a diameter of 20.1 m. Each toroid magnet is made of eight coils that generate a magnetic field in the order of about 1 T.

3.2.2 Inner detector

The inner detector (ID) [80] has three main objectives. First, it provides the measurement of charged particle tracks in a pseudo-rapidity range of $|\eta| < 2.5$ with a designated resolution of $\sigma_{p_{\mathrm{T}}}/p_{\mathrm{T}} = 5 \times 10^{-4}\, \mathrm{p_T/GeV} \oplus 0.01$. Measurements of the inner detector are combined with the muon spectrometer for the track reconstruction of muons. Second, the ID performs particle identification, separating electrons and hadrons in the range $500\,\mathrm{MeV} < p_{\mathrm{T}} < 150\,\mathrm{GeV}$, $|\eta| < 2.0$. Finally, it reconstructs the

primary and potential secondary vertices with an expected resolution of $\sigma_{xy} < 30\,\mu\text{m}$ in the x-y plane, and $\sigma_z < 50\,\mu\text{m}$ along the z-axis.

The design principles of the ID are posed by the high luminosity environment of up to 23 interactions in the same bunch crossing and the proximity of the ID to the interaction point. Hence, exceptional radiation hardness is required, as well as a high granularity to resolve the high multiplicity of particle tracks, while attaining a short dead time of the read-out electronics to minimise pile-up effects.

The ID is located inside the 2 T field of the central solenoid magnet and consists of three subsystems with a barrel and a forward segment each. Closest to the interaction point is the high-resolution semiconducting Pixel Detector (PD), followed by the two-part Semiconductor Tracker (SCT), and the Transition Radiation Tracker (TRT). The physical dimension of the ID amount to a length of 6.2 m and a diameter of 2.1 m. The Pixel Detector and the SCT cover a pseudo-rapidity of $|\eta| < 2.5$, whereas the TRT extends to $|\eta| < 2.0$. The layout of the ID is shown in Figure 3.3.

The semiconducting Pixel Detector is made of three layers in the barrel, and five discs on either side. The silicon pixels have a size of $50 \times 400\,\mu\text{m}^2$ and provide a resolution of $14 \times 115\,\mu\text{m}^2$ in $\phi - z$ and $\phi - R$ for the barrel and the discs, respectively. In total, the PD consists of 80.4 million read-out channels and an active surface of $1.7\,\text{m}^2$.

Similar to PD, the Semiconductor Tracker consists of four cylindrical barrel layers and 18 planar end cap discs in the forward direction. Each layer is equipped with silicon microstrips on both sides with perpendicular orientation. The strips have a size of $80\,\mu\text{m} \times 64\,\text{mm}$ and provide a resolution of $17\,\mu\text{m} \times 580\,\mu\text{m}$ in $\phi - z$ for the barrel and in $\phi - R$ for the discs, respectively. The SCT has 6.3 million read-out channels in total on an area of $61\,\text{m}^2$.

The Transition Radiation Tracker measures both transition radiation for particle identification and tracks of charged particles using straw tubes filled with a Xenon gas mixture. The tube has a diameter of 4 mm and holds a 0.03 mm gold-plated tungsten wire along its central axis, measuring the distance of the charged particle track to the wire with a resolution of 170 µm. The TRT consists of 100000 straws in the barrel and another 320000 in both end caps, filling a volume of $16\,\text{m}^3$.

The primary vertex coordinate resolution has been measured using pp collision data at a centre-of-mass energy of $\sqrt{s} = 7$ TeV at an early stage of data taking, corresponding to an integrated luminosity of $\mathcal{L} = 6\,\text{nb}^{-1}$ [84]. For events with 70 charged particle tracks, or a quadratic sum of transverse momenta of all charged particle tracks, $\sqrt{\sum p_\text{T}^2}$, larger than 8 GeV, the resolution was found to be $\sigma_r \approx 30\,\mu\text{m}$ in the transverse plane and $\sigma_z \approx 50\,\mu\text{m}$ in the longitudinal direction. The momentum resolution has been measured in cosmic ray data as $\sigma_p/p = 4.83 \pm 0.16 \times 10^{-4}\,\text{p}_\text{T}/\text{GeV}$ [85].

3.2.3 Calorimeter

The ATLAS calorimeter is used to measure the energy of photons, electrons, τ-leptons and jets. Furthermore, it determines the missing transverse energy that is carried away by undetectable particles, such as neutrinos. Due to the characteristic signature of different particles in the calorimeter, it also provides useful information for the particle identification.

The ATLAS calorimeter consists of two main layers: the electromagnetic calorimeter (EM) and the hadronic calorimeter (HAD). All layers are segmented along the pseudo-rapidity η. The barrel in the central region extends to $\eta = 1.475$ for the electromagnetic layer, and $\eta = 1.7$ for the hadronic layer, respectively. The *end-cap* calorimeters cover the pseudo-rapidity up to $\eta = 3.2$, and the forward calorimeter ranges from $\eta = 3.2$ to 4.9. A layout of the ATLAS calorimeter is shown in Figure 3.4.

All segments of the ATLAS calorimeter are sampling calorimeters, but differ with respect to the technologies used. Liquid Argon (LAr) as the active medium in combination with different absorber materials is used for the electromagnetic layer of the barrel, and for both layers of the end-cap and the

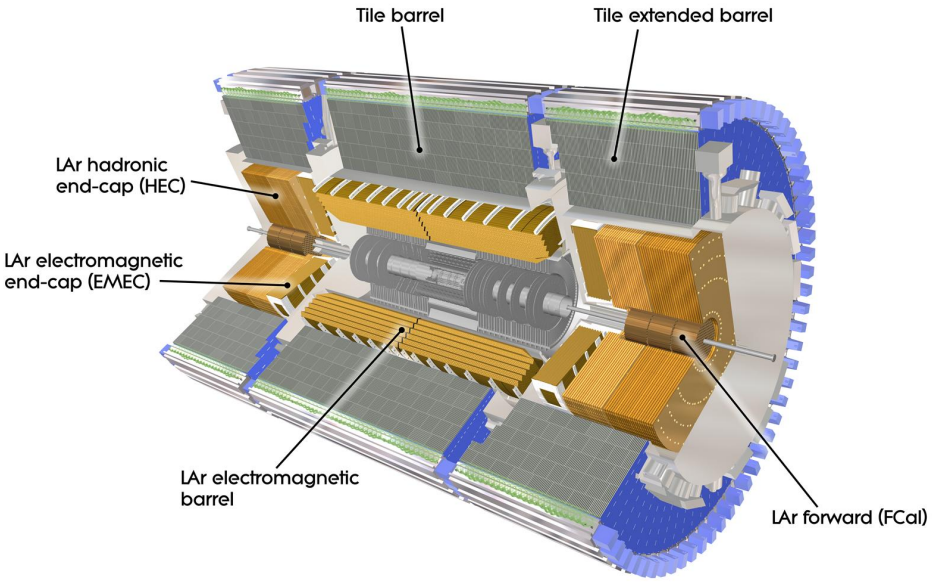

Figure 3.4: Layout of the ATLAS calorimeter, consisting of an electromagnetic and a hadronic layer as well as a segmentation into a barrel, an extended barrel, an end-cap and a forward calorimeter. Segments based on liquid Argon (LAr) technology as active medium and lead, copper or tungsten as passive material can be identified from the *golden colours*, while the segments based on scintillating tiles as active material and steel as absorber are shown in *grey* [86].

forward region of the calorimeter. For the hadronic layer of the barrel, scintillating tiles are used as the sensitive medium, and steel as the absorber. The latter also serves as return yoke for the solenoid magnet of the inner detector.

The separation into an electromagnetic and a hadronic layer is motivated by the fact that the energy deposition from electromagnetic showers are much shorter than those from hadronic showers. Electrons and photons deposit almost all their energy in the EM. The total spatial depth of the EM in terms of the radiation length[8] X_0 is $22\,X_0$ in the barrel and $24\,X_0$ in the end cap. The jets and τ-leptons deposit a considerable fraction of their energy in the electromagnetic layer, but the shower usually extends to the hadronic layer. The interaction length[9] of the electromagnetic layer amounts to $2.3\,\lambda$, and $7.4\,\lambda$ in the hadronic layer.

The resolution can be parametrised by the standard functional form expected for calorimeter-based resolutions as

$$\frac{\sigma(E)}{E} = \frac{N}{E} \oplus \frac{S}{\sqrt{E}} \oplus C, \tag{3.2}$$

where the parameters N, S and C denote the noise term, the stochastic term, and the constant term, respectively. The first term includes detector and electronic noise, as well as contributions from pile-up fluctuations. It depends only weakly on the energy, and thus dominates at $E < 30\,\text{GeV}$. The second term includes statistical fluctuations in the shower evolution and the sampling in the detector. The last

[8] The radiation length X_0 is defined as the distance of an electron after which its energy E has decreased to a fraction $1/e$ by bremsstrahlung.

[9] The interaction length λ is defined as the mean travelling distance in matter after which the numbers of relativistic, charged particles is reduced by the factor $1/e$.

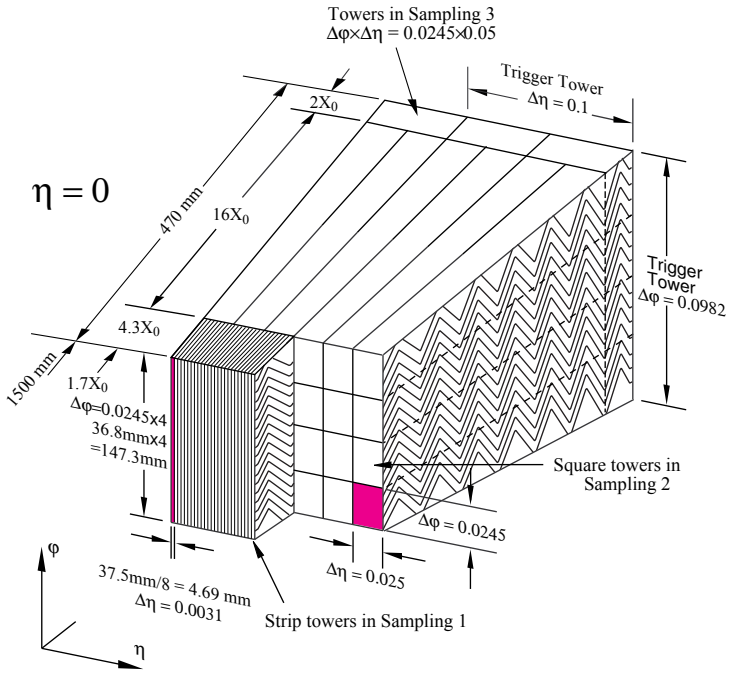

Figure 3.5: Layout of the accordion structure of the electromagnetic barrel calorimeter. The *coloured areas* indicate the granularity in $\Delta\phi$ and $\Delta\eta$ of the strip towers in Sampling 1 and the square towers in Sampling 2, respectively. Also given is the radiation length X_0 for the different samplings [87].

term accounts for signal loss in non-instrumented detector regions or non-uniformities in the response across the detector. Since the fractional contributions are constant with the energy, they usually become significant at $E > 400\,\text{GeV}$.

The electromagnetic barrel calorimeter consists of alternating layers of lead absorbers, chosen for its high cross-section for bremsstrahlung and pair production, and liquid Argon as the active medium with a thickness of 2.1 mm. The measurement principle is as follows. Electromagnetic showers induced in the absorber generate an ionisation charge in the active medium. The charge is collected and read-out by a copper electrode with an operating voltage of 2000 V, resulting in a drift time of about 450 ns. The alternating layers are bend in an accordion shape to provide a seamless coverage in the azimuthal angle ϕ. In radial distance to the interaction point, the electromagnetic barrel calorimeter is segmented in three *Samplings* with different granularity. The layout of the accordion structure and the dimensioning of the different samplings at $\eta = 0$ is given in Figure 3.5. The envisaged energy resolution of the electromagnetic calorimeter is $\sigma_E/E = 0.10\ \sqrt{GeV}/\sqrt{E} \oplus 0.03$ [88]. Test beam studies confirmed that this requirement is met in the measurement [89].

The hadronic barrel calorimeter (TileCal) is made of steel absorbers and scintillating tiles that are excited by the hadronic shower that penetrates the calorimeter. The tiles have a thickness of 3 mm and are placed in parallel to the direction of the traversing particles. The scintillation light is read-out by two wavelength shifting fibres at both ends of the tiles and measured using photomultiplier tubes installed on top of the modules. The layout of a single tile calorimeter module is shown in Figure 3.6.

The TileCal consists of two parts, the barrel that covers a pseudo-rapidity of $\eta < 1.0$, and the extended barrel, which extends to $\eta = 1.7$. The transition region between the two at around $\eta = 1.0$ contains a large amount of material from support structure and cabling of the inner detector components. Therefore it is equipped with additional scintillating tiles to capture the showers in the passive material.

The designated energy resolution for the TileCal is $\sigma_E/E = 0.50\ \sqrt{GeV}/\sqrt{E} \oplus 0.03$ [88]. Measurements of the energy resolution in test beam studies are in reasonable agreement with these specifications [91].

Both the *hadronic end-cap* (HEC) and *forward calorimeter* (FCAL) use LAr as the active medium.

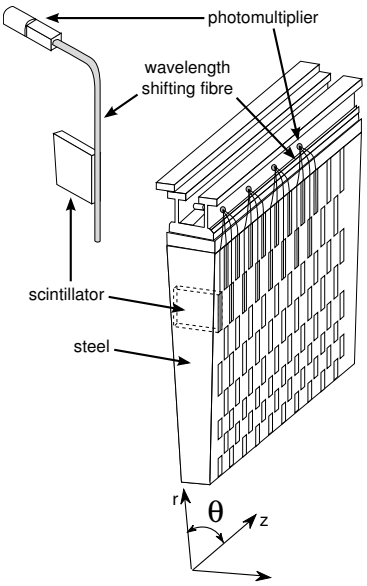

Figure 3.6: Layout of a tile calorimeter module, consisting of alternating layers of steel absorbers and scintillating tiles, which are read out with photomultiplier tubes via wavelength shifting fibres [90].

Due to the demanding rate and background conditions in the forward region, copper and tungsten are chosen as absorber materials. The envisaged energy resolutions are $\sigma_E/E = 0.50/\sqrt{E} \oplus 0.03$ for the HEC and $\sigma_E/E = 1.00/\sqrt{E} \oplus 0.10$ for the FCAL, respectively, both confirmed by test beam studies [92, 93].

The energy resolution of the ATLAS calorimeter for particle jets has been measured in pp collision data corresponding to an integrated luminosity of $35\,\mathrm{pb}^{-1}$. A detailed discussion of the results is given in Section 5.3.

In addition to the calorimeter inside of the detector volume, ATLAS comprises the Zero Degree Calorimeter (ZDC) [94]. It is located at a distance of 140 m on either side of the interaction point and approximately zero degree from the beam trajectories at the collision. Measuring the neutral particles that are produced in the collision, the purpose of the ZDC is the determination of the centrality of the colliding protons or heavy ions, providing a trigger on ultra-peripheral collisions.

The ATLAS calorimeter furthermore contains a set of scintillation counters for triggering purposes only. The Minimum Bias Trigger Scintillator (MBTS) [95] comprises two discs that are located at the inner face of the end-cap calorimeters at both sides of the detector, 356 cm from the interaction vertex. Each discs covers a pseudo-rapidity of $2.09 < |\eta| < 3.84$ and consists of 16 scintillating tiles with a thickness of 2 cm. The MBTS provides a trigger for events containing jets with a high efficiency and negligible bias.

3.2.4 Muon spectrometer

The ATLAS muon spectrometer is used to determine the momenta of muons from deflections in the magnetic field of the air-core toroid magnet of the outer magnet system. The tracks of muons are reconstructed from the vertex and tracking information of the inner detector and the position measurement in the three stations of the ATLAS muon spectrometer. The designated relative momentum resolution of the muon spectrometer is 3% over a wide p_T range, and 10% at $p_\mathrm{T} = 1\,\mathrm{TeV}$ [88].

The design of the muon system is given by the need for a strong magnetic field while limiting the material amount inside the spectrometer to minimise multiple-scattering effects that influence the accuracy of the momentum measurement. Due to the large size of the detector, gaseous tracking chambers are

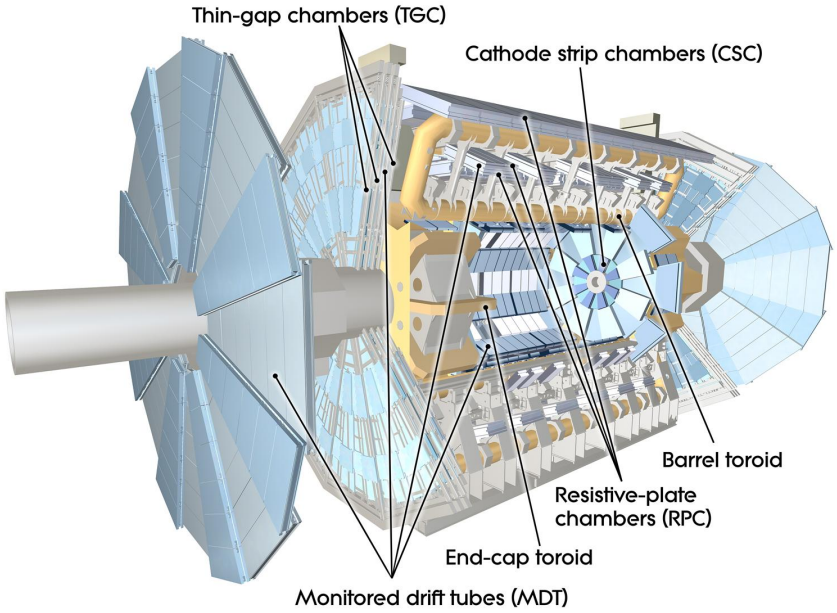

Figure 3.7: Layout of the outer magnet system and the muon spectrometer. Indicated in *yellow* is the outer magnet system, consisting of a barrel and an end-cap toroid magnet, each built from eight coils. The muon spectrometer is made from four different technologies, namely monitored drift tubes, resistive-plate chambers, cathode strip chambers, and thin-gap chambers. [96].

used for the position measurement of the muons.

The muon spectrometer consists of four different systems to account for the different geometry required in the barrel and end-cap regions, and to combine fast trigger and precision tracking capabilities. The modules of monitored drift tubes (MDT) are assembled by about 300 aluminium tubes with a diameter of 30 mm and a 50 µm wire in its centre. Each tube has a track-to-wire resolution of 80 µm. The MDT modules are employed to measure the track curvature in the three layers of the barrel and the two outer layers of the end cap. The coordinate in the first layer in the end cap is determined by the cathode strip chambers (CSC), the high particle density in the forward direction requires a higher granularity. It has a resolution of 60 µm and covers the pseudo-rapidity range of $|\eta| < 2.7$. The MDT and CSC are complemented by the resistive-plate chamber (RPC) and the thin-gap chamber (TGC) detectors for the purpose of triggering and measuring the coordinates orthogonal to the bending direction of the magnetic field. They cover a pseudo-rapidity range of $|\eta| < 2.4$. The layout of the ATLAS muon spectrometer is shown in Figure 3.7.

The momentum resolution of muons has been measured in $Z \to \mu\mu$ events using pp collision data at a centre-of-mass energy of $\sqrt{s} = 7\,\text{TeV}$ corresponding to an integrated luminosity of $\mathcal{L} = 2.54\,\text{fb}^{-1}$ [97]. In the barrel region, a resolution of

$$\frac{\sigma(p)}{p} = \frac{0.25\,\text{TeV}}{p_\text{T}} \oplus 3.27 \times 10^{-2} \oplus 0.168\,\text{p}_\text{T}/\text{TeV} \tag{3.3}$$

has been found.

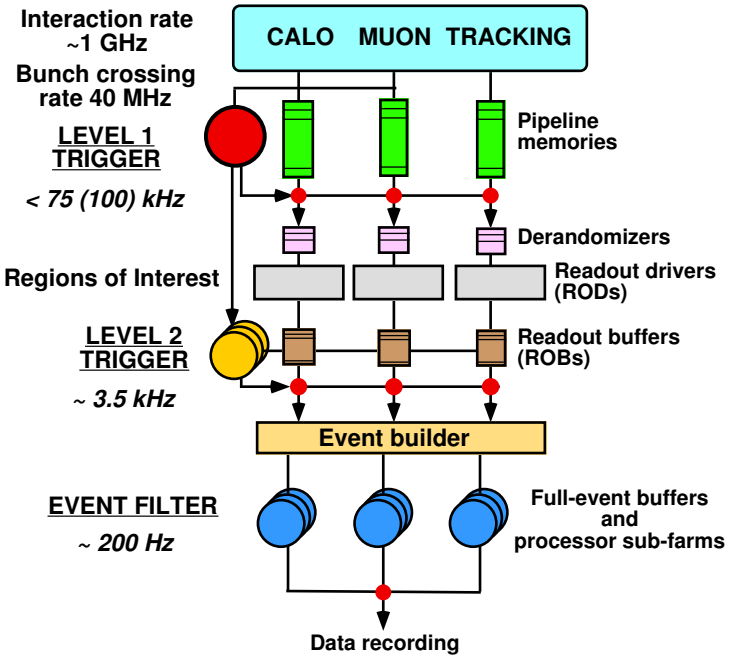

Figure 3.8: Block diagram of the ATLAS trigger and data acquisition system. It shows the data path and the rate reduction in the three levels of the trigger system [80].

3.2.5 Luminosity detectors

ATLAS employs several sub-detectors to measure the instantaneous luminosity at the experiment. The two main luminosity devices are the ATLAS beam conditions monitor (BCM) [98] and the LUCID[10] [88]. Both are rate counters, which provide a rate proportional to the instantaneous luminosity. The calibration of these detectors is performed using *van-der-Meer* scans and is discussed in Section 4.

The two purposes of the ATLAS Beam Conditions Monitor are the protection of the inner detector from hazardous beam conditions and the measurement of the luminosity. Due to its proximity to the interaction point, the BCM uses radiation hard diamond sensors placed between two electrodes, which measure the ionisation signal from traversing charged particles. The BCM consists of two stations, each at a distance of 1.84 m on both sides of the interaction point, and 55 mm from the beam line. A station comprises four sensors arranged in a cross-shape pattern. For reasons of redundancy, the read-out is performed independently for the horizontal and vertical pair, labelled BCMH and BCMV, respectively.

The LUCID is a Cherenkov detector dedicated only to the measurement of the luminosity. It consists of 16 aluminium tubes with a diameter of 15 mm and a length of 1.5 m which are located 17 m away on either side of the interaction point in a cylindrical compound around the beam line. The tubes are filled with C_4F_{10} gas and read-out by photomultiplier tubes located behind a quartz window, which further enhances the Cherenkov light.

3.3 Trigger system

The LHC is designed to provide on average 23 overlapping collisions at an interaction rate of 40 MHz. This poses challenges on the trigger and data acquisition system, since the maximal output rate for

[10] LUCID - *Luminosity measurement using Cherenkov integrating detector.*

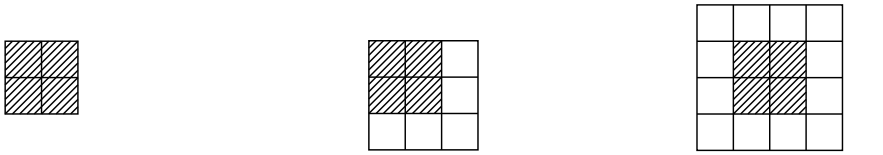

Figure 3.9: Illustration of the sliding window of the jet finding algorithm. The algorithm is based on a granularity of $\Delta\eta \times \Delta\phi = 0.2 \times 0.2$ in the calorimeter, with a configurable window size. The region of interest is indicated by the *shaded area*.

permanent storage is about 200 Hz and hence requires a reduction by a factor of 10^5. The ATLAS trigger system consists of three levels: the Level-1 (L1) trigger, the Level-2 (L2) trigger, and the Event Filter (EF), each with increasing processing time of the collision event, higher resolution and larger number of accessible detector systems for a successive rate reduction. An overview over the ATLAS trigger and data acquisition system is given in Figure 3.8.

The Level-1 trigger decision is based on the reconstruction of highly energetic objects on one hand, such as photons, electrons, muons, τ-leptons or jets, and large missing transverse energy in the event on the other. Due to the limited available time, it relies on the reduced information from two detector systems, the muon spectrometer and the calorimeter including the ZDC and the MBTS. No data from the inner detector is used at the first level. Hence, the main systems are the Level-1 calorimeter trigger and the Level-1 muon trigger, complemented by the central trigger processor (CTP), which combines the information of the two.

Generally, the Level-1 trigger searches for objects with energies or momenta above a defined threshold, but the actual trigger decision only depends on their multiplicity, while the topology of the given event is not evaluated. The latter is exploited on Level-2 on basis of the *regions of interests* (RoI), which are provided by the CTP. The CTP furthermore holds the trigger menu, defining the multiplicity thresholds of the different trigger items, and *trigger prescales* to suppress triggers items with high rate, as described below.

During the decision process of the Level-1 trigger, the full event information is stored in pipeline memories on the detector, and either read-out or discarded after a latency of 2.5 µs. For a fast processing time, the algorithms at Level-1 are implemented using custom-built, pipelined, parallel electronics with configurable thresholds and recognition patterns. It provides a rate reduction to 75 kHz.

The building blocks of the Level-1 calorimeter trigger are the *PreProcessor*, the *Cluster Processor* (CP) and the *Jet/Energy Processor* (JEP). The PreProcessor performs the digitisation, energy calibration and alignment of the 7200 analogue input signals of the independent trigger read-out from the calorimeter, and distributes the digitised signal to the CP and the JEP in parallel. Both, CP and JEP, employ sliding window techniques to search and measure localised energy depositions. The CP is designed to identify energy depositions from photon, electron and τ-lepton candidates, whereas the JEP is specialised on the measurement of jets and the determination of the missing energy in the event. Figure 3.9 shows the sliding window of the jet finding algorithm. It uses a granularity of 0.2×0.2 in η-ϕ, with a configurable window size and energy thresholds. Apart from the number of local energy maxima above the threshold found be the sliding window, the Level-1 Calorimeter trigger also reports their positions as RoIs to the Central Trigger Processor.

The Level-1 muon trigger is based on the reconstruction of muon tracks using 800000 channels from the RPC and TPC trigger chambers. Muon hits are analysed in terms of coincidences in the three different stations using fixed trajectories that correspond to the estimated curvature of muons at a given

p_T threshold. The multiplicity of track candidates and their RoIs are provided to the CTP.

The Level-2 trigger has access to the information from all detector components at full resolution in the regions of interest provided by the Level-1. Due to the higher granularity, it can employ more refined algorithms using for instance cluster shape variables. Jets are reconstructed using a simplified cone algorithm. The Level-2 trigger uses a large computing network, at which the incoming events are processed in parallel. The processing time depends on the complexity of the event and amounts to 40 ms on average. The output event rate of the Level-2 trigger is approximately 3.5 kHz.

The Event Filter performs the reconstruction of the full event topology, based on algorithms that are similar to the algorithms used in offline analyses. Jets are reconstructed using the anti-k_t algorithm with topological clusters of energy depositions in the calorimeter as input. The procedure is close to the offline jet reconstruction described in Section 5.1. The Event Filter has a latency of typically 4 s and is implemented on a large computer farm. The output rate of the Event Filter is in the order of 200 Hz at which events are written to disk for permanent storage.

Trigger definition

Defined by the algorithm and threshold used, triggers from Level-1, Level-2 and Event Filter are grouped in *trigger chains*. In case of a jet-based trigger, a typical trigger chain consists of `L1_J10` at Level-1 trigger, `L2_j25` at Level-2, and `EF_j30_jetNoEF` at the Event Filter. The terms `J10`, `j25`, and `j30` in the trigger items denote the energy thresholds. Since the calorimeter trigger is calibrated at the electromagnetic scale, there is no direct correspondence between the given threshold and the actual energy threshold at which the trigger is fully efficient. For technical reasons, there are separate jet trigger items at Level-1 for the central region with $|\eta| < 3.2$, and the forward region $3.2 \leq |\eta| < 4.9$, denoted with the prefixes `L1_J` and `L1_FJ`, respectively. To reach a full efficiency at the transition between the two, both triggers have to be combined in this region. Jet trigger efficiencies are discussed in Sections 6.3.2 and 7.2.2.

The output rate of individual trigger chains is controlled by the aforementioned *prescale factors*, which are used to preselect a certain fraction of events. The particular trigger is only performed on this subset of events to save bandwidth. Prescale factors can be applied individually to each trigger at each level in the trigger chain. Hence, the prescale factors allow to assign certain fractions of the bandwidth of the data acquisition system to the trigger chains of interest, depending on the physics program of ATLAS. Furthermore, prescales are used to maintain a constant rate at the three trigger levels under different running conditions, in particular to account for the degradation of the beam intensity during a fill.

Since prescaled triggers only run on a subset of events, the prescale factors also determine the effective integrated luminosity of the acquired data sample. Therefore, the data taking is divided into time intervals in which the running conditions such as the instantaneous luminosity, the trigger prescale, but also the detector conditions can be considered as constant. This atomic time interval is denoted *luminosity block* (LB) in ATLAS terminology, and has typically a duration of 120 s. The integrated luminosity for a dataset using a prescaled trigger is calculated as

$$\mathcal{L}_{\text{tot}} = \sum_i \frac{\mathcal{L}_i}{p_i}, \tag{3.4}$$

where i runs over all luminosity blocks of the dataset, $\mathcal{L}_i$ is the integrated luminosity in the luminosity block i, and p_i is the corresponding trigger prescale.

CHAPTER 4

Luminosity measurement

The luminosity determination is an essential component of cross-section measurements and potentially a major systematic uncertainty. Hence, the ATLAS experiment employs several subsystems for an accurate measurement of the luminosity in the detector, of which the two most important are the BCM and LUCID, as described in Section 3.2.5. These detectors are rate counters that provide a rate R proportional to the instantaneous luminosity, $\mathcal{L}_{\text{inst}}$. The proportionality constant between R and $\mathcal{L}_{\text{inst}}$ is system dependent and needs to be calibrated in a dedicated measurements, so-called *van-der-Meer scans* (vdM) [99, 100] with special running conditions of the LHC.

ATLAS performed luminosity measurements for the pp collision data in 2010 and 2011 at $\sqrt{s} = 7$ TeV [101], and in 2012 at $\sqrt{s} = 8$ TeV [102]. The calibration for the pp collision data at $\sqrt{s} = 2.76$ TeV in 2011 has been evaluated in the course of this analysis. Hence, results presented here are mainly for $\sqrt{s} = 2.76$ TeV, but the same methodology as for $\sqrt{s} = 7$ TeV, described in [101], is used.

This chapter consists of four sections. In Section 4.1 the measurement principle of the luminosity detectors is explained. The two essential calibration steps, the van-der-Meer scan and bunch charge measurement, are described in Sections 4.2 and 4.3, respectively. The results and a summary of the systematic uncertainties is given in Section 4.5.

4.1 Measurement principle

Using the instantaneous luminosity $\mathcal{L}_{\text{inst}} = d\mathcal{L}/dt$, the definition of the inclusive jet cross-section in Equation 1.30 can be rewritten for the case of inelastic interaction as

$$\sigma_{\text{inel}} = \frac{R_{\text{inel}}}{\mathcal{L}_{\text{inst}}}, \tag{4.1}$$

where $R_{\text{inel}} = N/dt$ is the interaction rate. While this expression is normally used to obtain σ_{inel} from the measured quantities R_{inel} and $\mathcal{L}_{\text{inst}}$, it may also be used the other way around: if the cross-section of a certain process is well-known, and the rate of this process can be measured with high accuracy, the luminosity can be calculated from Equation 4.1. Ideally, the luminosity is determined from the total inelastic cross-section of the pp collisions, according to

$$\sigma_{\text{inel}} = \frac{R_{\text{inel}}}{\mathcal{L}_{\text{inst}}} = \frac{\mu_{\text{inel}}\, f_r\, n_c}{\sigma_{\text{inel}}}. \tag{4.2}$$

For the last transformation, the rate R_{inel} is expressed in terms of the accelerator properties f_r and n_c, which correspond to the revolution frequency and the number of colliding bunches. The observable reduces to μ_{inel}, which is the average number of inelastic interactions per bunch crossing. However, instead of determining the experimentally difficult quantity μ_{inel}, each of the luminosity devices only measures a fraction ε of the total inelastic cross-section, denoted as $\mu_{\text{vis}} = \varepsilon\mu_{\text{inel}}$. The fraction ε is given by the geometrical coverage and the efficiency of the detector. With the corresponding visible cross-section $\sigma_{\text{vis}} = \varepsilon\mu_{\text{inel}}$ for a certain luminosity device, it follows

$$\sigma_{\text{vis}} = \frac{\mu_{\text{vis}} f_r n_c}{\mathcal{L}_{\text{inst}}}. \tag{4.3}$$

In this expression, μ_{vis} is the experimentally observable quantity, and σ_{vis} represents the luminosity scale for a particular luminosity device. The luminosity scale σ_{vis} is not known a priori, but has to be measured. This is accomplished under dedicated running conditions, which allow to extract the absolute luminosity at one point in time, and hence determine the visible cross-section from Equation 4.3.

As given in Equation 3.1, the luminosity can also be expressed in terms of the beam parameters,

$$\mathcal{L}_{\text{inst}} = \frac{n_c f_r \cdot n_a n_b}{2\pi \Sigma_x \Sigma_y}. \tag{4.4}$$

While the number of colliding bunches, n_c, and the revolution frequency, f_r, are fixed by the filling scheme and the accelerator design, the number of protons, n_a and n_b, and the convolved beam widths, $\Sigma_x \cdot \Sigma_y$, are run dependent quantities and have to be measured. Dedicated devices are installed at the LHC to monitor the beam currents in the collider ring, hence the number of protons in each beam can be determined. The convolved beam widths are measured in the aforementioned van-der-Meer scans, during which the beams are gradually separated.

During the data taking at a centre-of-mass energy of $\sqrt{s} = 2.76\,\text{TeV}$ in 2011, two calibration runs using van-der-Meer scans have been performed in separate fills of the LHC, namely fill 1653, denoted scan I, and fill 1658, denoted scan II in the following. For both fills, the number of colliding bunches was $n_c = 8$, each providing modest peak interaction rates for optimal working conditions of the luminosity detectors. Two different counting methods have been applied: The `eventOR` algorithm corresponds to an inclusive counting, in which a hit on any side of the interaction point is taken into account. In the `eventAND` algorithm, only coincidental hits at both sides are considered.

4.2 Van-der-Meer scans

Equation 4.4 can be rewritten in a generalised form using the normalised particle densities in the transverse plane at the interaction point, $\hat{\rho}(x, y)$ as

$$\mathcal{L}_{\text{inst}} = n_c f_r \cdot n_a n_b \int \hat{\rho}_a(x, y)\, \hat{\rho}_b(x, y)\, dxdy. \tag{4.5}$$

Assuming that the particle densities can be factorised into independent horizontal and vertical components, i.e. $\hat{\rho}_a(x, y) = \hat{\rho}_a x(x) \cdot \hat{\rho}_a y(y)$, the expression above turns into

$$\mathcal{L}_{\text{inst}} = n_c f_r \cdot n_a n_b \underbrace{\int \hat{\rho}_a x(x) \hat{\rho}_b x(x) dx}_{\Omega_x(x)} \underbrace{\int \hat{\rho}_a y(y) \hat{\rho}_b y(y) dy}_{\Omega_y(y)}, \tag{4.6}$$

where Ω_x and Ω_y are the beam-overlap integrals in x and y direction, respectively. The method is based on the fact that the convoluted beam density is proportional to the average number of inelastic interactions [99]. Hence, the beam-overlap integral can be calculated from a rate measurement of inelastic interactions at different beam separations ξ according to

$$\Omega_x(\xi) = \frac{R_x(0)}{\int R_x(\xi)d\xi}, \tag{4.7}$$

and similarly for Ω_y. The quantity $R_x(\xi)$ is a luminosity at an arbitrary unit, which can be identified with the mean visible interaction rate μ_{vis}. Measured as a function of the beam separation ξ, its distribution is also called *luminosity curve*. The value $\xi = 0$ represents the case of central collisions. This procedure of scanning the convolved beam profile by separating the beams along the x and y axis is called van-der-Meer scan. Using Equation 4.7, the width of the convolved beams, Σ_x, can be defined as

$$\Sigma_x = \frac{1}{\sqrt{2\pi}\,\Omega_x} = \frac{1}{\sqrt{2\pi}} \frac{\int R_x(x)dx}{R_x(0)}, \tag{4.8}$$

which results in an expression for the instantaneous luminosity based on machine parameters as

$$\mathcal{L}_{\text{inst}} = \frac{n_c f_r \cdot n_a n_b}{2\pi\,\Sigma_x \Sigma_y}, \tag{4.9}$$

given already in Equation 4.4. In case that the luminosity curve can be described by a Gaussian distribution, Σ_x and Σ_y coincide with the standard deviation. However, Equations 4.8 and 4.9 are also valid for non-Gaussian shapes.

Equation 4.9 in its given form applies to beams, in which each colliding bunch pair has the same cross-section area. However, this is usually not the case. Instead, the procedure described above has to be applied to each bunch pair individually, resulting in

$$\mathcal{L}^{(i)}_{\text{inst}} = \frac{f_r \cdot n^{(i)}_a n^{(i)}_b}{2\pi\,\Sigma^{(i)}_x \Sigma^{(i)}_y}, \tag{4.10}$$

where the index (i) denotes the colliding bunch pair i. Provided that the counting rate depends linearly on the instantaneous luminosity, the calibration factors $\sigma^{(i)}_{vis}$ are the same for all i.

Figure 4.1 shows the specific rate $R^{(i)}_{\text{sp}} = \mu^{(i)}_{\text{vis}}/(n^{(i)}_a \cdot n^{(i)}_b)$ measured with the LUCID `eventOR` algorithm as a function of the beam separation ξ in x and y direction during a van-der-Meer scan. The convolved beam profile is scanned in steps of $\Delta\xi \approx 80\,\mu\text{m}$. To interpolate the discrete scan points for the calculation of the integral in Equation 4.8, the fit on the data is performed using several functional forms. The best agreement with data and the most consistent result for the visible cross-section over all bunch crossings is obtained using a Gaussian distribution multiplied with a fourth-order polynomial plus a constant offset. Other functional forms are used to assess the systematic uncertainty introduced by the fit model choice.

Beside the uncertainty due to the fit model choice, several other sources of uncertainty on the calibration procedure are considered [102, 103]. The dominating component is found to be the non-reproducibility of the visible cross-section between the two van-der-Meer scans, scan I and scan II, which differ by 1.8%. The total systematic uncertainty on the visible cross-section is 2.3%.

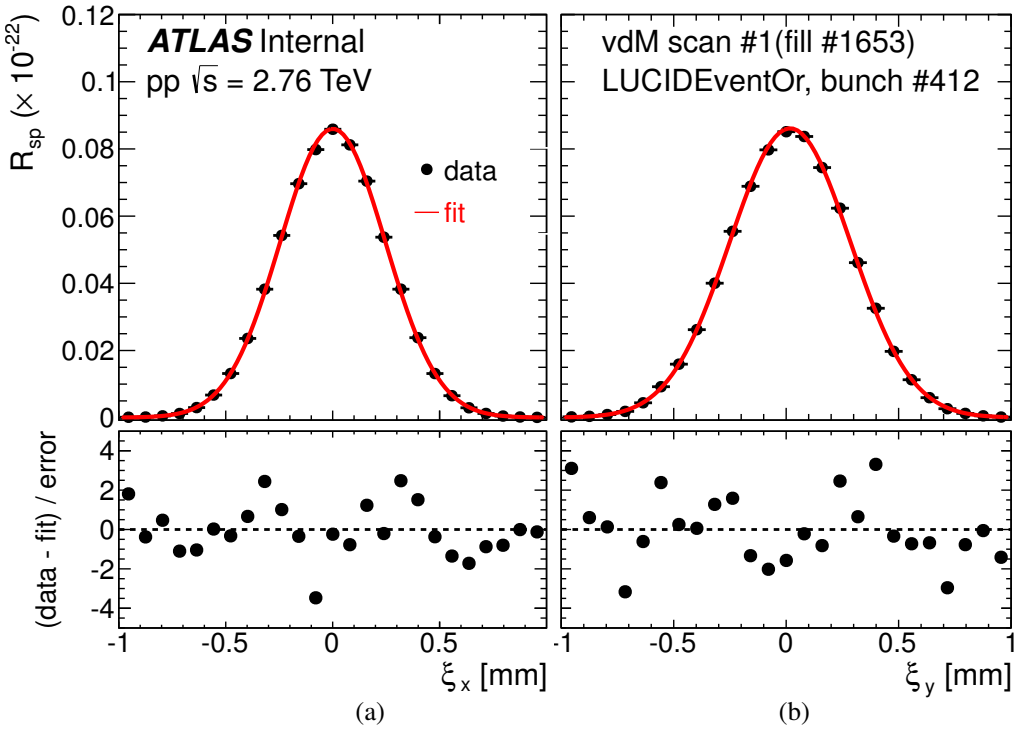

Figure 4.1: Specific rate $R_{\mathrm{sp}}^{(i)} = \mu_{\mathrm{vis}}^{(i)}/(n_a^{(i)} \cdot n_b^{(i)})$ measured with the LUCID `EventOR` algorithm as a function of the beam separation ξ for the (a) horizontal and (b) vertical directions of the van-der-Meer scan. The data corresponds to bunch crossing $i = 412$ from scan I at $\sqrt{s} = 2.76\,\mathrm{TeV}$, $n_a^{(i)} \cdot n_b^{(i)}$ is the bunch charge product, and $\mu^{(i)}$ the mean visible rate. The *solid curve* shows a fit of the data using a Gaussian distribution with a constant offset. The data is compared to the fit in the bottom panels in units of the statistical uncertainty in each data point [3].

4.3 Bunch charge measurement

The LHC is equipped with two dedicated systems to determine the bunch charges of the beams. The total current is measured by two redundant DC current transformers (DCCT) [104] per beam. While this kind of device is very precise regarding the total current, it cannot resolve the charge of an individual bunches, which is necessary for the determination of the visible cross-section given in Equation 4.10. The measurement of the relative bunch charges is performed using the two fast-beam-current transformers (FBCT) per beam, which are able to measure precisely the fractional bunch charge in each of the individual bunch slots, but do not have the ability to determine the total bunch charge.

Apart from the charge in the filled bunch slots, the beam also may contain small charges in nominally unfilled bunch slots from migrations, which occur especially during the LHC filling procedure. This charge is denoted *ghost* charge. *Satellite* charges on the other hand are charges that are captured outside the proper 2.5 ns RF bucket within the nominally filled bunch slot. Those charges do not contribute to the luminosity, but influence the bunch current measurement. The total number of charges in one beam, N^{tot}, can be written as

$$N^{\mathrm{tot}} = N^{\mathrm{ghost}} + \sum_i n_i + n_i^{\mathrm{sat}}, \tag{4.11}$$

where n_i is the charge in the correct bucket of bunch slot i, n_i^{sat} the corresponding satellite charge, and N^{ghost} the total number of ghost charges in the beam. In general, the fraction of ghost and satellite charges is small. While the DCCT is very sensitive to N^{ghost} and $N^{\mathrm{sat}} = \sum_i n_i^{\mathrm{sat}}$, the FBCT cannot

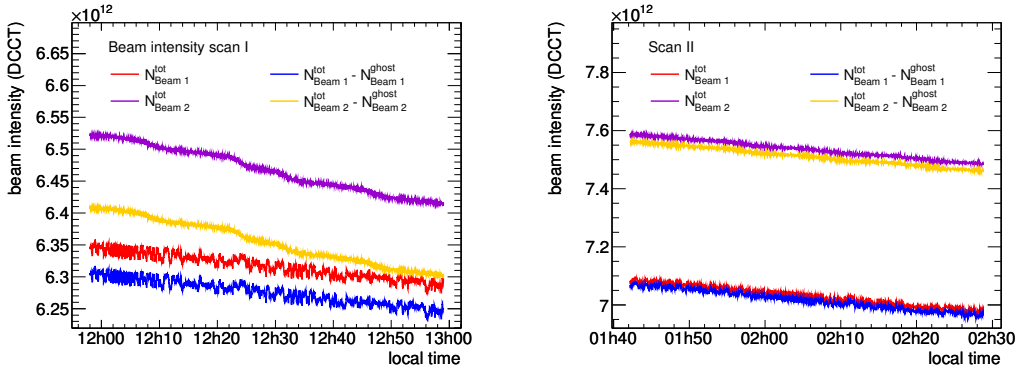

(a) scan I (b) scan II

Figure 4.2: Beam intensity, measured as the number of charges for the two beams in both van-der-Meer scans at $\sqrt{s} = 2.76\,\text{TeV}$ in 2011, with and without the contributions from ghost charges. The DCCT [104] is used for the measurement of total charges, N^{tot}, and the LHCb beam-gas rate measurement [105] to determine the ghost charge N^{ghost}.

measure N^{ghost}. Using the fractional bunch charge f_i^{slot} from the FBCT, the charge of one bunch follows as

$$n_i + n_i^{\text{sat}} = (N^{\text{tot}} - N^{\text{ghost}}) \cdot f_i^{\text{slot}}. \tag{4.12}$$

As mentioned before, N^{tot} and f_i^{slot} are measured by the DCCT and FBCT, respectively. The parasitic charges n_i^{sat} and N^{ghost} are determined using the longitudinal density monitor and a beam-gas rate measurement. The results for the individual contributions are summarised in the following.

Total beam current

The total beam charge N^{tot} is measured using the DCCT and is shown in Figure 4.2. During the two van-der-Meer scans at $\sqrt{s} = 2.76\,\text{TeV}$ in 2011, the total number of circulating charges varied from 6.2×10^{12} to 7.6×10^{12}. The corresponding uncertainties on the bunch current measurement are shown in Table A.2 of the appendix. The dominating contributions are the non-linearity of the analogue-to-digital converter and the long-term stability, amounting to 0.4% each. A detailed discussion of the uncertainty sources can be found in [104]. The total systematic uncertainty of the beam current product amounts to 0.80% for scan I and ±0.70% for scan II . Although some of the components of the DCCT uncertainty are correlated between different scans, the uncertainty is conservatively considered as uncorrelated.

Fractional bunch charge

The fractional bunch charge is determined by the FBCT as

$$f_i^{\text{slot}} = \frac{\hat{n}_i}{\sum \hat{n}_i}, \tag{4.13}$$

where $\hat{n}_i$ includes all charges in the bunch slot i, i.e. $\hat{n}_i = n_i + n_i^{\text{sat}}$. Any resulting offset or non-linearity of the FBCT measurement is accounted for by a systematic uncertainty. It is found to be 0.08% for scan I, and 0.09% for scan II [106], and considered as correlated between the two scans.

	scan I	scan II	Correlation b/w scans
absolute beam current	±0.80%	±0.70%	yes
ghost charge correction	±0.51%	±0.13%	yes
satellite charge	±0.76%	±1.05%	no
relative bunch charge	±0.08%	±0.09%	yes
bunch charge uncertainty per beam	±1.22%	±1.27%	
total bunch charge uncertainty	±1.04%		

Table 4.1: Uncertainties on the bunch charge measurement in both van-der-Meer scans at $\sqrt{s} = 2.76$ TeV in 2011.

Ghost charge

The best estimate for the ghost charge population during the van-der-Meer scans is given by the beam-gas rate measurement from the LHCb collaboration [105]. The largest fraction of ghost charges was found for beam 2 in scan I, amounting to $N^{\text{ghost}}/N^{\text{tot}} = 1.75 \pm 0.37\,\%$. The dominating uncertainty originates from the trigger efficiency in this measurement. Since both scans are affected similarly by this uncertainty, they are treated as fully correlated.

Satellite charge

The number of satellite charges is determined with the longitudinal density monitor (LDM) [107]. The LDM is based on the measurement of synchrotron radiation from the beam using avalanche photo-diodes operating in Geiger mode, which allows to determine the longitudinal distributions of charged particles in the LHC beam with high timing resolution. Due to technical reasons, only the satellite charge for one beam direction, beam 2, in scan I is available, measured as $N^{\text{sat}}/N^{\text{tot}} = 0.10^{+0.05}_{-0.03}\%$. As a consequence, the satellite charge is not corrected for, but an uncertainty is applied instead. For beam 2 in scan I, the uncertainty is taken as 15% of the absolute measurement value. For beam 1 of the scan I and both beam directions in scan II, the maximal ghost charge fraction during previous van-der-Meer scans is conservatively taken as the uncertainty. It amounts to $N^{\text{sat}}/N^{\text{tot}} = 0.57^{+0.17}_{-0.12}\%$, and hence an uncertainty of 0.74% is assumed. Since this represents a conservative estimate, the uncertainty on the satellite charge is considered as uncorrelated for both beams and scans, respectively.

Summary of bunch charge product uncertainties

In total, the bunch charge product uncertainty for both scans is very similar, amounting to 1.22% for scan I and 1.27% for scan II . The different contributions originate from the measurements of the total beam current, the ghost and satellite charges, and the fractional bunch charges are listed in Table 4.1. The uncertainty is dominated by the absolute beam current component and the satellite charge for both scans. Exploiting the correlations between the two measurements for the combination of both scans, the uncertainty on the visible cross-section is reduced to 1.06%.

4.4 Luminosity consistency

While in principle all luminosity devices are supposed to give a consistent result for the measurement of the luminosity after calibration, this is often not the case due to their different acceptance, response

to pile-up conditions, sensitivity to instrumental effects and beam-induced backgrounds. Hence, the consistency of the luminosity measurement is investigated, and an additional uncertainty is introduced. It consists of three subcomponents: the consistency of the different luminosity measurements; the non-linear dependency from the instantaneous luminosity; and the long-term stability.

Considered are all luminosity blocks in the dataset at $\sqrt{s} = 2.76\,\text{TeV}$ from 2011 with stable running conditions. The luminosity value is measured as the mean luminosity in intervals of one luminosity block for the `eventOR` algorithms of LUCID, BCMH and BCMV, and for the `eventAND` algorithm of LUCID. The luminosity from LUCID with the `eventOR` counting rate algorithm is chosen as reference, since it turns out to be the most stable.

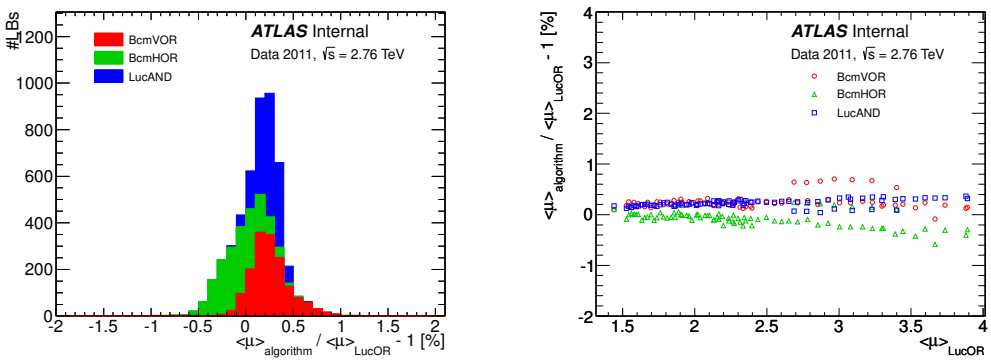

(a) (b)

Figure 4.3: Consistency of different luminosity devices and algorithms at $\sqrt{s} = 2.76\,\text{TeV}$ in 2011: (a) distribution of the measured luminosity for all luminosity blocks (b) luminosity as function of the mean number of collisions per bunch crossing, $\langle\mu\rangle$, averaged over 20 luminosity blocks. The reference is the LUCID `eventOR` algorithm.

Figure 4.3a shows the consistency of the different luminosity algorithms as the distribution of the measured luminosity for all luminosity blocks. Good agreement is observed in general. The BCMV `eventOR` and LUCID `eventAND` algorithms yield a small tendency of 0.3% towards larger values, while BCMH `eventOR` is slightly lower. An uncertainty of 0.5% accounts for the differences of the mean values between the different algorithms.

The number of collisions per bunch crossing, $\langle\mu\rangle$, varies between 1.5 and 4.0 over the dataset. As shown in Figure 4.3b, only a small dependency on the instantaneous luminosity, i.e. on $\langle\mu\rangle$, is observed with respect to the reference. It is accounted for by an uncertainty due to non-linearities of 0.3%.

The distinct sidebands at $2.7 < \langle\mu\rangle < 3.4$ in Figure 4.3b can be attributed to a single run, where the two luminosity detectors LUCID and BCM exhibit different results. This can be seen in Figures 4.4a and 4.4b, which show the time development of the instantaneous luminosity for the different algorithms independently and as ratio with respect to the LUCID `eventOR` algorithm during the four runs of the dataset at $\sqrt{s} = 2.76\,\text{TeV}$ in 2011. General deviations of the mean values between the different algorithms visible in Figure 4.4b are already accounted for. However, the second run yields an increased luminosity for both, BCMV and BCMH with respect to other runs. While the reason for this behaviour is unknown, an uncertainty of 0.5% is applied to address the long-term stability of the luminosity measurement.

In total, an uncertainty of 0.8% is assigned to account for the consistency, non-linearity and long-term stability of the luminosity measurement in the dataset at $\sqrt{s} = 2.76\,\text{TeV}$ from 2011. This is comparable to the corresponding uncertainty of 0.5% in the dataset at $\sqrt{s} = 7\,\text{TeV}$ in 2010 [101].

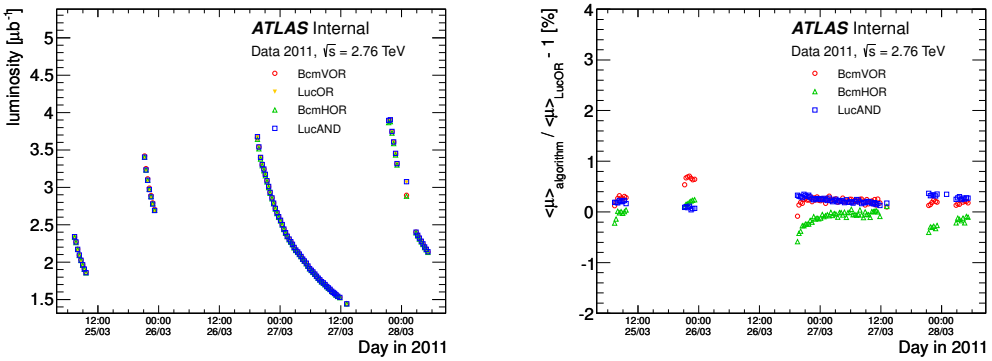

(a) (b)

Figure 4.4: Time evolution of the instantaneous luminosity (a) independently for the different algorithms, and (b) as ratio with respect to the LUCID `eventOR` algorithm, averaged over 20 luminosity blocks. Considered are all luminosity blocks with stable beam conditions at $\sqrt{s} = 2.76\,\text{TeV}$ in 2011, except the van-der-Meer scans, and a range with exceptional low μ.

4.5 Summary

The calibration of the luminosity devices in terms of the visible cross-section has been performed using van-der-Meer scans and the measurement of the bunch charge product. In contrast to the pp data taking period in 2010 at $\sqrt{s} = 7\,\text{TeV}$, where the BCM was chosen as the default device to measure the luminosity, the LUCID detector with `eventOR` algorithm serves as reference for the luminosity measurement for pp collisions at $\sqrt{s} = 2.76\,\text{TeV}$ in 2011. Its visible cross-section was determined as $\sigma_{vis} = 31.68 \pm 0.72\,\text{mb}$ [3].

The luminosity uncertainty is summarised in Table 4.2. The uncertainty for the 7 TeV dataset from 2010 is dominated by the bunch charge product measurement, whereas the largest contribution for the 2.76 TeV dataset from 2011 is the non-reproducibility component of the van-der-Meer scan. The total uncertainty amounts to 3.4% at 7 TeV and 2.7% at 2.76 TeV.

During the finalisation of this thesis, the luminosity scale for the dataset at $\sqrt{s} = 7\,\text{TeV}$ from 2010 has been adjusted to account for additional beam-beam effects during the vdM scans [103]. The change in the luminosity scale was found to be a constant factor of $1/1.0187$, with a slightly larger uncertainty of 3.5%. Since this change does not have a significant impact on the results of the presented work, the preliminary value and uncertainty for the integrated luminosity of the dataset at $\sqrt{s} = 7\,\text{TeV}$ in 2010 is retained.

$\sqrt{s}$	7 TeV	2.76 TeV
year	2010	2011
bunch charge product	3.1%	1.1%
van-der-Meer scan	1.3%	2.3%
long-term stability	0.5%	0.8%
total	3.4%	2.7%

Table 4.2: Luminosity uncertainties for proton-proton collision data at $\sqrt{s} = 7\,\text{TeV}$ in 2010 and $\sqrt{s} = 2.76\,\text{TeV}$ in 2011 [3, 108].

CHAPTER 5

Jet reconstruction and calibration

The hard interaction, the parton shower and the hadronisation take place at distances on the scale of the hard interaction, which is in the order of a few femtometer. Hence, the entire process is limited to a very small space, much smaller than experimentally accessible. At the detector, jets arrive as a collimated spray of hadrons. In this analysis, the jets of hadrons are reconstructed from the energy deposition in the calorimeter, because the calorimeter has a large coverage in rapidity and a large longitudinal depth in order to fully contains the particle shower from the jet. As before the anti-k_t algorithm is used to form the jets.

A major challenge for the jet measurement is the calibration of the *jet energy scale* (JES), since the ATLAS calorimeter is non-compensating and consequently has a different response to electromagnetic and hadronic energy depositions. By default, the calorimeter is calibrated at the electromagnetic scale, so that the energy measurement for jets without the appropriate correction for their hadronic fraction only accounts for $50 - 90\%$ of its true energy. A precise calibration is important for the measurement of the jet production cross-section. The cross-section falls steeply with increasing energy, and a modest mismeasurement of the energy therefore translates into a considerable deviation in the cross-section. Therefore a good understanding of the JES and in particular of its uncertainty is essential for a precise measurement.

In addition to the reconstruction and calibration of jets, a major task is the jet selection. It ensures that jets considered in the measurement originate from collision events, whereas jets reconstructed from cosmic rays, beam effects or detector noise are rejected. The corresponding quality criteria are based on the timing information and the fractional energy deposition in different layers of the calorimeter.

In general, the description of the jet reconstruction and calibration in this chapter follows closely the comprehensive documentation of the jet energy calibration procedure derived for $\sqrt{s} = 7\,\text{TeV}$, given in [109]. However, the calibration and quality criteria have been validated in detail in the course of the inclusive jet cross-section measurement at $\sqrt{s} = 2.76\,\text{TeV}$ presented in this thesis. Hence, results from $\sqrt{s} = 2.76\,\text{TeV}$ are shown where applicable.

The chapter is structured as follows. In Section 5.1 the jet reconstruction is described. The choice of the calibration scheme, a detailed discussion of the systematic uncertainties and the measurements used to validate the JES are given in Section 5.2, followed by the determination of the jet energy resolution in Section 5.3. In Section 5.4, the jet quality criteria are presented with a special focus on the dataset with $\sqrt{s} = 2.76\,\text{TeV}$.

5.1 Jet reconstruction

A jet typically consists of a few hundred particles, where each incoming particle deposits its energy among many cells again. To cope with the large number of cells, the jet reconstruction consists of two steps. First, cells are combined to energy clusters. In a second step, these clusters are used as input to the jet algorithm.

5.1.1 Clustering algorithm

Ideally, the clustering algorithm is able to resolve single particles, while it is at the same time robust against noise fluctuations in the detector. The algorithm used here is a topological clustering algorithm [110, 111], also denoted *topo-cluster algorithm*. It is based on the energy significance with respect to the noise level in each cell, as a first measure to reduce the influence of noise. Since the shape of the energy deposition of the jet constituents varies largely, the algorithm employs a flexible number of cells when forming the cluster. No requirements on the geometry of the energy deposition is imposed to maximise the energy and spatial resolution.

The topo-cluster algorithm consists of a clustering and a splitting step. Cells are clustered according to their signal-to-noise ratio S/N, which is calculated from the absolute value of deposited energy divided by the root mean square (RMS) of the noise of the cell. The clustering is seeded by a cell with $S/N > 4$. Subsequently, neighbouring cells are iteratively added to the seed as long as $S/N \geq 2$. Finally, all cells with $S/N \geq 0$ directly adjacent to the formed cluster are added as well. This so-called $(4, 2, 0)$ scheme was chosen because it gives a large noise suppression while it introduces only a small bias on the cluster energy [111].

In the splitting step, each cluster with more then three cells is re-evaluated in terms of local maxima. Only the cells from the current cluster are considered. Each local maximum is the starting point for a new, individual cluster. The same cluster algorithm is used for the splitted clusters. Cells are iteratively reassigned to the new seeds using the same $(4, 2, 0)$ scheme until splitted cluster adjoin completely. Cells at the borders of two clusters can be shared, and the energy of the shared cells is divided between the two associated clusters according to the energy and the distance to the cluster centroids.

5.1.2 Jet algorithm

Jets are reconstructed using the anti-k_t algorithm, as defined in Section 1.4, with two different radius parameters of $R = 0.4$ and $R = 0.6$. The implementation is done with the FastJet package [112, 113].

Two different inputs are used for the jet algorithm. The default are calorimeter-based jets using topo-clusters. The physics properties of the clusters for the recombination scheme are defined as follows: the energy is the sum of the cell energies; the mass is set to zero, since no particle identification is performed; the direction is calculated from the pseudo-rapidity and the azimuthal angle of the constituent cells, using the absolute energies as weights. The reference point of the angles is the nominal centre of the ATLAS coordinate system. Generally, only jets with a $p_{\mathrm{T}}^{\mathrm{em}} > 7\,\mathrm{GeV}$ are considered. The resulting jets are calibrated to the electromagnetic energy scale, i.e. the response of their hadronic component is not yet accounted for in the energy measurement.

The second type of jets are so-called *track jets* that are reconstructed from the momentum of measured tracks of charged particles in the inner detector[1]. Due to the smaller coverage of the inner detector, jets only can be reconstructed within $|y| < 1.9$, and the minimum p_{T} for track jets is 4 GeV.

[1] The requirements on the tracks are $p_{\mathrm{T}} > 500\,\mathrm{MeV}$, at least one hit in the pixel detector, six hits in the silicon strip detector, and transverse and longitudinal impact parameters of $d_0 < 1.5\,\mathrm{mm}$ and $|z_0 \sin\theta < 1.5\,\mathrm{mm}$, respectively.

5.1.3 Jet reconstruction efficiency

The jet reconstruction efficiency is determined with an in-situ measurement using track jets that provide an independent reference [109]. Only events with dijet back-to-back topologies, $\Delta\phi^{(1,2)} \geq 2.8\,\text{rad}$, are used to guarantee proper collision events. The leading jet is required to have $p_{\text{T}} > 15\,\text{GeV}$. The subleading jet serves as reference for the reconstruction efficiency measurement, and therefore no other track jet is allowed in the vicinity of the second jet, $\Delta\phi^{(1,2)} \geq 2.8\,\text{rad}$. Calorimeter jets are matched to the track jets within a distance of $\Delta r^{\text{trk}} = \sqrt{(y_{calo} - y_{track})^2 + (\phi_{calo} - \phi_{track})^2} < 0.6$, and the efficiency from the track jet in-situ measurement, $\epsilon_{\text{reco}}^{\text{in-situ}}$, is defined by the ratio of matched calorimeter jets and reference track jets.

Both, data and the Monte Carlo simulation show an efficiency of about 85% at a transverse momentum of $p_{\text{T}}^{\text{had}} = 20\,\text{GeV}$, which steeply increases and reaches a plateau close to 100% at around 30 GeV. On average, the deficiency in the region $20\,\text{GeV} \leq p_{\text{T}} < 30\,\text{GeV}$ is 6%, primarily due to the energy resolution of the calorimeter jet in combination with the p_{T} threshold of 7 GeV in the jet reconstruction. Data and simulation are in good agreement. The systematic uncertainty on the measurement is derived by varying the requirement on $\Delta\phi^{(1,2)}$ and Δr. It is of the order of 5% at $p_{\text{T}} = 20\,\text{GeV}$ and decreases for larger p_{T}.

The good description of the data result by the simulation indicates that both components, the track jet measurement and the calorimeter jet measurement, are modelled well. Hence, it is justified to determine the absolute reconstruction efficiency of calorimeter jets in the simulation, $\epsilon_{\text{reco}}^{MC}$. It is defined by the fraction of matched jets at particle and detector level within $\Delta r^{\text{match}} = \sqrt{\left(y_{\text{det}} - y_{\text{particle}}\right)^2 + \left(\phi_{\text{det}} - \phi_{\text{par}}\right)^2} < 0.6$, divided by the number of jets at particle level. In the simulation, the reconstruction efficiency $\epsilon_{\text{reco}}^{MC}$ is found to be fully efficient from $p_{\text{T}} \geq 20\,\text{GeV}$. To cover the residual differences between the central value of data and Monte Carlo simulation in the in-situ measurement of the efficiency, $\epsilon_{\text{reco}}^{\text{in-situ}}$, an uncertainty of 2% is conservatively assigned for $20\,\text{GeV} \leq p_{\text{T}} < 30\,\text{GeV}$, and 1% above. Since no measurement of the reconstruction efficiency is available for $|y| > 2.1$, this uncertainty is extended up to $|y| < 4.4$.

5.2 Jet energy calibration

The ATLAS calorimeter is non-compensating, i.e. the energy response to electromagnetic and hadronic energy deposition is different. Since electrons and photons provide much simpler and precise probes than hadrons, especially through the decays of $Z \to e^+e^-$, the calibration of the jet energy calibration is performed as a relative calibration with respect to the well-defined electromagnetic scale. Figure 5.1 shows the energy response of jets at the electromagnetic scale from the Monte Carlo simulation, as a function of the pseudo-rapidity. For low-energetic jets, the response at electromagnetic scale is only about half of the true energy. The response reaches almost 90% for very high jet energies, but still shows large variations along the pseudo-rapidity, due to the non-instrumented regions in the transition between different calorimeter segments.

All available calibration schemes for the data periods considered in the jet measurements of the following chapters apply a calibration based on Monte Carlo simulation. This is due to the fact that in-situ calibration techniques such as balancing of γ and jet in the final state of the same event suffer from statistical uncertainties in the available dataset. Therefore, these techniques are only used to validate the calibration, while the calibration itself is performed using the Monte Carlo simulation.

In general, the jet energy calibration consists of a correction for additional energy in the detector in events with multiple interactions, and a calibration factor to account for the jet energy scale. It is applied

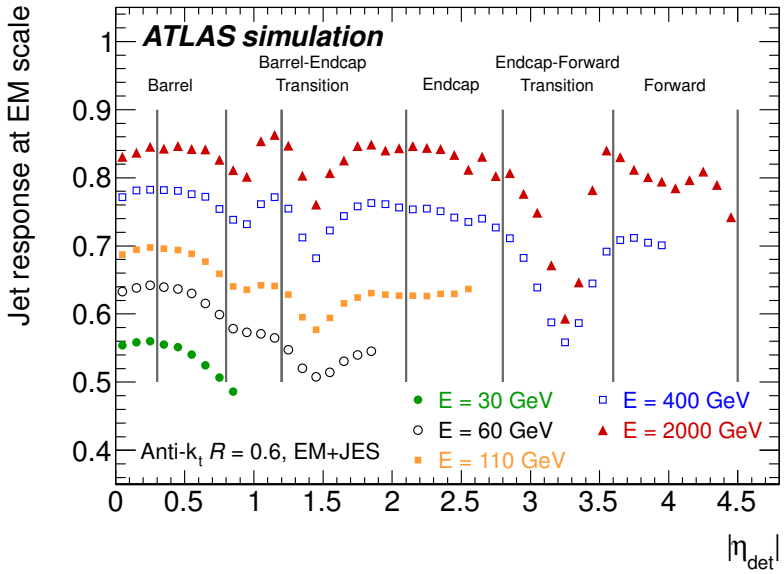

Figure 5.1: Averaged simulated jet response at the electromagnetic scale for jets in the *EM+JES* calibration scheme with $R = 0.6$, shown for several jet energies as a function of the pseudo-rapidity in the detector, $|\eta_{det}|$ [109].

using

$$E^{\text{had}}(E^{\text{em}}, \eta) = \left(E^{\text{em}}(\eta) - E^{\text{em}}_{\text{offset}}(N_{\text{PV}}, \eta)\right) \cdot c(E^{\text{em}}, \eta). \tag{5.1}$$

Depending on the calibration scheme, E can be either the energy of a jet or of single clusters. E^{em} is the energy of the according object at electromagnetic scale, and η its pseudo-rapidity. E_{offset} accounts for additional energy in the calorimeter due to multiple interactions in the same bunch crossing and is a function of the number of primary vertices[2], N_{PV}, as a measure of the in-time pile-up [84]. The energy correction factor c depends on E^{em} as well as η, and provides the main calibration. It is basically the inverse of the jet response shown in Figure 5.1.

5.2.1 Pile-up correction

Multiple interactions in the same bunch crossing give rise to small additional energy deposition that can either form new jets, or add energy to the jets from the hardest interaction. The energy of additional jets from pile-up interactions is mostly below the typical threshold of $E^{\text{jet}}_{\text{min}} = 20\,\text{GeV}$, but in general no distinction is made between jets from different vertices in the presented inclusive jet measurements. However, the additional small energy deposition that overlap with high p_{T} jets lead to an increase of their reconstructed energy. This bias has to be corrected for.

The effect of additional energy from pile-up interactions is quantified by an averaged offset energy at electromagnetic scale, $E^{\text{em}}_{\text{offset}}(\eta, N_{\text{PV}})$, as a function of the pseudo-rapidity η and the number of reconstructed primary vertices [84], N_{PV}. It is derived from minimum bias data[3] by measuring the average deposited energy among all projective towers in the calorimeter in a certain pseudo-rapidity region for

[2] A *primary vertex* denotes the primary interaction point of a proton-proton interaction, while a *secondary vertex* describes the vertex of e.g. a subsequent decay in the same interaction. In bunch crossings with multiple interactions, several primary vertices are present.

[3] In ATLAS terminology, the used dataset corresponds to period D of the ATLAS data taking period in 2010.

a given number of reconstructed primary vertices. $E^{\mathrm{em}}_{\mathrm{offset}}(\eta, N_{\mathrm{PV}})$ then results in

$$E^{\mathrm{em}}_{\mathrm{offset}}(N_{\mathrm{PV}}, \eta) = \left(\langle E^{\mathrm{em}}_{\mathrm{tower}}(N_{\mathrm{PV}}, \eta)\rangle - \langle E^{\mathrm{em}}_{\mathrm{tower}}(1, \eta)\rangle\right) \cdot \langle N^{\mathrm{jet}}_{\mathrm{tower}}\rangle, \tag{5.2}$$

where $\langle N^{\mathrm{jet}}_{\mathrm{tower}}\rangle$ is the average number of projective towers in a jet using the topo-cluster algorithm. The average correction per additional primary vertex is about 250 MeV in the central and 1 GeV in the forward region [109].

Since the bunch spacing τ_{bunch} was above 450 ns for the analysed dataset, only contributions from in-time pile-up need to be taken into account.

5.2.2 Jet origin correction

The topo-clustering algorithm and the jet algorithm use the nominal interaction point of the ATLAS detector to calculate the four-momentum of the jet. However, the actual position of the collision varies, in particular along the beam axis where the deviation is $RMS^{z}_{PV} = 29.7$ mm [84]. This causes a mismeasurement of the rapidity of the jet. In the jet origin correction, the four-momenta of the topo-clusters are recalculated using the reconstructed primary vertex of the hardest scattering in the event, just as the four-momenta of the jets. The angular resolution and the p_{T} response improve slightly from this correction, while the energy of the jet remains unchanged.

5.2.3 Calibration scheme

Several approaches for the jet energy calibration are pursued at the ATLAS experiment. This section provides a compact overview on the available strategies. A detailed description is given in Ref. [109].

EM+JES scheme

The *EM+JES* scheme is based on a jet-by-jet correction factor derived from the Monte Carlo simulation. It is a simple calibration scheme, applying a mean energy correction for a jet measured at the electromagnetic scale. Thus it does not account for fluctuations of the hadronic fraction inside the individual jet, and results in a comparably poor energy resolution. However, it produces a reliable calibration of the mean energy and has the advantage of a well understood, fully-fledged uncertainty. In summary, this calibration scheme is the most robust for the data sample used in this work.

Local cluster weighting

The *local cluster weighting* (LCW) scheme is a calibration at cluster level and thus independent of the jet algorithm. It is based on the probability p for each cluster to be an energy deposition from a hadronic shower, and $(1 - p)$ from an electromagnetic shower. The properties to determined the probability p are the cell energy density, the longitudinal shape of the shower, i.e. the fraction of energy in the different layers of the calorimeter, the isolation of the energy deposition and the total shower depth. The corresponding parameters are derived from simulation of single charged hadrons and neutral pions. Any jet-level effects like dead material, leakage and out-of-cone effects are corrected for in the subsequent calibration of Equation 5.1 using the factor c.

Global cell energy density weighting

The *global cell energy density weighing* (GCW) scheme attempts to determine the fraction of electromagnetic and hadronic shower contributions at jet level. The energy of each cell contained in the jet

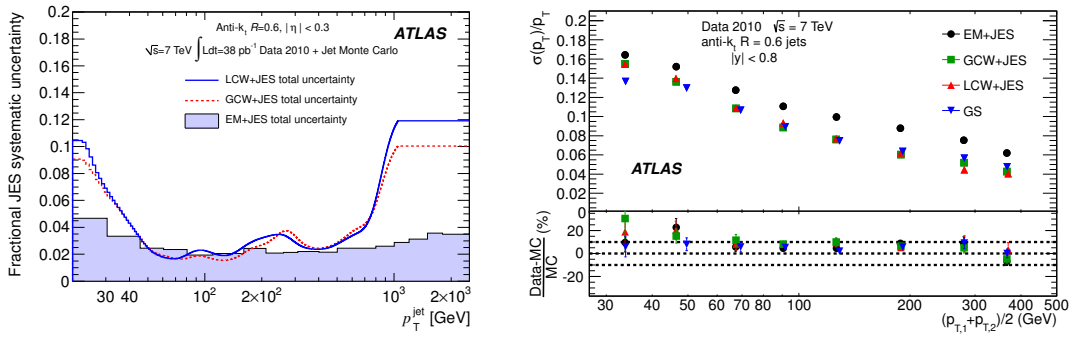

(a) (b)

Figure 5.2: Comparison of (a) the systematic uncertainty of different jet calibration schemes in the central rapidity region $\eta < 0.3$ as a function of the jet p_T [109], and (b) the jet energy resolution for different calibration schemes in the region $|y| < 0.8$, including a comparison to Monte Carlo simulation. Both use anti-k_t jets with $R = 0.6$ and data at $\sqrt{s} = 7$ TeV from 2010 [114].

is corrected according to its energy density, E/V, and calorimeter layer, i, using the GCW calibration constants $w(E/V, i)$. Subsequently, the jet energy is recalculated using the new, reweighted cell energies. The constants $w(E/V, i)$ of the GCW scheme are described by polynomial functions. Their parameters are determined from a global fit such that the jet energy resolution becomes minimal. Since $w(E/V, i)$ is derived from the ratio of reconstructed energy and true energy, the procedure also corrects for inefficiencies due to non-instrumented calorimeter regions, leakage and out-of-cone effects.

Global sequential calibration

The *global sequential* (GS) calibration is generally based on the *EM+JES* calibration scheme. It attempts to improve the jet energy resolution by exploiting the jet shape. Thus it introduces a jet-dependent correction to account for fluctuations in the hadronic fraction of the constituents forming the jet and the different response of jets from gluons or quarks. The method is based on multivariate techniques and mostly employs the energy fraction in different layers of the calorimeter to extract the longitudinal shape, and the width of the jet. It preserves the mean jet energy that is already well calibrated by the *EM+JES* scheme.

Choice of calibration scheme

Figure 5.2a shows the systematic uncertainties of the calibration schemes *EM+JES* , LCW and GCW for the central rapidity region $|\eta| < 0.3$. They are determined using in-situ measurements of the single hadron response [115], E/p, in a dataset corresponding to an integrated luminosity of $\mathcal{L} = 38\,\text{pb}^{-1}$ and from Monte Carlo simulations. The systematic uncertainty is at a level of 2% in the range $60\,\text{GeV} < p_T < 600\,\text{GeV}$ for all calibration schemes. For transverse momenta below 60 GeV and above 600 GeV, the systematic uncertainties of the LCW and GCW schemes suffer from a larger uncertainty in the single hadron response measurement, whereas the *EM+JES* scheme only increased mildly. The uncertainty of the GS calibration scheme is in principle the same as for the *EM+JES* scheme, since it does not change the mean value of the calibration, but with an additional uncertainty of 1% added in quadrature to account for the uncertainty of the method itself. In summary, the systematic uncertainty on the jet energy response is significantly larger for LCW and GCW in comparison to the *EM+JES* scheme, mostly

due to the limited statistical precision of the small dataset from 2010 used for the E/p measurement. The measurement is in good agreement between the data and Monte Carlo simulation, except some differences observed in the low p_{T} region.

The jet energy resolution of the calibration schemes LCW, GCW and the GS is found to be very similar [114], as shown in Figure 5.2b. It ranges from 15% at 30 GeV to 4% at 400 GeV. The *EM+JES* scheme performs about 2% worse compared to the others. Nevertheless, the *EM+JES* calibration scheme is selected as calibration for this jet analysis, because of its much smaller jet energy scale uncertainty. The methods used to determine the jet energy resolution is presented in Section 5.3.

5.2.4 Jet energy scale uncertainty

For most measurements involving jets, the uncertainty of the jet energy scale is the dominating contribution to the total uncertainty. The reason is the steeply falling spectrum of the jet cross-section with increasing energy, which is roughly proportional to E_{jet}^{-5}. Therefore, already very moderate uncertainties on the jet energy translate into a huge uncertainty in the cross-section.

The design goal for the understanding of the hadronic energy scale of the calorimeter is an uncertainty of 1% [80]. Since the measurement of the inclusive jet cross-section presented in this work is the first of its kind at the ATLAS experiment, larger uncertainties are expected.

This section lists the different contributions to the uncertainty of the *EM+JES* jet energy scale calibration scheme, grouped in the following categories: uncertainty due to the single hadron response measurement; intrinsic uncertainty in the calibration method; uncertainties connected to the theoretical model of the Monte Carlo simulations; propagation of the jet energy scale to the forward region. For cross-referencing to the ATLAS terminology, each source is provided with an identifier, JES *x*.

Uncertainty due to the single hadron response measurement

The jet energy response in the Monte Carlo simulation depends on the correct description of the jet constituents. Therefore, the measurement of the response of single hadrons is an essential verification of the Monte Carlo simulation and can be used to assess the uncertainty of the calibration.

The calorimeter response for single particles is determined with an in-situ measurement of single isolated hadrons in Monte Carlo simulation, collision data [115] and test beam data [116]. The observable for the measurement is the E/p response, which relates the energy measured in the calorimeter to the momentum measurement of charged particles measured in the tracking devices. The resolution of the tracking is determined as $\sigma_p/p = 4.83 \pm 0.16 \times 10^{-4}\,\mathrm{p_T/GeV}$ [85], and thus provides a good reference in the low momentum regime. The hadrons are selected from a single, isolated track of a charged particle, to which an isolated energy deposition in the calorimeter within a radius of $r^{\mathrm{trk}} < 0.1$ with respect to the track is matched. Possible biases of the measurement are overlapping energy depositions from neutral hadrons, mostly $\pi^0 \to \gamma\gamma$. This background contribution is estimated using hadrons with a *late hadronic shower*, i.e. particles that traverse the electromagnetic calorimeter with a minimal energy loss, $E_{\mathrm{em}} < 1.1\,\mathrm{GeV}$ for $r^{\mathrm{trk}} < 0.1$, and deposit their whole energy in the hadronic calorimeter, fulfilling $E_{\mathrm{had}}/p > 0.4$ for $r^{\mathrm{trk}} < 0.1$. The residual energy deposition in the electromagnetic calorimeter along the track of the particle in an annulus of $0.1 < \Delta r^{\mathrm{trk}} < 0.2$ is then attributed to the background from neutral particles.

Several different contributions to the JES uncertainty are derived from this measurement, as follows.

***E/p* response (JES 7)** The systematic uncertainty on the measurement of the E/p response is due to the selection of isolated and well-measured tracks, the track momentum scale uncertainty, and

the difference in the background subtraction between the measurements at $\sqrt{s} = 7\,\text{TeV}$ and $\sqrt{s} = 900\,\text{GeV}$.

E/p selection (JES 8) The selection of the isolated charged hadrons is subject to this source of uncertainty. It relies on the energy limit for E^{em} and the ratio E^{had}/p for $r^{\text{trk}} < 0.1$.

E/p bias (JES 12) The background estimation from showers of neutral close-by particles shows some discrepancy between data and the Monte Carlo simulation. The corresponding difference in the E/p measurement is taken as uncertainty on the jet energy scale [115].

EM + neutrals (JES 9) In the combined test beam campaign, a beam of charged particles was used. A dedicated measurement with neutral hadrons, which contribute to about $10\% - 12\%$ of the jet energy, was not performed. While the measurement of single charged hadrons only relies on the E/p response, the uncertainty on the absolute electromagnetic energy scale has to be considered for neutral hadrons. It is determined using $Z \to e^+e^-$ decays with an uncertainty of 1.5% on the cell energy measurement for the test beam campaign with single hadrons [115].

HAD E-scale (JES 10) A larger difference was found between data and the Monte Carlo simulation in the energy measurement of anti-protons, neutrons and anti-neutrons. However, since their fraction in jets is small, the impact is small.

Test beam bias (JES 13 The measurement of the single hadron response uses collision data, as well as data from the combined test beam campaign. An additional uncertainty is assigned to account for differences in the test setup of the actual calorimeter. Considered are potential shifts of the global energy scale independently in each calorimeter, non-uniformities along the pseudo-rapidity and differences in the dead material in front of the calorimeter.

High p_{T} particles (JES 11) Since pions from test beam measurements only cover a range up to $p_{\text{T}} < 350\,\text{GeV}$, the uncertainty for single charged particles with $p_{\text{T}} > 400\,\text{GeV}$ is chosen to be 10%. This accounts for punch-through and non-linearities in the energy response of the calorimeter at very high p_{T} [115].

Uncertainty due to the calibration method

The calibration factors are derived from the Monte Carlo simulation in bins of p_{T} and y. In each bin, the energy ratio of matched isolated jets at detector and particle level is calculated as $R_{\text{jet}} = E^{\text{det}}_{\text{jet}}/E^{\text{part}}_{\text{jet}}$. The energy response is determined from the mean of a Gaussian fit to the ratio distribution, such that

$$\langle R_{\text{jet}} \rangle = \langle E^{\text{det}}_{\text{jet}}/E^{\text{part}}_{\text{jet}} \rangle. \tag{5.3}$$

Non-closure (JES 4) After calibration, residual differences of the calibrated p_{T} of the jets at detector level and the jet p_{T} at particle level in the Monte Carlo simulation are still present. The reason for this inconsistency are deficits in the fit of the average jet response and the fact that the same calibration is used for E and p_{T}, which is only applicable when the reconstructed mass of the jet at particle levels agrees with the mass at particle level [115].

Dead material (JES 5) A potential mismodelling of the non-instrumented regions in the detector simulation, often denoted as *dead material*, is another source of uncertainty on the jet response. It is estimated by varying the amount of dead material and the detector geometry. For the in-situ measurement of the single hadron response at low p_{T}, only the amount of dead material in the

inner tracker layers is varied, since the modelling of dead material in the calorimeter simulation does not enter in this measurement.

Noise thresholds (JES 1) The noise thresholds have a significant impact in the topo-cluster algorithm, which is based on the signal-to-noise ratio of calorimeter cells. Differences between the noise model in data and Monte Carlo simulation can influence the cluster shape and bias the reconstruction and calibration of jets. The comparison of noise thresholds in the data and the simulation yields an uncertainty of below 3% for jets with $p_{\mathrm{T}} > 45\,\mathrm{GeV}$, and negligible influence at larger p_{T} [115].

Pile-up (JES 14) The uncertainty on the pile-up correction is estimated from systematic variations in the determination of the jet-based offset correction. $\langle E^{\mathrm{em}}_{\mathrm{tower}}(\eta, N_{\mathrm{PV}})\rangle$ in Equation 5.2 is evaluated with an alternative trigger selection to detect a possible bias on the mean tower energy, and the tower multiplicity $\langle N^{\mathrm{jet}}_{\mathrm{tower}}\rangle$ is varied. In addition, the average offset energy is also determined in an independent study based on charged particle tracks, and the difference between $\langle E^{\mathrm{em}}_{\mathrm{tower}}(\eta, N_{\mathrm{PV}})\rangle$ and $\langle E^{\mathrm{em}}_{\mathrm{tracks}}(\eta, N_{\mathrm{PV}})\rangle$ is considered as an additional uncertainty on the pile-up correction.

Uncertainty on the theoretical model

Since the *EM+JES* calibration scheme is based on Monte Carlo simulation, it is subject to any uncertainties of the theoretical model. They are addressed as follows.

Theory showering (JES 3) The uncertainty in the modelling of the parton shower is estimated using a different parameter set for the Monte Carlo simulation. The default tune AMBT 1 is compared to the Perugia 2010 tune [117], which offers an improved modelling of the jet shape [118].

Theory underlying event (JES 2) The uncertainty in the theoretical prediction of the underlying event is assessed by comparing the nominal Monte Carlo simulation Pythia with the simulation from the combined generator consisting of Alpgen for the matrix element calculation, Herwig for the simulation of the parton shower and hadronisation, and Jimmy for the modelling of the underlying event. Both simulations have different approaches for the matrix element ($2 \to 2$ vs. $2 \to n$ process), parton shower (p_{T}-ordering vs. angular ordering), hadronisation (Lund-string model vs. cluster model), modelling of the underlying event (Pythia with MC 10 tune vs. Jimmy with MC 09 tune) and hence can be used to estimate the uncertainty due to the simulation [119].

Propagation of the jet energy scale uncertainty to the forward region

As the ATLAS calorimeter covers a very large pseudo-rapidity region, it combines many different detector technologies, of which the energy responses differs widely. Although the jet energy response $\langle R_{\mathrm{jet}}\rangle$ can be derived from the Monte Carlo simulation for any η, the uniformity of the calorimeter response has to be verified. This is studied using the *η-intercalibration* approach, which makes use of dijet event topologies. Assuming a well-calibrated jet energy scale, the p_{T} measurement of the two jets is expected to yield the same result. The η-intercalibration approach is used to determine the uncertainty of the JES at $\sqrt{s} = 7\,\mathrm{TeV}$ in the forward region, and to validate the calibration at $\sqrt{s} = 2.76\,\mathrm{TeV}$ in preparation of the jet-cross-section measurement at this centre-of-mass energy.

There are two variants of the η-intercalibration. The first variant uses a fixed reference region with a well-understood calibration, i.e. the central region where the detector geometry is very homogeneous. This way, a well-measured reference jet can be balanced against a probe jet in the forward region. The

second variant is the *matrix method*, in which no dedicated reference region is defined. Instead any combination of η_1, η_2 of the two jets is used to check the relative balance of the calibration. Hence, it yields a better statistical uncertainty. Both methods give compatible results [109], but the matrix method is used in the calibration because of its smaller uncertainty. For reasons of simplicity the η-intercalibration with fixed reference region is described here. A detailed description of the matrix method can be found in [109].

In order to make the transverse momentum conservation hold for dijet event topologies at detector level, the following selection criteria are applied:

$$\Delta\phi^{(1,2)} > 2.6\,\text{rad} \tag{5.4}$$

$$p_{\text{T}}^{(3)} < max(0.15 p_{\text{T}}^{\text{avg}}, 7\,\text{GeV}) \tag{5.5}$$

$$p_{\text{T}}^{\text{avg}} = \frac{p_{\text{T}}^{(1)} + p_{\text{T}}^{(2)}}{2} > 20\,\text{GeV} \tag{5.6}$$

Here, $p_{\text{T}}^{(\text{n})}$ denotes the n-th jet in the event, and $\Delta\phi^{(1,2)}$ is the azimuthal angle between the leading and sub-leading jet. The threshold on $p_{\text{T}}^{\text{avg}}$ in Eq. 5.6 is required to ensure that both jets are in a measurable p_{T} range. Eq. 5.4 selects events where the two leading jets are back-to-back, and Eq. 5.5 guarantees that no hard radiations distort the balance of the leading jets[4].

The p_{T} balance of the dijet system is described by the asymmetry, $\mathcal{A}$, and the η-intercalibration factor, c:

$$\mathcal{A} = \frac{p_{\text{T}}^{\text{probe}} - p_{\text{T}}^{\text{ref}}}{p_{\text{T}}^{\text{avg}}} \tag{5.7}$$

$$\frac{p_{\text{T}}^{\text{probe}}}{p_{\text{T}}^{\text{ref}}} = \frac{2 + \mathcal{A}}{2 - \mathcal{A}} = 1/c \tag{5.8}$$

c is used to calibrate the probe region in the detector. It is derived in bins of p_{T} and η from the mean asymmetry, $\langle\mathcal{A}\rangle$, determined by a Gaussian fit to the asymmetry distribution:

$$c_{i,j} = \frac{2 - \langle\mathcal{A}\rangle}{2 + \langle\mathcal{A}\rangle}, \tag{5.9}$$

where i, j are the bins in p_{T} and η, respectively.

The jet response measurement using the η-intercalibration method provides a consistency check of the jet energy scale calibration derived directly from the Monte Carlo simulation. The result is presented in Figure 5.3, showing the jet response for $\sqrt{s} = 7$ TeV using the matrix method in a selection of Monte Carlo simulations and in data, based on the dataset of $\mathcal{L} = 38\,\text{pb}^{-1}$ from 2010.

In the barrel region, the correction factors have been found to be close to 1 in both, the Monte Carlo simulation and data, for $p_{\text{T}} > 60$ GeV. Nevertheless, some structure along η is visible, in particular at the transition of detector regions [120]. In the forward region, the relative jet response $1/c$ tends to smaller values and the data is not well reproduced by the nominal Monte Carlo simulation. This general tendency is more pronounced at small p_{T}.

The resulting systematic uncertainty on the JES from the η-intercalibration is as follows.

Forward JES (JES 6, JES 15) The uncertainty of the jet energy scale in the forward region consists of two components. The first contribution, JES 6, is the differences of the in-situ measurement of the

[4] In the original study of the η-intercalibration [120], a selection of $p_{\text{T}}^{(3)} < 0.25 p_{\text{T}}^{\text{avg}}$ was used to improve the statistical uncertainty.

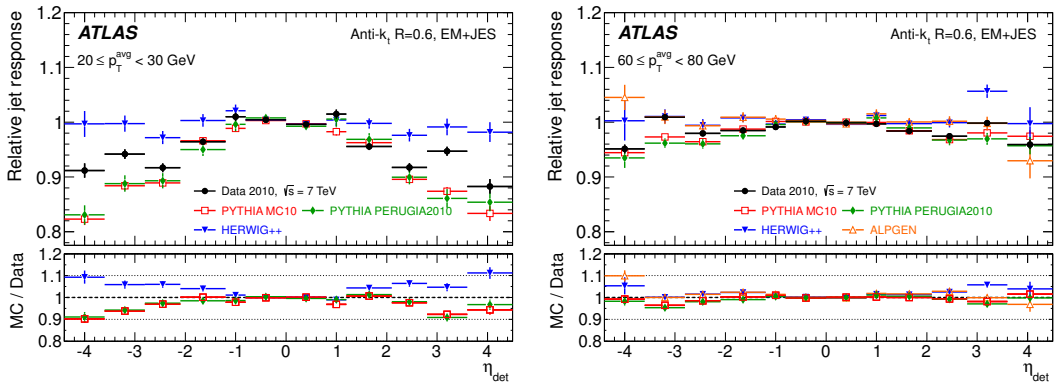

(a) 20 GeV ≤ p_T < 30 GeV (b) 60 GeV ≤ p_T < 80 GeV

Figure 5.3: Jet energy response at $\sqrt{s} = 7$ TeV as function of η_{jet} for anti-k_t jets with $R = 0.6$ in data and a selection of Monte Carlo simulations, for two transverse momentum ranges: (a) 20 GeV ≤ p_T < 30 GeV and (b) 60 GeV ≤ p_T < 80 GeV [109]. Jets are calibrated with the *EM+JES* calibration scheme, and $p_T^{avg} = \left(p_T^{(1)} + p_T^{(2)}\right)/2$. The response is determined with the matrix method for intercalibration.

jet energy response using various Monte Carlo generators and tunes. The RMS of the correction factor c in each bin of p_T and η is used as uncertainty. The second component, JES 15, is given by the agreement of the data and the nominal prediction, namely Pythia with the MC 10 tune. In some measurements, the two components are treated as one combined uncertainty, denoted as JES 6 only.

Summary of the JES uncertainty

The JES uncertainty is shown in Fig. 5.4 for jets with $R = 0.6$ in two rapidity regions. In the barrel region of the detector, $0.3 \leq |\eta| < 0.8$, the JES uncertainty is at a level of 2.5% for 45 GeV < p_T < 800 GeV. Below 45 GeV, it increases to 4.5%, dominated by the uncertainties on the simulation and the non-closure of the calibration. At high p_T, the contribution from the single particle response increases the uncertainty to about 4.0%. While the uncertainty in the forward region is only slightly increased for the accessible transverse momenta at $p_T > 60$ GeV, the additional contribution from the η-intercalibration inflates the uncertainty in the lowest p_T-bins to a value of up to 6.5% for $2.1 \leq |\eta| < 2.8$, and 11% for $3.6 \leq |\eta| < 4.4$. The uncertainty for jets with $R = 0.4$ is similar.

The correlation between different contributions of the JES uncertainty has been carefully studied [2]. It is summarised in Table 5.1. Each source is fully correlated in p_T, except the uncertainty due to pile-up (JES 14). The correlation in the rapidity is given by the numbering scheme. Bins with the same number are fully correlated, while bins with different numbers are uncorrelated. In general, only the first two y-bins covering $0.0 \leq |y| < 0.8$ are fully correlated, due to the homogeneous detector geometry, and the contribution from the η-intercalibration (JES 6, JES 15).

5.2.5 Jet calibration at different centre-of-mass energies

The jet measurement in a single event does not depend on the centre-of-mass energy, but only on the running conditions in the particular bunch crossing. Hence, if the same jet calibration is used in two measurements, the correlation of the JES uncertainty is expected to be 100%. An exception is the jet selection efficiency because it is closely related to the running conditions, which are uncorrelated

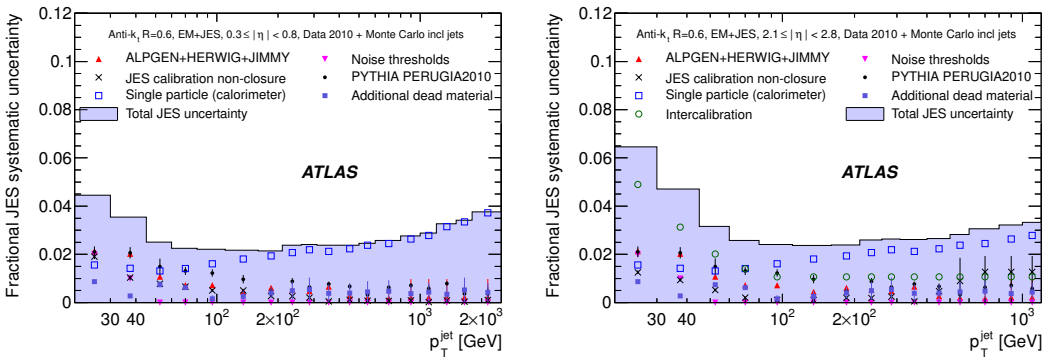

(a) $0.3 \leq |\eta| < 0.8$ (b) $2.1 \leq |\eta| < 2.8$

Figure 5.4: Systematic uncertainty of the *EM+JES* scheme for anti-k_t jets with $R = 0.6$ as function of p_{T} in the ranges $0.3 \leq |\eta| < 0.8$ (a) and $2.1 \leq |\eta| < 2.8$ (b). Also shown are the fractional contributions of the main components of the uncertainty.

between different centre-of-mass energies. The potential correlation between measurements at different centre-of-mass energies is given in the rightmost column of Table 5.1.

5.2.6 In-situ validation

Although the statistical precision of the dataset at $\sqrt{s} = 7$ TeV from 2010 is insufficient to derive the JES directly from data, the data is used to validate the simulation based calibration. Various complementary in-situ methods have been utilised [109]:

- Similar to the single hadron response, the jet energy measurement in the calorimeter is cross-checked by the *comparison to associated charged particle tracks* in the inner detector. The central value of both measurements agrees within 1% over a wide range of transverse momentum and is well within the JES uncertainty. The method is limited by the uncertainty on the charged track multiplicity per jet, the detector description and the acceptance of the tracking system.

- In the *direct γ-jet p_{T} balance* method, a natural calibration of the jet energy scale is acquired using events with a quark radiating a highly energetic photon in the final state, e.g. in processes like $qg \rightarrow q\gamma$ or $qq \rightarrow g\gamma$. The electromagnetic energy deposition of the photon is used as a reference for the balancing jet. In data, the agreement between $p_{\mathrm{T}}^{\mathrm{jet}}$ and p_{T}^{γ} is good, except for very low p_{T}. However, this behaviour is reproduced by the simulation within the JES uncertainty. This measurement is supplemented by investigating the same events looking at the full hadronic recoil instead of a single jet in opposite direction to the photon. Both methods give very similar results.

- With the *multi-jet transverse momentum balance* it is possible to access the region of jets with high p_{T}. The study utilises multi-jet event topologies, where one of the two outgoing tree-level partons creates a single hard jet, while the other parton splits into several moderate jets. The latter serve as reference jets, since they are in an energy regime which is well-understood by means of the other methods. The multi-jet transverse momentum balance is limited due to the number of events with the desired event topology.

Table 5.1: Bin-to-bin correlations of the sources of systematic uncertainty in the measurement of the inclusive jet cross-section. Each source is fully correlated in the p_T of the jet, unless stated otherwise. The correlation in y is given by the numbers, where bins with the same number are considered as fully correlated in y, while bins with different numbers are uncorrelated. The numbering scheme is inherited from the corresponding measurements at $\sqrt{s} = 2.76\,\text{TeV}$ [1] and $\sqrt{s} = 7\,\text{TeV}$ [2]. The correlation between the measurements at different centre-of-mass energies is specified in the right column. The source JES 15 has been treated separately in the measurement at $\sqrt{s} = 2.76\,\text{TeV}$. Added in quadrature, JES 6 and JES 15 are fully correlated with the combined JES 6. The pile-up correction JES 14 is not considered in the measurement at $\sqrt{s} = 2.76\,\text{TeV}$. The table is taken from [1, 2].

uncertainty source	rapidity bin $\lvert y\rvert$							correlation
	0.0–0.3	0.3–0.8	0.8–1.2	1.2–2.1	2.1–2.8	2.8–3.6	3.6–4.4	between $\sqrt{s}$
noise thresholds (JES 1)	1	1	2	3	4	5	6	yes
theory UE (JES 2)	7	7	8	9	10	11	12	yes
theory showering (JES 3)	13	13	14	15	16	17	18	yes
non-closure (JES 4)	19	19	20	21	22	23	24	yes
dead material (JES 5)	25	25	26	27	28	29	30	yes
forward JES (JES 6)	31	31	31	31	31	31	31	
generator (JES 6)	88	88	88	88	88	88	88	yes
detector (JES 15)	89	89	89	89	89	89	89	
E/p response (JES 7)	32	32	33	34	35	36	37	yes
E/p selection (JES 8)	38	38	39	40	41	42	43	yes
EM + neutrals (JES 9)	44	44	45	46	47	48	49	yes
HAD E-scale (JES 10)	50	50	51	52	53	54	55	yes
high p_T (JES 1 1)	56	56	57	58	59	60	61	yes
E/p bias (JES 12)	62	62	63	64	65	66	67	yes
test-beam bias (JES 13)	68	68	69	70	71	72	73	yes
pile-up (JES 14)	uncorrelated in p_T and y							n/a
jet energy resolution	76	76	77	78	79	80	81	yes
jet angle resolution	82	82	82	82	82	82	82	yes
jet reconstruction eff.	83	83	83	83	84	85	86	yes
jet selection eff.	uncorrelated in p_T and y							no
trigger efficiency	uncorrelated in p_T and y							no
unfolding: closure test	74	74	74	74	74	74	74	no
unfolding: jet matching	75	75	75	75	75	75	75	no
luminosity	87	87	87	87	87	87	87	no

In summary, the applied in-situ techniques yield very good agreement between the data and the Monte Carlo simulation within the systematic uncertainty of the JES, confirming the consistency of the *EM+JES* calibration scheme and its uncertainty.

The in-situ methods mentioned here are applied for $\sqrt{s} = 7\,\text{TeV}$, using the dataset from 2010. A verification at a comparable precision is not possible at $\sqrt{s} = 2.76\,\text{TeV}$ in the dataset from 2011 due to the very limited number of events. However, no explicit dependence of the jet calibration on the centre-of-mass energy is expected, as stated above. Likewise, the absolute energy scale is expected to remain stable during the technical shutdown in the turn of the year 2010/2011, since it is an intrinsic detector property that only may suffer from long-term effects like hardware degradation due to radiation damage. On the other hand, individual channels in the detector can show defects after the shutdown, indeed, leading to inefficiencies in the jet selection. This is discussed in Sec. 5.4.

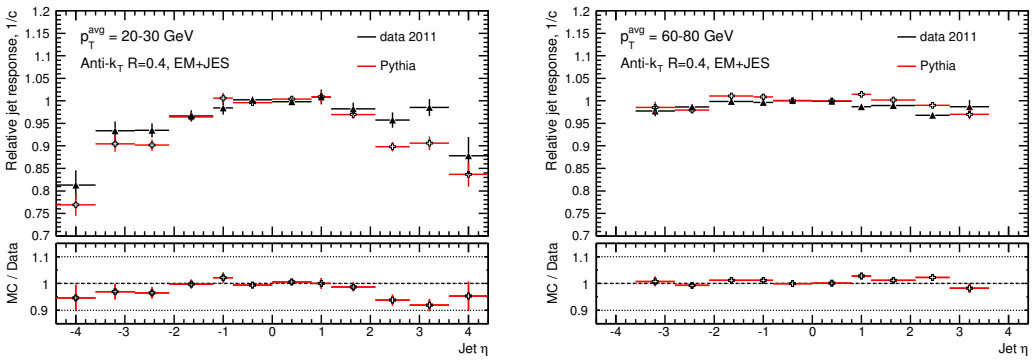

(a) $20\,\text{GeV} \leq p_\text{T} < 30\,\text{GeV}$ (b) $60\,\text{GeV} \leq p_\text{T} < 80\,\text{GeV}$

Figure 5.5: Jet energy response at $\sqrt{s} = 2.76\,\text{TeV}$ as function of η_jet for anti-k_t jets with $R = 0.4$ in data and the Monte Carlo simulation, for two transverse momentum ranges, $20\,\text{GeV} \leq p_\text{T} < 30\,\text{GeV}$ (a) and $60\,\text{GeV} \leq p_\text{T} < 80\,\text{GeV}$ (b). Jets are calibrated with the *EM+JES* calibration scheme, and $p_\text{T}^\text{avg} = \left(p_\text{T}^{(1)} + p_\text{T}^{(2)}\right)/2$. The response is determined with the η-intercalibration method.

Despite the small number of events, the JES was tested ad hoc using the η-intercalibration method with fixed reference region to reveal potential new problems of the calibration. The result is shown in Fig. 5.5 for jets with $R = 0.4$ in the regions $20\,\text{GeV} \leq p_\text{T} < 30\,\text{GeV}$ and $60\,\text{GeV} \leq p_\text{T} < 80\,\text{GeV}$. In both transverse momentum ranges, data and the Monte Carlo simulation agree within their uncertainty. The shape of the jet response as determined by the η-intercalibration method is similar to the one found for $\sqrt{s} = 7\,\text{TeV}$, shown in Figure 5.3.

5.3 Jet resolution

The *jet energy resolution* (JER) is determined with in-situ methods using the dataset from 2010 at $\sqrt{s} = 7\,\text{TeV}$ with an integrated luminosity of $\mathcal{L} = 35\,\text{pb}^{-1}$ [114]. Two methods have been applied, the dijet balance method, very similar to the one described in the η-intercalibration, and the bisector method [121], which directly utilises the angle information of the dijet event topology. Both methods give compatible results well within their uncertainty. The resulting jet energy resolution for the bisector method is shown in Figure 5.2b for jets with $R = 0.6$, $|y| < 0.8$. It ranges from 17% at $p_\text{T}^\text{avg} = 30\,\text{GeV}$ to 6% at $p_\text{T}^\text{avg} = 500\,\text{GeV}$, and the according relative uncertainties are 20% and 10%, respectively. The agreement of the in-situ method between data and the Monte Carlo simulation is found to be at a level of 10%.

The jet angular resolution is obtained from the nominal Monte Carlo simulation by comparing the rapidity y and the azimuthal angle ϕ of the jet at particle level with the ones at detector level after the jet reconstruction. In general, the position measurement of jets is expected to be very precise in comparison to the energy measurement. To exclude shifts of the jet axis originating from other close-by jets, an isolation cut is applied. It requires no other jets to be present within a radius of $\Delta r = \sqrt{(\Delta y)^2 + (\Delta\phi)^2} < 2.5 \cdot R$, where R is the radius parameter of the anti-k_t algorithm, i.e. $\Delta r = 1.0$ for $R = 0.4$, and $\Delta r = 1.5$ for $R = 0.6$, respectively. For $R = 0.4$, the obtained resolution in the y-ϕ space is about 6% at most among the rapidity bins at $p_\text{T} = 20\,\text{GeV}$, and approaches asymptotically a value of below 1% at large p_T. The resolution for $R = 0.6$ is slightly worse, starting at 7% and reaching 1% [122]. The uncertainty on the jet angular resolution is assessed by refraining from the jet isolation, which yields a result that is

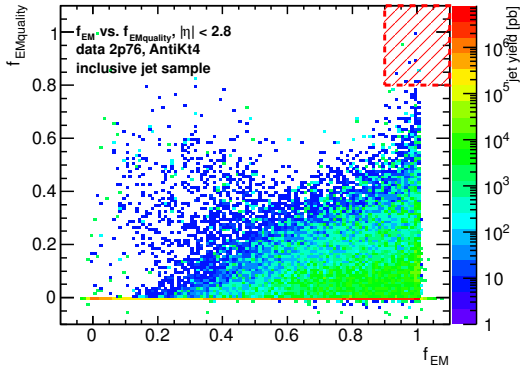

Figure 5.6: Distribution of the energy fraction deposited in the EM layer of the barrel calorimeter, f_{EM}, versus the fraction of cells with bad pulse shape, $f_{\mathrm{EMquality}}$, in the dataset from 2011 with $\sqrt{s} = 2.76\,\mathrm{TeV}$, to select fake jets from coherent noise in the electromagnetic calorimeter. A radius parameter of $R = 0.4$ is used.

only marginally worse than the nominal one.

5.4 Quality criteria

Each jet is required to pass dedicated quality criteria, ensuring that jets are not reconstructed from detector noise, cosmic rays or beam background. Although the rate of *fake jets* is generally small and the measurement of the inclusive jet cross-section is not prone to single distorted event topologies, the contribution of fake jets to the p_{T} spectrum becomes significant at about 100 GeV.

The selection criteria were established in 2010 with the dataset at $\sqrt{s} = 7\,\mathrm{TeV}$ and extensively studied [123, 124]. Details are given in the following, and at the same time the selection is revisited for the dataset at $\sqrt{s} = 2.76\,\mathrm{TeV}$ in 2011 to verify that it still applies under the different running conditions and after the detector maintenance during the shutdown 2010/2011.

Similarly to previous investigations at $\sqrt{s} = 7\,\mathrm{TeV}$, the jet selection criteria are studied using two subsets of the data at $\sqrt{s} = 2.76\,\mathrm{TeV}$. The *bad jet* sample is enriched with events that show a large imbalance of the contained jets, indicating topologies where jets is either poorly measured, or does not belong to the collision. The corresponding cuts are $p_{\mathrm{T}}^{(1)} > 20\,\mathrm{GeV}$, $\Delta\phi^{(1,E_{\mathrm{T}}^{\mathrm{miss}})} > 2.8\,\mathrm{rad}$ and $E_{\mathrm{T}}^{\mathrm{miss}}/p_{\mathrm{T}}^{(1)} > 0.7$, where $E_{\mathrm{T}}^{\mathrm{miss}}$ is the missing transverse energy. The *good jet* sample contains clean dijet event topologies with well-balanced transverse momentum, requiring the leading jets to be back-to-back, $\Delta\phi^{(1,2)} > 2.8\,\mathrm{rad}$, and a low $E_{\mathrm{T}}^{\mathrm{miss}}$significance, $E_{\mathrm{T}}^{\mathrm{miss}}/\sqrt{\sum E_{\mathrm{T}}} \leq 4$.

5.4.1 Coherent noise in the barrel of the electromagnetic calorimeter

Fake jets are reconstructed from coherent noise induced by rare noise bursts in the barrel of the EM . They are characterised by a large energy fraction deposited in the EM layer of the barrel calorimeter, f_{EM}, and a distinct pulse shape. The quality of the pulse shape can be quantified by comparing the pulse shape in each cell with a reference. Jets in the region $f_{\mathrm{EM}} > 0.9$, $|\eta| < 2.8$ are rejected if the fraction of cells with bad pulse shape, $f_{\mathrm{EMquality}}$, is above 0.9. The distribution of jets in the $f_{\mathrm{EMquality}}$-f_{EM} plane is shown in Figure 5.6 for jets with $R = 0.4$, $|\eta| < 2.8$, and $\sqrt{s} = 2.76\,\mathrm{TeV}$. Only a negligible fraction of jets is found in the rejected region, indicating that coherent noise in the EM is well under control in this datatset.

5.4.2 Sporadic noise bursts in the hadronic end-cap calorimeter

Another type of fake jets originates from sporadic noise bursts of single cells in the end cap of the hadronic calorimeter. These jets can be identified by a large fraction of energy deposited in the HEC,

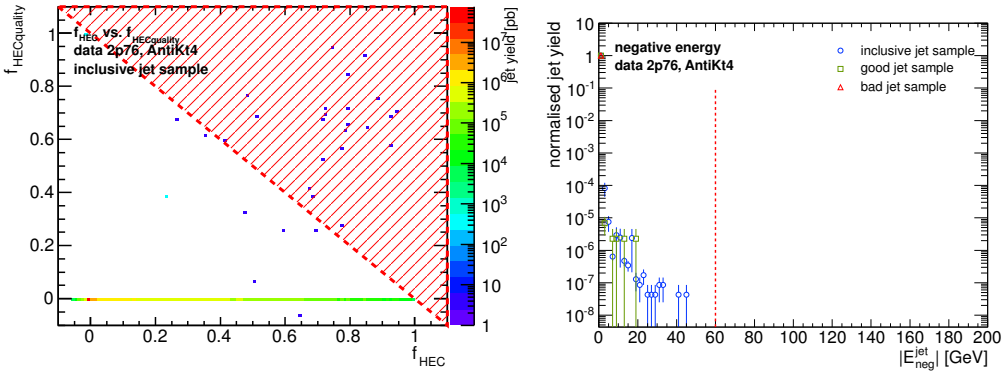

(a) (b)

Figure 5.7: Distributions of the normalised jet yield to select fake jets from sporadic noise bursts in the hadronic end-cap calorimeter in the dataset from 2011 with $\sqrt{s} = 2.76\,\text{TeV}$: (a) energy fraction deposited in the hadronic end-cap calorimeter, f_{HEC}, versus the fraction of cells with bad pulse shape, $f_{\text{HECquality}}$. The *hatched area* indicated the area where jets are rejected. (b) normalised jet yield as a function of $|E^{\text{jet}}_{\text{neg}}|$ before rejection of jets with $|E^{\text{jet}}_{\text{neg}}| > 60\,\text{GeV}$, indicated by the *dashed line*. The latter is shown separately for the inclusive samples, the sample enhanced with *bad jets*, and the sample enhanced with *good jets*. A radius parameter of $R = 0.4$ is used.

f_{HEC}, and distorted pulse shapes. The latter is evaluated the same way as the pulse shapes in the EM layer. Jets are rejected if the fraction of cells with bad pulse shape, $f_{\text{HECquality}}$, and f_{HEC} fulfil $f_{\text{HEC}} > 1 - |f_{\text{HECquality}}|$. The area where jets are rejected is shown in Figure 5.7a for jets with $R = 0.4$ at $\sqrt{s} = 2.76\,\text{TeV}$. Only very few jets are found in this region in this dataset.

Due to the capacitive coupling, a large noise pulse also creates a pulse with opposite sign in the adjacent cells, measured as negative energy, $E^{\text{cell}}_{\text{neg}}$. Studies at $\sqrt{s} = 7\,\text{TeV}$ identified jets with $|\sum E^{\text{cell}}_{\text{neg}}| = |E^{\text{jet}}_{\text{neg}}| > 60\,\text{GeV}$ to originate from noise bursts. The normalised jet yield is shown in Figure 5.7b as a function of $E^{\text{jet}}_{\text{neg}}$ for jets with $R = 0.4$ at $\sqrt{s} = 2.76\,\text{TeV}$, individually for the *good jet* and *bad jet* sample. No jets with $|E^{\text{jet}}_{\text{neg}}| > 60\,\text{GeV}$ are present in this data set.

5.4.3 Non-collision background

The distinctive features of jets from the pp collision are at least a minimal amount of energy deposition in the EM layer of the calorimeter, some charged particles leaving tracks in the inner detector, and a fixed timing with respect to the bunch crossing frequency. These properties are exploited to reject jets that originate from non-collision background, such as cosmic rays, beam halo and beam-gas interactions, by examining the energy distribution, track measurements and timing information.

A general jet selection is made using energy fraction in the EM layer, as shown in Figure 5.8a for jets with $R = 0.4$ outside the tracking system, $|\eta| \leq 2.0$. A clear excess is observed at low values of f_{EM} for the *bad jet* sample, whereas only a negligible number of events is present in the *good jet* sample. Jets with $f_{\text{EM}} < 0.05$ are rejected. Within the acceptance of the tracking system, $|\eta| < 2.0$, jets are rejected if $f_{\text{EM}} < 0.05$ and the charged fraction, f_{ch}, is $f_{\text{ch}} < 0.15$. The charged fraction measures the fraction of the jet momentum p^{trk}_T from the charged particle tracks with respect to the momentum p^{calo}_T in the calorimeter. Tracks within a defined radius around the jet axis, $r^{\text{trk}} = R$, are considered. The charged fraction is shown for jets with $R = 0.4$ at $\sqrt{s} = 2.76\,\text{TeV}$ in Figure 5.9a for the *good jet* sample and in Figure 5.9b for the *bad jet* sample, respectively.

Particles created in beam-gas interactions can be reconstructed as jets. Being produced at an arbitrary

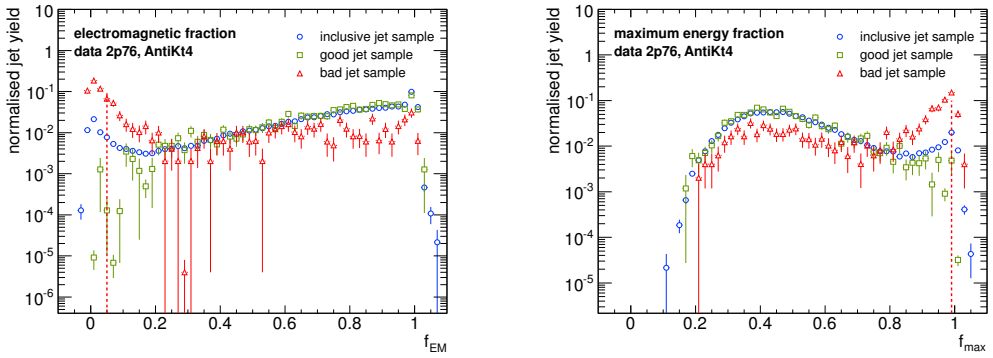

(a) (b)

Figure 5.8: Normalised jet yield for anti-k_t jets with $R = 0.4$ in the dataset from 2011 with $\sqrt{s} = 2.76\,\text{TeV}$ as a function of (a) the fraction of energy deposition in the EM layer and (b) the maximum energy fraction in any of the calorimeter layers, f_{max}, separately for the inclusive samples, the sample enhanced with *bad jets*, and the sample enhanced with *good jets*.

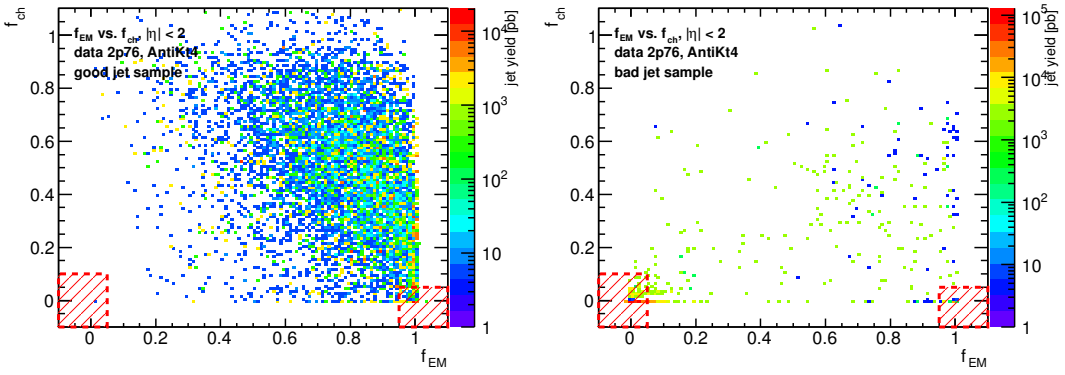

(a) *good jet* sample (b) *bad jet* sample

Figure 5.9: Distributions of the normalised jet yield as a function of the energy fraction in the EM layer of the calorimeter, f_{EM}, and the charged fraction, f_{ch}, to select fake jets from beam background in the dataset from 2011 with $\sqrt{s} = 2.76\,\text{TeV}$, separately for a sample enriched with (a) *good jets* and (b) *bad jets*. The regions where jets are rejected are indicated by the *hatched area*. Jets with a radius parameter of $R = 0.4$ are used.

point along the beam, their tracks typically do not point to the interaction vertex. Furthermore, the particles are strongly boosted in beam direction and hence deposit their energy close to the beam line. Thus they have a large energy fraction in the EM layer, $f_{\mathrm{EM}} > 0.95$, but a small charged fraction, $f_{\mathrm{ch}} < 0.05$. Figure 5.9b shows an accumulation of jets in the *bad jet* sample for this region, whereas in the *good jet* sample in Fig. 5.9a, the jet yield is smooth. Although proper jets might be removed by this criterion, the introduced bias is small in comparison to the potential impact of fake jets.

With growing emittance of the beams over time, particles from the beam halo enter the detector from the side, parallel to the beam axis. This category of fake jets is characterised by energy deposits in a single layer of the calorimeter. Jets are rejected if $f_{\mathrm{max}} > 0.99$, where f_{max} is the maximum energy fraction in any of the calorimeter layers. The distribution of f_{max} in Figure 5.8b shows this type of jets as an excess at high f_{max} for the *bad jet* sample.

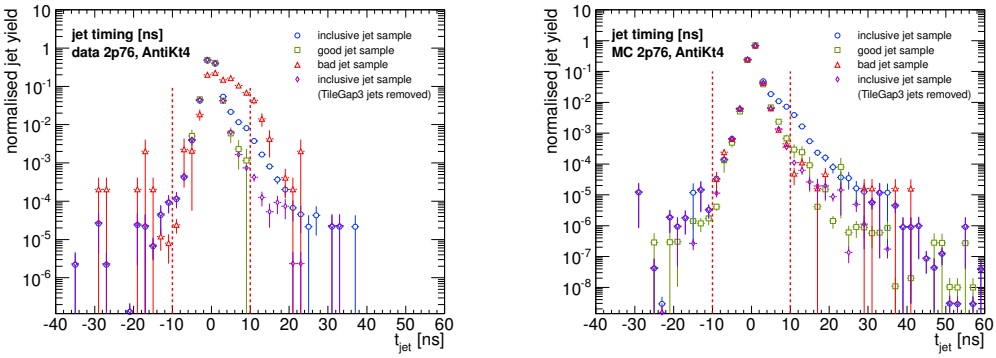

(a) data (b) Monte Carlo simulation

Figure 5.10: Timing distribution in (a) the dataset from 2011 and (b) the Monte Carlo simulation, at a centre-of-mass energy of $\sqrt{s} = 2.76\,\mathrm{TeV}$ for anti-k_t jets with $R = 0.4$. It is shown separately for the inclusive sample and the sample enriched with *good jets* and *bad jets*. In addition, the distribution of the inclusive sample where jets in the region of the `TileGap3` scintillators are removed is shown. Jets with $|t_{\mathrm{jet}}| > 10\,\mathrm{ns}$ are rejected, as indicated by the *dotted line*.

Jets reconstructed from energy depositions of cosmic rays are effectively rejected using the timing information of the constituent cells. The identification is based on the jet timing, t_{jet}, which is defined as the average energy-weighted cell time with respect to the nominal timing expected from particles that originate from the current bunch crossing. Figure 5.10a shows the jet timing distribution, required to be $|t_{\mathrm{jet}}| \leq 10\,\mathrm{ns}$. An asymmetrical distribution for the inclusive jet sample and a pronounced shoulder for the *bad jet* sample is observed. This shoulder is absent in the *good jet* sample, where all jets are within 10 ns. The delayed energy deposition is discussed in subsection 5.4.4.

The jet quality selection criteria are summarised in Table 5.2.

5.4.4 Transition region between barrel and extended barrel in the Tile calorimeter

The transition region between the barrel and the extended barrel region of the tile calorimeter at about $1.0 < |\eta| < 1.4$ contains a large amount of dead material from support structure and cabling of the inner detector and the EM [88]. Therefore it is equipped with additional scintillators, `TileGap1`, `TileGap2`, `TileGap3`, to capture the showers in the dead material. Nevertheless the amount of active material is small, and the jet energy measurement in this region is prone to noise fluctuations, in particular in `TileGap3`. This category of jets is characterised by a large energy fraction in the `TileGap3` layer,

source	selection
noise bursts in HEC	$f_{\text{HEC}} > 1 - f_{\text{HECquality}}$ $\lvert E_{\text{neg}}^{\text{cell}} \rvert < 60\,\text{GeV}$
coherent noise in EM	$(f_{\text{EM}} > 0.9) \wedge \left(\lvert f_{\text{EMquality}} \rvert > 0.8\right) \wedge (\lvert\eta\rvert < 2.8)$
non-collision background	$\lvert t_{\text{jet}}^{\text{cell}} \rvert > 10\,\text{ns}$ $(f_{\text{EM}} < 0.05) \wedge \left(\lvert f_{\text{charge}} \rvert < 0.1\right) \wedge (\lvert\eta\rvert < 2.0)$ $(f_{\text{EM}} < 0.05) \wedge (\lvert\eta\rvert \geq 2.0)$ $(f_{\text{max}} > 0.99) \wedge (\lvert\eta\rvert < 2.0)$ $(f_{\text{max}} > 0.95) \wedge \left(\lvert f_{\text{charge}} \rvert < 0.05\right) \wedge (\lvert\eta\rvert < 2.0)$
transition region `TileGap3`	$f_{\texttt{TileGap3}} > 0.5$

Table 5.2: Selection criteria to identify jets from non-collisions [109] and mis-measured jets in the transition region of the barrel and extended barrel of the tile calorimeter. A jet is rejected if it fulfils one ore more of the above categories.

$f_{\texttt{TileGap3}} > 0.5$, as shown in Figure 5.11a. The same tendency at large $f_{\texttt{TileGap3}}$ is found in the *bad jet* and the inclusive sample, whereas the *good jet* sample does not show such behaviour. The effect is more pronounced at low p_{T}.

Further investigations indicate that jets with large $f_{\texttt{TileGap3}}$ tend to have a delayed component in the jet time t_{jet}, as shown in Figure 5.14a. Hence, the shoulder in the jet time distribution t_{jet} of Figure 5.10a can be identified with jets in this calorimeter region. By removing jets with $f_{\texttt{TileGap3}} > 0.5$, the timing distribution becomes almost symmetrical, and the distribution of the *good jet* sample and the sample of jets with $f_{\texttt{TileGap3}} < 0.5$ almost superimpose.

The origin of the delayed component in the jet time distribution presumably are slow neutrons created in the dead material. However, the delayed component is not as pronounced in the data at $\sqrt{s} = 7\,\text{TeV}$, which makes it difficult to interpret the effect. Hence, jets with $f_{\texttt{TileGap3}} > 0.5$ are not used in the dataset at $\sqrt{s} = 2.76\,\text{TeV}$ from 2011. Instead, the efficiency of the selection is estimated as described in Section 5.4.6, and the measurement is corrected for it accordingly.

5.4.5 Jet selection in the Monte Carlo simulation

Contributions from jets originating from cosmic rays, beam background or calorimeter noise are not included in the Monte Carlo simulation. Although the samples should thus remain unaffected by the jet selection criteria, they are not applied because of the poor description of the variables used to reject fake jets in the simulation [125]. An exception are jets in the `TileGap3` layer, where an excess similar to data is observed, as shown in Figures 5.12b and 5.14. Similarly, the distribution of $f_{\texttt{TileGap3}}$ and t_{jet}, shown in Figure 5.11b and 5.10b, are very similar to the ones in data. The good description is an indication that this category of jets has a physical origin in the parton shower evolution. The good modelling of the effect in the detector simulation GEANT4 justifies the rejection of jets with $f_{\texttt{TileGap3}} > 0.5$, which lead to an effective suppression of the excess at $|\eta| = 1.1$ seen in Figure 5.12b. The effect in the `TileGap3` layer was first observed in the samples with $\sqrt{s} = 2.76\,\text{TeV}$, when the analysis at $\sqrt{s} = 7\,\text{TeV}$ was already published, but in fact it is also present in the samples with $\sqrt{s} = 7\,\text{TeV}$, although not as pronounced. The latter is shown in Figure 5.13. The potential bias that is introduced if the selection criteria for this category of jets is not applied, are discussed in Section 6.6.

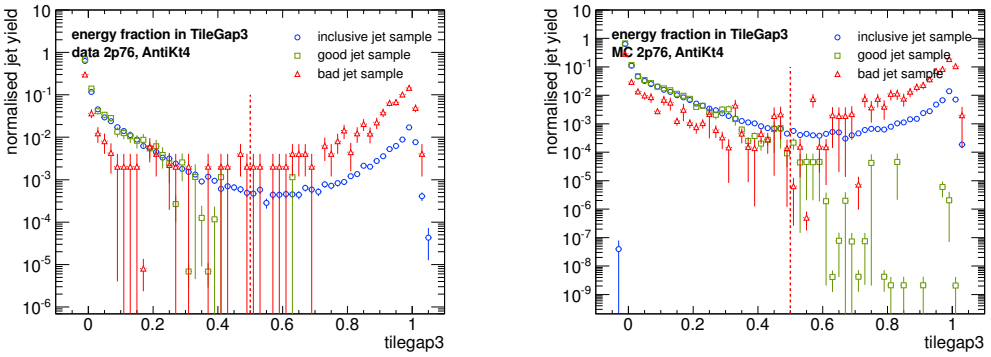

(a) data (b) Monte Carlo simulation

Figure 5.11: Energy fraction of anti-k_t jets with $R = 0.4$, deposited in the `TileGap3` scintillators, $f_{\texttt{TileGap3}}$, in (a) the dataset from 2011 and (b) the Monte Carlo simulation, at a centre-of-mass energy of $\sqrt{s} = 2.76\,\text{TeV}$. The distribution is shown separately for the inclusive sample and the sample enriched with *good jets* and *bad jets*. Jets with $f_{\texttt{TileGap3}} > 0.5$ are rejected, as indicated by the *dotted line*.

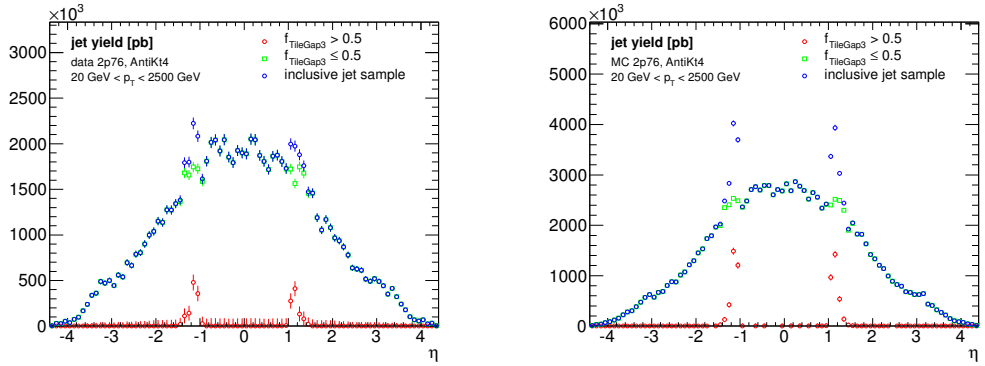

(a) data (b) Monte Carlo simulation

Figure 5.12: Normalised jet yield as function of the jet pseudo-rapidity ηusing the anti-k_t algorithm with $R = 0.4$ for (a) data and (b) Monte Carlo simulation at $\sqrt{s} = 2.76\,\text{TeV}$. The distribution is shown for the inclusive sample as well as for the subsamples with different energy fraction in the `TileGap3` layer, $f_{\texttt{TileGap3}}$.

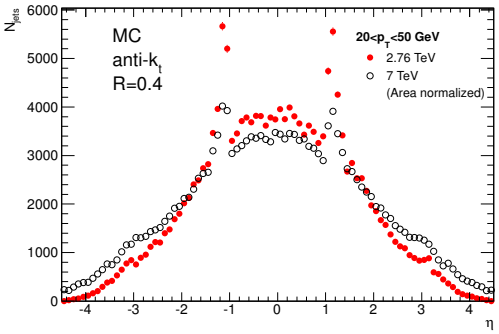

Figure 5.13: Comparison of the normalised jet yield in the Monte Carlo simulation as function of the jet pseudo-rapidity η using the anti-k_t algorithm with $R = 0.4$ at $\sqrt{s} = 2.76\,\text{TeV}$ and $\sqrt{s} = 7\,\text{TeV}$.

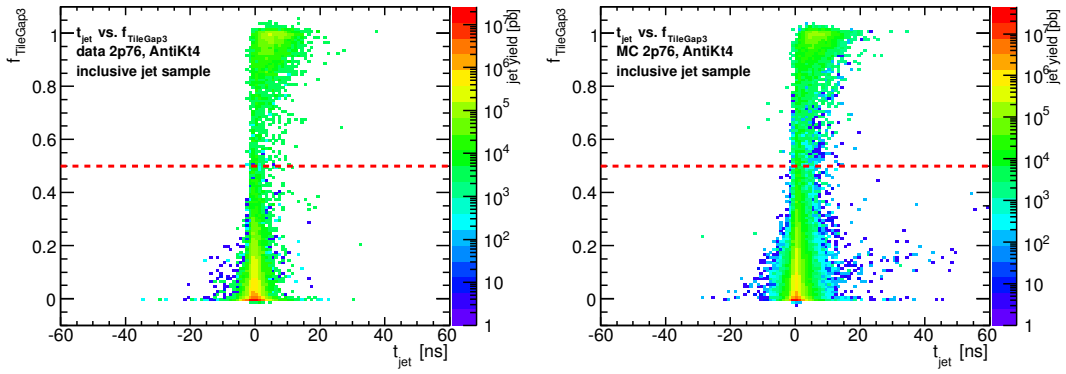

(a) data (b) Monte Carlo simulation

Figure 5.14: Timing distribution t_{jet} versus the energy fraction in the `TileGap3` layer, $f_{\texttt{TileGap3}}$, for anti-k_t jets with $R = 0.4$ (a) in data and (b) in the Monte Carlo simulation at $\sqrt{s} = 2.76\,\text{TeV}$. Jets with $f_{\texttt{TileGap3}} > 0.5$ are rejected, as indicated by the *dotted line*.

5.4.6 Jet selection efficiency

The efficiency of the jet selection is determined using a tag-and-probe technique that is based on dijet event topologies, very similar to the η-intercalibration method. The events are required to have two well-balanced back-to-back jets with $\left|p_{\text{T}}^{\text{probe}} - p_{\text{T}}^{\text{tag}}\right| / p_{\text{T}}^{\text{avg}} < 0.4$ and $\Delta\phi^{(\text{tag,probe})} > 2.6\,\text{rad}$. A more restrictive jet selection [109] compared to the criteria given in Section 5.4 are applied on the tag jet. Furthermore the tag jet is required to be in the central rapidity region, $|\eta^{tag}| < 2.0$. The efficiency is determined individually in each $(|y|, p_{\text{T}})$ bin by the ratio of probe jets passing the quality criteria and the total number of probed jets. The jet selection efficiency is determined separately for the jet selection against non-collision jets on one hand, and for jets in the transition region of the `TileGap3` scintillators on the other, since the former is applied in data only, whereas the latter is applied in both, the data and the Monte Carlo simulation. The result is shown in Figure 5.15a for the jet selection efficiency of

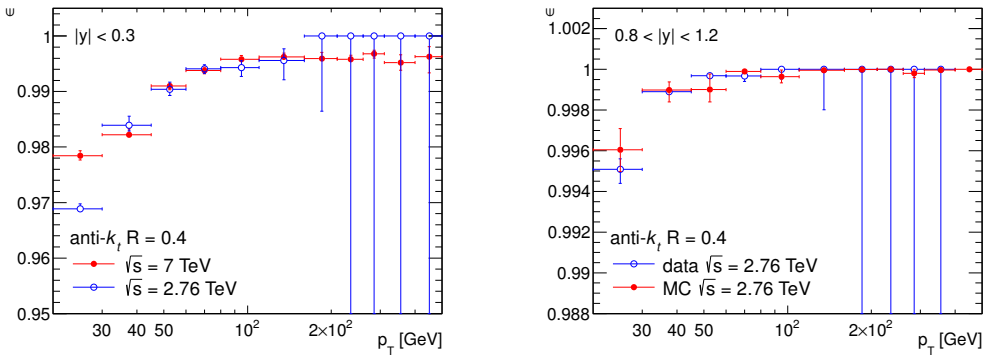

(a) (b)

Figure 5.15: Jet selection efficiency for anti-k_t jets with $R = 0.4$ for (a) non-collision jets in the dataset at $\sqrt{s} = 7\,\text{TeV}$ from 2010 and $\sqrt{s} = 2.76\,\text{TeV}$ from 2011, and for (b) jets in the transition region of the `TileGap3` scintillators at $\sqrt{s} = 2.76\,\text{TeV}$ in data and Monte Carlo simulation.

non-collision jets in the central region $|y| < 0.3$ as a function of p_{T}. For $\sqrt{s} = 7\,\mathrm{TeV}$, the efficiency is about 98% in the lowest p_{T} bin and reaches a plateau of 99.5% at about 100 GeV. In the $\sqrt{s} = 2.76\,\mathrm{TeV}$ dataset, the inefficiency in the lowest p_{T} bin is slightly larger with about 3%, but very similar otherwise. Due to the limited statistical precision of this dataset at large p_{T}, the result using the dataset at $\sqrt{s} = 7\,\mathrm{TeV}$ from 2010 is used for the jet selection efficiency correction. The statistical error is taken as the systematic uncertainty on the jet selection efficiency, but a minimal uncertainty of 0.5% is retained. The latter accounts for the differences in the determined efficiency between the two centre-of-mass energies, except for the lowest p_{T} bin where the difference is larger.

The selection efficiency for jets in the transition region of the `TileGap3` scintillators is shown in Figure 5.15b for data and simulation in the bin that is affected most, $0.8 < |y| < 1.2$. The efficiency is found to be close to 100%. The results from both datasets at $\sqrt{s} = 2.76\,\mathrm{TeV}$ and $\sqrt{s} = 7\,\mathrm{TeV}$ agree well within their uncertainties. Due to the smaller statistical uncertainty at large p_{T}, the one obtained at $\sqrt{s} = 7\,\mathrm{TeV}$ is used for the correction of the jet selection efficiency in the transition region.

CHAPTER 6

Inclusive jet cross-section at $\sqrt{s} = 7\,\text{TeV}$

The inclusive jet cross-section at a centre-of-mass energy of $\sqrt{s} = 7\,\text{TeV}$ was first measured by the ATLAS collaboration at an early stage of the data taking period in the year 2010, with a dataset corresponding to an integrated luminosity of $\mathcal{L} = 17\,\text{nb}^{-1}$ [126]. Despite the comparatively small dataset, the measurement provided a first glimpse on jet physics at the LHC, covering a kinematic region of $60\,\text{GeV} \leq p_\text{T} < 600\,\text{GeV}$ and $|y| < 2.8$. Essentially, the determination of the trigger and reconstruction efficiency, as well as the calorimeter response to jet energy performed in this first measurement laid the foundation for the jet measurements presented here. However, large improvements in the systematic and statistical uncertainties as well as a considerable extension of the kinematic reach up to $|y| < 4.4$ and $20\,\text{GeV} \leq p_\text{T} < 1500\,\text{GeV}$ are provided by the measurement of the inclusive jet cross-section at $\sqrt{s} = 7\,\text{TeV}$ using the full dataset in 2010 [2], as shown in the following chapters. The kinematic reach of the two measurements is compared in Figure 6.1.

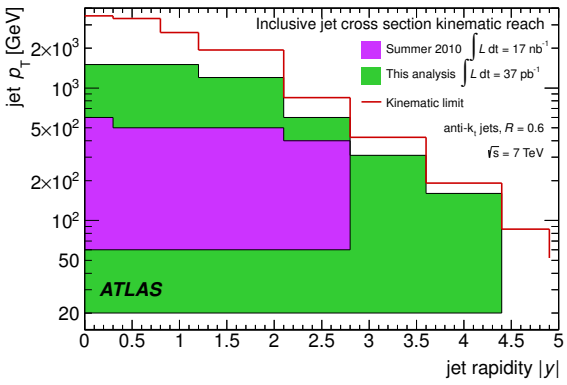

Figure 6.1: Kinematic reach of the inclusive jet cross-section measurements at $\sqrt{s} = 7\,\text{TeV}$ using datasets from 2010 corresponding to an integrated luminosity of $\mathcal{L} = 17\,\text{nb}^{-1}$ [126] and $\mathcal{L} = 37\,\text{nb}^{-1}$ [2]. The former represents a subset of the latter. Jets are reconstructed using the anti-k_t algorithm with $R = 0.6$. Also shown is the kinematic limit for collisions at a centre-of-mass energy of $\sqrt{s} = 7\,\text{TeV}$ [2].

The definition of the inclusive jet cross-section is given in Section 6.1. The theory predictions are summarised in Section 6.2. Section 6.3 deals with the data selection, including the trigger scheme, the event and jet selection, and the studies performed to guarantee the validity of the data. The unfolding method of the experimental data to particle level is explained in Section 6.4, followed by the discussion of the systematic uncertainties on the measurement in Section 6.5. The results of the measurement are presented in Section 6.6.

6.1 Cross section definition

Jets in this measurement are defined by the anti-k_t algorithm [35] with two different radius parameters, $R = 0.4$ and $R = 0.6$. Two different parameters are used because non-perturbative effects from the parton shower and underlying event are very sensitive to the radius parameter, as described in Section 2.2.3. Also, the effect of pile-up interactions in the same bunch crossing should be more pronounced with increasing radius parameter. The jet algorithm is implemented with the FastJet package [112, 113].

In order to compare to the theoretical prediction presented in Section 2.2, the inclusive jet cross-section is defined at particle level, i.e. from stable particles, where stable refer to a proper lifetime of the particles $c\tau > 10\,\text{mm}$. The definition includes muons and neutrinos from hadron decays.

The inclusive jet cross-section is obtained as a function of the jet transverse momentum p_T and the rapidity y. Jets are measured in the range $p_\text{T} \geq 20\,\text{GeV}$ and $|y| < 4.4$, limited by the availability of a jet calibration and the fiducial region of the detector. The choice of binning of the double-differential cross-section $\frac{d^2\sigma}{dp_\text{T}dy}$ is generally determined by the jet calibration. The measurement is divided in seven rapidity bins, which reflect the segmentation of the calorimeter and separate homogeneous regions from the transition between detector technologies. The binning in p_T is a compromise between a fine granularity on one hand, and the statistical uncertainty and bin migrations on the other. The bin size in $(\Delta y, \Delta p_\text{T})$ ranges from $(0.3 \times 10\,\text{GeV})$ in the low p_T central region to $(0.9 \times 200\,\text{GeV})$.

6.2 Theoretical prediction

The nominal theoretical prediction of the inclusive jet cross-section in this analysis is provided by a fixed-order perturbative QCD calculation at NLO. The Nlojet++ 4.1.2 program is employed here to generate the matrix element of the hard interaction. The factorisation and renormalisation scale are chosen per event as the maximum jet p_T in each rapidity bin, $\mu_F = \mu_R = p_\text{T}^\text{max}(y_i)$. The CT 10 PDF set is employed as baseline. Non-perturbative corrections to the theoretical prediction are derived using the Pythia event generator, as given below. Electroweak corrections were not available at the time this analysis was performed, and hence are not included in the theory predictions. A more detailed description of the perturbative QCD calculation and its uncertainties is presented in Section 2.2.

The Pythia generator is employed as the nominal Monte Carlo simulation to generate jet events in proton-proton collisions at $\sqrt{s} = 7\,\text{TeV}$. It provides the non-perturbative corrections for the NLO calculation of the matrix element, and the distribution of the final observables at particle and detector level used in the unfolding process, described in Section 6.4. Pythia 6.435 with the tune AUET 2b and the PDF set Cteq 6L1 is used for the central value of the non-perturbative correction, whereas the unfolding method utilises Pythia 6.423 with the tune AMBT 1 and the LO* PDF set MRST 2007. A full simulation of the ATLAS detector and the trigger is performed with the Geant4 toolkit. The generated events are subsequently processed with the same reconstruction and calibration chain as the data. A list the used Monte Carlo sample is given in Table A.3 in the appendix, while the details of the simulation and the uncertainties on the non-perturbative corrections are given in Section 2.

Predictions from a NLO matrix element calculation with a matched parton shower simulation are obtained using the Powheg dijet event generator interfaced to the Pythia or Herwig generators. Powheg Box 1.0 with the *cut approach* described in Section 2.4.2 is used to generate the generate the sample[1], rejecting events where $p_{\text{T, particle}}^{(1)} > 7 \cdot p_{\text{T, parton}}^{(1)}$. No optimisation for the tunes for the matched parton shower approach of Powheg has been performed. Three different configurations for the simulation of

[1] The modification of the matching scale and the `doublefsr` option only became available for the measurement at $\sqrt{s} = 2.76\,\text{TeV}$ have not been considered for the analysis at $\sqrt{s} = 7\,\text{TeV}$.

the parton shower are applied: Pythia with the tune AUET 2B; Pythia with the tune Perugia 2011; and Herwig with the tune AUET 2. The used PDF set is CT 10. Since no mechanism to efficiently vary the μ_F, μ_R, α_S, or the PDF sets exists for the Powheg formalism, only the statistical uncertainty is considered for these predictions. Alike, the prescription to assess a matching scale uncertainty is not yet fixed as described in Section 2.4.4, and no uncertainty is assigned. The configuration for the event generation with Powheg at $\sqrt{s} = 7$ TeV can be found in Appendix A.1.4.

6.3 Data selection

6.3.1 Dataset

The measurement is based on the full dataset of proton-proton collisions in 2010. The delivered integrated luminosity from the LHC amounts to $\mathcal{L}_{\text{del}} = 48.1\,\text{pb}^{-1}$ [101], of which the ATLAS experiment recorded a dataset with an integrated luminosity of $\mathcal{L}_{\text{rec}} = 45.0\,\text{pb}^{-1}$. This corresponds to a data taking efficiency of 94%. Only luminosity blocks with a good operational status of the tracking and vertex detector and the solenoid magnet, the calorimeter, the luminosity algorithms and the trigger system are employed. A list of luminosity blocks used in this analysis are given in Table A.13. The resulting total integrated luminosity of the dataset is $\mathcal{L} = 37.3 \pm 1.2\,\text{pb}^{-1}$. In ATLAS terminology, the dataset corresponds to the 2010 data taking periods A – I and includes 116 runs in the range 152166 – 167844.

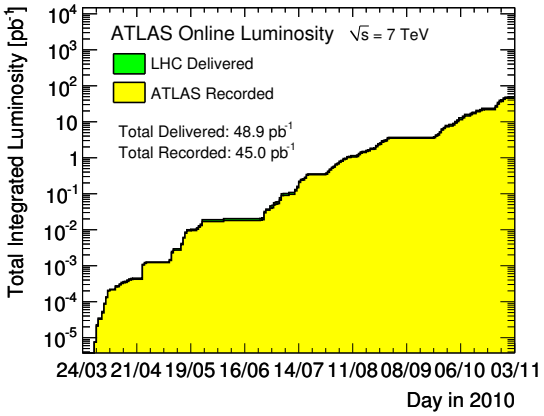

Figure 6.2: Total integrated delivered and recorded luminosity of proton-proton collision data in 2010 as function of time.

6.3.2 Trigger strategy

Two different triggers are applied to select the jet data for this analysis. A minimum bias trigger, `MBTS_1`, is used in the very early stage of the data taking[2], when dedicated jet triggers, in particular the timing, had not been commissioned yet. The `MBTS_1` requires a single hit in any of the segments of the minimum bias trigger scintillators, and thus selects inelastic proton-proton collisions with high efficiency [95]. The data sample is free of any bias, which allows to reconstruct jets down to a transverse momentum of 20 GeV. Since dedicated jet triggers at ATLAS generally only become fully efficient above 60 GeV, the `MBTS_1` trigger is utilised in general for the jet measurement in the p_{T} range within 20 GeV to 60 GeV. The upper limit is imposed due to the steeply falling p_{T} spectrum.

Above 60 GeV, single jet triggers are assigned to each ($|y|$, p_{T}) bin. Only trigger chains that are > 99% efficient in the range of the given bin are considered, and the one with the largest rate after prescale is used. In rapidity, the resulting trigger scheme is separated in five distinct regions with similar turn-on behaviour of the trigger items. Since the energy thresholds at which the available jet triggers become efficient mostly coincide with the p_{T} binning of the analysis, the latter is adopted for the trigger scheme.

[2] This data has been the basis for the first jet production measurement [126].

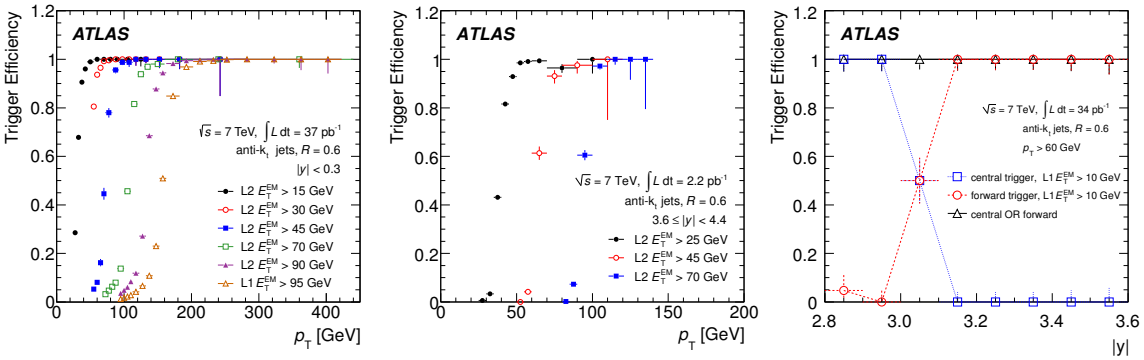

(a) $|y| < 0.3$ (b) $3.6 < |y| < 4.4$ (c) $p_T > 60\,\text{GeV}$

Figure 6.3: Trigger efficiencies for anti-k_t jets with $R = 0.6$ for various jet trigger items as function of jet p_T in the rapidity region (a) $|y| < 0.3$ and (b) $3.6 < |y| < 4.4$, and (c) as function of rapidity $|y|$ in the transition region between central and forward jet trigger items. The p_T thresholds for the trigger items are given at the electromagnetic energy scale. [2]

Trigger efficiency The inclusive definition of the trigger efficiency is used, i.e. the ratio of all jets in the events with a positive decision of a particular trigger divided by all jets in the considered events of the unbiased reference event sample. This is the most natural choice and does not require any matching between the jet that actually triggered the event and the jets entering the inclusive jet cross-section. The reference samples for the trigger efficiency determination are obtained using independent triggers or a bootstrap method. In the latter, a jet trigger with a low p_T threshold serves as reference for another jet trigger with a higher p_T threshold, i.e. in a p_T region where the efficiency of the reference trigger reached already its plateau. The trigger efficiency for the jet trigger with the lowest p_T threshold is obtained using the `MBTS_1` trigger, whereas for the higher p_T thresholds, the bootstrap method is applied. It is shown for jets with $R = 0.6$ in Figures 6.3a and 6.3b for the central rapidity bin and in the most forward bin, respectively. All utilised trigger chains reach a stable plateau. A small inefficiency in the forward jet trigger with the lowest p_T threshold due to a known problem with a dead trigger tower is observed, and a systematic uncertainty is assigned.

A special trigger strategy is required in the transition region between the barrel and the forward region at $2.8 \leq |y| < 3.6$, where the central and forward jet trigger items at Level-1 overlap, but neither of the two is 100% efficient by itself. Thus, a logical *or* among the two is applied. The corresponding trigger efficiency for $p_T \geq 60\,\text{GeV}$ as a function of the rapidity is shown in Figure 6.3c. The plateau of the central and forward triggers individually extends to $|y| < 3.0$ and $|y| > 3.2$, respectively, while in the cross-over bin in between only the combination reaches 100%.

A conservative uncertainty of 1% is applied on the trigger efficiency for all triggers to cover the minor deficits such as the problem with a dead trigger tower in the forward region mentioned above.

Trigger scheme With increasing luminosity in the course of the year 2010, prescales were introduced to limit the data rate from triggers with e.g. low p_T thresholds or the minimum bias trigger. As a consequence, the majority of jets with $p_T < 60\,\text{GeV}$ were taken in the early phase of the data taking, period A – C, where the prescales of the `MBTS_1` are moderate. Additionally, the restriction on periods A –C limits contributions from pile-up events in the same bunch crossing, as described in Section 6.3.5. Data from period A – C were not considered for jets in the region $|y| > 2.8$ and $p_T > 60\,\text{GeV}$, since the forward jet trigger was not yet fully commissioned. Jet triggers with the highest available p_T threshold

remained unprescaled throughout the whole data taking in 2010. In the early phase of the data taking, only the Level-1 trigger was active, while from period D onwards, Level-1 and Level-2 were used both. The event filter was set on pass through throughout the 2010 data taking. The complete trigger scheme is listed in Appendix A.3.

A special treatment of prescales is necessary in the transition region where central and forward triggers are combined, in order to avoid double counting in the luminosity calculation. Events are divided in three categories according to which jet trigger they pass: only the central one (ct), only the forward one (fw), or both. From Equation 3.4, the integrated luminosity in the categories are

$$\mathcal{L}^{\mathrm{ct}} = \sum_i \frac{\mathcal{L}_i}{p_i^{\mathrm{ct}}} \tag{6.1}$$

$$\mathcal{L}^{\mathrm{fw}} = \sum_i \frac{\mathcal{L}_i}{p_i^{\mathrm{fw}}} \tag{6.2}$$

$$\mathcal{L}^{\mathrm{both}} = \sum_i \mathcal{L}_i \left(\frac{1}{p_i^{\mathrm{ct}}} + \frac{1}{p_i^{\mathrm{fw}}} - \frac{1}{p_i^{\mathrm{ct}} p_i^{\mathrm{fw}}} \right) \tag{6.3}$$

$\mathcal{L}^j$ is the total luminosity in the category $j = [ct, fw, both]$, and $\mathcal{L}_i$ the luminosity in the luminosity block i. p_i denotes the prescale of the probed trigger. The cross-section from this trigger combination is obtained using

$$\sigma = \frac{N^{\mathrm{ct}}}{\mathcal{L}^{\mathrm{ct}}} + \frac{N^{\mathrm{fw}}}{\mathcal{L}^{\mathrm{fw}}} + \frac{N^{\mathrm{both}}}{\mathcal{L}^{\mathrm{both}}} = \frac{N^{\mathrm{ct}} + N^{\mathrm{fw}} + N^{\mathrm{both}}}{\mathcal{L}_{\mathrm{eff}}}. \tag{6.4}$$

N^j denotes the number of events in each category j, and $\mathcal{L}_{\mathrm{eff}}$ is the effective luminosity in case a single trigger had been applied. This approach is equivalent to the method described in [127], which uses event weights instead of an effective luminosity.

The total integrated luminosity after the trigger selection in each (y, p_{T}) bin used in the measurement at $\sqrt{s} = 7\,\mathrm{TeV}$ is shown in Figure 6.4. At high p_{T} where unprescaled triggers can be applied, the full luminosity of $\mathcal{L} = 37\,\mathrm{pb}^{-1}$ is used. At small p_{T}, the integrated luminosity amounts to approximately $730\,\mathrm{nb}^{-1}$; nevertheless, the statistical uncertainty in this region is in the order of $1 - 3\%$.

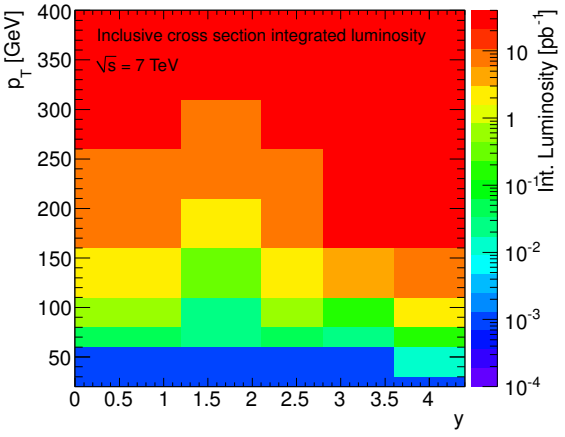

Figure 6.4: Total integrated luminosity after the trigger selection in each (y, p_{T}) bin of the inclusive jet cross-section measurement at $\sqrt{s} = 7\,\mathrm{TeV}$.

6.3.3 Event selection

In order to select proper proton-proton collisions, each event is required to have at least one well-reconstructed vertex, defined by having at least five associated tracks of charged particles each with a minimum p_{T} of 150 MeV [84]. No explicit requirement is imposed on the z-position of the vertex with respect to the beam spot.

6.3.4 Jet selection

Jets are considered in the kinematic region of $p_{\mathrm{T}} > 20\,\mathrm{GeV}$ and $|y| < 4.4$. The reconstruction and calibration is performed using the *EM+JES* scheme, as described in Sections 5.1 and 5.2, including the

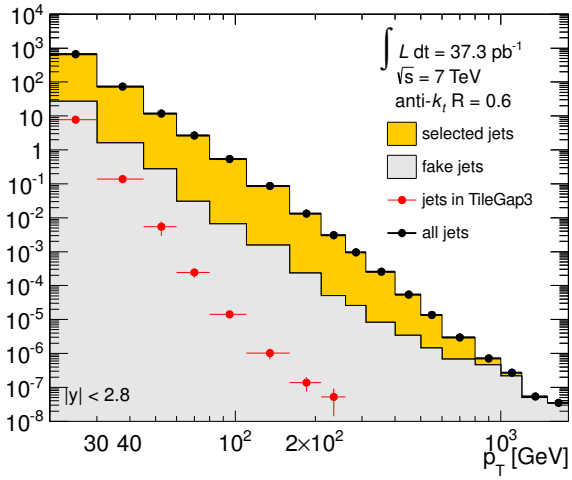

Figure 6.5: Normalised jet yield of anti-k_t jets with $R = 0.6$ in the dataset of 2010 at $\sqrt{s} = 7\,\text{TeV}$ as function of p_T. The distribution is shown separately for all jets, jets with a large energy fraction in the transition between barrel and extended barrel in the Tile calorimeter, `TileGap3`, fake jets from non-collisions and jets selected for the analysis.

jet origin and pile-up corrections. Each jet has to pass a trigger as defined for the according ($|y|$, p_T) bin, as well as the quality selection criteria given in Section 5.4 to reject fake jets reconstructed from non-collisions, such as detector noise, cosmic rays or beam-induced background. Mismeasured jets in the poorly instrumented region in the transition between the barrel and extended barrel in the Tile calorimeter are not rejected explicitly, but a substantial number of these jets are removed by the timing cut of the quality criteria. Hence, their fraction is on the sub-percent level and the impact on the data is negligible. A correction for the efficiency of the jet selection is applied. In total, 2.7 mio jets with $R = 0.6$ are present in the data sample after the trigger selection, of which 98.4% pass the jet selection criteria, as shown in Figure 6.5. The fraction of fake jets is increasing towards large p_T and becomes dominant at around $1 \times 10^3\,\text{GeV}$. The same observation can be made in the tail of the E_T^missdistribution [122]. Events with $E_\text{T}^\text{miss} > 500\,\text{GeV}$ without any presence of fake jets have been inspected visually and generally found to be proper collision events, in which low p_T jets and muons escape the detector at low azimuthal angle θ.

6.3.5 Stability studies

Vertex position The impact of deviations of the collision vertex position from the nominal beam spot on the inclusive jet cross-section measurement is investigated to exclude effects on the energy measurement for particles entering the calorimeter from a displaced collision vertex. The data sample is divided into three subsets according to the z coordinate of the collision vertex with the largest momentum sum of all associated tracks, $\sum p_\text{T}^2$. 89.9% of the events have $|z| < 100\,\text{mm}$, 10.1% have $100\,\text{mm} \leq |z| < 200\,\text{mm}$, and 0.1% have $|z| > 200\,\text{mm}$. The subsets are compared to the full data sample in Figure 6.6a. Events with $100\,\text{mm} \leq |z| < 200\,\text{mm}$ show deviations from the full dataset mostly below 10%, with exception of a few bins. Since the number of events in the sample is small compared to the full sample, the resulting bias is below 1%. Similarly, the discrepancies in the sample with $|z| > 200\,\text{mm}$ only introduce negligible bias.

Deviations in the $x - y$ plane are small, $RMS_{PV}^{x-y} < 50\,\mu\text{m}$, and can be neglected. The four-momenta of the jets are corrected for the actual reconstructed vertex position, as described in Section 5.2.2.

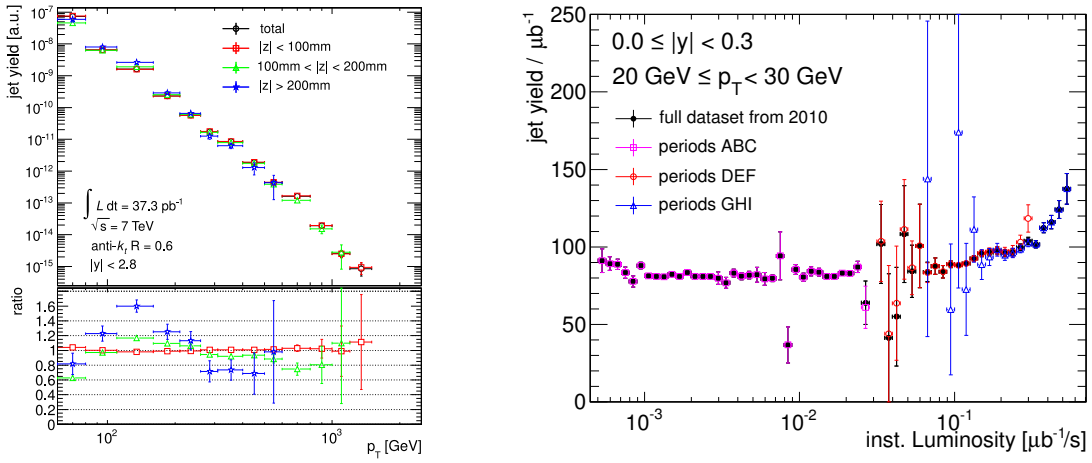

(a) (b)

Figure 6.6: Stability studies for anti-k_t jets with $R = 0.6$ at $\sqrt{s} = 7\,\text{TeV}$: (a) comparison of jet yields for different displacements of the vertex position along the z axis in the central rapidity $|y| < 2.8$ with respect to the full dataset (b) normalised jet yield in the bin $p_\text{T} < 30\,\text{GeV}$, $|y| < 0.3$ as a function of the instantaneous luminosity for different periods of data taking and the full dataset from 2010.

Jet yield To detect potential problems during the data taking, the jet yield is monitored over time in each ($|y|$, p_T) bin. A stable jet yield is found for $p_\text{T} \geq 30\,\text{GeV}$ across all runs, in particular no increase with the higher pile-up conditions towards the end of the data taking. Such an effect is, however, observed below 30 GeV in the central region, where the jet yield increases by up to 30% over time. The effect vanishes in the forward region. The normalised jet yield in the bin $20\,\text{GeV} \leq p_\text{T} < 30\,\text{GeV}$, $|y| < 0.3$ as a function of the instantaneous luminosity is shown in Figure 6.6b. Above $0.1\,\mu\text{b}^{-1}/\text{s}$, a clear rise is visible, indicating that the offset correction in the energy calibration does not fully account for the pile-up contributions. For comparison, an increase of 30% at 20 GeV corresponds to an additional jet energy of about 1.2 GeV. To avoid a bias in this region of phase space, only periods A – C are considered for $20\,\text{GeV} \leq p_\text{T} < 60\,\text{GeV}$, $|y| < 3.6$. In the most forward region $3.6 \leq |y| < 4.4$, where the jet yield is perfectly constant, also data from the later periods is used. Auxiliary material showing the jet yield as a function of the luminosity plot are presented in Appendix A.3.1.

6.4 Unfolding

Although effects on the jet measurement from e.g. energy loss in dead material, non-compensation of the calorimeter, or out-of-cone depositions are taken into account by the jet calibration procedure, there are other analysis-specific effects that have to be corrected for to obtain a particle-level cross-section. The dominant ones in this analysis are resolution effects, which can cause bin migrations in rapidity and transverse momentum, and detector inefficiencies. To obtain the particle-level cross-section from the detector-level distributions, a so-called *unfolding* is performed. Several methods to perform the unfolding are available [128–131]. The method applied in this analysis is the *iterative, dynamically stabilised* (IDS) unfolding [131], which pursues a Bayesian approach and is based on a multidimensional unfolding method [128]. The description given here is similar to the one in the multidimensional unfolding method.

6.4.1 Introduction

The most obvious approach to perform an unfolding is a bin-by-bin correction using the Monte Carlo simulation, building the ratio of jets at particle level and jets at detector level for each bin in the simulation, and applying this to the measured number of jets in data. However, a bin-by-bin correction does not take into account bin migrations and hence only yields good results if the simulation describes the data very well, or if migrations are small, e.g. by means of a large bin size. Furthermore, a bin-by-bin unfolding does not allow for the correlations of bins, which is necessary to correctly evaluate the uncertainties.

Bin migrations and correlations can be included in the unfolding using a matrix approach. It is based on a matrix which maps the particle-level distribution to the one at detector-level and is constructed using the information from the simulation about the propagation of the jets at particle level to the detector level, where they are observed. Then the direct approach to perform the unfolding of the data distribution is the matrix inversion. However, this matrix can be singular, so its inversion is not trivial in general. This can be easily understood with a simple example. Assuming a measurement of an observable in two bins, and a detector resolution of 50% for each bin, an event at particle level has a 50% chance to be measured at detector level in one bin or the other. A corresponding folding matrix P reflecting this resolution in a probability formulation is $(P_{ij}) = \left(\begin{smallmatrix} 0.5 & 0.5 \\ 0.5 & 0.5 \end{smallmatrix}\right)$, where i, j are the bin indices at particle and detector level, respectively. This matrix obviously is degenerate.

This particular example also illustrates why the unfolding matrix $\tilde{P}$ is not unambiguous from a probabilistic point of view. Given a flat distribution at detector level $\vec{d}$, it is not possible to draw conclusions on the particle-level distribution $\vec{p}$ just from the information of the detector resolution. Both bins have the same migration probabilities, and in the extreme case all events in the detector-level distribution can originate from just one particle-level bin:

$$\vec{p} \cdot \tilde{P} = \vec{d} \qquad \Rightarrow \begin{pmatrix} n & 0 \end{pmatrix} \cdot \begin{pmatrix} 0.5 & 0.5 \\ 0.5 & 0.5 \end{pmatrix} = \begin{pmatrix} 0.5n \\ 0.5n \end{pmatrix} \tag{6.5}$$

$$\vec{p'} \cdot \tilde{P} = \vec{d'} \qquad \Rightarrow \begin{pmatrix} 0 & n \end{pmatrix} \cdot \begin{pmatrix} 0.5 & 0.5 \\ 0.5 & 0.5 \end{pmatrix} = \begin{pmatrix} 0.5n \\ 0.5n \end{pmatrix} \tag{6.6}$$

Both equations result in the same detector-level distributions, $\vec{d} = \vec{d'}$. This ambiguity of the folding process can only be resolved in the unfolding with additional information about the true particle-level distribution. The unfolding matrix $\tilde{P}$ thus depends on the accuracy of the physics description in the Monte Carlo simulation, whereas the folding matrix is well-defined on basis of the detector resolution exclusively.

Among the available methods to overcome the matrix inversion and construct a unfolding matrix with the information of the particle-level distribution, the IDS unfolding has the advantage that it includes a comparison of the Monte Carlo simulation with the data distribution. This iteratively improves the agreement between the two and hence provides a more accurate unfolding result.

To perform the unfolding, some prerequisites are necessary, which are given in the following. The derivation of the unfolding matrix, which represents the most essential component in this procedure is explained hereafter.

6.4.2 Procedure

Since the true particle-level cross-section cannot be measured, the Monte Carlo simulation described in Section 2.1 is used to relate particle-level to detector-level. It is done by means of a transfer matrix

A with the entries A_{ij}, which allocates the jets in bin i at particle level to the jets in bin j at detector level using a matching in y-p_{T} space. Only unambiguous one-to-one combinations to the closest jet that fulfil the matching radius requirement, $\Delta r \leq 0.3$, are considered. The transfer matrix employs the same binning as the measurement to account for bin migrations. Since migrations are large only across p_{T} bins, a separate transfer matrix is used in each $|y|$ bin, and i, j in A_{ij} correspond only to the p_{T} bin at particle and detector level, respectively.

To account for unmatched jets, a matching efficiency is determined by taking the ratio of the p_{T} spectra of matched jets and all jets, at both detector level and particle level. Subsequently, ϵ_j^{det} denotes the matching efficiency in the p_{T} bin j at detector level to find a corresponding jet at particle level, and ϵ_i^{part} vice versa.

The unfolding is performed as three-step procedure. First, the detector-level matching inefficiency ϵ_j^{det} is applied to the p_{T} spectrum in data. Hence, this detector-level distribution can be related to the particle-level one using the unfolding matrix $\tilde{P}_{ij}$, which is derived on the basis of the transfer matrix A_{ij}, using the iterative, stabilised unfolding method (IDS) [131], as described below. In the third step, the resulting unfolded data spectrum at particle-level is corrected for the particle-level matching efficiency ϵ_i^{part}. Thus the unfolded result can be written as

$$N_i^{part} = \sum_j N_j^{det} \cdot \epsilon_j^{det} \tilde{P}_{ij} / \epsilon_i^{part}. \tag{6.7}$$

Here, N_k^{part} and N_k^{det} denote the number of jets in the p_{T} bin k, and i and j are the indices of the p_{T} bin at particle level and detector level, respectively.

6.4.3 Derivation of the unfolding matrix

Two matrices are employed in the IDS method: a folding matrix P with the entries P_{ij}, which gives the probability for a jet at particle level in the p_{T}^{part} bin i to originate from a jet at detector level in the p_{T}^{det} bin j; and an unfolding matrix $\tilde{P}$ with the entries $\tilde{P}_{ij}$, which gives the probability for a jet at detector level in the p_{T}^{det} bin j to originate from a jet at particle level in the p_{T}^{part} bin i. Both are derived from the transfer matrix A as follows:

$$P_{ij} = \frac{A_{ij}}{\sum_k A_{kj}} \tag{6.8}$$

$$\tilde{P}_{ij} = \frac{A_{ij}}{\sum_k A_{ik}} \tag{6.9}$$

Thus, P_{ij} and $\tilde{P}_{ij}$ are composed of the normalised rows and columns of A_{ij}, respectively, in order to provide a well-defined total probability of 1 for each jet at particle level to be reconstructed in a bin j at detector level, and vice versa. This approach to construct the folding and unfolding matrix is straightforward and avoids the problem of the matrix inversion.

As described above, the folding matrix just requires the correct simulation of the migrations due to detector resolution. The unfolding matrix however also depends on the accuracy of the physics description. Therefore, the shape of the particle-level distribution in the Monte Carlo simulation is improved iteratively as follows. First, the measured distribution in data is unfolded to allow to compare the data and Monte Carlo sample at particle-level. This unfolding is performed using the initial unfolding matrix $\tilde{P}$ as constructed from the transfer matrix and hence still includes the potential deficits in the simulation. Nevertheless, given that the description of the data by the Monte Carlo simulation is good in general, this initial step already represents the main correction of the data. Subsequently the Monte Carlo simu-

lation is improved by reweighting the particle-level distribution according to the unfolded data. In order to obtain a self-consistent sample, the reweighted particle-level spectrum is propagated to the detector level using the unmodified folding matrix P from Equation 6.8. From this improved sample a new unfolding matrix $\tilde{P}'$ is constructed. The folding matrix P is never modified in this process, since it only relies on the description of the detector resolution.

This procedure is repeated until the difference of the unfolded data and the yet improved particle-level distribution becomes sufficiently small. For the present Monte Carlo samples, this is achieved after one iteration.

6.4.4 Uncertainty on the unfolding method

Three aspects of the unfolding method are investigated to determine its uncertainty: a data-driven closure test in which the self-consistency of the method is studied; the dependence of the unfolding on the matching procedure; the impact of statistical uncertainties of the simulation and the data spectrum. Additionally, the performance of the IDS unfolding is compared to alternative unfolding methods.

The data-driven closure test is based on the nominal Monte Carlo simulation, which is reweighted such that the agreement of its detector-level distribution with the one observed in data is improved. To obtain a self-consistent sample, the reweighting is performed at particle level, while the comparison to data is performed after convoluting the particle-level spectrum with the original folding matrix. This way, only the information about detector effects in the folding process enters the reweighted distribution, while no assumption on the true particle-level spectrum is made. Subsequently, the unfolding of this modified detector-level distribution is performed on basis of a new unfolding matrix, derived using the same IDS unfolding procedure as described above with the nominal Monte Carlo sample. The difference between the unfolded modified detector-level distribution and the particle-level distribution in the modified Monte Carlo sample is considered as the bias of the unfolding method.

To estimate the uncertainty due the matching efficiency, the matching radius Δr is varied within 0.2 and 0.4, and a new transfer matrix is derived. The difference in the newly unfolded particle-level spectrum with respect to the original one is taken as the systematic uncertainty on the matching procedure.

Finally, the impact of the statistical uncertainty in the transfer matrix due to the limited number of events in the Monte Carlo sample, and of the statistical uncertainty in the particle-level distribution in data on the unfolding procedure are assessed. The uncertainty on the transfer matrix is studied generating an ensemble of transfer matrices using a large number of pseudo-experiments where the entries are varied within their statistical uncertainty. Subsequently, the unfolding is repeated for each of these transfer matrices, and the differences in the final spectrum are attributed to the statistical uncertainty. The statistical uncertainty of the data spectrum is attained with pseudo-experiments, varying the spectrum in compliance with its correlations, and repeating the unfolding, as before.

The uncertainty from the closure test, the matching studies and statistical uncertainties are found to be on the per mill level, apart from a few bins in the high-p_{T} forward region, where it reaches $1-2\%$. In comparison to other sources of uncertainty described in the next section, this is negligible. Additionally, the results from the IDS unfolding method is also compared to the ones from a bin-by-bin unfolding and an unfolding based on *singular value decomposition* (SVD) [130], using the same data-driven closure test. In comparison to the IDS and SVD methods, the bin-by-bin unfolding relies much stronger on the correct description of the jet spectrum by the simulation. Accordingly, a good result is only obtained when the Monte Carlo simulation is reweighted from a LO to a NLO PDF following the procedure described in Section 2.3. However, after reweighting the determined bias is of a similar size than that of the IDS unfolding. The SVD method on the other hand yields a larger bias.

6.5 Systematic uncertainties

The experimental systematic uncertainties consist of the uncertainties in the jet measurement presented in Section 5 and the analysis-specific uncertainties on the components described above. Altogether, it comprises 21 different sources, namely the jet reconstruction (Section 5.1.3), the jet energy measurement which contributes with 14 different components (Section 5.2.4), the jet selection efficiency (Section 5.4.6), the trigger efficiency (Section 6.3.2), the resolution of the jet energy and angular measurement (Section 5.3), the unfolding including the matching efficiency (Section 6.4.4), and the luminosity (Section 4.5)

6.5.1 Uncertainty propagation

The Monte Carlo simulation is used to evaluate the impact of the different sources of systematic uncertainty on the cross-section because it provides a larger number of events and thus a smaller statistical uncertainty than the data. This is justified by the generally good description of the detector-level distributions and by the fact that the obtained relative size of the uncertainty after the unfolding depends only to a small degree on the detector-level distribution.

All uncertainty components, excluding the unfolding and luminosity, are derived for the observable at detector level, i.e. the measurement of a jet. Consequently, the uncertainty on the jet measurement has to be translated to the particle level to restore the bin migrations due to the finite detector resolution. Hence, the uncertainty due to the jet reconstruction, the jet energy scale components, the jet selection and the trigger efficiency are propagated through the unfolding. For each component, the measured spectrum is varied separately by its one-sigma-uncertainty in positive and negative direction, and the unfolded result is compared with the unfolded result of the nominal spectrum. The obtained difference is assigned as the uncertainty of the particular component on the inclusive jet cross-section.

For jet reconstruction, the jet energy scale components, the jet selection and trigger efficiency, the nominal unfolding matrix is used. The situation is different for the jet energy and angular resolution. Their uncertainty does not affect the final distributions directly, but through the unfolding, which relies on the accurate description of the detector effects in the simulation. Hence, to estimate the uncertainty due to mismodelling of the resolution, the reconstructed jets at detector levels are smeared such that the obtained resolution is increased by one standard deviation of its corresponding uncertainty. Subsequently, a new unfolding matrix is derived, and the nominal detector-level distribution is unfolded with the modified unfolding matrix. The difference of the obtained particle-level distribution to the nominal one is taken as the uncertainty.

All experimental uncertainties are added in quadrature at the particle level. Exception is the uncertainty due to the luminosity, since it is an overall scale factor on the cross-section measurement, which was determined completely independent from this analysis, as described in Section 4.5. Thus it is not included in the systematic uncertainties on the measurement, but kept as separate source of uncertainty in the graphical representations below.

6.5.2 Correlations of the systematic uncertainties

Beyond the per-bin uncertainty described above, the correlation across different bins is important for further studies on basis of the inclusive jet data. In particular for the fits of the parton density functions of the proton (PDF), the information about the correlation can provide more flexibility in the fit, as well as allow for stronger constraints, depending on the type of the correlation.

Among the 21 uncorrelated sources of uncertainty, the correlations in p_T and $|y|$ have been studied. As a basic principle, either no or full correlation is assigned. Although this can potentially lead to overly aggressive or conservative estimates of the correlation, it is justified by the fact that an exact quantification often is not available.

Full correlation in p_T is assumed for most of the uncertainty sources. This can be seen e.g. for the dead material correction, where an under- or overestimation is expected to affect the jet energy measurement in each bin of p_T to an equal amount. In bins of the rapidity, on the other hand, the level of correlation should be small due to the inhomogeneous layout of the detector. Therefore, most of the uncertainty sources are treated as uncorrelated, with exception of the two rapidity bins from $|y| < 0.3$ and $0.3 \leq |y| < 0.8$ in the barrel region. Here the calorimeter in fact is homogeneous, and full correlation is assumed in general. Another example, which is fully correlated along the rapidity, is the uncertainty due to the η-intercalibration, since it is entirely based on the measurement in the barrel region, and any uncertainty there translates into the forward regions similarly.

Three sources are assumed to be uncorrelated in $|y|$ and p_T: the pile-up uncertainty, since the running conditions during the data taking period have been highly volatile, and pile-up effects can be both underestimated and overestimated in different p_T and rapidity regions; the trigger efficiency, since different trigger items from independent trigger systems are employed in each bin; the jet selection, which depends on different effects at low and high p_T, such as noisy cells or noise bursts.

The integrated total luminosity as an overall scale factor on the cross-section measurement. Therefore it is fully correlated in $|y|$ and p_T.

In total, the bin-by-bin correlations in the jet measurement over the full phase space are described by 87 independent sources of uncertainty, with another 3 individual sources for which each bin in the measurement is treated as uncorrelated. All sources are listed in Table 5.1, where a consecutive index is assigned to number each source. Bins with the same indices are treated as fully correlated.

The same numbering is used when the information about the correlation is exploited in fits. A *nuisance parameter* is identified with each source, and the sources are then varied independently within the individual uncertainties such that a good agreement of the data and the fit model is obtained.

6.5.3 Summary of systematic uncertainties

The total experimental systematic uncertainty is shown in Figure 6.7 as a function of p_T for three representative bins in rapidity, with the most significant contributions indicated. For $|y| < 0.3$, the total uncertainty reaches $\pm 10\%$ in the intermediate region around $p_\text{T} = 100\,\text{GeV}$, and rises to about $\pm 30\%$ at both low and high p_T. In general, the obtained uncertainty is very similar in each bin of rapidity up to $|y| < 2.1$ and then increases by a factor of $2 - 3$ towards the very forward bin.

Both, absolute size and shape of the total systematic uncertainty, are almost entirely driven by the jet energy measurement, namely by the scale uncertainty and the resolution of the jet energy. Due to the very steeply falling p_T spectrum of the inclusive jet cross-section, already moderate uncertainties translate to very large uncertainties on the final spectrum. Thus, although the JES uncertainty in the intermediate p_T region of the barrel amounts to just above 2%, the resulting uncertainty in the final observable is about five times higher. For the same reason, the contribution from the JER amounts to almost 20% in the lowest p_T bin in the forward region, albeit the fraction is still small in comparison to the by far dominating JES contribution. All other components together stay below 3% across basically the entire phase space, and thus only have very small impact on the final result.

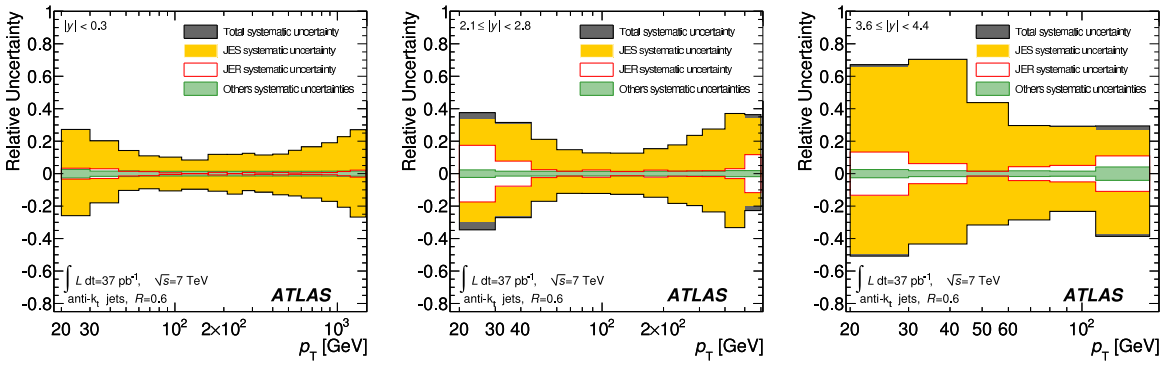

(a) $|y| < 0.3$ (b) $2.1 < |y| < 2.8$ (c) $3.6 < |y| < 4.4$

Figure 6.7: Total systematic uncertainties in the measurement of the inclusive jet cross-section at $\sqrt{s} = 7\,\text{TeV}$ for anti-k_t jets with $R = 0.6$ in representative rapidity regions. The contributions from the jet energy scale, the jet energy resolution and other sources are shown separately. The uncertainty due to the luminosity is not shown. [2]

6.6 Results and discussion

The result of the measurement is presented in Figures 6.8 and 6.9. They show the double-differential inclusive jet cross-section at $\sqrt{s} = 7\,\text{TeV}$ for anti-k_t jets with a radius parameter of $R = 0.4$ and $R = 0.6$, respectively, as a function of p_T in seven different ranges of rapidity. The measurement probes a very large kinematic region, ranging from 20 GeV to about 1500 GeV in p_T and $|y| < 4.4$. The dataset corresponds to an integrated luminosity of $\mathcal{L} = 37.3 \pm 1.2\,\text{pb}^{-1}$ and was recorded in the year 2010. It is compared to predictions from a perturbative QCD calculation at NLO, to which corrections for non-perturbative effects are applied. NLOJET++ is used with CT 10 as the nominal PDF set, and PYTHIA with the AUET 2B tune and the CTEQ 6L1 PDF set for the simulation of non-perturbative effects, as described in Section 6.2. In general, a good agreement is observed between the theoretical prediction and the data over up to 10 orders of magnitude in the central rapidity region, and six orders in the most forward rapidity bin. A detailed comparison of the data with predictions employing several different PDF sets can be found in Figures 6.10 and 6.11, showing the ratio of data with respect to the theoretical prediction using the CT 10 PDF set, separately for jets with $R = 0.4$ and $R = 0.6$. The uncertainties of data and theory are of similar size. Only in the forward rapidity regions, the experimental uncertainties dominate at low p_T, while the theoretical uncertainties are larger at high p_T for the nominal prediction. No significant differences between data and theory is observed in any of the bins.

However, the normalisation turns out to be different between jets with $R = 0.4$ and $R = 0.6$. A much better agreement of the central values is obtained for $R = 0.6$. For $R = 0.4$, the curve of the theory prediction is above the data points across the whole phase space by $10 - 20\%$. As such, the ratio for $R = 0.6$ is constantly closer to unity than the one at $R = 0.4$. A different level of agreement between data and theory for two jet radii indicates a problem with the non-perturbative corrections. In this particular case, however, a considerable difference is also found at large p_T, where the corrections from the parton shower are generally small and well tuned. Since the theoretical framework behind the NLO calculation of the hard matrix element itself is solid, the different normalisation most likely originates from contribution to the jet from initial state radiation of the underlying event. This problem can not be resolved by the present measurement, but requires dedicated studies of the jet cross-section as a function of the radius parameter R, which are planned for the future at ATLAS. Despite the differences in the

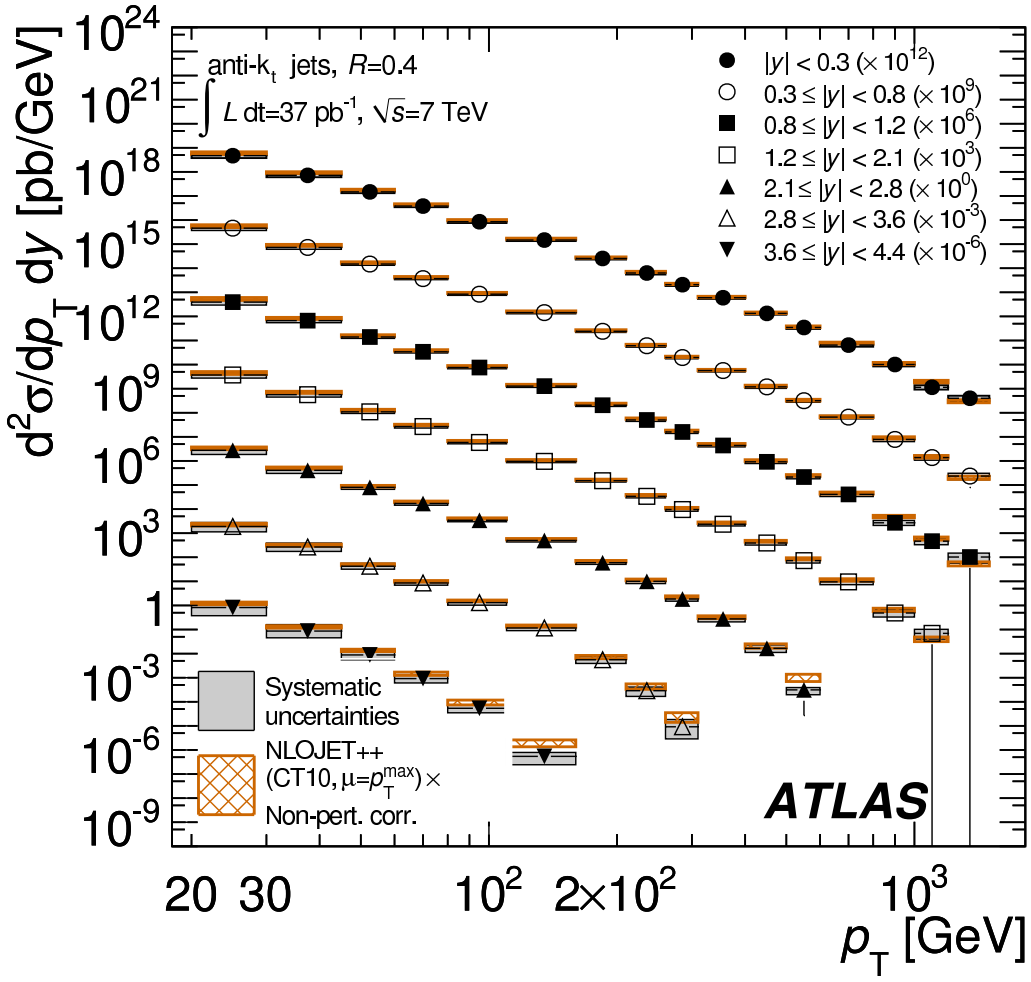

Figure 6.8: Double-differential inclusive jet cross-section at $\sqrt{s}$ = 7 TeV for anti-k_t jets with a radius parameter of R = 0.4 as a function of p_T in seven different ranges of rapidity. The dataset corresponds to an integrated luminosity of $\mathcal{L}$ = 37.3 ± 1.2 pb^{-1}, recorded in the year 2010. The systematic uncertainties on the measurement are indicated with the *shaded area*. The data are compared to predictions from a perturbative QCD calculation at NLO precision using NLOJET++ with CT 10. Corrections of the prediction for non-perturbative effects are obtained using PYTHIA with the AUET 2B tune and the CTEQ 6L1 PDF set. The uncertainty on the theoretical prediction is shown by the *hatched area*. The uncertainty due to the luminosity measurement of 3.4% is not shown. For a better visibility, the cross-section is multiplied with a factor in each rapidity range, as indicated in the legend [2].

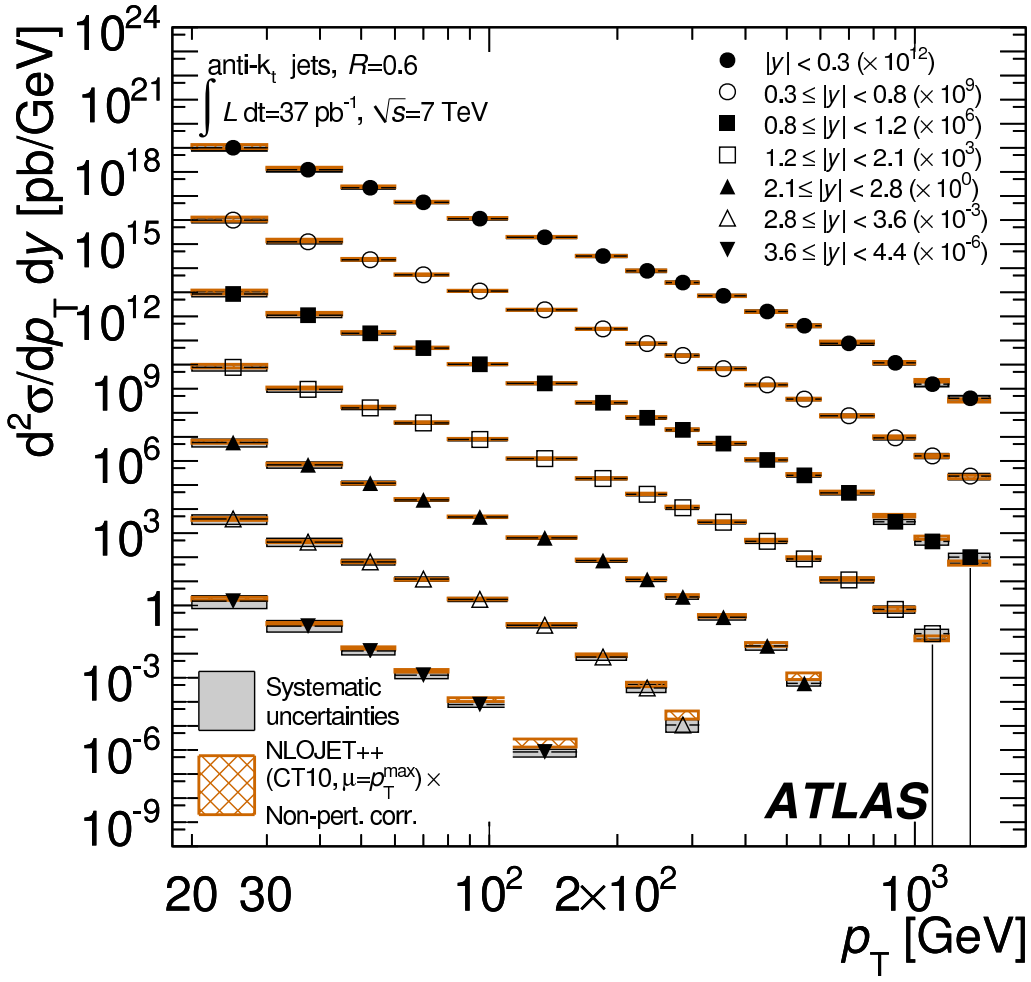

Figure 6.9: Double-differential inclusive jet cross-section at $\sqrt{s} = 7\,\text{TeV}$ for anti-k_t jets with a radius parameter of $R = 0.6$ as a function of p_T in seven different ranges of rapidity. The dataset corresponds to an integrated luminosity of $\mathcal{L} = 37.3 \pm 1.2\,\text{pb}^{-1}$, recorded in the year 2010. The systematic uncertainties on the measurement are indicated with the *shaded area*. The data are compared to predictions from a perturbative QCD calculation at NLO precision using NLOJET++ with CT 10. Corrections of the prediction for non-perturbative effects are obtained using PYTHIA with the AUET 2B tune and the CTEQ 6L1 PDF set. The uncertainty on the theoretical prediction is shown by the *hatched area*. The uncertainty due to the luminosity measurement of 3.4% is not shown. For a better visibility, the cross-section is multiplied with a factor in each rapidity range, as indicated in the legend [2].

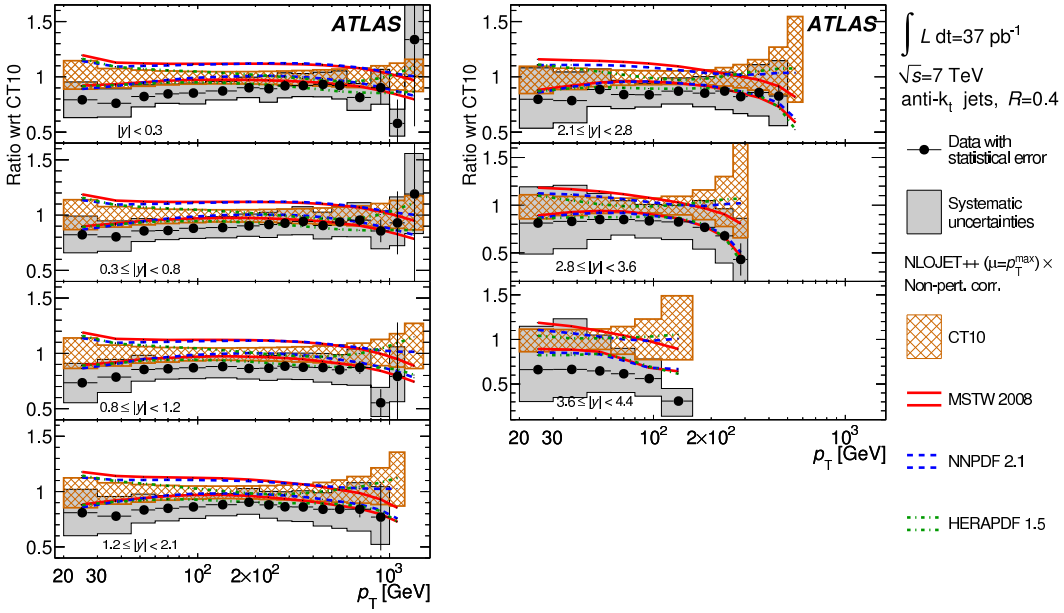

Figure 6.10: Ratio of the measured double-differential inclusive jet cross-section at $\sqrt{s} = 7\,\text{TeV}$ for anti-k_t jets with a radius parameter of $R = 0.4$ with respect to the theoretical predictions from a perturbative QCD calculation at NLO precision using NLOJET++ with the CT 10 PDF set, corrected for non-perturbative effects. The ratio is shown as function of p_T separately for seven different bins of rapidity. The *shaded* and *hatched area* indicate the experimental and theoretical systematic uncertainties, respectively. The figure also shows same theoretical calculation for a selection of different PDF sets, namely MSTW 2008, NNPDF 2.1, and HERAPDF 1.5. Statistically insignificant data points at large p_T are omitted. The uncertainty due to the luminosity measurement of 3.4% is not shown [2].

normalisation, the shape of the ratio is very similar for $R = 0.4$ and $R = 0.6$, and all of the following observations apply to the measurements with both radius parameters alike.

Two regions show larger deviations of the central values of theory and data. In the central rapidity region, the theory predictions has a trend to larger values for the cross-sections towards low p_T. The dominant uncertainty on the matrix element calculation in this region is the scale choice, and a smaller value for μ_R could accommodate such a behaviour. However, within the uncertainty the theory prediction is in agreement with the data and apart from the better agreement of the central values, there is no justification for a different choice. The uncertainty on the data on the other hand has many different components of similar size in this region, and it is difficult to disentangle which one could be responsible for the difference.

A small peculiarity can be noticed in the rapidity range $0.8 < |y| < 1.2$, where the lowest p_T bin is below the second lowest p_T bin, in contrast to the other rapidity regions. This observation is most likely due to jets in the transition region between barrel and extended barrel in the Tile calorimeter in the Monte Carlo simulation, as described in Section 5.4.5. While the impact of this category of jets has been found to be negligible in data, it is considerable in the simulation and enters the measurement through the unfolding process. It leads to a shift by 13% in the bin $20\,\text{GeV} \leq p_\text{T} < 30\,\text{GeV}$ for $R = 0.4$, and 10%

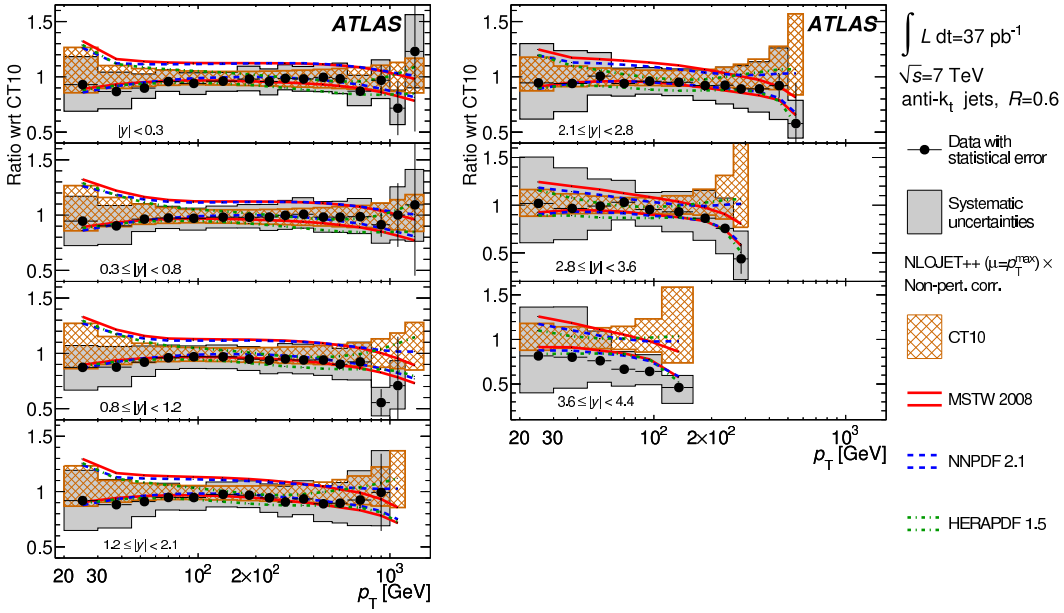

Figure 6.11: Ratio of the measured double-differential inclusive jet cross-section at $\sqrt{s} = 7\,\text{TeV}$ for anti-k_t jets with a radius parameter of $R = 0.6$ with respect to the theoretical predictions from a perturbative QCD calculation at NLO precision using NLOJET++ with the CT 10 PDF set, corrected for non-perturbative effects. The ratio is shown as function of p_T separately for seven different bins of rapidity. The *shaded* and *hatched area* indicate the experimental and theoretical systematic uncertainties, respectively. The figure also shows same theoretical calculation for a selection of different PDF sets, namely MSTW 2008, NNPDF 2.1, and HERAPDF 1.5. Statistically insignificant data points at large p_T are omitted. The uncertainty due to the luminosity measurement of 3.4% is not shown [2].

for $R = 0.6$, respectively[3]. This effect was only discovered in the course of the analysis of the inclusive jet cross-section at $\sqrt{s} = 2.76\,\text{TeV}$ [1] and is therefore not incorporated in the result presented here. A bias of this size is not covered by the uncertainty on the jet selection efficiency, which should in principle account for such an effect. Yet in total the systematic uncertainty was chosen very conservatively, so that a shift of 13% is well covered. It is nonetheless corrected for in the ratio measurement described in Section 8.

In the forward region $|y| > 2.8$ the theory prediction overestimates the inclusive jet cross-section measured in data. The differences reach up to 50% at very large transverse momentum and rapidity. The experimental uncertainty in this region it comparable or even smaller than the theoretical uncertainty. For the latter, the contribution due to the PDFs dominate, in particular in the gluon momentum distribution. The nominal PDF set CT 10 is the least constrained in this region compared to the others, namely MSTW 2008, HERAPDF 1.5 and NNPDF 2.1. They also follow the trend slightly better, in particular the MSTW 2008 set, which also assigns the smallest uncertainty. The deviation between the different PDF sets and the small experimental uncertainties in this region show the ATLAS jet data can be useful to constrain the PDF.

[3] Minor shifts in other bins are 1.5% and 2.6% in the bin $30\,\text{GeV} \le p_\text{T} < 45\,\text{GeV}$, $0.8 < |y| < 1.2$ for $R = 0.4$ and $R = 0.6$, and 1.8% and 1.9% in the bin $20\,\text{GeV} \le p_\text{T} < 30\,\text{GeV}$, $1.2 < |y| < 2.1$, respectively

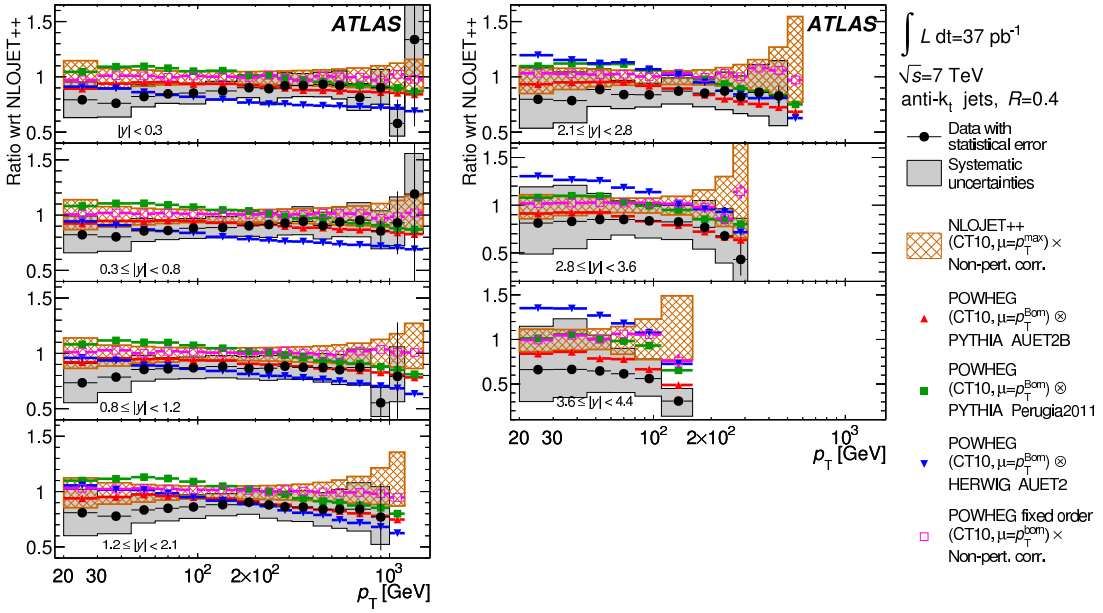

Figure 6.12: Ratio of the measured double-differential inclusive jet cross-section at $\sqrt{s} = 7\,\text{TeV}$ for anti-k_t jets with a radius parameter of $R = 0.4$ with respect to the theoretical predictions from a perturbative QCD calculation at NLO precision using NLOJET++ with the CT 10 PDF set, corrected for non-perturbative effects. The ratio is shown as function of p_T separately for seven different bins of rapidity. The *shaded* and *hatched area* indicate the experimental and theoretical systematic uncertainties, respectively. Also shown are theoretical predictions obtained with the POWHEG generator, interfaced to the parton shower simulators PYTHIA using the tunes AUET 2B and PERUGIA 2011, and HERWIG using the tune AUET 2, and POWHEG using a fixed-order calculation at NLO precision with non-perturbative corrections applied. Only the statistical uncertainty is shown on the POWHEG prediction. Statistically insignificant data points at large p_T are omitted. The uncertainty due to the luminosity measurement of 3.4% is not shown [2].

The same ratio of data with respect to the nominal theoretical prediction using NLO perturbative QCD with non-perturbative corrections is shown in Figures 6.12 and 6.13 for jets with $R = 0.4$ and $R = 0.6$. It is compared to predictions from the POWHEG NLO generator, which is interfaced to various options for the parton shower simulation: PYTHIA with the PERUGIA 2011 tune; PYTHIA with the AUET 2B tune; HERWIG with the AUET 2B tune; the fixed-order calculation from POWHEG with the same non-perturbative corrections as for NLOJET++. The *cut approach* is used to suppress large fluctuations in the final distribution. Only the statistical uncertainty is shown, but the uncertainty due to the PDF set, μ_F, μ_R, and α_S, are expected to be similar than for NLOJET++. An additional uncertainty due to the matching scale μ_M is expected, as described in Section 2.4.4.

To check the consistency of the pure NLO perturbative QCD calculation between NLOJET++ and POWHEG, the POWHEG prediction is derived at fixed order. This NLO calculation is identical to NLOJET++ regarding the virtual corrections, but the hardest branching of the outgoing parton for the real correction is treated differently in POWHEG. Nevertheless, the two predictions are expected to give very similar results. The particle-level cross-section is obtained using the same bin-wise non-perturbative correction factors as for NLOJET++. Good agreement within 5% is observed among the two for most of the phase space. Thus, larger deviations for POWHEG with the matched parton-shower simulation can be attributed

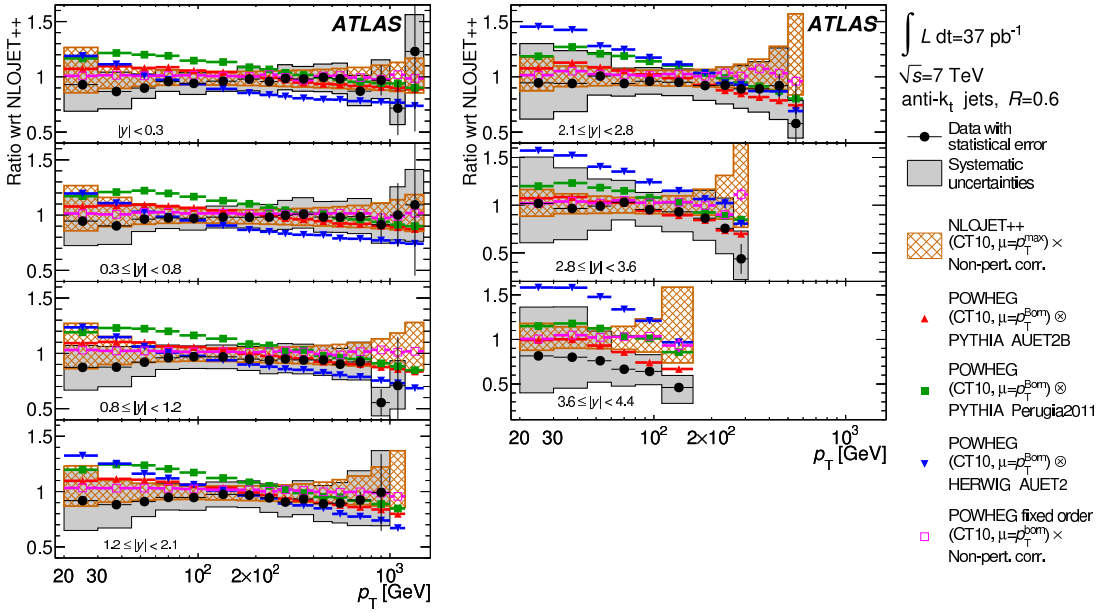

Figure 6.13: Ratio of the measured double-differential inclusive jet cross-section at $\sqrt{s} = 7$ TeV for anti-k_t jets with a radius parameter of $R = 0.6$ with respect to the theoretical predictions from a perturbative QCD calculation at NLO precision using NLOJET++ with the CT 10 PDF set, corrected for non-perturbative effects. The ratio is shown as function of p_T separately for seven different bins of rapidity. The *shaded* and *hatched area* indicate the experimental and theoretical systematic uncertainties, respectively. Also shown are theoretical predictions obtained with the POWHEG generator, interfaced to the parton shower simulators PYTHIA using the tunes AUET 2B and PERUGIA 2011, and HERWIG using the tune AUET 2, and POWHEG using a fixed-order calculation at NLO precision with non-perturbative corrections applied. Only the statistical uncertainty is shown on the POWHEG prediction. Statistically insignificant data points at large p_T are omitted. The uncertainty due to the luminosity measurement of 3.4% is not shown [2].

dominantly to the different approach for the application of non-perturbative corrections with respect to the nominal prediction.

Very different results in comparison to the above are obtained when POWHEG is interfaced to HERWIG with the AUET 2B tune. In the central rapidity region, the predicted cross-section for $R = 0.4$ is larger by 10% at low p_T, and 20 smaller at high p_T. This shape difference is much more pronounced for $R = 0.6$. In the forward region, the shape difference with respect to the data is reduced, but the cross-section differs by a factor of two in the total amount. Altogether the agreement between data and POWHEG using the parton shower simulation from HERWIG is found to be poor, indicating that the matching in the angular-ordered approach is problematic.

Much better agreement is attained for POWHEG when interfaced to PYTHIA with the same tune AUET 2B. A difference of $10 - 20\%$ is also observed for a central rapidity at low p_T, but the prediction follows the trend in data well in the forward region. Interestingly, it shows a similar agreement with the data for both radius parameters of $R = 0.4$ and $R = 0.6$, unlike the approach using a bin-wise correction for non-perturbative effects.

The influence of the tune is studied using POWHEG in combination with PYTHIA and the PERUGIA 2011 tune. A similar shape is observed for PERUGIA 2011 and AUET 2B, but the prediction with PERUGIA 2011

is consistently higher. The shift of 20% – 5% from low to high p_T reflects the differences between the tunes also seen in the derivation of the non-perturbative corrections of Figure 2.3. Thus, the obtained agreement at low p_T is not as good as for the AUET 2B tune.

In conclusion, differences with respect to the nominal prediction from NLOJET++ of up to 30% are observed for POWHEG when interfaced to PYTHIA for the parton shower simulation, and up to 60% for HERWIG. This difference is not covered by the uncertainty on the non-perturbative correction, which is below 10%. This indicates that the interplay between the scale of the matrix element calculation and the parton shower is a considerable effect, and the matching scale needs further studies, in particular for the combination of POWHEG and HERWIG.

Summary

In general, good agreement has been found between data and the predictions based on a perturbative QCD calculation at NLO, to which non-perturbative correction have been applied. Within the uncertainties, a different trend is observed in the as yet unprobed region at high p_T and large rapidity, as well as a generally different level of agreement in the order of 10 – 20% between the jet distance parameters $R = 0.4$ and $R = 0.6$. The theory predictions from the POWHEG event generator, i.e. a perturbative QCD calculation at NLO that is interfaced with a parton shower Monte Carlo simulation, show a large dependency on the used simulation and tune, of which only PYTHIA with the AUET 2B tune is able to describe the data across the entire phase space. However, the POWHEG prediction is potentially biased by events with large weights and the countermeasures thereof. The comparison of various PDF sets has yielded an improved description of the forward region in particular by MSTW 2008. Although the size of the experimental and theoretical uncertainties do not allow to select one prediction above the others, the data is expected to be useful in future fits of the parton distributions. The data including all systematic uncertainties and the used non-perturbative corrections have been published via the Durham HepData project [132].

CHAPTER 7

Inclusive jet cross-section at $\sqrt{s} = 2.76\,\text{TeV}$

In the beginning of 2011, the LHC performed a short data taking period of proton-proton collisions at a centre-of-mass energy of $\sqrt{s} = 2.76\,\text{TeV}$, corresponding to an integrated luminosity of $\mathcal{L} = 0.20\,\text{pb}^{-1}$. The primary motivation for this dataset clearly is based on the heavy ion programme of the LHC, since this energy corresponds to the nucleon-nucleon centre-of-mass energy in lead-lead collisions, $\sqrt{s_{NN}} = 2.76\,\text{TeV}$. Therefore, the proton-proton collision data can serve as independent reference in measurements like centrality-dependent dijet asymmetry [133].

Nevertheless, the recorded data is also interesting for jet measurements beside the heavy ion programme for two reasons. First, an integrated luminosity of $0.20\,\text{pb}^{-1}$ is sufficient to allow for a solid measurement of the inclusive double-differential cross-section itself, for the same physics interest like for $\sqrt{s} = 7\,\text{TeV}$, namely probing the QCD calculations with a high precision. Of course, higher centre-of-mass is preferable, but $\sqrt{s} = 2.76\,\text{TeV}$ on the other hand is close to the energies of $\sqrt{s} = 1.96\,\text{TeV}$ reached at the jet measurements at the Tevatron [134–140]. Hence, it provides not only a cross-check to these measurements, but also an intermediate measurement point between $\sqrt{s} = 1.96\,\text{TeV}$ and $\sqrt{s} = 7\,\text{TeV}$ to investigate the scaling behaviour of the cross-section with $\sqrt{s}$.

The second, even stronger motivation for studying the $\sqrt{s} = 2.76\,\text{TeV}$ data are the possibilities offered by a ratio measurement of the cross-section at $\sqrt{s} = 2.76\,\text{TeV}$ and $\sqrt{s} = 7\,\text{TeV}$. If the same experimental setup is employed for both measurements, one can profit from the fact that many of the systematic uncertainties between the two measurements are strongly correlated. To exploit this fact to the full extend, the measurement of the inclusive double-differential jet cross-section at $\sqrt{s} = 2.76\,\text{TeV}$ uses the same reconstruction and calibration as the $\sqrt{s} = 7\,\text{TeV}$ analysis, rather then aiming for an improvement of the individual uncertainties, since the cancellation of the associated uncertainties is much more effective in this case.

The setup for this analysis is mainly driven by optimising the ratio measurement, and it follows closely the corresponding $\sqrt{s} = 7\,\text{TeV}$ analysis presented in the previous Chapter 6. The same jet definition is used, with the two radius parameters of $R = 0.4$ and $R = 0.6$, as well as the same binning in rapidity. Two different binnings in p_T are employed in preparation of the ratio measurement, namely a binning identical to the previous measurement, and a binning in $x_\text{T} = 2p_\text{T}/\sqrt{s}$. The latter will be discussed again in Chapter 8, while in this section, only the results for the p_T binning are reported.

Due to the large similarities between the cross-section measurements at $\sqrt{s} = 2.76\,\text{TeV}$ and $\sqrt{s} = 7\,\text{TeV}$, only the differences between the analyses are explained in this section, rather than repeating the information from the previous chapter. Special focus is put on the verification of the corrections

determined with the dataset at $\sqrt{s} = 7\,\text{TeV}$, i.e. the jet calibration. Additionally, a careful cross-check of the kinematic distributions of the dataset is performed to detect potential problems.

The resulting structure of this chapter is as follows. Section 7.1 gives a brief overview of the theory predictions used for this measurement. The dataset, the trigger, event and jet selection, and extensive data cross-checks are presented in Section 7.2. It is followed by a summary of the systematic uncertainties in Sections 7.3. The results of the measurement are discussed in Section 7.4.

7.1 Theory prediction

The theory prediction for the inclusive jet cross-section measurement at $\sqrt{s} = 2.76\,\text{TeV}$ uses mostly identical parameters as the one at $\sqrt{s} = 7\,\text{TeV}$, in preparation for the ratio measurement. A general description of the event generators and the Monte Carlo simulation and their uncertainties is given in Section 2, whereas here only the used configurations for the nominal prediction and simulations is listed. The corresponding steering files and samples are documented in Appendix A.1.

The NLO perturbative QCD predictions are generated using NLOJET++ 4.1.2. The factorisation and renormalisation scales in the calculation of the matrix element are set to $\mu_F = \mu_R = p_{\text{T}}^{\text{max}}(y_i)$. The CT 10 NLO PDF set is used as baseline. No correction for electroweak effects is applied. The non-perturbative corrections are derived using PYTHIA 6.425 with the tune AUET 2B and the CTEQ 6L1 PDF set, as it is done for the corrections at $\sqrt{s} = 7\,\text{TeV}$. Also for the Monte Carlo simulation, the same configuration is used, but a reweighing from the LO to a NLO PDF is performed to obtain a better description of the data, following the procedure described in Section 2.3. The reweighting factors are determined from the bin-wise ratio of the calculated cross-section using the MSTW 2008 NLO PDF set and the MRST 2007 LO* PDF set. The reweighting is applied on a jet-by-jet basis according to their $|y|$ and p_{T}. Additional proton-proton collisions in the same bunch crossing have not been included in the Monte Carlo simulation, since the average number of interactions per bunch crossing in data is very small. The used Monte Carlo sample is listed in Table A.2 in the appendix.

The prediction using a NLO matrix element calculation interfaced to a parton shower simulation is obtained using the POWHEG dijet generator in combination with PYTHIA. POWHEG Box 1.0 in revision 2169 with the option `doublefsr` is used. The CT 10 PDF set is employed. Two different tunes for the parton shower simulation are tested, namely PYTHIA with the AUET 2B tune, and PYTHIA with the tune PERUGIA 2011. No comparison is done with HERWIG due to unsolved problems with spikes in the final observables despite the `doublefsr` option. As before, only the statistical uncertainty is given for the POWHEG prediction.

7.2 Data Selection

7.2.1 Dataset

The dataset for this analysis was recorded in March 2011 and amounts to a total integrated luminosity of $211\,\text{nb}^{-1}$ of delivered proton-proton collision data, of which $201\,\text{nb}^{-1}$ were recorded by the ATLAS experiment. The proton bunches were grouped in nine bunch trains with a minimal separation between each proton bunch of 525 ns. Hence, an influence from out-of-time pile-up due to the long signal length in the LAr calorimeter is excluded. The average number of interactions per bunch crossing was measured to be $\mu = 0.24$, so that the dataset shows very relaxed running conditions, and only a negligible impact from pileup is expected.

trigger	integrated luminosity $[nb^{-1}]$	p_T range [GeV]			
		$\|y\| < 2.1$	$2.1 \leq \|y\| < 2.8$	$2.8 \leq \|y\| < 3.6$	$3.6 \leq \|y\| < 4.4$
EF_mbMbts_2_NoAlg	0.396	$p_T < 35$	$p_T < 30$	$p_T < 28$	$p_T < 26$
EF_j10_a4_EFFS_L1MBTS	3.91	$35 \leq p_T < 55$	$30 \leq p_T < 50$	$28 \leq p_T < 40$	-
L1_J10	200	$55 \leq p_T$	$50 \leq p_T$	-	-
L1_J10 or L1_FJ10	200	-	-	$40 \leq p_T$	-
L1_FJ10	200	-	-	-	$26 \leq p_T$

Table 7.1: Trigger scheme for the analysis at $\sqrt{s} = 2.76\,\text{TeV}$. A single trigger is used in each rapidity and p_T range, resulting in the given integrated luminosities. This table also appears in [64].

The dataset consists of four runs and corresponds to the data taking period 2011 C in ATLAS terminology. Two of the runs include van-der-Meer scans for the calibration of the luminosity algorithms. The corresponding luminosity blocks are excluded from the analysis, as well as a special run phase with exceptionally low μ, dedicated to the study of minimum bias events[1].

The same requirements on the operational status of the different detector components relevant for jet measurements as in the previous analysis are applied. Table A.14 lists all luminosity blocks fulfilling these criteria. In total, a dataset with an integrated luminosity of $\mathcal{L} = 200 \pm 5\,\text{nb}^{-1}$ is obtained.

7.2.2 Trigger scheme

Four different triggers are used in this analysis to select jet events, according to their efficiency and resulting statistical uncertainty. The kinematic plane is divided into four different ranges in rapidity with similar turn-on behaviour of the used triggers. In the low p_T region, a minimum bias trigger, MBTS_2, is employed. It requires two hits in any of the minimum bias scintillating tiles. For jets above 30 GeV, the trigger rates using MBTS_2 suffer from large prescales, and jet-based triggers are assigned. In an intermediate p_T range, the jet-based trigger is still seeded by the MBTS with lower prescale, but a jet reconstruction is performed at Level-2. At large p_T, single jet triggers are used, where in the transition region $2.8 < |y| < 3.6$, the central and forward trigger items are combined to achieve full trigger efficiency. The complete trigger scheme is summarised in Table 7.1.

Each triggers is required to be $> 99\%$ efficient in its defined range. The efficiency in this analysis is determined from the leading jet in the event, which basically results in a sharper turn-on curve than for the inclusive efficiency definition applied in the previous analysis, but with a similar 99%-efficiency point.

The efficiency of the single jet triggers at high p_T are determined with a bootstrap method. The trigger item in the intermediate p_T range is tested for its efficiency using the MBTS_2 trigger. However, since the minimum bias trigger also acts as seed for the probed trigger at Level-1, this only accounts for the efficiency of the trigger algorithm at the event filter. Thus, the efficiency of the MBTS_2 trigger is determined in a separate study, especially because of potential deficiencies of the minimum bias trigger scintillating tiles, which are expected to have degraded during the first year of operation due to radiation damage. Moreover, a discontinuity in the two forward rapidity bins at around $p_T = 30\,\text{GeV}$ can be observed in the jet spectrum, coinciding with the initial choice of the transition the MBTS_2 and EF_j10_a4_EFFS_L1MBTS trigger. It is shown in Figure 7.1c as the ratio of the normalised jet

[1] No calibration of the luminosity detectors is available for these unusual running conditions. Since this phase only contains a negligible number of events with large transverse momentum jets, it can be neglected.

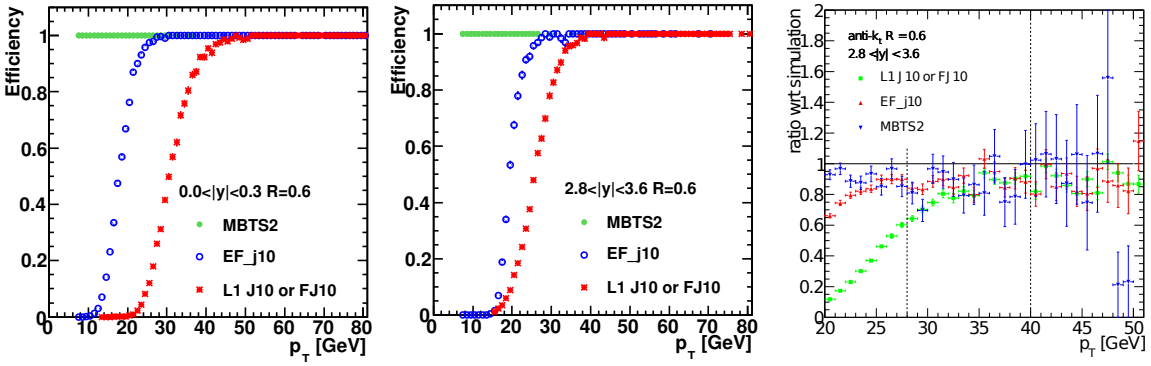

(a) $|y| < 0.3$ (b) $2.8 < |y| < 3.6$ (c) $2.8 < |y| < 3.6$

Figure 7.1: Trigger efficiencies at $\sqrt{s} = 2.76\,\text{TeV}$ in the dataset from 2011 as function of p_T in different ranges of rapidity, (a) $|y| < 0.3$ and (b) $2.8 < |y| < 3.6$ [1], and (c) ratio of the normalised jet yield from different trigger items with respect to the simulation. In the latter, transition between different trigger items are indicated by the *dotted lines*.

yield in data using different trigger items with respect to the Monte Carlo simulation. Although the statistical uncertainty becomes large for increasing p_T in the `MBTS_2` triggered data, the observed trend for $p_\text{T} \to 30\,\text{GeV}$ could indicate an inefficiency of the minimum bias scintillator for high p_T jets in forward direction. Forward jets with a narrow, collimated parton shower may escape detection due to the limited coverage of the scintillators, which is $2.09 < |\eta| < 3.84$.

The effect is studied using independent triggers, namely random triggers and a trigger from the zero degree calorimeter. Typically, only a small bandwidth is granted to these unspecific trigger items. Hence the obtained data sample suffers from large statistical uncertainties in the p_T range under study, and basically no events with jets above 25 GeV are present. Yet, an efficiency of 100% is found in the range below, although the statistical uncertainty is high. To cover the higher p_T region, the trigger decision of `MBTS_2` before prescaling is monitored in the samples obtained using single jet triggers. Only very low number of events show a negative `MBTS_2` decision, so that no indication of inefficiency is observed. Nevertheless the thresholds of the single jet triggers are lowered as close to the 99% efficiency boundary as possible, to limit the influence of a potential inefficiency of the minimum bias trigger in this region, and an increased uncertainty of 2% is assigned in $2.8 < |y| < 3.6$ for $p_\text{T} < 45\,\text{GeV}$, and in $3.6 < |y| < 4.4$ for $p_\text{T} < 30\,\text{GeV}$. Everywhere else, a 1% uncertainty is applied conservatively on the trigger efficiency.

The trigger efficiency curves are shown in Figures 7.1a and 7.1b for jets with $R = 0.6$ in two different rapidity regions. All trigger items reach a stable plateau with an efficiency > 99% above the defined p_T thresholds in the trigger scheme.

7.2.3 Event and jet selection

Due to the limited number of events in the data sample, the event selection criteria are slightly relaxed in comparison to the previous analysis. However, it was carefully checked that no bias was introduced. At least one well-reconstructed vertex has to be present in the event, where the required number of associated tracks with $p_\text{T} > 150\,\text{MeV}$ is lowered from 5 to 3. Jets are required to have a minimum p_T of 20 GeV, and $|y| < 4.4$. The same jet reconstruction as in the previous measurement is used, described in Section 5.1, with two different radius parameters for the anti-k_t algorithm of $R = 0.4$ and $R = 0.6$. The origin correction to account for the actual vertex position in the event is applied on the four-momenta

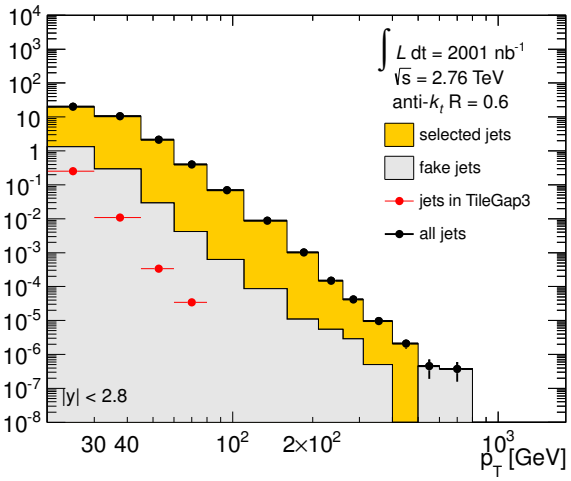

Figure 7.2: Normalised jet yield of anti-k_t jets with $R = 0.6$ in the dataset of 2011 at $\sqrt{s} = 2.76\,\text{TeV}$ as function of p_T. The distribution is shown separately for all jets, jets with a large energy fraction in the transition between barrel and extended barrel in the Tile calorimeter, `TileGap3`, fake jets from non-collisions and jets selected for the analysis.

of the jets. Jets are calibrated to the jet energy scale using the *EM+JES* calibration scheme. No pile-up correction is introduced, since the impact of additional energy deposition from multiple collisions is expected to be negligible due to the low number of interactions per bunch crossing in the dataset. Each jet is required to pass the trigger defined in the according ($|y|$, p_T) range. Furthermore, jets have to fulfil the jet quality selection in order to exclude fake jets reconstructed from beam background, cosmic rays and detector noise, as well as jets with a large energy fraction in the region of the `TileGap3` scintillators, as described in Section 5.4. The contribution of fake jets is shown in Figure 7.2. The efficiency of the jet selection is corrected for in the final result.

7.2.4 Data cross-checks

Since the present study is the first to analyse the dataset at $\sqrt{s} = 2.76\,\text{TeV}$ from 2011, a series of dedicated cross-checks is performed. Two types of potential problems have to be excluded. First, malfunctions of the detector, such as dead cells in the calorimeter, after the maintenance of the detector in the winter shutdown between 2010 and 2011. Second, the agreement of the data with the Monte Carlo simulation in the basic kinematic distributions for validation of the calibration and the shape of the simulation. The latter is important for the unfolding step of the data because a good shape agreement improves the unfolding result, although the iterative unfolding can compensate modest disagreements. The nominal Monte Carlo simulation described in Section 7.1 is used for this comparison.

Data integrity The p_T spectrum of the normalised yield of jets with $R = 0.4$ for the central rapidity bin is shown in Figure 7.3a. No abnormalities are observed in general in the range from $p_\text{T} \geq 20\,\text{GeV}$ in all rapidity bins. To check the continuity of the distribution in detail, especially at the transition between different trigger regions, a comparison to a generic fit function is performed. No discontinuity is found, except in the transition of the minimum bias and the intermediate trigger in the very forward bins. As described in Section 7.2.2, no conclusion can be drawn on a potential inefficiency, and it is considered as statistical fluctuation.

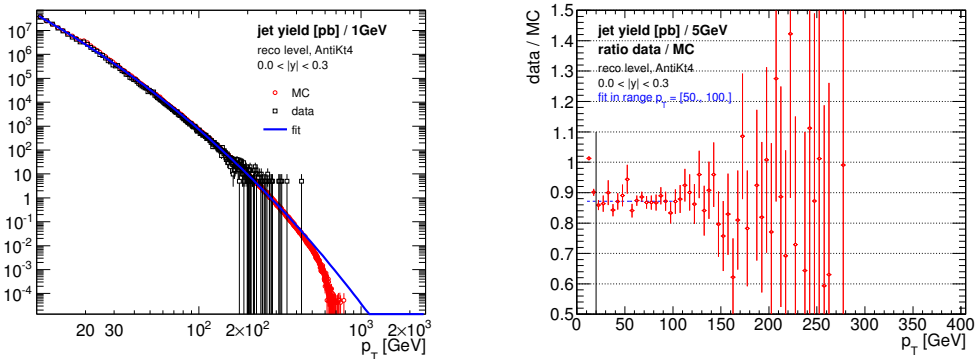

(a) (b)

Figure 7.3: (a) p_T spectrum of the normalised jet yield for the central rapidity bin $|y| < 0.3$ in data and the Monte Carlo simulation Pythia and (b) the ratio of the jet yields in data and simulation. In the former, a generic fit function is shown to check for discontinuities. The anti-k_t algorithm with $R = 0.4$ is used.

Furthermore, the distribution of jets across the η-ϕ plane is smooth and shows no sign of noisy or irresponsible cells. Alike, no asymmetries between A and C side of the detector along η, or in ϕ, i. e. top versus bottom side of the detector, are observed. The according distributions can be found in Appendix A.4.3.

Agreement of data and Monte Carlo simulation The shape of the p_T spectrum in data is well described by the Monte Carlo simulation in general. Figure 7.3b shows the ratio of the p_T spectrum in data and the simulation for the central rapidity, $|y| < 0.3$. The ratio is flat for $p_\text{T} > 20\,\text{GeV}$ apart from statistical fluctuations. However, a downward shift of 10% - 15% is observed in all rapidity bins $0.0 \leq |y| < 2.1$. Figure 7.4a shows the η distribution of the yield ratio between data and the simulation for jets with $R = 0.4$ in the region $60\,\text{GeV} \leq p_\text{T} < 80\,\text{GeV}$. The ratio is flat in both, the region covered by the extended tile calorimeter and the hadronic end cap, but shows a very pronounced discontinuity at the transition of the two at $\eta \approx \pm 1.8$, clearly indicating a detector effect. This discontinuity is not restricted to a particular p_T region, as shown by the y-p_T plane in Figure 7.4c, where the jet yield in data is about 10% - 15% lower than predicted by the simulation for $|y| < 1.8$. The observed discrepancy of data and the Monte Carlo simulation clearly indicates a mismodelling of the jet response e.g. due to dead material in the detector description, which in turn also affects the data via the jet energy calibration. In any case, a miscalibration of the jet energy scale of 2% can easily produce a chance of 10% in the jet yield.

As described in Section 5.2.4, the energy scale calibration in this region is determined via the η-intercalibration method. If the energy response of the probe jet is mismeasured, e.g. by 2% due to a wrong amount of dead material, the correction factor derived from the Monte Carlo simulation does not match the data. After applying the calibration to data, a deviation of about the same 2% between the response obtained from the Monte Carlo simulation and the data should be visible. In the lowest p_T bin, such a difference can be observed indeed, as shown in Figure 5.5a. The corresponding Figure 5.5b for $60\,\text{GeV} \leq p_\text{T} < 80\,\text{GeV}$, however, does not exhibit this tendency, and in general the statistical power of the dijet balance method does not allow to draw conclusions in the $\sqrt{s} = 2.76\,\text{TeV}$ dataset.

On the other hand, a deficit in the detector description and the corresponding effect in the jet energy calibration also should affect the data at $\sqrt{s} = 7\,\text{TeV}$. This is confirmed by Figures 7.4b and 7.4d, showing a very similar level of agreement for ratio of the jet yield in data and the Monte Carlo simulation

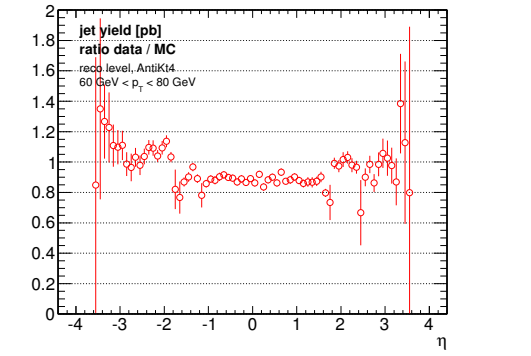

(a) $\sqrt{s} = 2.76\,\text{TeV}$

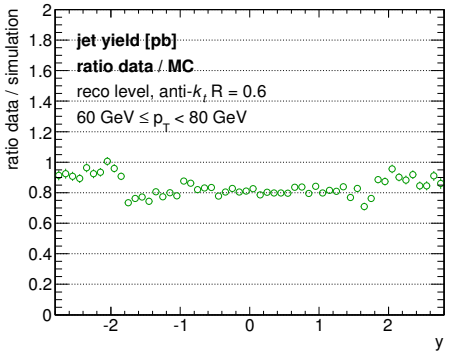

(b) $\sqrt{s} = 7\,\text{TeV}$

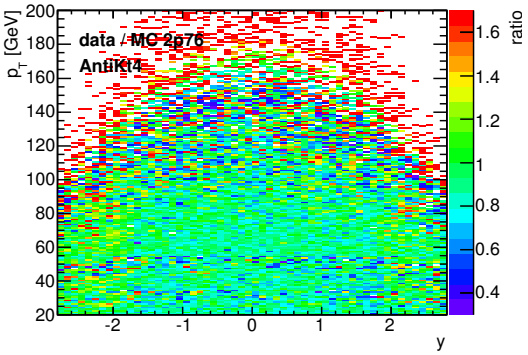

(c) $\sqrt{s} = 2.76\,\text{TeV}$

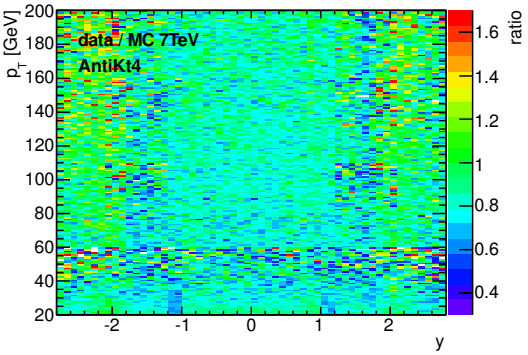

(d) $\sqrt{s} = 7\,\text{TeV}$

Figure 7.4: Comparison of the jet yield in data and the Monte Carlo simulation Pythia as function of the rapidity and in the y-p_T plane for $\sqrt{s} = 2.76\,\text{TeV}$ and $\sqrt{s} = 7\,\text{TeV}$.

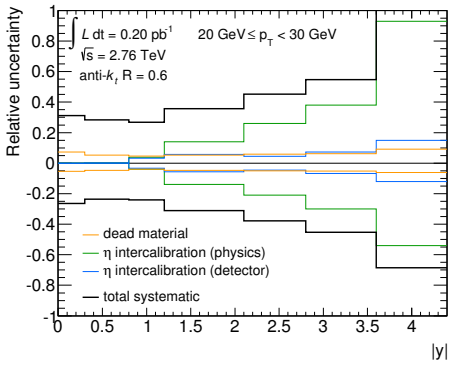

(a)

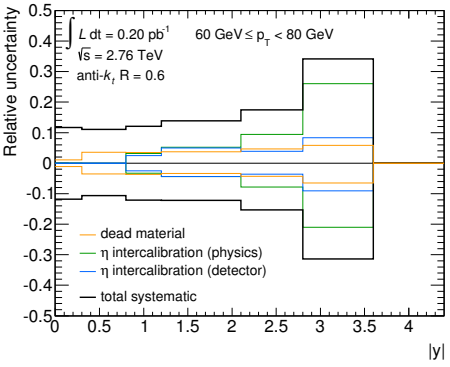

(b)

Figure 7.5: Systematic uncertainty on the inclusive jet cross-section due to the jet energy scale as function of the rapidity $|y|$ for two p_T ranges for anti-k_t jets with $R = 0.6$ at $\sqrt{s} = 2.76\,\text{TeV}$. Also shown are the physics and detector components of the η-intercalibration method, as well as component due to the global dead material variation.

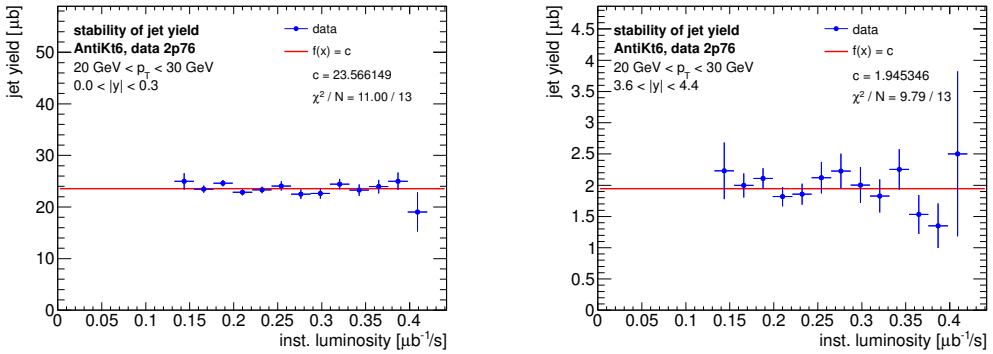

(a) $|y| < 0.3$ (b) $3.6 < |y| 4.4$

Figure 7.6: Normalised jet yield as a function of the instantaneous luminosity for anti-k_t jets with $R = 0.6$, $20\,\text{GeV} \leq p_\text{T} < 30\,\text{GeV}$ in two rapidity ranges. Also shown is the fit of the distribution using a constant function.

for $\sqrt{s} = 7\,\text{TeV}$. In general, this kind of discrepancy is taken into account in the conservative uncertainty estimation for the η-intercalibration method [109]. Figure 7.5 shows the systematic uncertainty on the inclusive jet cross-section due to the jet energy scale and also due to the physics and detector components of the η-intercalibration method and the global dead material variation. While the shift at $|y| \approx 1.8$ is within the uncertainty due to these components in the low p_T region of Figure 7.5a, it is hardly covered for higher p_T, as shown in Figure 7.5b. This is an indication that the uncertainty in η-intercalibration might be underestimated, since it only accounts for differences in the parton shower simulations, but not on the potential deviation in jet energy response among the detector technologies of the calorimeter or the amount of dead material distribution along the rapidity in the detector simulation.

Data stability under pile-up conditions The stability of the measurement during the course of the data taking is monitored by means of the jet yield to detect problems such as temporary malfunctions or drifts in the calibration. A stable jet yield is observed in all bins of rapidity and p_T. In particular, the result is stable across runs with different running conditions, i.e. instantaneous luminosity. Figure 7.6 shows the jet yield as a function of the instantaneous luminosity for jets with $R = 0.6$, $20\,\text{GeV} \leq p_\text{T} < 30\,\text{GeV}$, where the largest influence of pileup events may be anticipated. Neither in the forward, nor in the central rapidity region a trend is observed; both are well in agreement with a flat distribution, as expected from the moderate running conditions. Auxiliary material showing the jet yield as a function of the luminosity plot are presented in Appendix A.3.1.

In summary, no statistically significant deviations in the data consistency checks are found. The basic kinematic distributions in data are described by the Monte Carlo simulation within the systematic uncertainties. The jet yield is found to be stable over time and does not show any dependence on the running conditions.

7.2.5 Unfolding

The iterative, dynamically stabilised unfolding method is used, as in the previous analysis. The nominal Monte Carlo simulation as described in Section 2.1 is employed. As before, the unfolding matrix converges after only one iteration.

7.3 Systematic uncertainties

The experimental systematic uncertainty is composed of 21 different uncertainty sources, as listed in Table 5.1. It includes the uncertainty due to the following components: the jet energy and angular resolution; the jet reconstruction, jet selection and trigger efficiency; the matching efficiency and closure of the unfolding; the luminosity; and 14 subcomponents, grouped in the uncertainty due to the JES. In contrast to the previous measurement, no offset correction to account for pileup interactions was applied, and accordingly no uncertainty is assigned. The uncertainty on the η-intercalibration is split into a detector and physics component, JES 6 and JES 15 respectively, as described in Section 5.2.4.

The same correlations as in the previous measurement are assumed. In total, 88 independent sources of uncertainty are identified to describe the bin-by-bin correlations of the jets in this measurement. Additionally, two sources without any correlation between the bins in $|y|$ and p_{T} are included, namely the jet selection and trigger efficiencies. As in the previous measurement, the luminosity uncertainty of 2.7% is not included in the systematic uncertainty, but treated separately.

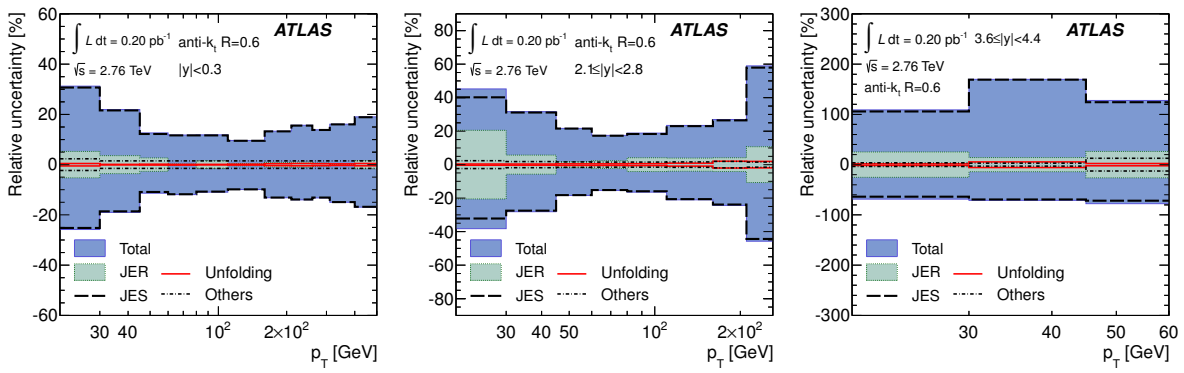

(a) $|y| < 0.3$ (b) $2.1 < |y| < 2.8$ (c) $3.6 < |y| < 4.4$

Figure 7.7: Total systematic uncertainties in the measurement of the inclusive jet cross-section at $\sqrt{s} = 2.76\,\mathrm{TeV}$ for anti-k_t jets with $R = 0.6$ in representative rapidity regions. The contributions from the jet energy scale, the jet energy resolution, the unfolding procedure and other sources are shown separately. The uncertainty due to the luminosity measurement is not shown. [1]

Figure 7.7 shows the total experimental systematic uncertainty in three representative rapidity regions for $R = 0.6$. Results for $R = 0.4$ are similar qualitatively, but slightly reduced, as shown in Figure A.3 of the appendix. In the central rapidity, the systematic uncertainty is just above 10% at $p_{\mathrm{T}} = 100\,\mathrm{GeV}$. At small and high p_{T}, it is larger by a factor of about three and two, respectively. The uncertainty is rather constant up to a rapidity of $|y| < 2.1$, and raises to about 40% at low p_{T}, 20% at intermediate p_{T}, and 50% at the maximum p_{T} reached in $2.1 < |y| < 2.8$. It increases further towards the forward region, where the uncertainty generally exceeds $^{+100}_{-80}$%.

In summary, the systematic uncertainty is very similar to the one of the measurement at $\sqrt{s} = 7\,\mathrm{TeV}$, with only minor differences due to the slightly different shape of the p_{T} spectrum between the two centre-of-mass energies. Again, the JES is the dominant component of the total uncertainty. Small contributions come from the JER at low p_{T} and in the forward region at high p_{T}.

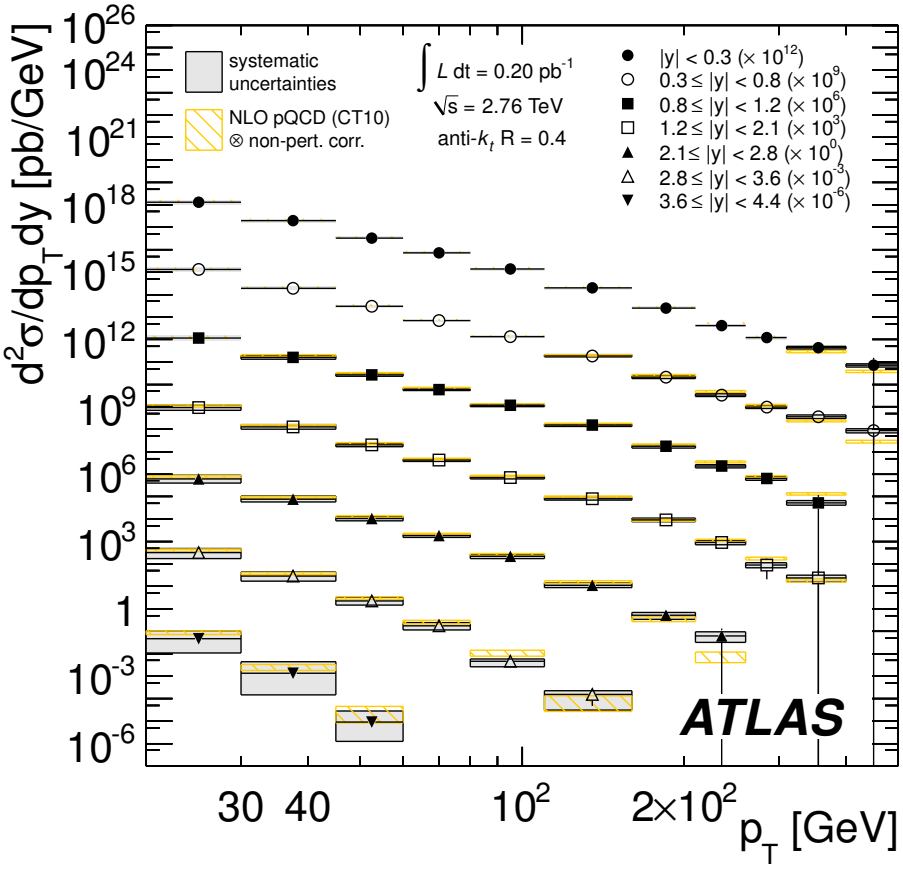

Figure 7.8: Double-differential inclusive jet cross-section at $\sqrt{s} = 2.76\,\text{TeV}$ for anti-k_t jets with a radius parameter of $R = 0.4$ as a function of p_T in seven different ranges of rapidity. The dataset corresponds to an integrated luminosity of $\mathcal{L} = 200 \pm 5\,\text{pb}^{-1}$, recorded in the year 2011. The systematic uncertainties on the measurement are indicated with the *shaded area*. The data are compared to predictions from a perturbative QCD calculation at NLO precision using NLOJET++ with the PDF set CT 10. Corrections of the prediction for non-perturbative effects are obtained using PYTHIA with the AUET 2B tune and the CTEQ 6L1 PDF set. The uncertainty on the theoretical prediction is shown by the *hatched area*. The uncertainty due to the luminosity measurement of 2.7% is not shown. For a better visibility, the cross-section is multiplied with a factor in each rapidity range, as indicated in the legend. [1]

7.4 Results and Discussion

The results for the inclusive jet cross-section in proton-proton collision at a centre-of-mass energy of $\sqrt{s} = 2.76\,\text{TeV}$ are presented in this section. The dataset was recorded in the beginning of the data taking period of 2011 and corresponds to an integrated luminosity of $\mathcal{L} = 0.20 \pm 0.01\,\text{pb}^{-1}$. The anti-$k_t$ algorithm is used with two different radius parameters of $R = 0.4$ and $R = 0.6$. Jets are considered in the range $p_\text{T} \geq 20\,\text{GeV}$, $|y| < 4.4$ and the measurement reaches a maximum p_T of 428 GeV.

The data is compared to a perturbative QCD calculation at NLO, with non-perturbative correction applied. NLOJET++ with the CT 10 PDF set is used for the nominal theoretical prediction. The corrections for parton shower, hadronisation and the underlying event are derived with PYTHIA, using the AUET 2B tune and the CTEQ 6L1 PDF set. The result is shown in Figures 7.8 and 7.9 for jets with $R = 0.4$ and $R = 0.6$, respectively, as a function of p_T for seven different ranges of rapidity. Good agreement across

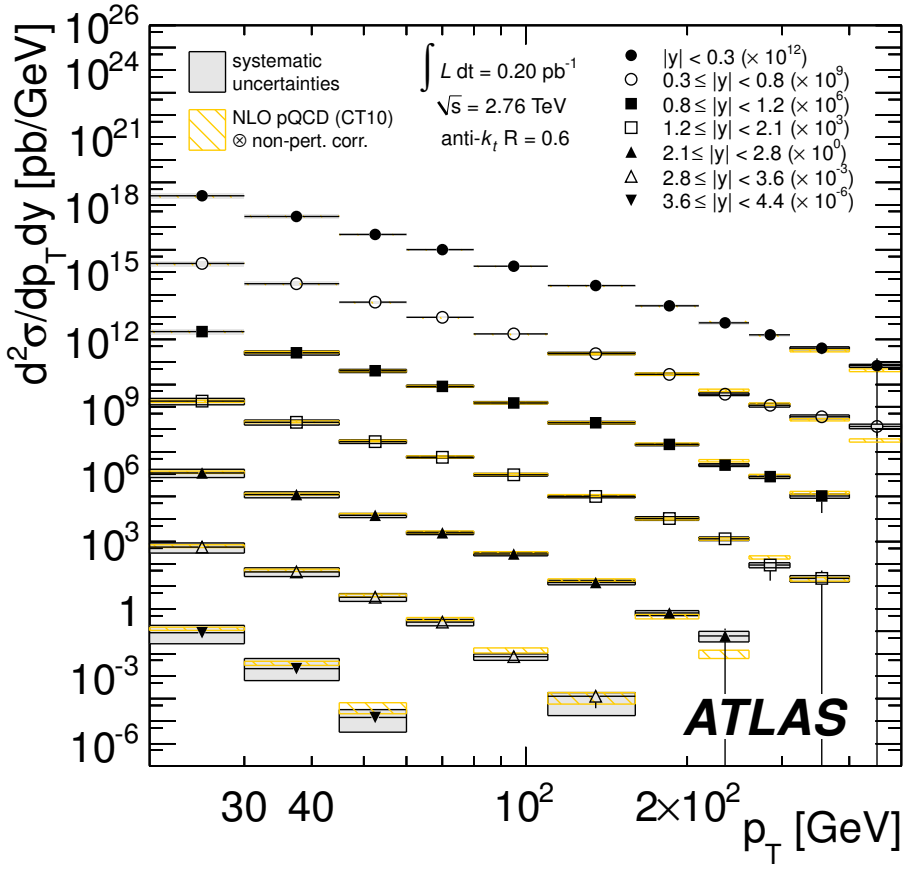

Figure 7.9: Double-differential inclusive jet cross-section at $\sqrt{s} = 2.76\,\text{TeV}$ for anti-k_t jets with a radius parameter of $R = 0.6$ as a function of p_T in seven different ranges of rapidity. The dataset corresponds to an integrated luminosity of $\mathcal{L} = 200 \pm 5\,\text{pb}^{-1}$, recorded in the year 2011. The systematic uncertainties on the measurement are indicated with the *shaded area*. The data are compared to predictions from a perturbative QCD calculation at NLO precision using NLOJET++ with the PDF set CT 10. Corrections of the prediction for non-perturbative effects are obtained using PYTHIA with the AUET 2B tune and the CTEQ 6L1 PDF set. The uncertainty on the theoretical prediction is shown by the *hatched area*. The uncertainty due to the luminosity measurement of 2.7% is not shown. For a better visibility, the cross-section is multiplied with a factor in each rapidity range, as indicated in the legend. [1]

the entire phase space of the measurement and seven orders of magnitude in cross-section is found.

For a more detailed comparison, the ratio of the data with respect to the nominal theory prediction is presented in Figures 7.10 and 7.11 for $R = 0.4$ and $R = 0.6$, respectively. In general, no substantial deviations between the data and the nominal prediction are observed. However, a difference in the normalisation of about $10 - 20\%$ is found for $R = 0.4$, whereas the ratio for $R = 0.6$ is very close to unity. It is the same observation that was already made for the previous measurement at $\sqrt{s} = 7\,\text{TeV}$. Yet, it is difficult to draw conclusions from the fact that the difference is present in both measurements, and only a dedicated study can give new insight. Apart from the normalisation, the shape is very similar, and most statements on $R = 0.6$ in the following are also valid for $R = 0.4$. The size of the uncertainty is at the same order for data and theory, with the theoretical uncertainties being slightly smaller than the experimental ones. The statistical uncertainty becomes sizeable above 200 GeV and reflects the rather small integrated luminosity of the dataset.

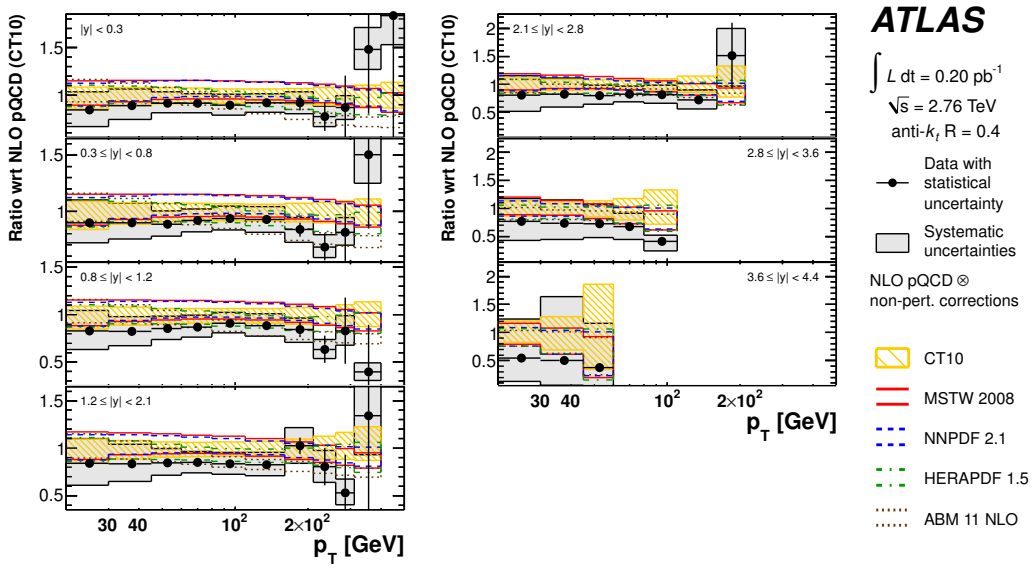

Figure 7.10: Ratio of the measured double-differential inclusive jet cross-section at $\sqrt{s} = 2.76\,\text{TeV}$ for anti-k_t jets with a radius parameter of $R = 0.4$ with respect to the theoretical predictions from a perturbative QCD calculation at NLO precision using NLOJET++ with the PDF set CT 10, corrected for non-perturbative effects. The ratio is shown as function of p_T separately for seven different bins of rapidity. The *shaded* and *hatched area* indicate the experimental and theoretical systematic uncertainties, respectively. The figure also shows the same theoretical calculation for a selection of different PDF sets, namely MSTW 2008, NNPDF 2.1, and HERAPDF 1.5. Statistically insignificant data points at large p_T are omitted. The uncertainty due to the luminosity measurement of 2.7% is not shown. [1]

In the central rapidity region, the ratio is basically flat, i.e. the prediction using the PDF set CT 10 describes the data well. In contrast to the measurement at $\sqrt{s} = 7\,\text{TeV}$, there is only a very mild trend to overestimate the data at low p_T for $R = 0.4$, and basically no deviation at $R = 0.6$. This indicates that the differences found in the previous measurement could originate from the higher instantaneous luminosity present in this dataset, since this momentum range is potentially affected by contributions from pile-up or noise thresholds.

Starting from $|y| = 2.1$ the prediction shows a slight tendency to overestimate the cross-section towards large p_T, resulting in a skewed ratio. In the very forward region, the difference is most pronounced, with a deviation of $20 - 50\%$ in the central values of data and prediction. Nevertheless, the difference is covered by the large experimental and theoretical uncertainty.

In the figures 7.10 and 7.11 the data is furthermore compared to theoretical predictions using alternative NLO PDF sets, namely MSTW 2008, HERAPDF 1.5, NNPDF 2.1, and ABM 11. Most observations made in the previous measurement are valid for this one as well. The prediction using these PDF sets give similar results as the nominal PDF set CT 10. A slightly larger cross-section is obtained in the barrel for MSTW 2008 and NNPDF 2.1, whereas HERAPDF 1.5 is very close to CT 10 and the data in the central region. At large rapidities, the uncertainty of the alternative PDF sets is substantially smaller than the uncertainties of CT 10, and they follow better the trend of the data. This similar behaviour of the predictions with respect to the data at the two centre-of-mass energies indicates the potential for an improvement of the PDF fits using the ATLAS jet data.

A general exception to these observation is the ABM 11 NLO PDF set. It is only included in this

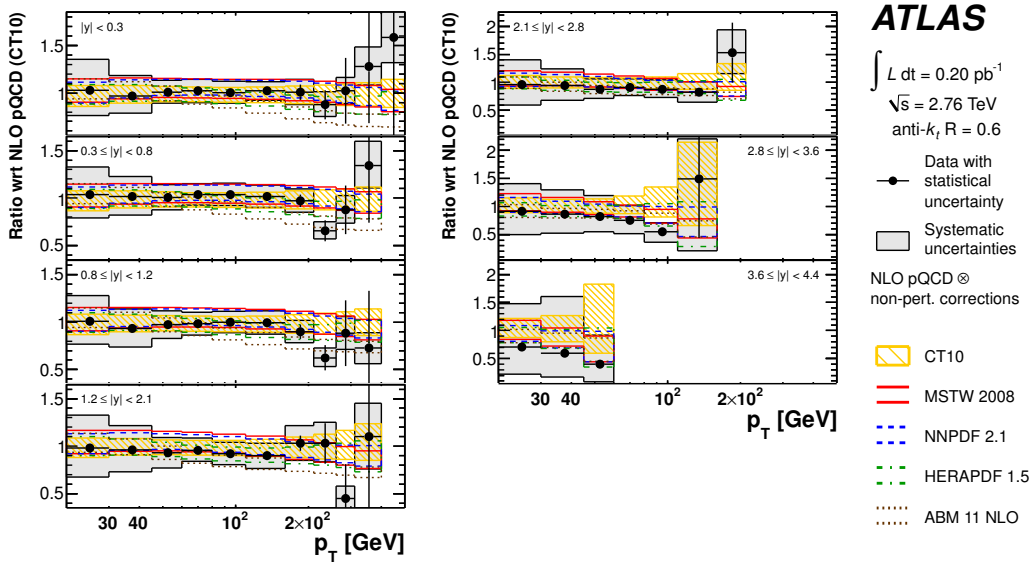

Figure 7.11: Ratio of the measured double-differential inclusive jet cross-section at $\sqrt{s} = 2.76\,\text{TeV}$ for anti-k_t jets with a radius parameter of $R = 0.6$ with respect to the theoretical predictions from a perturbative QCD calculation at NLO precision using NLOJET++ with the PDF set CT 10, corrected for non-perturbative effects. The ratio is shown as function of p_T separately for seven different bins of rapidity. The *shaded* and *hatched area* indicate the experimental and theoretical systematic uncertainties, respectively. The figure also shows the same theoretical calculation for a selection of different PDF sets, namely MSTW 2008, NNPDF 2.1, and HERAPDF 1.5. Statistically insignificant data points at large p_T are omitted. The uncertainty due to the luminosity measurement of 2.7% is not shown. [1]

measurement, since it employs different choices for e.g. α_S, heavy quark flavour scheme and the PDF parametrisation. As a result, it shows larger differences with respect to the others in the high p_T central region with a small uncertainty at the same time. While it describes the data very well in that region for $R = 0.4$, the agreement for $R = 0.6$ is poor.

The measured double-differential inclusive jet cross-section is also compared to theoretical predictions obtained using a perturbative QCD calculation at NLO with a matched parton shower approach instead of a bin-wise correction factor for non-perturbative effects. POWHEG provides the event generation at NLO, with the option `doublefsr` to solve the issue of events with large weights causing distortions of the final observables. PYTHIA is employed as parton shower simulator with two different tunes, AUET 2B and PERUGIA 2011. The comparison is showed with respect to the nominal prediction in Figures 7.12a and 7.12b for jets with $R = 0.4$ and $R = 0.6$, respectively.

When POWHEG is interfaced to PYTHIA with the AUET 2B tune, extraordinary agreement of the attained prediction and the data in the central values is found. In particular in the forward region, $3.6 < p_\text{T} < 4.4$, where the approach with bin-wise corrections for non-perturbative effects shows larger deviations, POWHEG performs very well. In addition, the agreement of the POWHEG prediction with data is equally good for both distance parameters. Hence, it confirms the same observation as the previous measurement, i.e. that the coherent approach from the matched parton shower seems to have advantages in this region. The fact that in general a much better agreement of the POWHEG predictions with the data is obtained for $\sqrt{s} = 2.76\,\text{TeV}$ is primarily related to the `doublefsr` approach to suppress spikes. Interestingly, the cut approach still results in an overestimation of the cross-section, although it generally

introduces a bias by removing events.

The results for the same setup but with the Perugia 2B tune produces a very similar shape of the cross-section. However, a constant offset of 10% with respect to Powheg with Pythia and the AUET 2B tune is observed. Again, this was already seen in the previous measurement and can be related to the differences in the determination of the non-perturbative correction shown in Section 2.2.3.

Summary

In summary, good agreement between various theoretical predictions and the data within their uncertainties is found. Yet, the perturbative QCD calculation at NLO with non-perturbative correction applied yields a different level of agreement of $10 - 20\%$ between the jet distance parameters $R = 0.4$ and $R = 0.6$. No such difference for the two radius parameters is present when interfacing a perturbative QCD calculation directly to the parton shower Monte Carlo simulation by means of the Powheg event generator in its revised version, resulting in an excellent description of the data. Moreover, some of the compared PDF sets seem describe the data better at high transverse momenta and large rapidities. However, the size of the experimental and theoretical uncertainties do not allow to select one prediction above the others. Nevertheless, this data provides the opportunity to improve the theoretical models, tunes, and PDF sets. The data is made available within the Durham HepData project [141], including a complete description of all correlations of the systematic uncertainties and the non-perturbative corrections.

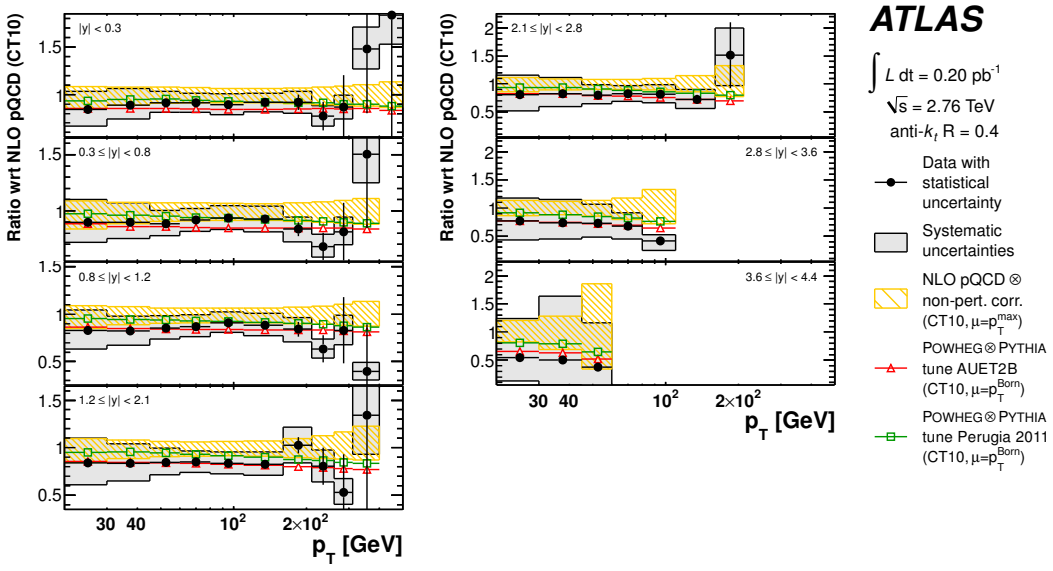

(a) radius parameter $R = 0.4$

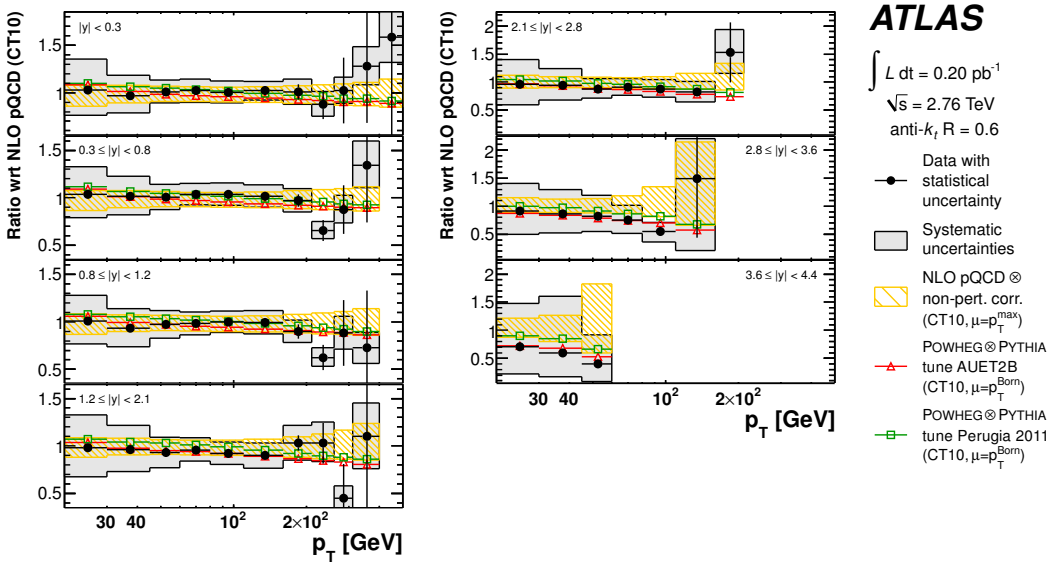

(b) radius parameter $R = 0.6$

Figure 7.12: Ratio of the measured double-differential inclusive jet cross-section at $\sqrt{s} = 2.76\,\text{TeV}$ for anti-k_t jets with respect to the theoretical predictions from a perturbative QCD calculation at NLO precision using NLOJET++ with CT 10, corrected for non-perturbative effects. The ratio is shown as function of p_T separately for seven different bins of rapidity. The *shaded* and *hatched area* indicate the experimental and theoretical systematic uncertainties, respectively. Also shown are theoretical predictions obtained with the POWHEG generator, interfaced to the parton shower simulator PYTHIA using the tunes AUET 2B and PERUGIA 2011. Only the statistical uncertainty is shown on the POWHEG prediction. Statistically insignificant data points at large p_T are omitted. The uncertainty due to the luminosity measurement of 2.7% is not shown. [1]

CHAPTER 8

Jet cross-section ratio

Inclusive jet cross-sections have been measured in various experiments with increasing centre-of-mass energies in the last decades. Before the LHC was put into operation, the most stringent tests of perturbative QCD at large energies have been performed at HERA[1], SPS[2] and the Tevatron[3]. At the HERA compound, electron-proton collisions were studied at energies of $\sqrt{s} = 300\,\text{GeV}$ and $\sqrt{s} = 319\,\text{GeV}$ [142–149]. Proton-antiproton collisions were analysed at the SPS particle accelerator with $\sqrt{s} = 546\,\text{GeV}$ and $\sqrt{s} = 630\,\text{GeV}$ [150–154], and at the Tevatron with $\sqrt{s} = 546\,\text{GeV}$, $\sqrt{s} = 630\,\text{GeV}$, $\sqrt{s} = 1.8\,\text{TeV}$ and $\sqrt{s} = 1.96\,\text{TeV}$ [134–140, 155–164]. Recently, proton-proton collisions at centre-of-mass energies above 900 GeV have been studied at the LHC. CMS has measured the inclusive jet cross-section at $\sqrt{s} = 7\,\text{TeV}$ [165–167], and ATLAS has provided results for $\sqrt{s} = 2.76\,\text{TeV}$ and $\sqrt{s} = 7\,\text{TeV}$ [1, 2, 126]. The latter have been presented in the previous chapters.

The increasing centre-of-mass energies have provided the possibility to investigate the scaling behaviour of the cross-section with $\sqrt{s}$. In this context, ratios of cross-sections at two different centre-of-mass energies at the same experiment are of particular interest. Many experimental uncertainties are detector dependent, and thus highly correlated between the two measurements entering the ratio. Since correlated uncertainties cancel in the ratio, the systematic uncertainty of the ratio can be reduced substantially with respect to the cross-section at one centre-of-mass energy only. Among the different sources of uncertainty, the most important one is the jet energy response of the calorimeter, which is, to first order, fully correlated. Residual differences are mostly due to the slightly different shape of the jet production cross-section at different centre-of-mass energy, as will be explained below.

Also for the theoretical predictions, some sources of uncertainty, such as the scale uncertainty, do not show a large dependence of $\sqrt{s}$ and can be significantly reduced by building the ratio. In a dedicated study of the opportunities of ratio measurements at the LHC [168], it has been shown that the residual uncertainties at high jet transverse momenta are dominated by the uncertainty on the PDFs. Hence, given a sufficiently small uncertainty on the experimental data, ratio measurements provide the possibility to improve the PDF determination at large x.

The same study [168] has also investigated the sensitivity of ratio measurements to physics effects beyond the SM. Considered are additional BSM contributions that add up to the cross-section predicted

[1] HERA - *Hadron-Elektron-Ring-Anlage* at DESY (*Deutsches Elektron-Synchrotron)*, Hamburg, Germany.
[2] SPS - *Super Proton Synchroton* at CERN, Geneva, Switzerland.
[3] Particle accelerator at Fermilab, Batavia, US.

by the SM as

$$\sigma_{\text{jet}} = \sigma_{\text{jet}}^{\text{SM}} + \sigma_{\text{jet}}^{\text{BSM}}. \tag{8.1}$$

The evolution of $\sigma_{\text{jet}}^{\text{BSM}}$ and $\sigma_{\text{jet}}^{\text{SM}}$ with $\sqrt{s}$ is required to be different in order to observe BSM phenomena in the ratio. A different dependency with respect to the SM is, however, present in many BSM models by introducing a new scale at which the additional contributions become accessible to the experiment at larger energies. Hence, given the small theoretical and experimental uncertainties, the cross-section ratio could provide a competitive approach to search for new phenomena.

Ratio measurements using jet production cross-sections at different centre-of-mass energies have been performed previously by several experiments, namely UA1[4] [154], UA2[5] [153], CDF[6] [156, 158] and D0[7] [161].

The ratio measurement presented here is based on the results of the analyses described in the previous chapters. While the approach for the measurement of the inclusive jet cross-section at $\sqrt{s} = 7\,\text{TeV}$ was driven by the jet calibration performance at that time, the analysis at $\sqrt{s} = 2.76\,\text{TeV}$ has been tailored to the ratio measurement. So instead of improving the individual contributions of the uncertainty, the same setup as in the measurement at $\sqrt{s} = 7\,\text{TeV}$ has been applied to sustain the correlations between the two measurements. The correlations between the different components of the systematic uncertainty are fully exploited for both, the theoretical and the experimental uncertainties.

To probe the impact of the ATLAS jet data in the PDF determination, a fit using the data from HERA and the inclusive jet cross-section measurement was performed in the course of the ratio analysis [1]. As in the ratio, the information about the correlations of the two analyses is fully exploited in the fitting procedure. Due to the close relation of this study to the ratio measurement, and since it is an excellent demonstration of the potential of ratio measurements, it is reported here.

The chapter is structured as follows. In Section 8.1, a definition of the ratio, the used binning and the calculation of correlated uncertainties is given. Sections 8.2 and 8.3 summarise the systematic uncertainties of theoretical predictions and the data, as well as their treatment for the ratio. The results for the ratio measurement are given in Section 8.4. The impact of the ratio with its reduced uncertainty on the PDF determination is presented in Section 8.5.

8.1 Definition of the cross-section ratio

The cross-section ratio is derived as function of the dimensionless quantity $x_{\text{T}} = 2p_{\text{T}}/\sqrt{s}$, as well as the transverse momentum. While the former provides a better sensitivity to the scaling behaviour of the strong interaction with the centre-of-mass energy, the latter is expected to result in a better cancellation of the experimental uncertainties.

Given the double-differential inclusive jet cross-section in Equation 1.29, a dimensionless, invariant cross-section $F(y, p_{\text{T}})$ can be defined as

$$p_{\text{T}}^4 E \frac{d^3\sigma}{dp^3} \longrightarrow \frac{p_{\text{T}}^3}{2\pi} \frac{d^2\sigma}{dp_{\text{T}}dy} = F(y, p_{\text{T}}). \tag{8.2}$$

Using the definition of x_{T} and $\frac{dp_{\text{T}}}{dx_{\text{T}}} = \frac{\sqrt{s}}{2}$, the corresponding dimensionless, invariant cross-section as

[4] UA1 - *Underground Area 1*, named after its location in the SPS accelerator ring.
[5] UA2 - *Underground Area 2* in the SPS accelerator ring.
[6] CDF - *Collider Detector at Fermilab*
[7] Named after its location in the Tevatron ring.

function of x_T follows as

$$F(y, x_T) = \frac{\sqrt{s^2}}{8\pi} x_T^3 \frac{d^2\sigma}{dx_T dy}. \tag{8.3}$$

In the simple quark-parton model [23, 24], the distribution of $F(y, x_T)$ obeys the Bjorken scaling, i.e. it only depends on the transverse momentum fraction x_T, but not on the absolute energy involved in the collision, as described in Section 1.2.2. Hence, the ratio ρ of the dimensionless invariant cross-section at two different centre-of-mass energies $\sqrt{s_1}$ and $\sqrt{s_2}$ is unity:

$$\rho(y, x_T) = \frac{F(y, x_T, \sqrt{s_1})}{F(y, x_T, \sqrt{s_2})} \overset{\text{Bjorken scaling}}{\longrightarrow} 1. \tag{8.4}$$

Quantum Chromodynamics, however, predicts a violation of the scaling behaviour due to the running of the strong coupling constant α_S and the evolution of the PDF with Q^2, so that $\rho(y, x_T) \neq 1$. The measurement of $\rho(y, x_T)$ thus is a stringent test of QCD. Using the definition of $F(y, x_T)$ from Equation 8.3 in the ratio, it follows

$$\rho(y, x_T) = \left(\frac{\sqrt{s_1}}{\sqrt{s_2}}\right)^3 \cdot \frac{\sigma(y, x_T, \sqrt{s_1})}{\sigma(y, x_T, \sqrt{s_2})}, \tag{8.5}$$

where $\sigma(y, x_T, \sqrt{s})$ corresponds to the measured cross-section $d^2\sigma/dp_T dy$ averaged over one bin (y, x_T). Since $x_T(p_T, \sqrt{s_1}) \neq x_T(p_T, \sqrt{s_2})$ for a given p_T, the transverse momenta of the two measurements are mixed in the ratio.

The ratio is also determined as function of p_T

$$\rho(y, p_T) = \frac{\sigma(y, p_T, \sqrt{s_1})}{\sigma(y, p_T, \sqrt{s_2})}, \tag{8.6}$$

where $\sigma(y, p_T, \sqrt{s})$ is the measured double-differential cross-section in a bin (y, p_T) at a centre-of-mass energy $\sqrt{s}$. Throughout this chapter, the centre-of-mass energies s_1 and s_2 are defined as $\sqrt{s_1} = 2.76\,\text{TeV}$ and $\sqrt{s_2} = 7\,\text{TeV}$, respectively.

8.1.1 Binning

The ratio measurement is performed double-differentially in seven bins of rapidity, and in bins of p_T and x_T, respectively. The boundaries for the binning are defined by the measurement at $\sqrt{s} = 7\,\text{TeV}$. For $\rho(y, p_T)$, the binning is identical for both cross-section measurements and $\sigma(y, p_T, \sqrt{s})$ can be used directly. In case of $\rho(y, x_T)$, the bin boundaries are obtained from the $\sqrt{s} = 7\,\text{TeV}$ measurement as $x_T^{(i)} = 2p_T{}^{(i)}/\sqrt{s} = 7\,\text{TeV}$, where $p_T{}^{(i)}$ and $x_T{}^{(i)}$ are the lower boundaries for a bin i. At $\sqrt{s} = 2.76\,\text{TeV}$, this translates into the bin boundaries given in Table 8.1.

8.1.2 Correlation between the measurements

A full correlation of an uncertainty component among the two measurements does not imply that their uncertainties cancel perfectly. If the two measurements have a different sensitivity on a particular component, a shift of one standard deviation results in a different relative shift for each of the two. In case of the jet energy calibration, a different dependence on the individual components is already given by

x_T	p_T [GeV] $\sqrt{s}$ = 7 TeV	p_T [GeV] $\sqrt{s}$ = 2.76 TeV
0.0171	60	23.65
0.0229	80	31.54
0.0314	110	43.37
0.0457	160	63.08
0.0600	210	82.80
0.0743	260	102.5
0.0886	310	122.2
0.1143	400	157.7
0.1429	500	197.1
0.1714	600	236.5
0.2286	800	315.4
0.2857	1000	394.2
0.3429	1200	473.1

Table 8.1: Bin boundaries in the variable x_T used in the extraction of $\rho(y, x_T)$, the cross-section ratio as a function of x_T at different centre-of-mass energies. Also shown are the corresponding jet p_T values at each centre-of-mass energy.

the different shape of the jet cross-section as function of p_T. Since the absolute value of the jet energy scale is not known, the residual difference in the variation by one standard deviation of the cross-section is taken as the uncertainty on the ratio. Using simplified expressions for the cross-section at a centre-of-mass energy $\sqrt{s}$, $\sigma(\sqrt{s})$, the systematic uncertainty can be written as

$$\Delta\sigma_j(\sqrt{s}) = \sigma_j(\sqrt{s}) - \sigma(\sqrt{s}), \tag{8.7}$$

where $\sigma_j(\sqrt{s})$ corresponds to the one standard deviation cross-section. Using the simplified expression for the cross-section ratio,

$$\rho = \frac{\sigma(\sqrt{s_1})}{\sigma(\sqrt{s_2})}, \tag{8.8}$$

the one standard deviation translates into

$$\rho_j = \frac{\sigma(\sqrt{s_1}) + \Delta\sigma_j(\sqrt{s_1})}{\sigma(\sqrt{s_2}) + \Delta\sigma_j(\sqrt{s_2})}. \tag{8.9}$$

Using Equations 8.7 and 8.9, the systematic uncertainty of a correlated uncertainty source j in the ratio can be written as

$$\frac{\Delta\rho_j}{\rho_j} = \frac{\rho_j - \rho}{\rho} = \frac{\rho_j}{\rho} - 1 = \frac{1 + \Delta\sigma_j(\sqrt{s_1})/\sigma(\sqrt{s_1})}{1 + \Delta\sigma_j(\sqrt{s_2})/\sigma(\sqrt{s_2})} - 1. \tag{8.10}$$

Uncorrelated sources of uncertainty k on the other hand are added in quadrature:

$$\frac{\Delta\rho_k}{\rho_k} = \sqrt{\left(\frac{\Delta\sigma_k(\sqrt{s_1})}{\sigma(\sqrt{s_1})}\right)^2 + \left(\frac{\Delta\sigma_k(\sqrt{s_2})}{\sigma(\sqrt{s_2})}\right)^2}. \tag{8.11}$$

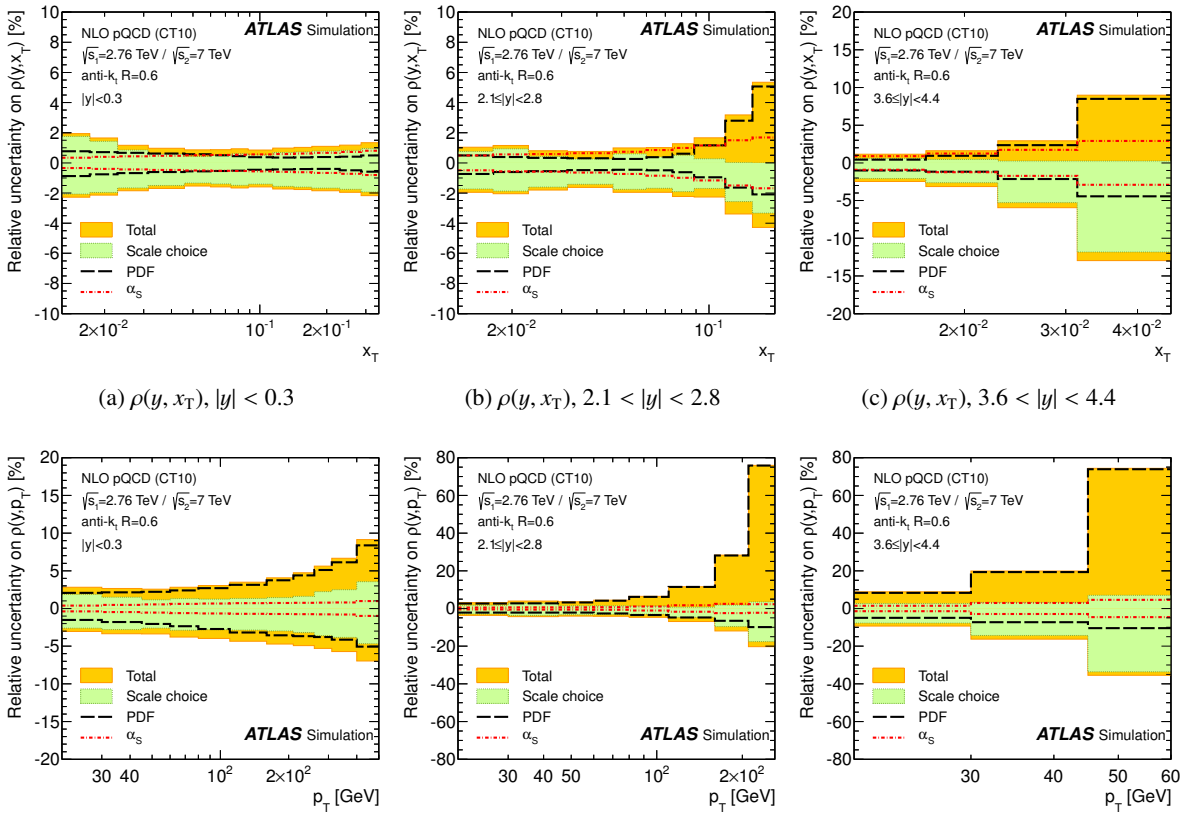

(a) $\rho(y, x_\mathrm{T})$, $|y| < 0.3$ (b) $\rho(y, x_\mathrm{T})$, $2.1 < |y| < 2.8$ (c) $\rho(y, x_\mathrm{T})$, $3.6 < |y| < 4.4$

(d) $\rho(y, p_\mathrm{T})$, $|y| < 0.3$ (e) $\rho(y, p_\mathrm{T})$, $2.1 < |y| < 2.8$ (f) $\rho(y, p_\mathrm{T})$, $3.6 < |y| < 4.4$

Figure 8.1: Theoretical uncertainty of the perturbative QCD prediction for the ratio of the inclusive jet cross-section at $\sqrt{s} = 2.76\,\mathrm{TeV}$ and $\sqrt{s} = 7\,\mathrm{TeV}$ (a)-(c) as function of x_T, and (d)-(f) as function of p_T, in three representative rapidity bins. The contributions from the factorisation and renormalisation scale, the PDF and the strong coupling constant α_S as shown separately. Jets are defined using the anti-k_t algorithm with $R = 0.6$. [1]

8.2 Theoretical predictions

The cross-section ratio is compared to the theoretical prediction from the perturbative QCD calculation at NLO with non-perturbative corrections applied. The same setup is used for the calculation at both centre-of-mass energies, and the ratio is obtained according to Equations 8.5 and 8.6, exactly as for the data, with the binning described above.

8.2.1 NLO perturbative QCD prediction

NLOJET++ 4.1.2 is employed for the NLO calculation, with the scale as for the individual cross-section measurements, $\mu_F = \mu_R = p_\mathrm{T}^{\max}(y_i)$. The CT 10 PDF set is used as the default. The considered sources of uncertainty for the NLO perturbative QCD calculation are the strong coupling α_S, the scales μ_F and μ_R, and the PDF set. All sources are considered as 100% correlated between the two centre-of-mass energies. The uncertainty for each source is calculated according to Equation 8.10. The residual difference to the nominal ratio is taken as uncertainty for the studied source. The theoretical uncertainty is presented in Figures 8.1a, 8.1b and 8.1c for the cross-section ratio $\rho(y, x_\mathrm{T})$ in three representative rapidity bins. In general, a reduction of the uncertainty by a factor of 3 to 10 is achieved, and the

fractional contribution of the PDF is largely reduced in comparison to the uncertainty for the prediction of the individual cross-section. Instead, the dominant uncertainty is the scale choice. In the barrel, shown in Figure 8.1a, the uncertainty is mostly below 2% and reaches 1% at $x_T = 0.1$. In the region $2.1 \leq y < 2.8$, shown in Figure 8.1b, the uncertainty is $d\sigma/\sigma = ^{+1}_{-2}$ % for low x_T and rises to a maximum of $d\sigma/\sigma = ^{+5}_{-4}$ % due to the contributions from the PDF at the upper bound, and the scale uncertainty at the lower one. The forward region, shown in Figure 8.1c, is similar, but with $d\sigma/\sigma = ^{+8}_{-13}$ % the uncertainties are larger at high x_T.

Figures 8.1d, 8.1e and 8.1f show the uncertainties on the theoretical prediction in bins of p_T. Although not as strong as for the ratio in bins of x_T, the reduction of the uncertainty in comparison to the individual cross-section is substantial, being a factor of about two. The shape is very similar as for the cross-section at a fixed centre-of-mass energy, but the fractional contribution of the strong coupling is very much reduced. The lower bound is dominated by the uncertainty on the scale. The upper bound is driven by the uncertainty on the PDF, especially at high p_T in the forward region. This is promising for the PDF determination using the ratio measurement.

8.2.2 Non-perturbative corrections

Pythia 6.425 with the AUET 2B tune provides the nominal non-perturbative corrections. The same set of tunes as for the inclusive jet cross-section described in Section 2.2.3 is considered to obtain the uncertainty on the non-perturbative corrections. For each tune, the ratio is determined individually, and the envelope of all tunes is taken as uncertainty.

The non-perturbative correction for $\rho(y, x_T)$ is essentially driven by the $\sqrt{s} = 2.76$ TeV measurement. The reason is the p_T range of the two individual cross-sections that enter the ratio measurement. For $\sqrt{s} = 2.76$ TeV, the lowest x_T bin corresponds to a p_T of about 23 GeV, where the non-perturbative corrections are large as has been shown in Figure 2.4. For $\sqrt{s} = 7$ TeV on the other hand, the lowest x_T bin corresponds to a p_T of 60 GeV. Here, the non-perturbative corrections are already close to unity. For jets with $R = 0.4$, shown in Figure 8.2a, the correction is about 0.9 at low x_T. For $R = 0.6$ it is 1.1, as shown in Figure 8.2b. The uncertainty band decreases from 10% to 2% from low to high x_T. Hence, it is about a factor of two smaller than for the individual cross-sections.

The corrections for the prediction in bins of p_T is shown in Figures 8.2c and 8.2d. For a radius parameter of $R = 0.4$, they are basically identical to the non-perturbative corrections at $\sqrt{s} = 2.76$ TeV, since those obtained at $\sqrt{s} = 7$ TeV are very close to unity. For $R = 0.6$, the corrections at the two cross-sections have the same shape, but they are larger in size at $\sqrt{s} = 7$ TeV. The latter being in the denominator, the correction factors start at 0.8 at low p_T, and rises slowly to 1.0 for larger p_T. For $\rho(y, p_T)$ the uncertainty is not reduced as much as in for $\rho(y, x_T)$ because Herwig++ with the underlying event tune UE 7000-2 gives a very different correction than Pythia at low p_T and enlarges the error band.

Summary on theoretical uncertainties

In summary, the uncertainties on the perturbative QCD calculation at NLO is largely reduced in the cross-section ratio. In particular for $\rho(y, x_T)$, the remaining uncertainty is very small. The uncertainty on the non-perturbative corrections is also reduced, but not as much as the uncertainties on the matrix element calculation. Hence, they dominate the total uncertainty on the theoretical predictions at low values for both x_T and p_T, while for large values, the uncertainties due to the PDF and the scale choice are still the major contributions.

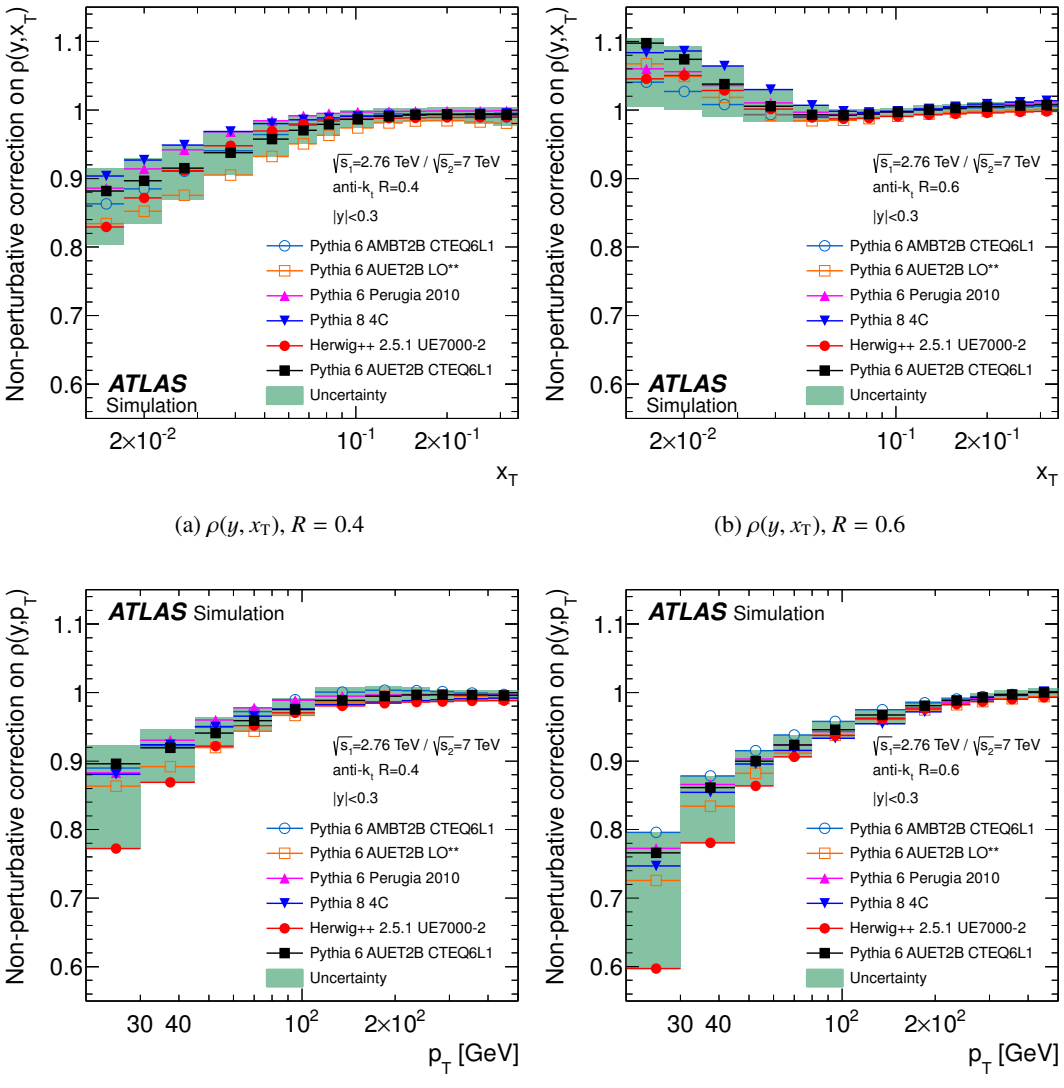

(a) $\rho(y, x_{\mathrm{T}})$, $R = 0.4$

(b) $\rho(y, x_{\mathrm{T}})$, $R = 0.6$

(c) $\rho(y, p_{\mathrm{T}})$, $R = 0.4$

(d) $\rho(y, p_{\mathrm{T}})$, $R = 0.6$

Figure 8.2: Non-perturbative corrections for the ratio of the inclusive jet cross-section at $\sqrt{s} = 2.76$ TeV and $\sqrt{s} = 7$ TeV, $\rho(y, x_{\mathrm{T}})$ and $\rho(y, p_{\mathrm{T}})$, for anti-k_t jets with $R = 0.4$ and $R = 0.6$ in the rapidity region $|y| < 0.3$. The nominal correction is obtained from the Pythia Monte Carlo generator with the tune Auet 2b, shown in *full squares*. The uncertainty band, indicated by the *shaded band*, is obtained from the envelope of different event generators and tunes. For better visibilities, only a selection is shown. [1]

8.3 Experimental data

The measurement of the cross-section ratio is based on the results of the ATLAS jet measurement at $\sqrt{s} = 2.76\,\text{TeV}$ [1] and $\sqrt{s} = 7\,\text{TeV}$ [1, 2]. The former is available in two different binnings. For $\sigma(y, p_\text{T}, 2.76\,\text{TeV})$, the results as presented in the previous Chapter 7 is used. For $\sigma(y, x_\text{T}, 2.76\,\text{TeV})$, the cross-section measurement is performed with an adapted p_T binning according to Table 8.1.

8.3.1 Jets in the transition region

A different treatment of jets in the transition region between the tile barrel and extended barrel was applied at the two centre-of-mass energies. For the data at $\sqrt{s} = 7\,\text{TeV}$, the impact of this category of jets is small, and no bias due to the different setup between the two measurements is expected. In the Monte Carlo samples however, their contribution is substantial, and the different treatment has effects on the unfolding process, thus imposing a bias of the measurement. Since the resulting bias is not covered by the jet selection efficiency component of the uncertainty, it is corrected for in the ratio by re-performing the unfolding of the 7 TeV data with a proper treatment of this kind of jets.

8.3.2 Systematic uncertainties

The determination of the systematic uncertainty on the data is based on the relative uncertainty $\Delta\sigma_j(\sqrt{s})/\sigma(\sqrt{s})$ due to the individual component j obtained in the cross-section measurements at a centre-of-mass energy $\sqrt{s}$. All sources listed in Table 5.1 are considered. Components are treated as either 100% correlated, or not correlated at all between the two measurements and treated according to Equations 8.10 and 8.11, respectively. Correlations within the individual measurement are already included in $\Delta\sigma_j(\sqrt{s})/\sigma(\sqrt{s})$.

Correlated sources of uncertainty are the jet reconstruction, JES, and the jet resolution, JER and JAR. This is motivated by the fact that the jet measurement itself primarily depends on the p_T and y of the individual jet, independent of $\sqrt{s}$. The centre-of-mass energy enters the jet cross-section measurement only indirectly, for instance through the PDFs, where it influences the gluon and quark fractions: for high $\sqrt{s}$, jets from gluons become more likely, which have a slightly different response than quark jets. Furthermore, the p_T spectrum of the underlying event and initial state radiation changes with $\sqrt{s}$. Nevertheless, these contributions can be considered as higher order effects, as the general validity of the jet calibration at $\sqrt{s} = 2.76\,\text{TeV}$ has been confirmed by dedicated studies presented in Section 5.2.6.

The following uncertainty sources possess a certain degree of correlation, but are conservatively treated as uncorrelated. The jet selection efficiency is influenced by running conditions in general, which are not correlated between the two data taking periods. Furthermore, the jet selection was only cross-checked with the 2.76 TeV data, but not determined at high precision due to the statistical limitations. Since differences are observed in the jet selection efficiency at low p_T for the datasets, it is conservatively treated as uncorrelated. No correlation is assumed for the trigger efficiency because different trigger items are employed for the two analysis. The unfolding depends to a certain degree on the correct description of the data in the Monte Carlo sample. Although the detector simulation is identical between the two centre-of-mass energies, slightly different configurations have been applied regarding the simulated running conditions. Hence, the matching efficiency can vary. In addition, the results for the closure tests of the unfolding are different, for which a correlation is hard to assess. Therefore, the uncertainties related to the unfolding method are treated as uncorrelated.

A correction for pile-up contributions is only applied in the measurement at $\sqrt{s} = 7\,\text{TeV}$. Hence, no cancellation of uncertainties is applicable, and it is added as is to the ratio uncertainty.

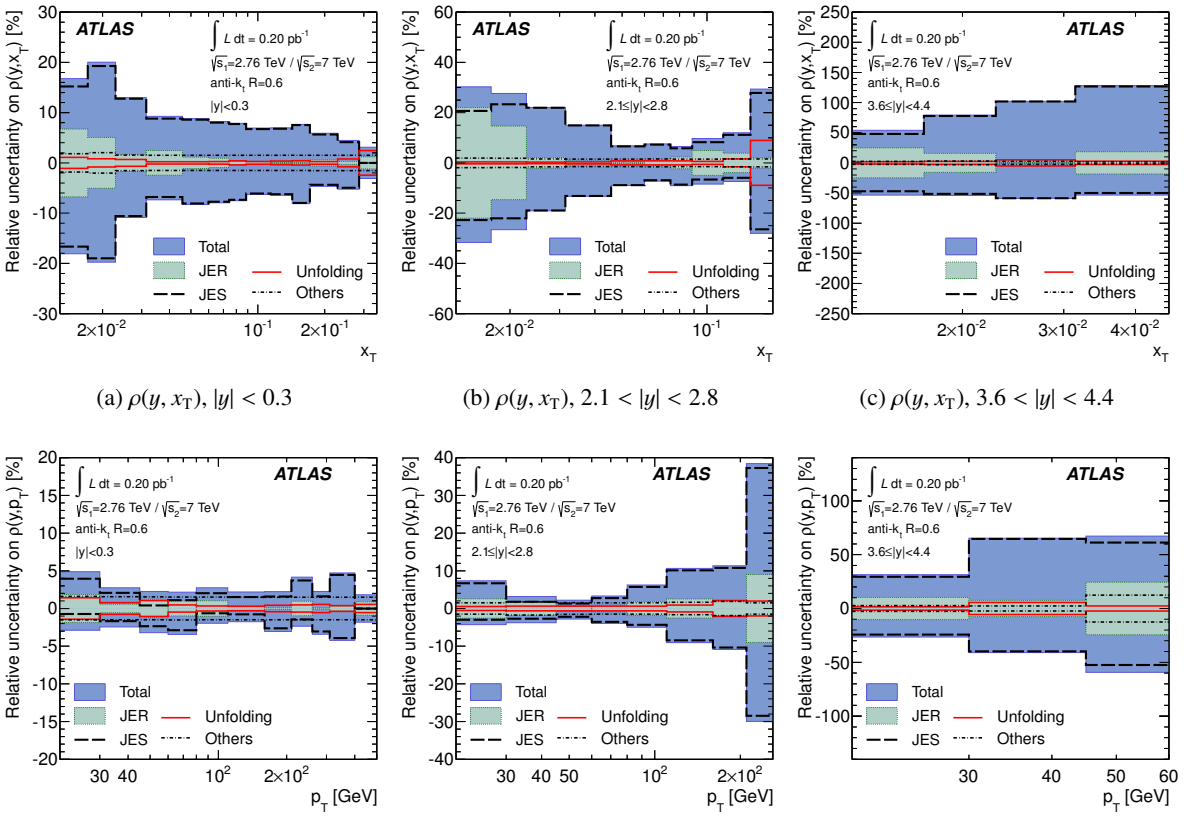

(a) $\rho(y, x_{\mathrm{T}})$, $|y| < 0.3$ (b) $\rho(y, x_{\mathrm{T}})$, $2.1 < |y| < 2.8$ (c) $\rho(y, x_{\mathrm{T}})$, $3.6 < |y| < 4.4$

(d) $\rho(y, p_{\mathrm{T}})$, $|y| < 0.3$ (e) $\rho(y, p_{\mathrm{T}})$, $2.1 < |y| < 2.8$ (f) $\rho(y, p_{\mathrm{T}})$, $3.6 < |y| < 4.4$

Figure 8.3: Systematic uncertainty on the ratio measurement of the inclusive jet cross-section at $\sqrt{s} = 2.76\,\mathrm{TeV}$ and $\sqrt{s} = 7\,\mathrm{TeV}$ (a)-(c) as function of x_{T} $\rho(y, x_{\mathrm{T}})$, and (d)-(f) as function of p_{T} $\rho(y, p_{\mathrm{T}})$, in three representative rapidity bins. Jets are defined using the anti-k_t algorithm with $R = 0.6$. The contributions from the jet energy scale, the jet energy resolution, the unfolding procedure and other sources are shown separately. The uncertainty due to the luminosity measurement in the two datasets is not included. [1]

Figures 8.3a, 8.3b and 8.3c show the systematic uncertainty on the cross-section ratio in bins of x_{T} for jets with $R = 0.6$. The result for $R = 0.4$ is similar, except being slightly smaller at low x_{T}, as shown in Figure A.7 in the appendix. In the central region, the total systematic uncertainty just reaches 20% at low x_{T} and falls below 10% at high x_{T}. Up to a rapidity of $|y| = 2.8$, the uncertainty at low x_{T} increases to about 30%, while it stays at 10% for high x_{T}. In the very forward region, the uncertainty reaches 60% for the lower bound, and 60 − 120% for the upper one. As before, the systematic uncertainty is dominated by the JES component, with additional contributions from the JER at low x_{T}. Other sources are negligible. The cancellation of the JES is not perfect for $\rho(y, x_{\mathrm{T}})$ due to the mixing of different p_{T} from the two measurements in one bin of x_{T}. Since the large systematic uncertainty for $p_{\mathrm{T}} < 60\,\mathrm{GeV}$ at $\sqrt{s} = 7\,\mathrm{TeV}$ does not enter the ratio, it's mostly the uncertainty from $\sqrt{s} = 2.76\,\mathrm{TeV}$ in that p_{T} region that is causing larger residual uncertainties.

The systematic uncertainty for $\rho(y, p_{\mathrm{T}})$ is shown in Figures 8.3d, 8.3e and 8.3f for jets with $R = 0.6$. Results for jets with $R = 0.4$ are similar, as shown in Figure A.7 in the appendix. For the ratio as a function of the same p_{T} in both numerator and denominator, the cancellation of the jet calibration components is much more effective, since the calibration is a function of p_{T} itself. Residual differences

between the systematic uncertainty of the two measurements only originate in the different shape of the cross-section, leading to different bin migrations. The total systematic uncertainty for $\rho(y, p_T)$ is below 5% in the central region, and almost as low as 2% in some bins. Between $0.8 < |y| < 2.8$ the uncertainty at high p_T increases, but mostly stays below 5%. Only in the highest bins, it reaches up to 40% due to the large uncertainty at $\sqrt{s} = 2.76\,\text{TeV}$. The uncertainty in the forward region is within $^{+100}_{-70}$ for the two radius parameters.

In total, a substantial reduction of the uncertainty is achieved in the ratio, especially for $\rho(y, p_T)$, where the uncertainty is reduced by a factor of up to 5. This shows the potential of the ratio measurement, reaching an unprecedented precision for a jet production measurement.

8.3.3 Luminosity uncertainty

The summary of the luminosity uncertainty is given in Table 4.2 of Section 4.5. Amounting to 2.7% and 3.4%, the luminosity uncertainties represent a substantial contribution to the uncertainty for the ratio in bins of p_T, where the systematic uncertainty is as low as a few percent. The correlation between individual components of the measurement are as follows. Significant modifications of the beam instrumentation to measure the bunch charge have been deployed between the data taking in 2010 and 2011. Therefore, this contribution has to be considered as uncorrelated to first order. The van-der-Meer scan depends strongly on the beam parameters during the scan and hence is largely uncorrelated; the common uncertainty components on the method, like the fit model, only make a small contribution. The long-term stability of the luminosity algorithms accounts for drifts of the calibration during the data taking, and is uncorrelated as well. Hence, the luminosity uncertainties must be considered as uncorrelated, and the combined uncertainty amounts to 4.3%.

8.3.4 Precision of the beam energy

No direct measurement of the beam energy at the LHC exists to date, since no precision spectrometer is installed. Instead, the beam energy is determined on basis of the magnetic model of the LHC. In general, the accuracy of the magnetic model has been determined on a subset of the magnets at a level of 0.1%. The absolute scale of the model is obtained from the beam energy at the injection, $E_{\text{beam}} = 450\,\text{GeV}$, which is precisely known from the injector calibration. Higher beam energies are determined from the extrapolation using the magnetic model and yield values of $1381 \pm 2\,\text{GeV}$ and $3502 \pm 4\,\text{GeV}$ [169].

The beam-beam correlations at a given $\sqrt{s}$ can be assumed as 100% because both beams are housed in the same dipole magnet and accelerated with the same frequency in the RF cavities. Very high correlation is given also between different centre-of-mass energies. Assuming an uncertainty of 0.1% on the ratio $(\sqrt{s_1})/\sqrt{s_2})^3$ in Equation 8.5, the resulting uncertainty on $\rho(y, x_T)$ is 0.4% and thus negligible.

8.4 Results

Figures 8.4a and 8.4b show the result of the ratio measurement $\rho(y, x_T)$ for seven bins of rapidity and jets with $R = 0.4$ and $R = 0.6$, respectively. It is based on the inclusive jet cross-section measurements at $\sqrt{s} = 2.76\,\text{TeV}$ with a corresponding integrated luminosity of $0.20\,\text{pb}^{-1}$ recorded in 2011, and at $\sqrt{s} = 7\,\text{TeV}$ with a corresponding integrated luminosity of $37.3\,\text{pb}^{-1}$ from the data taking in 2010. The ratio spans a rapidity range of $|y| < 4.4$ and covers $0.017 < x_T < 0.343$, exceeding previous measurements by almost one order of magnitude. The obtained ratio for $R = 0.6$ is approximately constant at $\rho(y, x_T) = 1.5$, while he ratio for $R = 0.4$ shows a dependency on both x_T and rapidity, but also approaches a value of 1.5 at larger x_T for the central region.

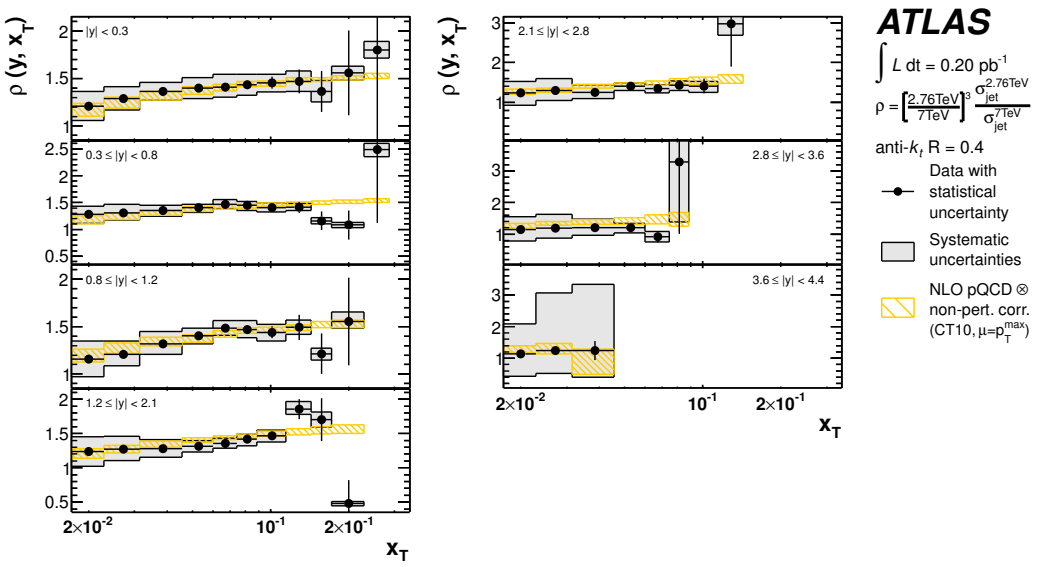

(a) radius parameter $R = 0.4$

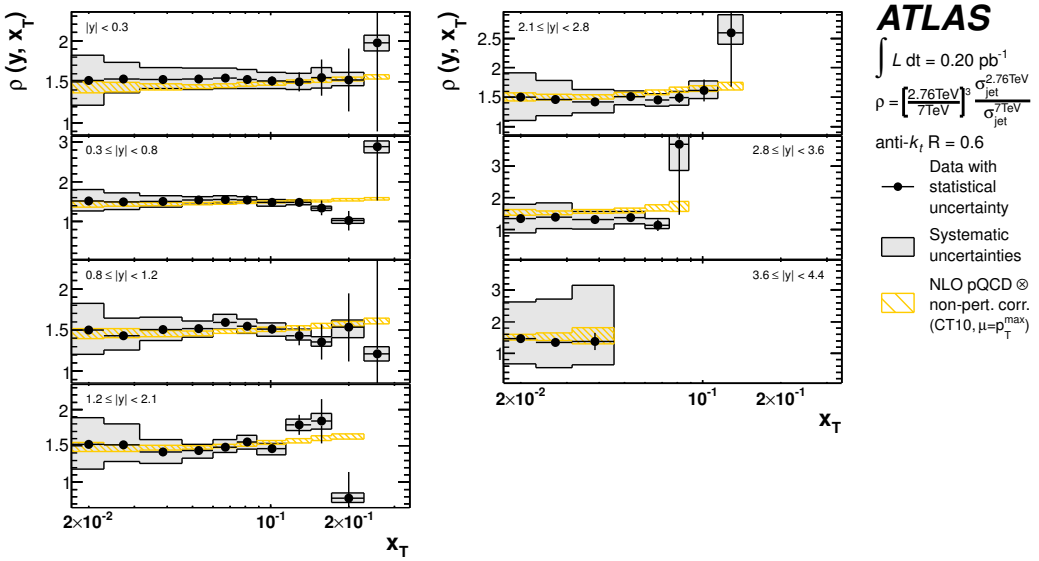

(b) radius parameter $R = 0.6$

Figure 8.4: Ratio $\rho(y, x_T)$ of the inclusive jet cross-section measurements as function of x_T at $\sqrt{s} = 2.76$ TeV with a corresponding integrated luminosity of $0.20\,\text{pb}^{-1}$, and at $\sqrt{s} = 7$ TeV with a corresponding integrated luminosity of $37.3\,\text{pb}^{-1}$. Jets are defined using the anti-k_t algorithm. The ratio is compared to the theoretical prediction obtained from a perturbative QCD calculation at NLO precision using the generator NLOJET++ with the CT 10 PDF set. Non-perturbative corrections from the PYTHIA event generator with the AUET 2B tune are applied. The systematic experimental and theoretical uncertainties are shown in the *shaded* and *hatched bands*. The uncertainty on the luminosity is not included. Statistically insignificant data points at large x_T are omitted. [1]

The data is compared to the prediction from a perturbative QCD calculation at NLO using NLOJET++. To account for non-perturbative effects, corrections obtained from PYTHIA are applied. Very good agreement with the data is found. The size of the theory uncertainty is much smaller than the experimental one across the entire phase space. The statistical uncertainty on the data dominates at high x_T due to the limited number of events in the dataset at $\sqrt{s} = 2.76\,\text{TeV}$. Particularly in the central rapidity region where the experimental uncertainty is small, $\rho(y, x_T)$ is clearly not consistent with unity. This confirms previous studies observing the scale breaking behaviour of the jet cross-section with $\sqrt{s}$ [153, 156, 158, 161, 170].

The cross-section ratio as function of p_T is shown in Figure 8.5a as the double-ratio with respect to the theory prediction for jets with $R = 0.4$. CT 10 is used as the nominal PDF set. The uncertainty on the data is generally smaller than the theory uncertainty, except the very forward region. The statistical uncertainty on the data is substantial at high p_T, again due to the small dataset at $\sqrt{s} = 2.76\,\text{TeV}$.

Due to the large reduction of the experimental uncertainty in the ratio, the comparison of data and theory shows some deviations that are not directly covered by the uncertainty bands. In the central region, a difference of up to 15% at a p_T of about 40 GeV and a slightly different shape is observed. For $|y| > 0.8$, the prediction describes the data well. In the very forward region, the data points are $10-40\%$ below the theory, but the difference is not as pronounced as for the individual jet cross-section measurements.

Results for $R = 0.6$ are very similar, as shown in Figure 8.5b. Unlike in the individual cross-section measurements, no difference in normalisation is observed between the two radius parameters. This indicates that the yet unknown effect leading to the deviation between data and theory cancels in the ratio.

The ratio is furthermore compared to theoretical prediction on basis of other PDF sets, namely MSTW 2008, HERAPDF 1.5, NNPDF 2.1, and ABM 11. Generally, the observations made for the previous measurements apply here as well: all PDF sets give similar predictions, apart from ABM 11 which does not describe the data well for $|y| < 2.8$. But the smaller experimental uncertainties in the ratio $\rho(y, p_T)$ suggest that the ATLAS jet data may contribute to the determination of the PDF. This will be investigated in the Section 8.5.

Comparison of jet cross-section measurements

A comparison of jet cross-section measurements at different centre-of-mass energies is shown in Figures 8.6 and 8.7 as function of p_T and x_T, respectively. It comprises measurements in pp collisions at the SPS with $\sqrt{s} = 546\,\text{GeV}$ and $\sqrt{s} = 630\,\text{GeV}$ from the UA1 and UA2 experiments [150, 152, 153],

Table 8.2: Overview of measurements used in the comparison of inclusive jet cross-sections from various experiments at different centre-of-mass energies in Figures 8.6 and 8.7). Table also appears in [171]

ref.	experiment	year	$\sqrt{s}$	luminosity	jet algorithm	p_T range	rapidity range
[150]	UA1	1985	546 GeV	64.6nb^{-1}	cone	$24 \le E_T < 120$ GeV	$\|\eta\| < 1.4$
[153]	UA2	1985	546 GeV	140nb^{-1}	cone	$31 \le p_T < 124$ GeV	$\|\eta\| < 0.85$
[152]	UA2	1991	630 GeV	7.54pb^{-1}	cone	$40 \le p_T < 180$ GeV	$\|\eta\| < 2$
[137]	CDF	2008	1960 GeV	1.13fb^{-1}	cone	$62 \le p_T < 700$ GeV	$\|y\| < 2.1$
[138]	D0	2008	1960 GeV	0.70fb^{-1}	cone	$50 \le p_T < 600$ GeV	$\|y\| < 2.4$
[165]	CMS	2011	7000 GeV	34pb^{-1}	anti-k_t	$18 \le p_T < 1100$ GeV	$\|y\| < 3.0$
[2]	ATLAS	2012	7000 GeV	37pb^{-1}	anti-k_t	$20 \le p_T < 1500$ GeV	$\|y\| < 4.4$
[1]	ATLAS	2013	2760 GeV	0.20pb^{-1}	anti-k_t	$20 \le p_T < 430$ GeV	$\|y\| < 4.4$

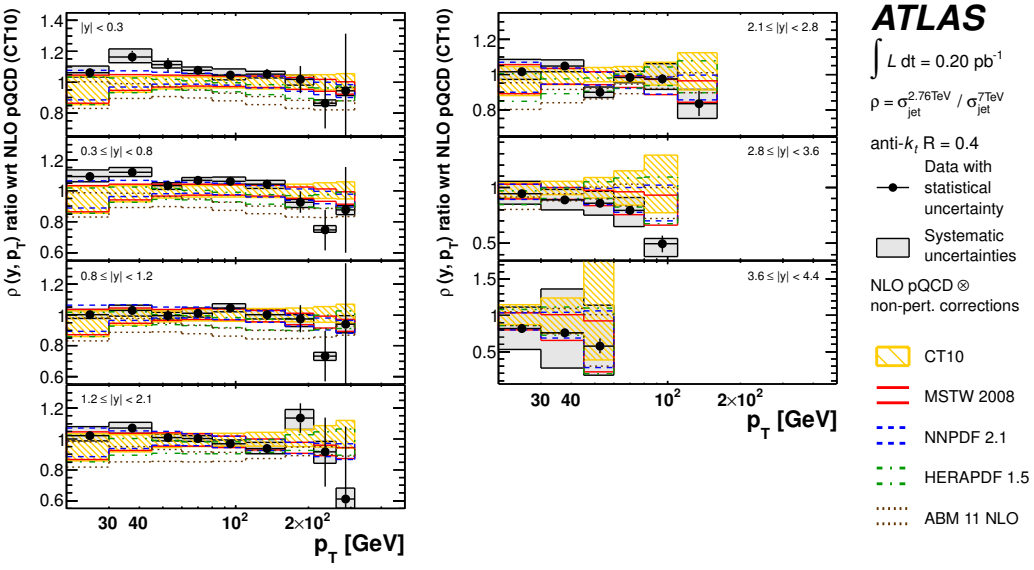

(a) radius parameter $R = 0.4$

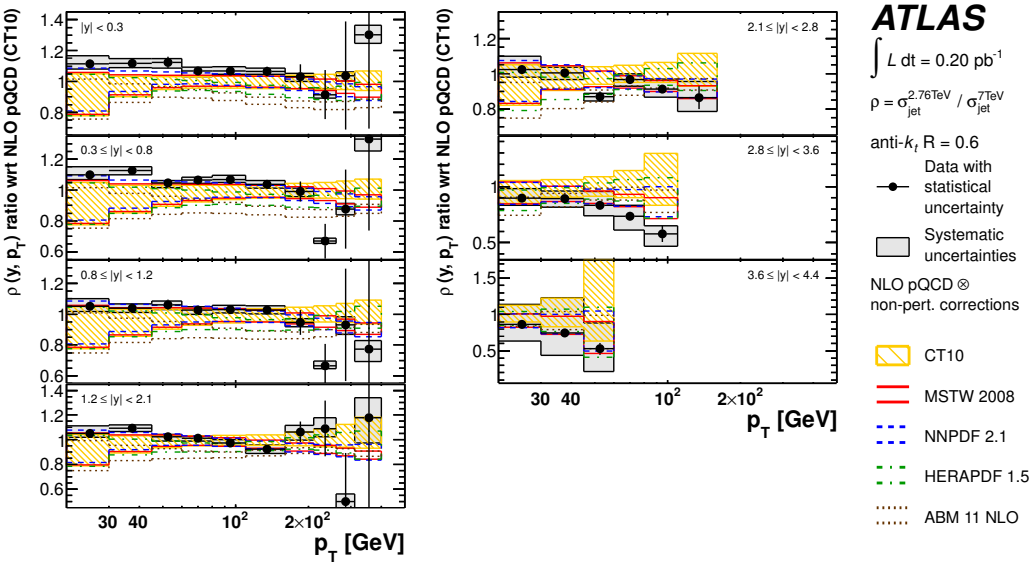

(b) radius parameter $R = 0.6$

Figure 8.5: Ratio $\rho(y, p_T)$ of the inclusive jet cross-section measurements as function of p_T at $\sqrt{s} = 2.76$ TeV and $\sqrt{s} = 7$ TeV, shown as double ratio of data divided by the theoretical predictions. Jets are defined using the anti-k_t algorithm. The theoretical prediction obtained from a perturbative QCD calculation at NLO precision using the generator NLOJET++ with the CT 10 PDF set. Non-perturbative corrections from the PYTHIA event generator with the AUET 2B tune are applied. The systematic experimental and theoretical uncertainties are shown in the *shaded* and *hatched bands*, respectively. Also shown are the same theoretical calculations for a selection of different PDF sets, namely MSTW 2008, NNPDF 2.1, HERAPDF 1.5 and ABM 11. The uncertainty on the luminosity is not included. Statistically insignificant data points at large x_T are omitted. [1]

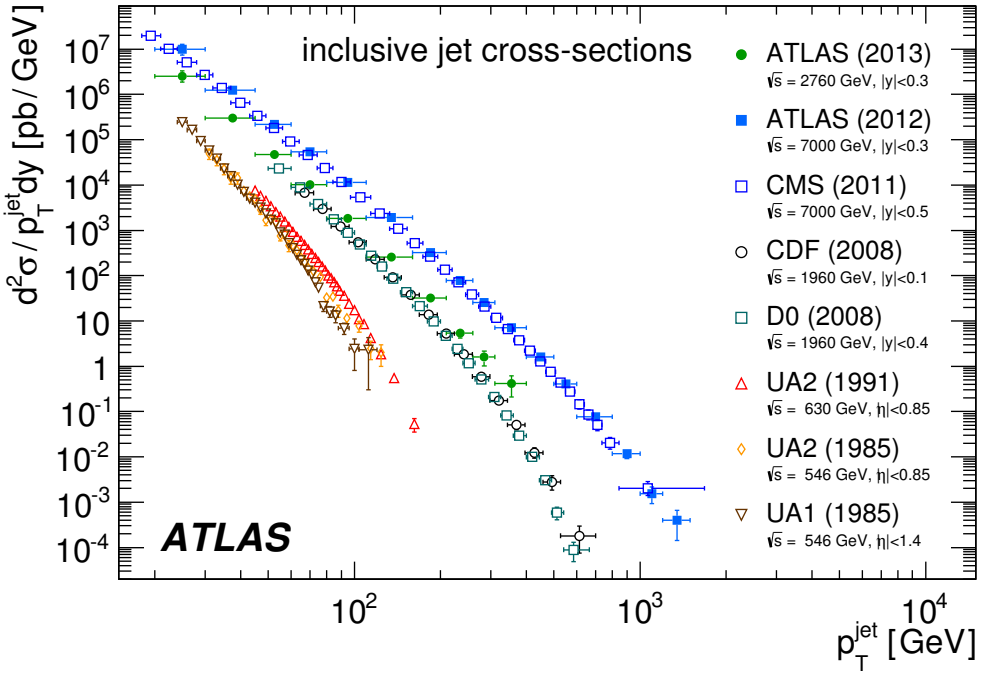

Figure 8.6: Inclusive jet cross-section as a function of p_{T} at different centre-of-mass energies $\sqrt{s}$ from various experiments [1, 2, 137, 138, 150, 152, 153, 165]. The used clustering algorithms, jet definitions, jet parameters and the used rapidity regions vary among the measurements. Hence, only a qualitative comparison is possible. Also appears in [171].

in $p\overline{p}$ collisions at the Tevatron with $\sqrt{s} = 1960\,\mathrm{GeV}$ from the D0 and CDF experiments [137, 138], and in pp collisions at the LHC using the ATLAS and CMS experiments [1, 2, 165]. In total, the selected measurements span a range of $18\,\mathrm{GeV} < p_{\mathrm{T}} < 1500\,\mathrm{GeV}$ and $5.1 \times 10^{-3} < x_{\mathrm{T}} < 0.71$. The data contains mostly central jets, $\eta = y = 0$, but extend to different ranges in the forward region. As well, the used clustering algorithms, jet definitions and the jet parameters differ. Hence, only a qualitative comparison is possible. An overview of the employed data, the year of publication, the centre-of-mass energy, luminosity, jet algorithm and kinematic range is given in Table 8.2.

Nevertheless, scale variations can be observed in Figure 8.7. While the dimensionless cross-section $p_{\mathrm{T}}^3 d\sigma/dp_{\mathrm{T}}dy$ at large transverse momentum fraction, $x_{\mathrm{T}} \approx 0.4$, shows large uncertainties and no separation between different centre-of-mass energies, measurements from the SPS and the LHC clearly differ at $x_{\mathrm{T}} \approx 0.1$ by a factor of 10. This order of magnitude is too large to be attributed solely to the different jet reconstruction algorithms.

8.5 PDF fit using ATLAS jet data

The knowledge about the PDF of the proton is obtained from several complementary types of measurements, mainly fixed target experiments and deep-inelastic ep scattering, by measuring the proton structure function $F_2(x, Q^2)$ over a large range in Bjorken x and momentum transfer Q^2. Especially at HERA, F_2 has been determined with high precision at the H1 and ZEUS experiments, resulting in a well-constrained parton density for $x < 0.01$. At larger x, however, in particular the gluon momentum distribution, $xg(x, Q^2)$ has not been determined as precisely. Here, additional information from deep-

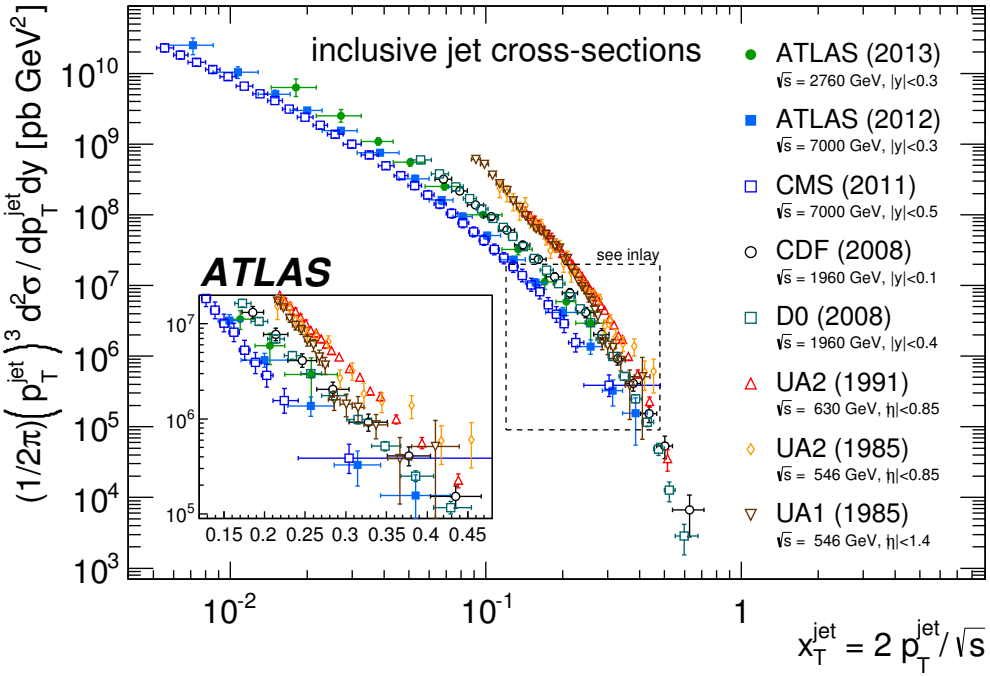

Figure 8.7: Inclusive jet cross-section as a function of x_T at different centre-of-mass energies $\sqrt{s}$ from various experiments [1, 2, 137, 138, 150, 152, 153, 165]. The used clustering algorithms, jet definitions, jet parameters and the used rapidity regions vary among the measurements. Hence, only a qualitative comparison is possible. Also appears in [171].

inelastic pp collisions may help to constrain xg further. Motivated by the small size of the experimental uncertainties in the ratio measurement of the inclusive jet cross-section, a study was performed to investigate the potential of the ATLAS jet data in the PDF determination [1]. The result is reported in the following.

The HERAFitter package provides the framework to perform the fit of the PDF. A summary of the employed parameters is given in [1]. The analysis is performed within a NLO perturbative QCD framework on basis of the factorisation theorem given in Equation 1.13. Essentially, it uses the theoretical prediction in form of the perturbative coefficients $\hat{\sigma}$ from the individual measurements and varies $q(x, Q^2)$ such that the best agreement of the theory prediction with the included data is attained. The systematic uncertainties of the individual measurements is taken into account by assigning a nuisance parameters to each independent source of uncertainty. The nuisance parameter is allowed to vary within its allocated uncertainty, resulting in an optimal shift of the uncertainty component with respect to the PDF fit among all included datasets. This procedure preserves correlations between components, but at the same time exploits the freedom given by the uncertainties on the measurement. This procedure relies on the theory prediction and hence potentially absorbs deficits in the QCD calculation like non-perturbative corrections in the PDF. Therefore only jet data with $p_T > 45\,\text{GeV}$ is used in the fit to avoid the region with large corrections.

The functional form of the PDF can not be derived from a perturbative calculation in the limit of free quarks in the proton. Instead, it must be parametrised at a scale Q_0^2, from which the evolution in Q^2 is given by the DGLAP equations. Q_0^2 is chosen as $1.9\,\text{GeV}^2$. A generic parametrisation following the

ansatz from a previous analysis [172] is used:

$$
\begin{aligned}
xu_v(x) &= A_{u_v} x^{B_{u_v}} (1-x)^{C_{u_v}} (1 + E_{u_v} x^2) \\
xd_v(x) &= A_{d_v} x^{B_{d_v}} (1-x)^{C_{d_v}} \\
x\bar{U}(x) &= A_{\bar{U}} x^{B_{\bar{U}}} (1-x)^{C_{\bar{U}}} \\
x\bar{D}(x) &= A_{\bar{D}} x^{B_{\bar{D}}} (1-x)^{C_{\bar{D}}} \\
xg(x) &= A_g x^{B_g} (1-x)^{C_g} - A'_g x^{B'_g} (1-x)^{C'_g}
\end{aligned}
\tag{8.12}
$$

In this set of equations, x is the Bjorken scaling variable, xu_v and xd_v are the light quark distributions of the proton, and $x\bar{U}$ and $x\bar{D}$ the light anti-quark distributions, where $\bar{D}$ consists of the *down* and *strange* type anti-quarks as $\bar{D} = \bar{d} + \bar{s}$. There is no parametrisation for heavy quarks, since the scale $Q_0 = 1.9\,\mathrm{GeV}^2$ is chosen to be below the heavy quark masses m_c, m_b, m_t. Instead, the heavy quarks enter the calculation via gluon splitting processes $g \to q\bar{q}$ following a heavy flavour quark scheme. The parameters A_q, B_q, C_q and E_q are determined in the fit. A_q is a normalisation parameter, B_q and C_q determine the slope of the distribution. The term E_{u_v} is introduced because it improves the fit quality substantially. The set of 19 parameters in total can be reduced to 13 independent ones using additional constraints such as the momentum sum and quark counting rules and by fixing the fraction of the strange quark in $\bar{D}$.

The impact of the ATLAS jet data is investigated using several different combinations of input dataset to the PDF determination. A fit to HERA data with the parametrisation given above is used as baseline for the study[8]. Subsequently, several combinations with the ATLAS jet data are employed as input:

- Data from HERA and the ATLAS jet data at $\sqrt{s} = 2.76\,\mathrm{TeV}$
- Data from HERA and the ATLAS jet data at $\sqrt{s} = 7\,\mathrm{TeV}$
- Data from HERA and the ATLAS jet data at both $\sqrt{s} = 2.76\,\mathrm{TeV}$ and $\sqrt{s} = 7\,\mathrm{TeV}$ combined

The fits are performed independently for the two jet radius parameters, $R = 0.4$ and $R = 0.6$, since the correlations between the two have not been evaluated.

The consistency of the determined PDF with the data is tested in terms of the χ^2 values, as listed in Table 8.3. This allows to compare the obtained agreement for the different input combinations. The χ^2 values for correlated and uncorrelated sources of uncertainty are listed separately. For the ATLAS jet measurements at two different $\sqrt{s}$, the correlations within the measurement and between the two are combined in χ^2_{cor}.

A good description of the HERA data is generally achieved, having a fit quality of $(\chi^2_{\mathrm{cor}}+\chi^2_{\mathrm{uncor}})/N_{\mathrm{points}} = 559/592$ for the baseline PDF fit using HERA data only, and maximally 568/592 for HERA and the ATLAS jet data for $R = 0.6$. Thus the description of the HERA data is mostly unaffected by the ATLAS jet data, indicating that the region in (x, Q^2) covered by HERA is already well constrained. However, a substantial improvement of the fit quality of the ATLAS jet data is observed when this data is used as input. For jets with $R = 0.6$, the uncorrelated component χ^2_{uncor} is reduced from 33 to 29 for $\sqrt{s} = 2.76\,\mathrm{TeV}$ data, and from 50 to 40 for $\sqrt{s} = 7\,\mathrm{TeV}$ data. The correlated component χ^2_{cor} of the two datasets decreases from 22 to 12. The fit quality is found to be similar for both radius parameters [1].

As described above, the fit is allowed to shift the data inside the systematic uncertainties. Shifts are typically within half a standard deviation and comparable in size for both radius parameters. A larger

[8] This fit includes a small modification in the parametrisation with respect to the HERAPDF 1.5 PDF set, but is equivalent otherwise.

Table 8.3: Quality of the PDF fit in terms of the χ^2 values. Two combinations of input datasets are compared, namely HERA data only, and HERA data together with the ATLAS jet cross-section data at $\sqrt{s} = 2.76$ TeV and $\sqrt{s} = 7$ TeV for $R = 0.6$, where all correlations between the measurements are taken into account. The χ^2 value of the fit with respect to individual test datasets is given separately for the uncorrelated and the correlated components as χ^2_{uncor} and χ^2_{cor}, where the shifts of the systematic uncertainties are summed in quadrature for each category [1].

input datasets	test dataset	χ^2_{uncor}	χ^2_{cor}	N_{points}
HERA	HERA	556	3.0	592
	ATLAS jets 2.76 TeV, $R = 0.4$	29	21	40
	ATLAS jets 7 TeV, $R = 0.4$	44		76
	ATLAS jets 2.76 TeV, $R = 0.6$	33	22	40
	ATLAS jets 7 TeV, $R = 0.6$	50		76
HERA ATLAS jets 2.76 TeV, $R = 0.6$ ATLAS jets 7 TeV, $R = 0.6$	HERA	564	4.0	592
	ATLAS jets 2.76 TeV, $R = 0.6$ jets	29	12	40
	ATLAS jets 7 TeV, $R = 0.6$	40		76
	ATLAS jets 2.76 TeV, $R = 0.4$	26	18	40
	ATLAS jets 7 TeV, $R = 0.4$	32		76

difference between the two is observed for the nuisance parameter assigned to the luminosity, despite the fact that the luminosity is 100% correlated between the datasets for the two radius parameters. However, since the correlations between the measurements at two radius parameters have not been investigated, the fits are performed independently. At $\sqrt{s} = 2.76$ TeV, the shift is consistent with 0.0% for $R = 0.4$ and -2.4% for $R = 0.6$. The origin for the inconsistency in this parameter may be due to the difference in normalisation with respect to the theory prediction. Interestingly, the shift is large for $R = 0.6$, although a much better agreement with theory was obtained for this radius parameter. Additional studies in which the luminosity parameter was fixed show that the impact of this inconsistency on the PDF is small, and the resulting PDF is similar for both radius parameters generally [1].

The largest impact of the ATLAS jet data is observed in the gluon momentum distribution $xg(x)$. Figure 8.8a shows xg as a function of x at the scale $Q_0^2 = 1.9\,\text{GeV}^2$. Several combinations of input datasets are compared, namely a fit to HERA data only; fits using HERA data and the individual ATLAS jet cross-section data; and a fit using HERA data and both ATLAS jet cross-section measurements combined. Jets with $R = 0.6$ are used for the ATLAS data. A larger gluon momentum fraction is observed for $x > 0.1$ when the ATLAS data is observed, while xg is smaller at $0.01 < x < 0.1$. The uncertainty is reduced with the additional constraints from the jet measurement. The pull is found to be strongest when both datasets are employed in the fit.

Due to the momentum sum rule, the change in xg has to be compensated by the quark momentum fractions accordingly. Most of it is absorbed in the sea quark momentum distributions, since they are less constrained than the ones from the valence quarks. The sea quark momentum distribution $xS(x)$ is shown in Figure 8.8b. A decrease of xS is observed for $x > 0.1$.

The effect of the ATLAS jet data can also be observed in the inclusive jet cross-section and the jet cross-section ratio, shown in Figures 8.9 and 8.10, respectively. They correspond to Figures 7.11 and 8.5a, except that jets with $R = 0.6$ are used here for both. In addition to the nominal prediction with the CT 10 PDF set, the data is also compared to the PDF sets described in this section, namely the fit using the HERA data only, and the fit based on data from HERA and the ATLAS jet cross-section measurements. As expected, the description of the data for both, cross-section and cross-section ratio,

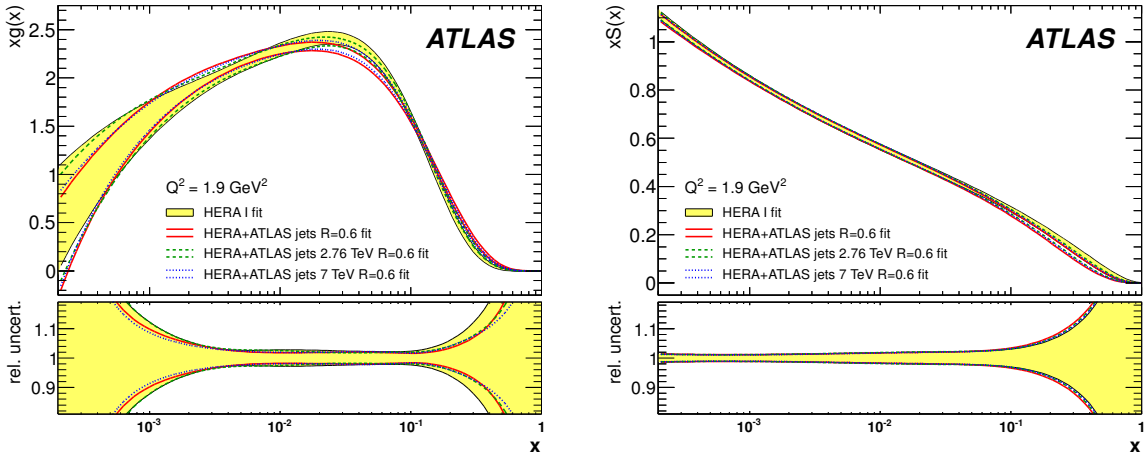

(a) xg (b) xS

Figure 8.8: Momentum distributions of (a) gluons, xg, and (b) sea quarks, xS, as a function of the Bjorken scale variable, x, in the proton PDF at $Q^2 = 1.9\,\text{GeV}^2$ for PDF fits with various input datasets: HERA data only, HERA data and ATLAS jet data at $\sqrt{s} = 2.76\,\text{TeV}$ and $\sqrt{s} = 7\,\text{TeV}$ combined, and HERA data in combination with each of the ATLAS jet datasets individually. Jets are defined using the anti-k_t algorithm with $R = 0.6$. Also shown is the relative uncertainty of the PDF fits, where the each PDF is centred on unity. [1]

is substantially improved when the ATLAS data is included, in particular at high p_T and in the forward region. However, the difference between the theory and the data in the ratio for the low p_T, central rapidity range is not resolved. This indicates that the constraints from the HERA data are very strong in this regime, and that the difference must originate from other sources.

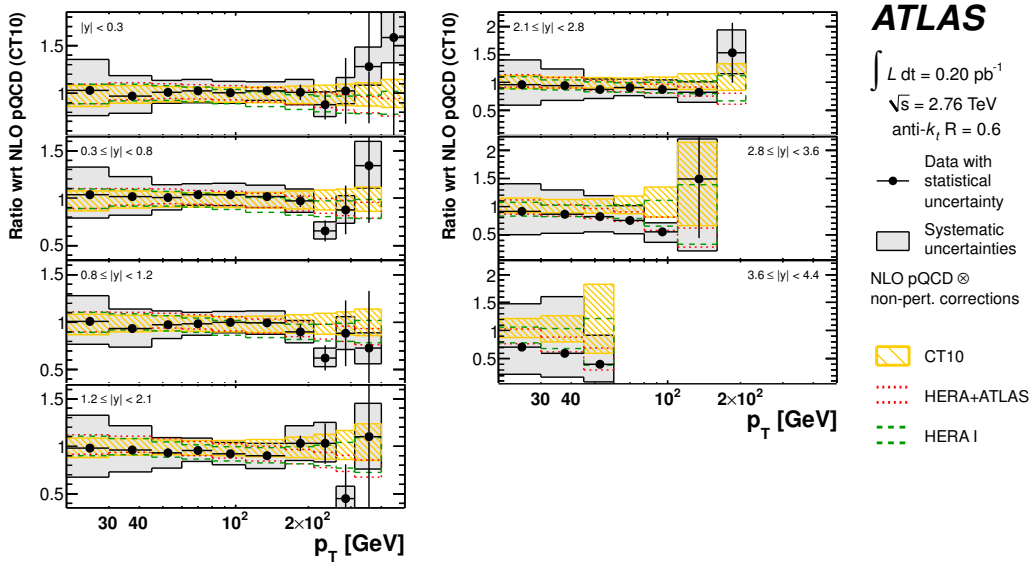

Figure 8.9: Comparison of the theoretical predictions for the inclusive jet cross-section at $\sqrt{s} = 2.76\,\text{TeV}$ using the nominal PDF set CT 10, the fitted PDF set using HERA data only, and the PDF determined using data from HERA and the ATLAS jet data. The prediction is derived using a perturbative QCD calculation at NLO precision with the generator NLOJET++, to which non-perturbative corrections from the PYTHIA event generator with the AUET 2B tune are applied. Jets are defined using the anti-k_t algorithm with $R = 0.6$. [1]

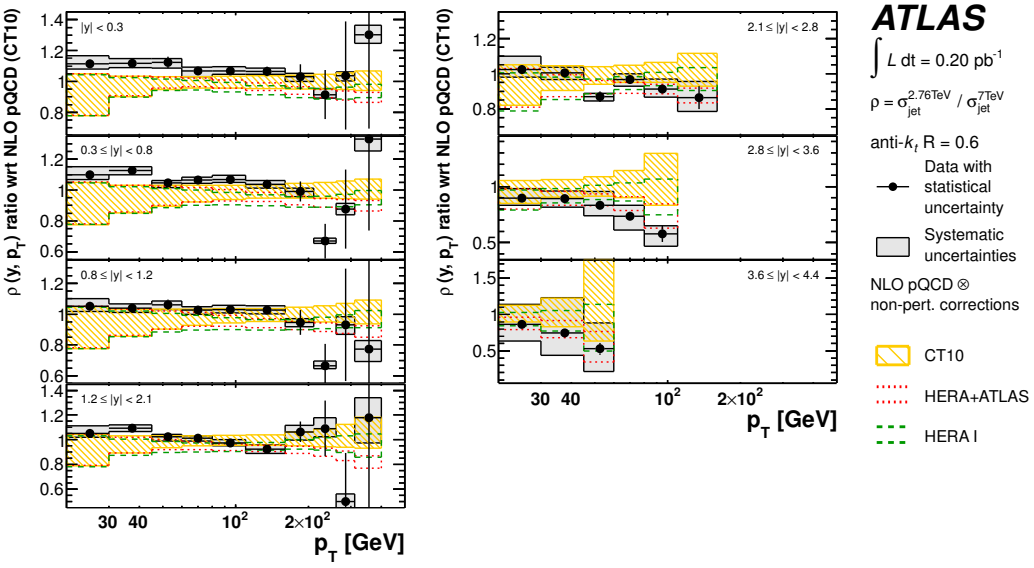

Figure 8.10: Comparison of the theoretical predictions for the ratio $\rho(y, p_\text{T})$ using the nominal PDF set CT 10, the fitted PDF set using HERA data only, and PDF determined using data from HERA and the ATLAS jet data. The prediction is derived using a perturbative QCD calculation at NLO precision with the generator NLOJET++, to which non-perturbative corrections from the PYTHIA event generator with the AUET 2B tune are applied. Jets are defined using the anti-k_t algorithm with $R = 0.6$. [1]

Summary

Jet production is the dominant process in proton-proton collisions at the Large Hadron Collider and allows for a precise test of the strong interaction at the smallest accessible distances in the framework of perturbative Quantum Chromodynamics. A measurement of the double-differential inclusive jet cross-section with the ATLAS detector at two different centre-of-mass energies, $\sqrt{s} = 2.76\,\text{TeV}$ and $\sqrt{s} = 7\,\text{TeV}$, and a ratio thereof has been presented. The data correspond to an integrated luminosity of $\mathcal{L} = 0.20\,\text{pb}^{-1}$ and $\mathcal{L} = 37\,\text{pb}^{-1}$, respectively. Jets are reconstructed using the anti-k_t algorithm with two radius parameters of $R = 0.4$ and $R = 0.6$, and measured as a function of their transverse momentum in seven ranges of rapidity. Covering transverse momenta of $20\,\text{GeV} \leq p_\text{T} < 1.5\,\text{TeV}$ and a rapidity of $|y| < 4.4$, the results substantially extend the kinematic reach of earlier jet cross-section measurements. The cross-section ratio is determined as a function of transverse momentum as well as the dimensionless transverse momentum fraction $x_\text{T} = 2p_\text{T}/\sqrt{s}$, which ranges from $0.02 < x_\text{T} < 0.34$.

In preparation of the jet cross-section measurement at $\sqrt{s} = 2.76\,\text{TeV}$, a calibration of the luminosity devices for this dataset has been carried out, consisting of the evaluation of two van-der-Meer scans, the determination of the bunch charge product and a study of the long-term stability. The resulting systematic uncertainty of 2.7% represents a significant improvement with respect to the initial calibration.

Various data verification studies have been performed to exclude the influence of pile-up conditions, trigger inefficiencies, or the z-position of the collision vertex on the cross-section. In particular, the validity of the calibration and selection of jets in the dataset at $\sqrt{s} = 2.76\,\text{TeV}$ has been analysed in detail.

The dominating systematic uncertainty on the inclusive jet cross-section measurements is the uncertainty on the jet energy scale. In total, more than 20 sources of systematic uncertainties have been identified, whose correlations have been encoded in about 90 independent nuisance parameters. The experimental and theoretical uncertainties are of similar size in some regions of phase space. In the cross-section ratio, the systematic uncertainty is significantly reduced due to the cancellation of correlated uncertainties in the two measurements.

The unfolded particle-level cross-sections have been compared to various theory predictions in order to test different approaches to account for non-perturbative effects, parton shower tunes, and PDF sets in the as yet unprobed kinematic region at high p_T and large rapidity. In general, the nominal predictions based on the perturbative QCD calculation at NLO to which non-perturbative correction factors were applied, have been found to describe the data well within the uncertainties over many orders of magnitude. However, a different trend is observed at large rapidities, as well as a consistently different level of agreement between data and theory in the order of $10 - 20\%$ between $R = 0.4$ and $R = 0.6$.

The latter indicates a mismodelling of non-perturbative effects and has been investigated using the Powheg event generator, which is interfaced directly to the parton shower Monte Carlo simulation. Excellent agreement with data for both radius parameters likewise is obtained for the revised version of Powheg when Pythia with the Auet 2b tune is used as Monte Carlo simulation. However, the result was

found to be sensitive to the matching scale between the event generator and the parton shower simulation as well as the ordering and parameter tunes of the latter, which needs further study from the theory side.

The differences between data and prediction in the forward rapidity region have been addressed by a comparison of various PDF sets to test the sensitivity of the data on the parton distributions. Although the size of the experimental and theoretical uncertainties do not allow to select one prediction above the others, in particular the MSTW 2008 PDF set yields a better agreement. The potential of the data has been further exploited in the ratio, which was analysed within a framework of next-to-leading order perturbative QCD calculations in the DGLAP formalism to determine the parton distribution functions of the proton, together with data from HERA. A harder gluon and softer sea quark momentum distributions in the high Bjorken-x region has been obtained, showing the potential of the ATLAS jet data for future improvements of the PDF sets.

Appendix

APPENDIX A

Appendix

A.1 Theoretical predictions

A.1.1 Non-perturbative correction factors

$\sqrt{s}$	radius R	rapidity	non-perturbative correction		
			$20 \leq p_{\mathrm{T}} < 30$ [GeV]	$80 \leq p_{\mathrm{T}} < 110$ [GeV]	$800 \leq p_{\mathrm{T}} < 1000$ [GeV]
7 TeV	0.4	$\lvert y\rvert < 0.3$	0.99	0.99	1.00
		$2.1 \leq \lvert y\rvert < 2.8$	0.96	0.98	-
		$3.6 \leq \lvert y\rvert < 4.4$	0.90	0.97	-
7 TeV	0.6	$\lvert y\rvert < 0.3$	1.61	1.08	1.01
		$2.1 \leq \lvert y\rvert < 2.8$	1.44	1.05	-
		$3.6 \leq \lvert y\rvert < 4.4$	1.19	0.99	-
			$20 \leq p_{\mathrm{T}} < 30$ [GeV]	$45 \leq p_{\mathrm{T}} < 60$ [GeV]	$310 \leq p_{\mathrm{T}} < 400$ [GeV]
2.76 TeV	0.4	$\lvert y\rvert < 0.3$	0.88	0.93	0.99
		$2.1 \leq \lvert y\rvert < 2.8$	0.88	0.94	-
		$3.6 \leq \lvert y\rvert < 4.4$	0.78	0.78	-
2.76 TeV	0.6	$\lvert y\rvert < 0.3$	1.24	1.06	1.02
		$2.1 \leq \lvert y\rvert < 2.8$	1.19	1.05	-
		$3.6 \leq \lvert y\rvert < 4.4$	0.99	0.92	-

Table A.1: Non-perturbative correction factors for different $\sqrt{s}$, radius parameters R of the anti-k_t algorithm and selected bins in y-p_{T} space. Data taken from [2] and [1].

A.1.2 Theoretical uncertainty of the perturbative QCD calculation

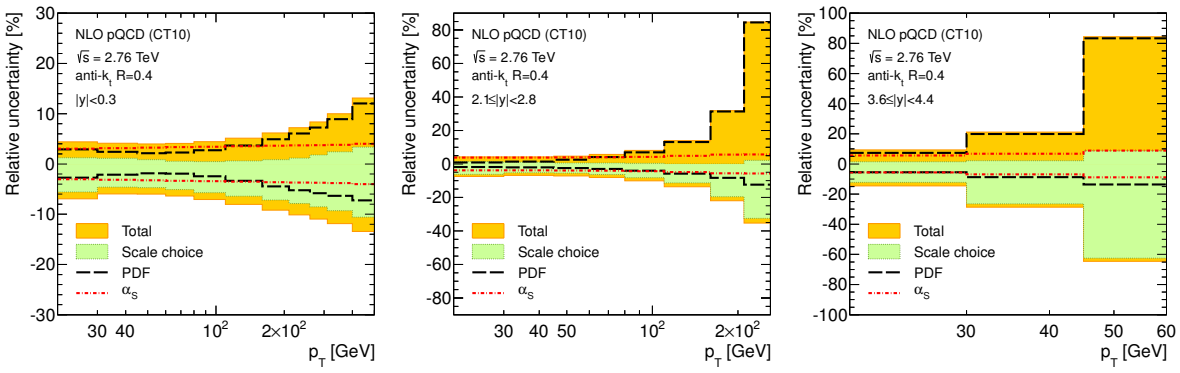

(a) (b) (c)

Figure A.1: Theoretical uncertainty of the perturbative QCD calculation for the inclusive jet cross-section at $\sqrt{s} = 2.76\,\text{TeV}$ as function of p_T, in three representative rapidity bins [64]. The contributions from the factorisation and renormalisation scale, the PDF and the strong coupling constant α_S is shown separately. Jets are defined using the anti-k_t algorithm with $R = 0.4$.

A.1.3 Monte Carlo samples

$\hat{p}_{\mathrm{T}}$ range [GeV]	ID	dataset
<17	MB	mc10_2TeV.105001.pythia_minbias.merge.NTUP_JETMET.e747_s1175_s1176_r2203_r2191_p522/
17 – 35	J1	mc10_2TeV.105010.J1_pythia_jetjet.merge.NTUP_JETMET.e747_s1175_s1176_r2203_r2191_p522/
35 – 70	J2	mc10_2TeV.105011.J2_pythia_jetjet.merge.NTUP_JETMET.e747_s1175_s1176_r2203_r2191_p522/
70 – 140	J3	mc10_2TeV.105012.J3_pythia_jetjet.merge.NTUP_JETMET.e747_s1175_s1176_r2203_r2191_p522/
140 – 280	J4	mc10_2TeV.105013.J4_pythia_jetjet.merge.NTUP_JETMET.e747_s1175_s1176_r2203_r2191_p522/
280 – 560	J5	mc10_2TeV.105014.J5_pythia_jetjet.merge.NTUP_JETMET.e747_s1175_s1176_r2203_r2191_p522/

Table A.2: Monte Carlo samples used as baseline for the analysis at $\sqrt{s} = 2.76\,\mathrm{TeV}$. Pythia is used for the event generation and parton shower simulation. To cover the full phase space, the event generation is divided into several samples according to the p_{T} of the $2 \to 2$ process at LO precision, $\hat{p}_{\mathrm{T}}$.

$\hat{p}_{\mathrm{T}}$ range [GeV]	ID	dataset
<8	MB	mc10_7TeV.105001.pythia_minbias.merge.NTUP_JETMET.e574_s932_s946_r1649_p350
8 – 17	J0	mc10_7TeV.105009.J0_pythia_jetjet.merge.NTUP_JETMET.e574_s934_s946_r1653_p350/
17 – 35	J1	mc10_7TeV.105010.J1_pythia_jetjet.merge.NTUP_JETMET.e574_s934_s946_r1653_p350/
35 – 70	J2	mc10_7TeV.105011.J2_pythia_jetjet.merge.NTUP_JETMET.e574_s934_s946_r1653_p350/
70 – 140	J3	mc10_7TeV.105012.J3_pythia_jetjet.merge.NTUP_JETMET.e574_s934_s946_r1653_p350/
140 – 280	J4	mc10_7TeV.105013.J4_pythia_jetjet.merge.NTUP_JETMET.e574_s934_s946_r1653_p350/
280 – 560	J5	mc10_7TeV.105014.J5_pythia_jetjet.merge.NTUP_JETMET.e574_s934_s946_r1653_p350/
560 – 1120	J6	mc10_7TeV.105015.J6_pythia_jetjet.merge.NTUP_JETMET.e574_s934_s946_r1653_p350/
1120 – 2240	J7	mc10_7TeV.105016.J7_pythia_jetjet.merge.NTUP_JETMET.e574_s934_s946_r1653_p350/
2240 – 4480	J8	mc10_7TeV.105017.J8_pythia_jetjet.merge.NTUP_JETMET.e574_s934_s946_r1653_p350/

Table A.3: Monte Carlo samples used as baseline for the analysis at $\sqrt{s} = 7\,\mathrm{TeV}$. Pythia is used for the event generation and parton shower simulation. To cover the full phase space, the event generation is divided into several samples according to the p_{T} of the $2 \to 2$ process at LO precision, $\hat{p}_{\mathrm{T}}$.

A.1.4 POWHEG event generation

```
numevts 50000        ! number of events to be generated
ih1  1               ! hadron 1 (1 for protons, -1 for antiprotons)
ih2  1               ! hadron 2 (1 for protons, -1 for antiprotons)
ebeam1 1380d0        ! energy of beam 1
ebeam2 1380d0        ! energy of beam 2
bornktmin 5d0        ! (default 0d0) Generation cut: minimum kt in underlying Born
bornsuppfact 200d0   ! (default 0d0) Mass parameter for Born suppression factor.
                     ! If < 0 suppfact = 1.

! To be set only if using internal (mlm) pdfs
! 131 cteq6m
! ndns1 131          ! pdf set for hadron 1 (mlm numbering)
! ndns2 131          ! pdf set for hadron 2 (mlm numbering)

! To be set only if using LHA pdfs
! 10050 cteq6m
! 10800 CT10
lhans1  10800        ! pdf set for hadron 1 (LHA numbering)
lhans2  10800        ! pdf set for hadron 2 (LHA numbering)

! To be set only if using different pdf sets for the two incoming hadrons
#QCDLambda5  0.25    ! for not equal pdf sets

#renscfact  1d0      ! (default 1d0) ren scale factor: muren  = muref * renscfact
#facscfact  1d0      ! (default 1d0) fac scale factor: mufact = muref * facscfact

! Parameters to allow or not the use of stored data
use-old-grid    1    ! If 1 use old grid if file pwggrids.dat is present (<> 1 regenerate)
use-old-ubound  1    ! If 1 use norm of upper bounding function stored
                     ! in pwgubound.dat, if present; <> 1 regenerate

! A typical call uses 1/1400 seconds (1400 calls per second)
ncall1 20000         ! No. calls for the construction of the importance sampling grid
itmx1 5              ! No. iterations for grid: total 100000 calls ~ 70 seconds
ncall2 20000         ! No. calls for the computation of the upper bounding
                     ! envelope for the generation of radiation
itmx2 5              ! No. iterations for the above

! Notice: the total number of calls is ncall2*itmx2*foldcsi*foldy*foldphi
! these folding numbers yield a negative fraction of 0.5% with bornktmin=10 GeV.
! With these settings: ncall2*itmx2*foldcsi*foldy*foldphi=5M, 60 minutes
foldcsi 5            ! No. folds on csi integration
foldy   5            ! No. folds on  y  integration
foldphi 2            ! No. folds on phi integration

nubound 500000       ! No. calls to set up the upper bounding norms for radiation.
                     ! This is performed using only the Born cross section (fast)

! OPTIONAL PARAMETERS
doublefsr 1          ! fix problem with spikes in final observables
par_diexp 4          ! recommended additional options to be used with doublefsr
par_dijexp 4         ! (by Paolo Nason, private communication)
par_2gsupp 4         ! "not sure of what happens if you don't"

withnegweights 1     ! (default 0). If 1 use negative weights.
pdfreweight 1        ! (default 0). If 1 use negative weights.
#bornonly 1          ! (default 0). If 1 compute underlying Born using LO
                     ! cross section only.

#ptsqmin    0.8      ! (default 0.8 GeV) minimum pt for generation of radiation
#charmthr   1.5      ! (default 1.5 GeV) charm treshold for gluon splitting
#bottomthr  5.0      ! (default 5.0 GeV) bottom treshold for gluon splitting
#testplots  1        ! (default 0, do not) do NLO and PWHG distributions
#charmthrpdf  1.5    ! (default 1.5 GeV) pdf charm treshold
#bottomthrpdf 5.0    ! (default 5.0 GeV) pdf bottom treshold
#xupbound 2d0        ! increase upper bound for radiation generation

#iseed    5421       ! Start the random number generator with seed iseed
#rand1     0         ! skipping  rand2*100000000+rand1 numbers (see RM48
#rand2     0         ! short writeup in CERNLIB).
manyseeds  1         ! Used to perform multiple runs with different random
                     ! seeds in the same directory.
                     ! If set to 1, the program asks for an integer j;
                     ! The file pwgseeds.dat at line j is read, and the
                     ! integer at line j is used to initialize the random
                     ! sequence for the generation of the event.
                     ! The event file is called pwgevents-'j'.lhe
```

Table A.4: Generation parameters for the POWHEG event generation at $\sqrt{s} = 2.76\,\text{TeV}$.

```
numevts 50000        ! number of events to be generated
ih1  1               ! hadron 1 (1 for protons, -1 for antiprotons)
ih2  1               ! hadron 2 (1 for protons, -1 for antiprotons)
ebeam1 3500d0        ! energy of beam 1
ebeam2 3500d0        ! energy of beam 2

bornktmin 5d0        ! (default 0d0) Generation cut: minimum kt in underlying Born
bornsuppfact 250d0   ! (default 0d0) Mass parameter for Born suppression factor.
                     ! If < 0 suppfact = 1.

! To be set only if using internal (mlm) pdfs
! 131 cteq6m
! ndns1 131          ! pdf set for hadron 1 (mlm numbering)
! ndns2 131          ! pdf set for hadron 2 (mlm numbering)

! To be set only if using LHA pdfs
! 10050 cteq6m
! 10800 CT10
lhans1  10800        ! pdf set for hadron 1 (LHA numbering)
lhans2  10800        ! pdf set for hadron 2 (LHA numbering)

! To be set only if using different pdf sets for the two incoming hadrons
#QCDLambda5  0.25    ! for not equal pdf sets

#renscfact  1d0      ! (default 1d0) ren scale factor: muren  = muref * renscfact
#facscfact  1d0      ! (default 1d0) fac scale factor: mufact = muref * facscfact

! Parameters to allow or not the use of stored data
use-old-grid    1    ! If 1 use old grid if file pwggrids.dat is present (<> 1 regenerate)
use-old-ubound  1    ! If 1 use norm of upper bounding function stored
                     ! in pwgubound.dat, if present; <> 1 regenerate

! A typical call uses 1/1400 seconds (1400 calls per second)
ncall1 20000         ! No. calls for the construction of the importance sampling grid
itmx1 5              ! No. iterations for grid: total 100000 calls ~ 70 seconds
ncall2 20000         ! No. calls for the computation of the upper bounding
                     ! envelope for the generation of radiation
itmx2 5              ! No. iterations for the above

! Notice: the total number of calls is ncall2*itmx2*foldcsi*foldy*foldphi
! these folding numbers yield a negative fraction of 0.5% with bornktmin=10 GeV.
! With these settings: ncall2*itmx2*foldcsi*foldy*foldphi=5M, 60 minutes
foldcsi 5            ! No. folds on csi integration
foldy   5            ! No. folds on  y  integration
foldphi 2            ! No. folds on phi integration

nubound 500000       ! No. calls to set up the upper bounding norms for radiation.
                     ! This is performed using only the Born cross section (fast)

! OPTIONAL PARAMETERS
doublefsr 1          ! fix problem with spikes in final observables
par_diexp 4          ! recommended additional options to be used with doublefsr
par_dijexp 4         ! (by Paolo Nason, private communication)
par_2gsupp 4         ! "not sure of what happens if you don't"

withnegweights 1     ! (default 0). If 1 use negative weights.
pdfreweight 1        ! (default 0). If 1 use negative weights.
#bornonly 1          ! (default 0). If 1 compute underlying Born using LO
                     ! cross section only.

#ptsqmin    0.8      ! (default 0.8 GeV) minimum pt for generation of radiation
#charmthr   1.5      ! (default 1.5 GeV) charm treshold for gluon splitting
#bottomthr  5.0      ! (default 5.0 GeV) bottom treshold for gluon splitting
#testplots  1        ! (default 0, do not) do NLO and PWHG distributions
#charmthrpdf  1.5    ! (default 1.5 GeV) pdf charm treshold
#bottomthrpdf 5.0    ! (default 5.0 GeV) pdf bottom treshold
#xupbound 2d0        ! increase upper bound for radiation generation

#iseed    5421       ! Start the random number generator with seed iseed
#rand1     0         ! skipping  rand2*100000000+rand1 numbers (see RM48
#rand2     0         ! short writeup in CERNLIB).
manyseeds  1         ! Used to perform multiple runs with different random
                     ! seeds in the same directory.
                     ! If set to 1, the program asks for an integer j;
                     ! The file pwgseeds.dat at line j is read, and the
                     ! integer at line j is used to initialize the random
                     ! sequence for the generation of the event.
                     ! The event file is called pwgevents-'j'.lhe
```

Table A.5: Generation parameters for the POWHEG event generation at $\sqrt{s} = 7\,\text{TeV}$.

A.2 Luminosity measurement

	Fill 1653		Fill 1658		Correlation
	Beam 1	Beam 2	Beam 1	Beam 2	b/w beams
Current source precision	±0.05%	±0.05%	±0.05%	±0.05%	yes
Bunch pattern dependence (lab. test)	±0.1%	±0.1%	±0.1%	±0.1%	yes
Non-linearity of 12-bit ADC	±0.40%	±0.39%	±0.36%	±0.33%	yes
Baseline correction	±0.11%	±0.11%	±0.10%	±0.09%	no
Long term stability of baseline on range 2	±0.16%	±0.16%	±0.14%	±0.13%	no
Long term stability of calibration on range 2	±0.40%	±0.39%	±0.36%	±0.33%	no
Difference between system A and B on range 2	±0.40%	±0.39%	±0.36%	±0.33%	no
bunch charge uncertainty per beam	±0.73%	±0.72%	±0.66%	±0.61%	
bunch charge uncertainty on beam product	±1.17%		±1.03%		
bunch charge uncertainty on beam product (gaussian)	±0.80%		±0.70%		

Table A.6: Systematic uncertainties of the total bunch charge measurement using the DCCT in both van-der-Meer scans at $\sqrt{s} = 2.76\,\text{TeV}$ in 2011. The uncertainties are given as an envelope error $\Delta(100\%CL)$, if not specified otherwise. The correlation of the measurement between the two beams are shown in the rightmost column.

A.3 Inclusive jet cross-section at $\sqrt{s} = 7$ TeV

p_T[GeV]	$0.0 \leq \lvert y \rvert < 1.2$	$1.2 \leq \lvert y \rvert < 2.1$	$2.1 \leq \lvert y \rvert < 2.8$	$2.8 \leq \lvert y \rvert < 3.6$	$3.6 \leq \lvert y \rvert < 4.4$
20 – 30	L1_MBTS_1	L1_MBTS_1	L1_MBTS_1	L1_MBTS_1	L1_MBTS_1
30 – 60	L1_MBTS_1	L1_MBTS_1	L1_MBTS_1	L1_MBTS_1	
≥ 60	L1_MBTS_1	L1_MBTS_1	L1_MBTS_1		

Table A.7: Trigger scheme for the measurement of the inclusive jet cross-section at $\sqrt{s} = 7$ TeV for period A, runs 152166 – 152508.

p_T[GeV]	$0.0 \leq \lvert y \rvert < 1.2$	$1.2 \leq \lvert y \rvert < 2.1$	$2.1 \leq \lvert y \rvert < 2.8$	$2.8 \leq \lvert y \rvert < 3.6$	$3.6 \leq \lvert y \rvert < 4.4$
20 – 30	L1_MBTS_1	L1_MBTS_1	L1_MBTS_1	L1_MBTS_1	L1_MBTS_1
30 – 60	L1_MBTS_1	L1_MBTS_1	L1_MBTS_1	L1_MBTS_1	
60 – 80	L1_J5	L1_J5	L1_J5		
80 – 110	L1_J15	L1_J5	L1_J15		
110 – 160	L1_J30	L1_J15	L1_J30		
160 – 210	L1_J55	L1_J30	L1_J55		
210 – 260	L1_J75	L1_J55	L1_J75		
≥ 260	L1_J75	L1_J75	L1_J75		

Table A.8: Trigger scheme for the measurement of the inclusive jet cross-section at $\sqrt{s} = 7$ TeV for period A – C, runs 152777 – 156682.

p_T[GeV]	$0.0 \leq \lvert y \rvert < 1.2$	$1.2 \leq \lvert y \rvert < 2.1$	$2.1 \leq \lvert y \rvert < 2.8$	$2.8 \leq \lvert y \rvert < 3.6$	$3.6 \leq \lvert y \rvert < 4.4$
60 – 80	L1_J5	L1_J5	L1_J5		
80 – 110	L1_J15	L1_J5	L1_J15		
110 – 160	L1_J30	L1_J15	L1_J30		
160 – 210	L1_J55	L1_J30	L1_J55		
210 – 260	L1_J75	L1_J55	L1_J75		
260 – 310	L1_J95	L1_J75	L1_J95		
≥ 310	L1_J95	L1_J95	L1_J95		

Table A.9: Trigger scheme for the measurement of the inclusive jet cross-section at $\sqrt{s} = 7$ TeV for period D, runs 158045 – 159224.

p_T[GeV]	$0.0 \leq \lvert y \rvert < 1.2$	$1.2 \leq \lvert y \rvert < 2.1$	$2.1 \leq \lvert y \rvert < 2.8$	$2.8 \leq \lvert y \rvert < 3.6$	$3.6 \leq \lvert y \rvert < 4.4$
60 – 80	L1_J5		L1_J5		
80 – 110	L1_J15		L1_J15		
110 – 160	L1_J30		L1_J30		
160 – 210	L1_J55		L1_J55		
210 – 260	L1_J75		L1_J75		
260 – 310	L1_J95		L1_J95		
≥ 310	L1_J95		L1_J95		

Table A.10: Trigger scheme for the measurement of the inclusive jet cross-section at $\sqrt{s} = 7$ TeV for period E1 – E4, runs 160387 – 160980.

p_T[GeV]	$0.0 \leq \lvert y \rvert < 1.2$	$1.2 \leq \lvert y \rvert < 2.1$	$2.1 \leq \lvert y \rvert < 2.8$	$2.8 \leq \lvert y \rvert < 3.6$	$3.6 \leq \lvert y \rvert < 4.4$
30 – 60					L1_FJ10
60 – 80	L1_J5	L1_J5	L1_J5	L1_J10,L1_FJ10	L1_FJ10
80 – 110	L1_J15	L1_J5	L1_J15	L1_J10,L1_FJ10	L1_FJ30
110 – 160	L1_J30	L1_J15	L1_J30	L1_J30,L1_FJ30	L1_FJ55
160 – 210	L1_J55	L1_J30	L1_J55	L1_J55,L1_FJ55	L1_FJ55
210 – 260	L1_J75	L1_J55	L1_J75	L1_J55,L1_FJ55	L1_FJ55
260 – 310	L1_J95	L1_J75	L1_J95	L1_J55,L1_FJ55	L1_FJ55
≥ 310	L1_J95	L1_J95	L1_J95	L1_J55,L1_FJ55	L1_FJ55

Table A.11: Trigger scheme for the measurement of the inclusive jet cross-section at $\sqrt{s} = 7$ TeV for period E5 – F, runs 161118 – 162882.

p_T[GeV]	$0.0 \leq \lvert y \rvert < 1.2$	$1.2 \leq \lvert y \rvert < 2.1$	$2.1 \leq \lvert y \rvert < 2.8$	$2.8 \leq \lvert y \rvert < 3.6$	$3.6 \leq \lvert y \rvert < 4.4$
60 – 80	EF_j20_jetNoEF	EF_j20_jetNoEF	EF_j20_jetNoEF		EF_fj30_jetNoEF
80 – 110	EF_j35_jetNoEF	EF_j20_jetNoEF	EF_j35_jetNoEF	EF_j30_jetNoEF or EF_fj30_jetNoEF	EF_fj30_jetNoEF
110 – 160	EF_j50_jetNoEF	EF_j35_jetNoEF	EF_j50_jetNoEF	EF_j50_jetNoEF or EF_fj50_jetNoEF	EF_fj50_jetNoEF
160 – 210	EF_j75_jetNoEF	EF_j50_jetNoEF	EF_j75_jetNoEF	EF_j50_jetNoEF or EF_fj50_jetNoEF	EF_fj75_jetNoEF
210 – 260	EF_j95_jetNoEF	EF_j75_jetNoEF	EF_j95_jetNoEF	EF_j75_jetNoEF or EF_fj75_jetNoEF	EF_fj75_jetNoEF
260 – 310	EF_L1J95_NoAlg	EF_j95_jetNoEF	EF_L1J95_NoAlg	EF_j75_jetNoEF or EF_fj75_jetNoEF	EF_fj75_jetNoEF
310 – 400	EF_L1J115_NoAlg	EF_L1J95_NoAlg	EF_L1J115_NoAlg	EF_j75_jetNoEF or EF_fj75_jetNoEF	EF_fj75_jetNoEF
≥ 400	EF_L1J115_NoAlg	EF_L1J115_NoAlg	EF_L1J115_NoAlg	EF_j75_jetNoEF or EF_fj75_jetNoEF	EF_fj75_jetNoEF

Table A.12: Trigger scheme for the measurement of the inclusive jet cross-section at $\sqrt{s} = 7$ TeV for period G – I, runs 165591 – 167963.

run	luminosity block numbers
152166	206 – 300
152214	159 – 201
152221	5 – 167
152345	128 – 207
152409	124 – 209, 286 – 716
152441	309 – 671
152508	196 – 204, 241 – 261
152777	60 – 299, 321 – 329
152844	178 – 234
152845	111 – 134, 145 – 169, 186 – 349
152878	99 – 159, 191 – 214
152933	44 – 173
152994	293 – 353
153030	120 – 164, 186 – 203
153134	312 – 334
153136	232 – 234
153159	87 – 104, 126 – 177
153200	156 – 178
153565	255 – 269, 281 – 1148
155073	82 – 394, 397 – 407
155112	127 – 166, 186 – 215, 217 – 322, 324 – 493, 495 – 592, 594 – 609, 612 – 625
155116	8 – 44, 46 – 54, 61 – 93
155160	240 – 503
155228	131 – 148
155280	360 – 375
155569	228 – 467
155634	144 – 147, 149 – 326, 328 – 333
155669	257 – 311
155678	241 – 308
155697	264 – 266, 268 – 334, 336 – 352, 354 – 506
156682	405 – 475, 477 – 507, 509 – 512
158045	117 – 177
158116	110 – 115, 120 – 138, 140 – 165, 167 – 169, 185 – 189, 191 – 231, 233 – 260, 262 – 264, 266 – 268, 270 – 290, 331 – 356, 358 – 552, 554 – 554
158269	6 – 41, 43 – 45, 47 – 59, 68 – 76, 78 – 81
158299	363 – 368, 377 – 434
158392	218 – 224, 236 – 281, 283 – 325, 337 – 340, 358 – 434, 440 – 447
158443	208 – 213, 216 – 230
158466	260 – 268, 273 – 277
158545	236 – 237, 239 – 255, 257 – 261
158548	110 – 111, 113 – 115, 117 – 117, 119 – 126, 128 – 140, 142 – 147, 149 – 163, 165 – 177, 179 – 196, 198 – 228, 230 – 245, 247 – 249, 251 – 257, 260 – 275, 277 – 285, 287 – 294, 296 – 303, 305 – 305, 307 – 312, 314 – 321
158549	7 – 7, 9 – 30, 32 – 46, 95 – 96, 101 – 138, 140 – 142
158582	56 – 64, 66 – 74, 77 – 81, 83 – 148, 150 – 203, 205 – 300, 303 – 341, 343 – 355, 357 – 360, 362 – 372
158632	157 – 166, 168 – 178, 182 – 205, 207 – 210, 212 – 252, 254 – 262, 264 – 268, 270 – 272
158801	135 – 311
158975	87 – 157, 159 – 161, 164 – 220, 222 – 234, 237 – 244, 253 – 276, 278 – 282, 315 – 335, 337 – 353
159041	105 – 117, 119 – 143, 164 – 196, 198 – 200, 202 – 207, 209 – 238, 240 – 240, 242 – 244, 246 – 247, 249 – 377, 379 – 379, 381 – 392
159086	116 – 140, 142 – 165, 167 – 168, 179 – 207, 209 – 227, 235 – 250, 252 – 252, 254 – 285, 287 – 313, 315 – 324, 326 – 362, 364 – 406, 408 – 421, 423 – 456, 458 – 490, 492 – 515, 522 – 556
159113	259 – 276, 278 – 384, 386 – 476, 478 – 519
159179	222 – 223, 225 – 251, 253 – 282, 284 – 306, 308 – 312, 314 – 334
159202	186 – 203, 205 – 225, 227 – 269
159203	3 – 58, 60 – 82
159224	249 – 278, 280 – 282, 284 – 298, 300 – 368, 370 – 385, 388 – 417
160387	155 – 158, 160 – 173, 175 – 293, 295 – 306, 308 – 336, 338 – 381, 383 – 394
160472	140 – 177, 179 – 186, 188 – 196, 198 – 205, 207 – 254, 256 – 325, 337 – 380, 382 – 521
160479	296 – 320
160530	188 – 201, 203 – 297, 301 – 358, 372 – 625
160613	108 – 125, 127 – 179, 194 – 226, 238 – 269, 272 – 323
160736	205 – 263
160800	1 – 24, 37 – 37, 40 – 41, 50 – 69, 71 – 87
160801	1 – 29, 31 – 96, 98 – 105, 112 – 112, 115 – 155, 167 – 423
160879	113 – 184, 194 – 254, 267 – 563
160899	114 – 128
160953	202 – 205, 208 – 210, 214 – 253, 255 – 260
160954	111 – 129, 131 – 133, 135 – 136
160958	1 – 10, 12 – 12, 14 – 26, 28 – 133, 135 – 177, 191 – 214
160963	1 – 15
160975	78 – 99
160980	10 – 39
161118	7 – 103
161379	118 – 140, 143 – 147, 154 – 267, 269 – 292, 294 – 306, 308 – 308, 324 – 423, 425 – 500
161407	75 – 139, 141 – 164, 166 - 177
161520	136 – 463, 465 – 467, 479 – 498
161562	41 – 261
161948	349 – 410, 412 – 701
162347	119 – 192, 195 – 199, 205 – 275, 277 – 280, 290 – 301, 303 – 350, 352 – 488, 490 – 546
162526	118 – 123, 125 – 128, 130 – 130, 143 – 148, 150 – 189, 191 – 320, 322 – 366, 371 – 381, 383 – 399, 401 – 403, 405 – 427, 432 – 439, 441 – 501
162576	2 – 10, 12 – 14, 30 – 65
162577	2 – 12
162620	166 – 185, 187 – 191, 193 – 226, 228 – 234
162623	2 – 75, 83 – 113, 115 – 135, 137 – 154, 156 – 191, 193 – 198, 200 – 263, 265 – 273, 275 – 281, 283 – 315, 317 – 338
162690	264 – 273, 276 – 276, 278 – 285, 287 – 288, 290 – 310, 313 – 333, 335 – 344, 346 – 347, 349 – 349, 351 – 399, 401 – 403, 405 – 406, 415 – 425, 429 – 469, 471 – 573, 575 – 617, 620 – 630, 632 – 634, 636 – 642
162764	138 – 141, 143 – 146, 148 – 163, 165 – 172, 194 – 237
162843	114 – 137, 139 – 161, 163 – 163, 165 – 165, 167 – 210, 212 – 254, 256 – 258, 260 – 263, 278 – 288, 290 – 333, 335 – 409, 411 – 448, 450 – 462, 464 – 517
162882	122 – 126, 128 – 148, 150 – 172, 174 – 176, 178 – 180, 182 – 230, 232 – 289, 291 – 330, 332 – 392, 394 – 448
165591	73 – 87, 89 – 135, 147 – 184, 187 – 207, 210 – 210, 212 – 216, 219 – 289, 291 – 383, 385 – 389, 391 – 392, 394 – 401, 403 – 410, 412 – 433, 435 – 466
165632	183 – 187, 191 – 198, 200 – 200, 202 – 213, 215 – 222, 224 – 234, 236 – 251, 253 – 253, 255 – 271, 273 – 278, 280 – 280, 282 – 283, 285 – 289, 291 – 304, 306 – 307, 309 – 321, 323 – 329, 331 – 335, 338 – 372, 374 – 392, 394 – 399, 414 – 436, 438 – 440, 442 – 468, 470 – 471, 473 – 473, 476 – 480, 482 – 532, 534 – 554, 556 – 557, 559 – 563, 576 – 608
165703	105 – 146
165732	91 – 97, 99 – 100, 102 – 102, 116 – 123, 125 – 125, 127 – 128, 130 – 130, 132 – 134, 136 – 138, 140 – 144, 146 – 146, 148 – 158, 160 – 163, 165 – 187, 189 – 192, 194 – 196, 198 – 205, 207 – 210, 212 – 214, 228 – 289, 297 – 302, 304 – 336, 338 – 340, 342 – 356, 358 – 391, 393 – 401, 408 – 416, 418 – 422, 424 – 430, 432 – 444, 446 – 499, 549 – 564
165767	210 – 220, 222 – 225, 227 – 233, 236 – 249, 251 – 255, 257 – 269, 272 – 275, 280 – 286, 295 – 303, 305 – 307, 309 – 309, 311 – 316, 319 – 322, 324 – 329, 331 – 351, 353 – 381, 383 – 422, 424 – 431, 433 – 486, 488 – 489, 491 – 500, 502 – 519, 521 – 533, 535 – 574
165815	117 – 128, 130 – 134, 136 – 139, 141 – 141, 143 – 147, 149 – 150, 153 – 153, 155 – 161, 163 – 165
165817	3 – 3, 5 – 7
165818	2 – 34, 46 – 65, 68 – 73, 75 – 80, 82 – 94
165821	2 – 21, 23 – 30, 42 – 63, 65 – 76, 78 – 82, 84 – 89
165954	121 – 124, 126 – 130, 132 – 138, 140 – 142, 144 – 145, 147 – 153, 155 – 155, 158 – 164
165956	2 – 6, 8 – 11, 13 – 23
166097	150 – 164, 166 – 169, 171 – 173, 185 – 185, 187 – 187, 189 – 196, 198 – 201, 203 – 214
166142	136 – 141, 143 – 146, 148 – 151, 153 – 153, 155 – 162, 164 – 168, 170 – 171, 174 – 176, 183 – 184, 186 – 193, 196 – 219, 221 – 221, 223 – 234, 236 – 262, 264 – 277, 279 – 285, 288 – 295
166143	4 – 48, 50 – 52, 54 – 62
166198	93 – 95, 118 – 129, 131 – 133, 135 – 136, 145 – 157, 291 – 296, 298 – 299, 301 – 309, 311 – 426, 428 – 429, 438 – 466, 468 – 499, 501 – 510, 513 – 520
166305	113 – 113, 131 – 144, 146 – 150, 153 – 155
166383	292 – 308, 310 – 320, 332 – 339, 341 – 343, 355 – 362, 364 – 365, 367 – 378, 380 – 406, 408 – 414, 416 – 431, 449 – 458, 461 – 461, 467 – 480
166466	81 – 81, 83 – 95, 118 – 138, 141 – 145, 147 – 159, 161 – 163, 165 – 181, 184 – 189, 191 – 213, 215 – 215, 217 – 244, 247 – 247, 249 – 252, 256 – 257, 259 – 269, 271 – 276
166658	144 – 155, 160 – 163, 165 – 176, 179 – 181, 183 – 203, 207 – 207, 209 – 231, 233 – 236, 238 – 256, 258 – 263, 267 – 270, 272 – 284, 286 – 288, 290 – 304, 314 – 319, 321 – 323, 325 – 334, 337 – 353, 355 – 363, 365 – 383, 385 – 385, 387 – 414, 416 – 430
166786	267 – 267, 269 – 276, 279 – 279, 281 – 281, 283 – 286, 288 – 288, 290 – 310, 316 – 316, 326 – 334, 336 – 339, 341 – 357, 359 – 371, 373 – 373, 375 – 378, 380 – 430, 432 – 476, 478 – 487, 490 – 516, 528 – 528, 530 – 536, 538 – 541
166850	146 – 169, 201 – 310
166856	142 – 142, 144 – 145, 147 – 155, 157 – 158, 160 – 164
166924	51 – 51, 53 – 60, 62 – 86, 88 – 117, 119 – 154, 156 – 176, 178 – 206
166927	7 – 11, 13 – 19, 21 – 63, 65 – 74, 76 – 93, 95 – 102
166964	319 – 322, 326 – 327, 329 – 333
167575	125 – 132
167576	8 – 14, 16 – 31, 33 – 67, 70 – 70, 74 – 100, 106 – 193, 196 – 222, 226 – 263, 265 – 293
167607	86 – 103, 105 – 112, 117 – 134, 141 – 143, 146 – 146, 148 – 183, 186 – 216, 218 – 247, 253 – 327, 331 – 386, 390 – 391, 394 – 426, 430 – 430
167661	372 – 382, 386 – 439
167680	33 – 48, 53 – 84, 86 – 129, 131 – 139, 142 – 223, 226 – 249, 251 – 266
167776	124 – 125, 127 – 127, 132 – 204, 206 – 242, 251 – 332, 334 – 512, 514 – 546
167844	79 – 89, 91 – 133, 139 – 190, 192 – 198, 201 – 270

Table A.13: Run and luminosity block numbers with good status of the detector components relevant for the analysis at $\sqrt{s} = 7\,\text{TeV}$.

A.3.1 Datachecks

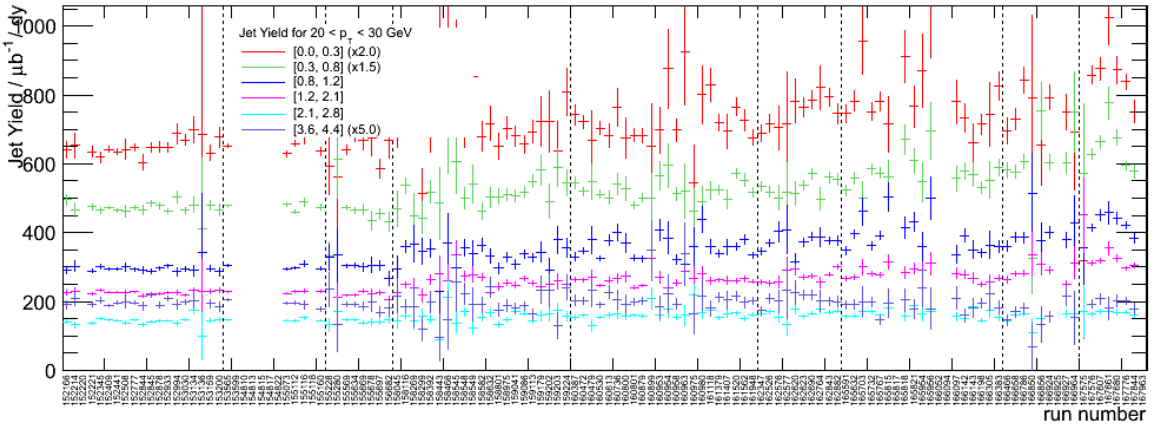

(a) 20 GeV $\leq p_{\mathrm{T}} <$ 30 GeV

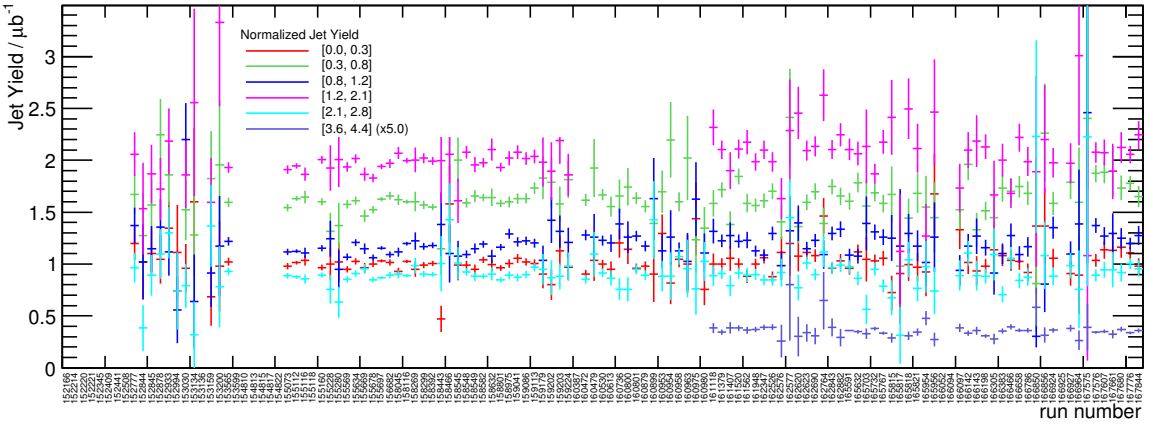

(b) 60 GeV $\leq p_{\mathrm{T}} <$ 80 GeV

Figure A.2: Stability of the jet yield using $R = 0.6$ in the dataset from 2010 at $\sqrt{s} = 7$ TeV. Shown is the mean jet yield as function of the run number in different rapidity and p_{T} regions.

A.4 Inclusive jet cross-section at $\sqrt{s} = 2.76\,\text{TeV}$

A.4.1 List of good luminosity blocks

run	luminosity block numbers
178264	85 – 183, 401 – 423, 425 – 556
178229	164 – 220, 222 – 595, 597 – 1062, 1092 – 1142
178211	160 – 307
178163	680 – 694, 709 – 799

Table A.14: Run and luminosity block numbers with good status of the detector components relevant for the analysis at $\sqrt{s} = 2.76\,\text{TeV}$.

A.4.2 Systematic uncertainty

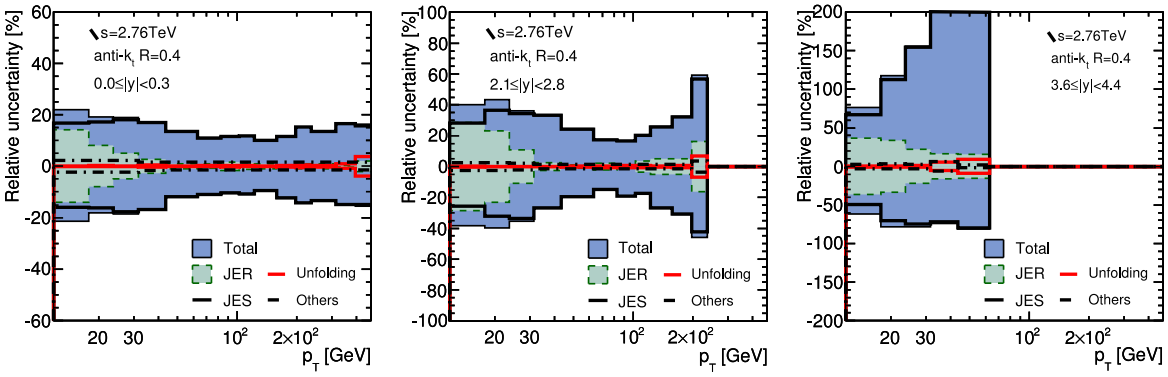

(a) $|y| < 0.3$ (b) $2.1 < |y| < 2.8$ (c) $3.6 < |y| < 4.4$

Figure A.3: Total systematic uncertainties in the measurement of the inclusive jet cross-section at $\sqrt{s} = 2.76\,\text{TeV}$ for anti-k_t jets with $R = 0.4$ in representative rapidity regions. The contributions from the jet energy scale, the jet energy resolution, the unfolding procedure and other sources are shown separately. The uncertainty due to the luminosity measurement is not shown. [64]

A.4.3 Data validation at $\sqrt{s} = 2.76\,\text{TeV}$

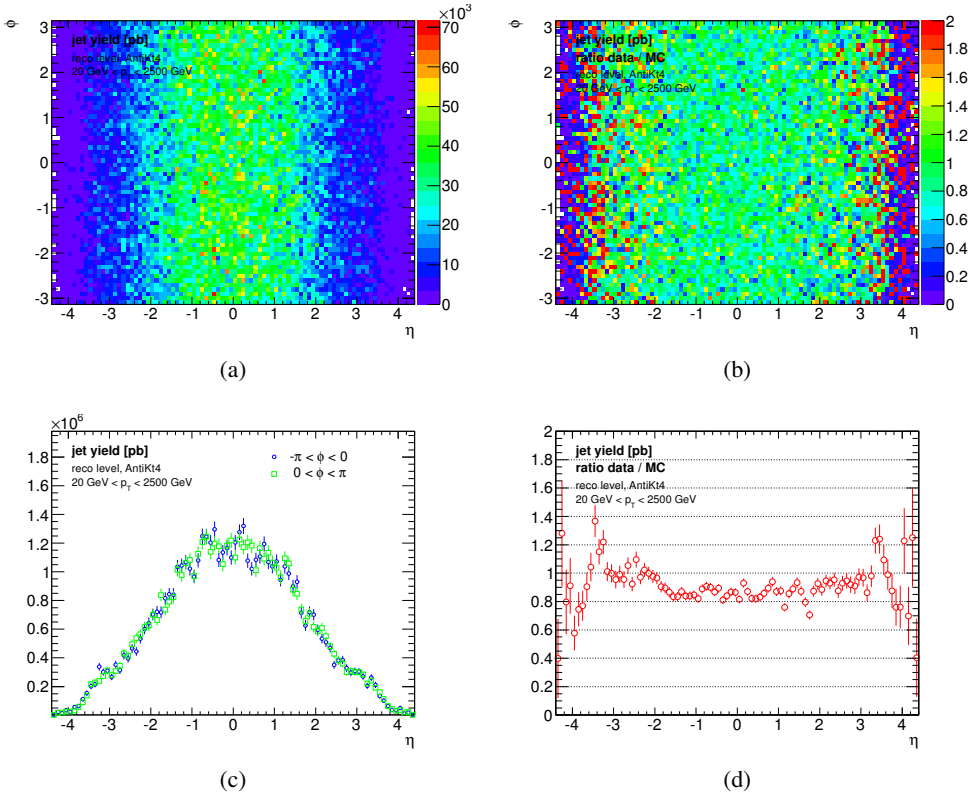

(a) (b)

(c) (d)

Figure A.4: Jet yield using $R = 0.4$ in the dataset at $\sqrt{s} = 2.76\,\text{TeV}$ from 2010 (a) η-ϕ plane of the jet yield in data, (b) ratio of the jet yield in data and Monte Carlo simulation in η-ϕ plane, (c) comparison of the jet yield in data for $-p_{\text{T}} < \phi < 0$ and $0 < \phi < \pi$ as a function of the pseudo-rapidity η, (d) ratio of the jet yield in data as a function of the pseudo-rapidity η. PYTHIA with the AUET 2B tune is used as Monte Carlo simulation.

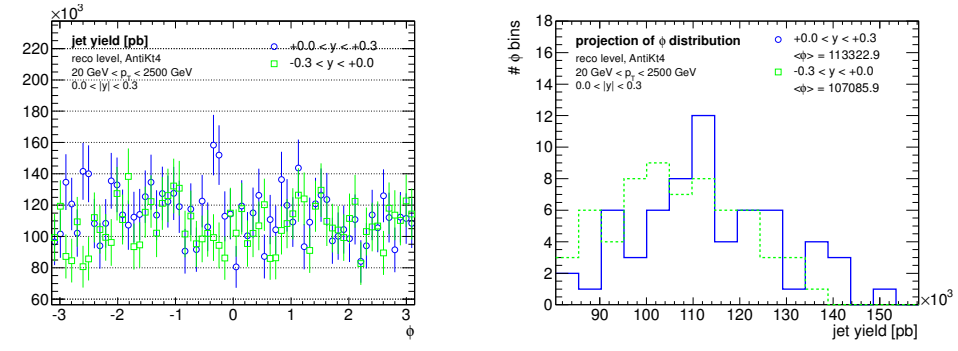

(a) (b)

Figure A.5: Azimuthal distribution of the jet yield using $R = 0.4$ in the dataset at $\sqrt{s} = 2.76\,\text{TeV}$ from 2010 (a) as a function of the azimuthal angle ϕ, separately for $-0.3 < y < 0.0$ and $0.0 < y < 0.3$, and (b) projection of the ϕ distribution.

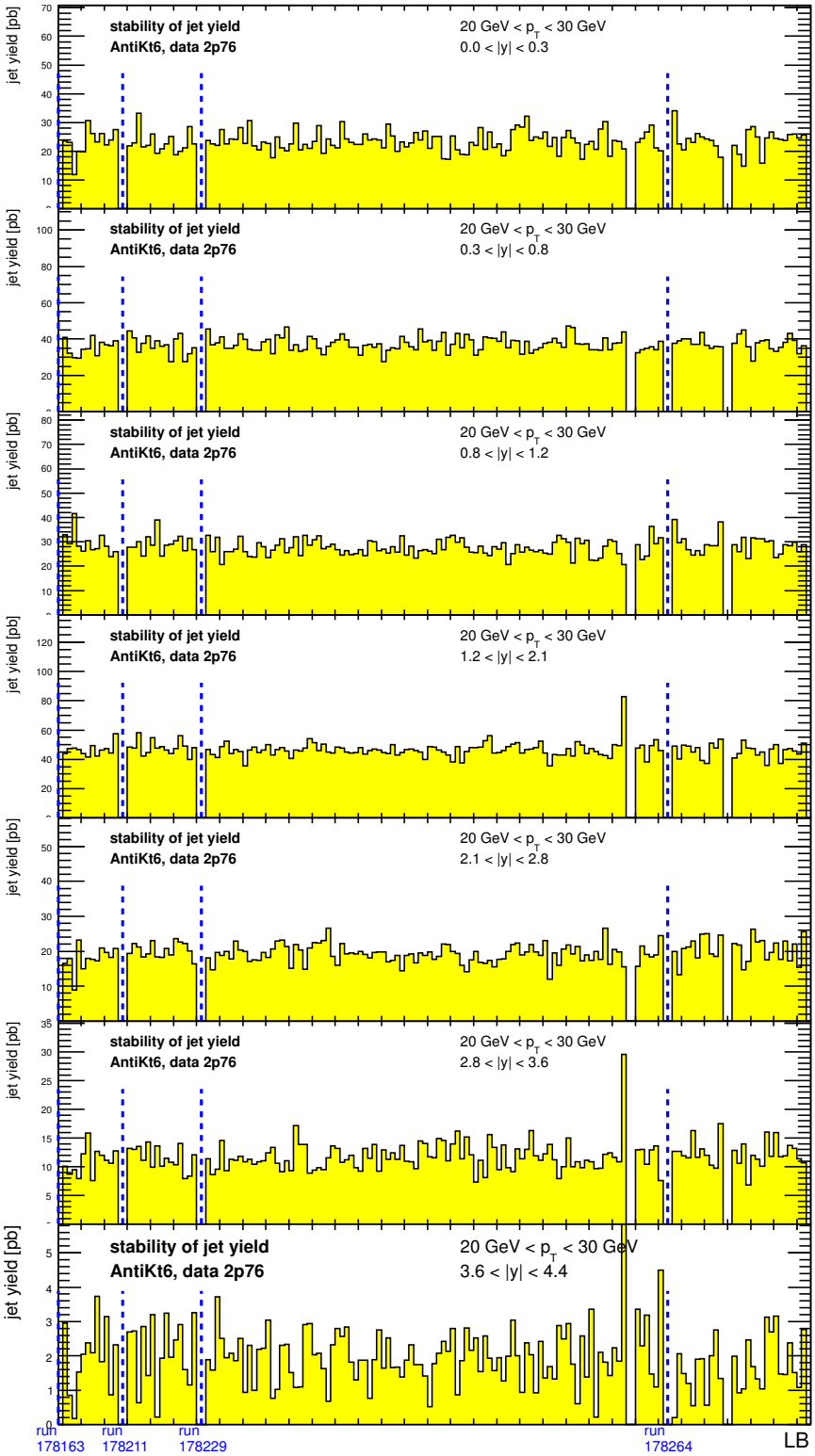

Figure A.6: Jet yield per 10 luminosity blocks, using anti-k_t jets with $R = 0.6$ in the range $20\,\text{GeV} \leq p_\text{T} < 30\,\text{GeV}$ in separate regions of rapidity. Transition between runs are indicated with the *dotted lines*.

A.5 Jet cross-section ratio

A.5.1 Systematic uncertainty in the ratio measurement

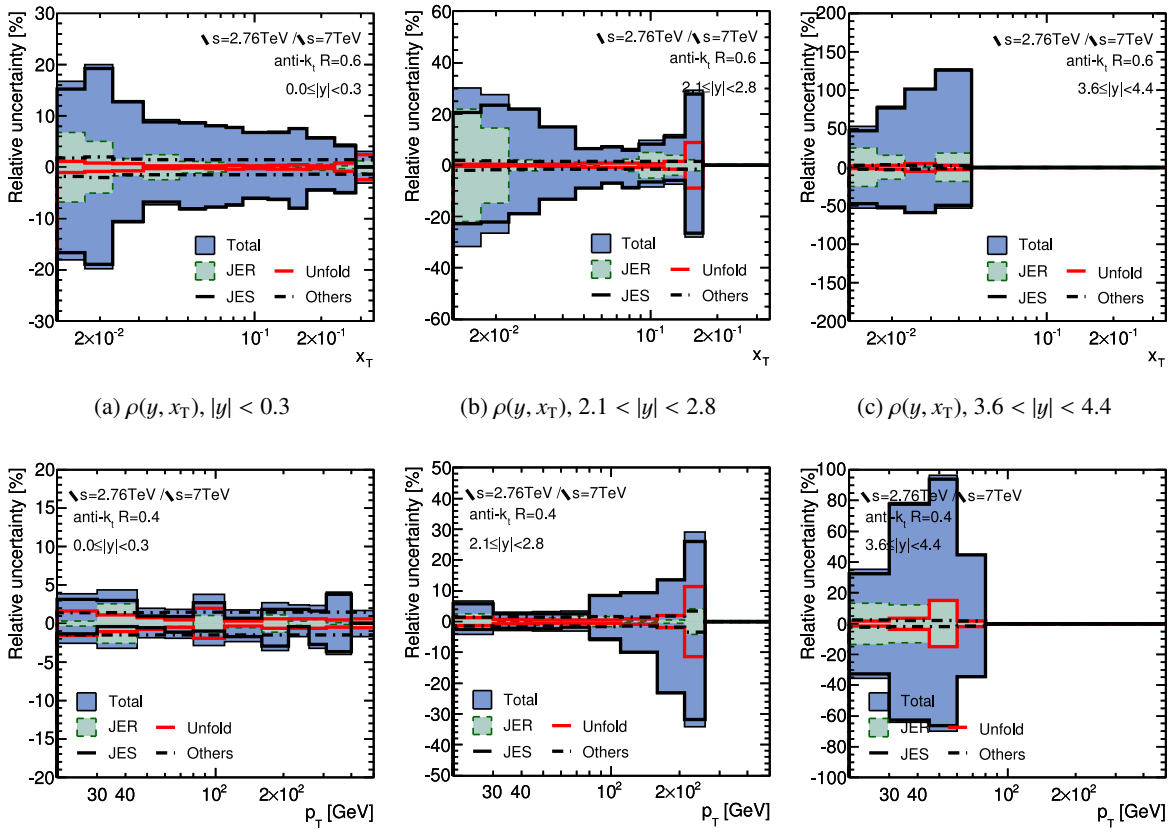

(a) $\rho(y, x_{\mathrm{T}})$, $|y| < 0.3$ (b) $\rho(y, x_{\mathrm{T}})$, $2.1 < |y| < 2.8$ (c) $\rho(y, x_{\mathrm{T}})$, $3.6 < |y| < 4.4$

(d) $\rho(y, p_{\mathrm{T}})$, $|y| < 0.3$ (e) $\rho(y, p_{\mathrm{T}})$, $2.1 < |y| < 2.8$ (f) $\rho(y, p_{\mathrm{T}})$, $3.6 < |y| < 4.4$

Figure A.7: Systematic uncertainty on the ratio measurement of the inclusive jet cross-section at $\sqrt{s} = 2.76\,\mathrm{TeV}$ and $\sqrt{s} = 7\,\mathrm{TeV}$ (a)-(c) as function of x_{T} $\rho(y, x_{\mathrm{T}})$, and (d)-(f) as function of p_{T} $\rho(y, p_{\mathrm{T}})$, in three representative rapidity bins. Jets are defined using the anti-k_t algorithm with $R = 0.4$. The contributions from the jet energy scale, the jet energy resolution, the unfolding procedure and other sources are shown separately. The uncertainty due to the luminosity measurement in the two datasets is not included. [64]

Bibliography

[1] ATLAS Collaboration, *Measurement of the inclusive jet cross section in pp collisions at* $\sqrt{s}$ = 2.76 TeV *and comparison to the inclusive jet cross section at* $\sqrt{s}$ = 7 TeV *using the ATLAS detector*, *Eur. Phys. J.* C73 (2013) 2509, DOI: 10.1140/epjc/s10052-013-2509-4, ARXIV: 1304.4739 [hep-ex].

[2] ATLAS Collaboration, *Measurement of inclusive jet and dijet production in pp collisions at* $\sqrt{s}$ = 7 TeV *using the ATLAS detector*, *Phys. Rev.* D86 (2012) 014022, DOI: 10.1103/PhysRevD.86.014022, ARXIV: 1112.6297 [hep-ex].

[3] D Perepelitsa et al., *Luminosity Determination in pp Collisions at* $\sqrt{s}$ = 2.76 TeV *using the ATLAS Detector*, ATLAS-COM-LUM-2013-004, in preparation, CERN, 2013.

[4] P. Nason and C. Oleari, *Generation cuts and Born suppression in POWHEG* (2013), ARXIV: 1303.3922 [hep-ph].

[5] C. Berger, *Results from the PLUTO Experiment on* e^+e^- *Reactions at High Energies*, *eConf* C790823 (1979) 19.

[6] B. R. Stella and H.-J. Meyer, Γ(9.46 GeV) *and the gluon discovery (a critical recollection of PLUTO results)*, *Eur. Phys. J.* H36.2 (2011) 203–243, ISSN: 2102-6459, DOI: 10.1140/epjh/e2011-10029-3, URL: http://dx.doi.org/10.1140/epjh/e2011-10029-3.

[7] G. Hanson et al., *Evidence for Jet Structure in Hadron Production by* e^+e^- *Annihilation*, *Phys. Rev. Lett.* 35 (24 1975) 1609–1612, DOI: 10.1103/PhysRevLett.35.1609, URL: http://link.aps.org/doi/10.1103/PhysRevLett.35.1609.

[8] C. Berger et al., *Jet analysis of the* Γ(9.46) *decay into charged hadrons*, *Phys. Lett.* B82.3–4 (1979) 449 –455, ISSN: 0370-2693, DOI: http://dx.doi.org/10.1016/0370-2693(79)90265-X, URL: http://www.sciencedirect.com/science/article/pii/037026937990265X.

[9] C. Berger et al., *Evidence for gluon bremsstrahlung in* e^+e^- *annihilations at high energies*, *Phys. Lett.* B86.3-4 (1979) 418 –425, ISSN: 0370-2693, DOI: http://dx.doi.org/10.1016/0370-2693(79)90869-4, URL: http://www.sciencedirect.com/science/article/pii/0370269379908694.

[10] R. Brandelik et al., *Evidence for planar events in* e^+e^- *annihilation at high energies*, *Phys. Lett.* B86.2 (1979) 243 –249, ISSN: 0370-2693, DOI: http://dx.doi.org/10.1016/0370-2693(79)90830-X, URL: http://www.sciencedirect.com/science/article/pii/037026937990830X.

[11] D. P. Barber et al., *Discovery of Three-Jet Events and a Test of Quantum Chromodynamics at PETRA*, *Phys. Rev. Lett.* 43 (1979) 830–833, DOI: 10.1103/PhysRevLett.43.830, URL: http://link.aps.org/doi/10.1103/PhysRevLett.43.830.

[12] W. Bartel et al., *Observation of planar three-jet events in e^+e^- annihilation and evidence for gluon bremsstrahlung*, *Phys. Lett.* B91.1 (1980) 142 –147, ISSN: 0370-2693, DOI: http://dx.doi.org/10.1016/0370-2693(80)90680-2, URL: http://www.sciencedirect.com/science/article/pii/0370269380906802.

[13] R. Ellis, W. Stirling and B. Webber, *QCD and Collider Physics*, Cambridge Monographs on Particle Physics, Nuclear Physics and Cosmology, Cambridge University Press, 2003, ISBN: 9780521545891, URL: http://books.google.de/books?id=TqrPVoS6s0UC.

[14] R. Devenish and A. Cooper-Sarkar, *Deep Inelastic Scattering*, Oxford University Press, 2004, ISBN: 9780198506713, URL: http://books.google.de/books?id=L68zn24GgkcC.

[15] J. Beringer et al., *Review of Particle Physics*, *Phys. Rev.* D86 (2012 and 2013 partial update for the 2014 edition) 010001, DOI: 10.1103/PhysRevD.86.010001.

[16] ATLAS Collaboration, *Observation of a new particle in the search for the Standard Model Higgs boson with the ATLAS detector at the LHC*, *Phys. Lett.* B716 (2012) 1–29, DOI: 10.1016/j.physletb.2012.08.020, ARXIV: 1207.7214 [hep-ex].

[17] CMS Collaboration, *Observation of a new boson at a mass of* 125 GeV *with the CMS experiment at the LHC*, *Phys. Lett.* B716 (2012) 30–61, DOI: 10.1016/j.physletb.2012.08.021, ARXIV: 1207.7235 [hep-ex].

[18] Wikipedia, *Standard Model of elementary particles*, 2013, URL: http://en.wikipedia.org/wiki/File:Standard_Model_of_Elementary_Particles.svg.

[19] Y. Fukuda et al., *Measurements of the solar neutrino flux from Super-Kamiokande's first 300 days*, *Phys. Rev. Lett.* 81 (1998) 1158–1162, DOI: 10.1103/PhysRevLett.81.1158, ARXIV: hep-ex/9805021 [hep-ex].

[20] Wikipedia, *Elementary particle interactions*, 2013, URL: http://en.wikipedia.org/wiki/File:Elementary_particle_interactions.svg.

[21] H. D. Politzer, *Reliable Perturbative Results for Strong Interactions?*, *Phys. Rev. Lett.* 30 (1973) 1346–1349, DOI: 10.1103/PhysRevLett.30.1346.

[22] D. Gross and F. Wilczek, *Ultraviolet Behavior of Nonabelian Gauge Theories*, *Phys. Rev. Lett.* 30 (1973) 1343–1346, DOI: 10.1103/PhysRevLett.30.1343.

[23] J. D. Bjorken and E. A. Paschos, *Inelastic Electron-Proton and γ-Proton Scattering and the Structure of the Nucleon*, *Phys. Rev.* 185 (5 1969) 1975–1982, DOI: 10.1103/PhysRev.185.1975, URL: http://link.aps.org/doi/10.1103/PhysRev.185.1975.

[24] R. P. Feynman, *Very High-Energy Collisions of Hadrons*, *Phys. Rev. Lett.* 23 (24 1969) 1415–1417, DOI: 10.1103/PhysRevLett.23.1415, URL: http://link.aps.org/doi/10.1103/PhysRevLett.23.1415.

[25] W. Verkerke, *Measurement of Charm production in deep inelastic scattering*, PhD thesis, 1998.

[26] V. Gribov and L. Lipatov, *Deep inelastic ep scattering in perturbation theory*, *Sov. J. Nucl. Phys.* 15 (1972) 438–450.

[27] G. Altarelli and G. Parisi, *Asymptotic Freedom in Parton Language*, *Nucl. Phys. B* 126 (1977) 298, DOI: 10.1016/0550-3213(77)90384-4.

[28] Y. L. Dokshitzer, *Calculation of the Structure Functions for Deep Inelastic Scattering and e^+e^- Annihilation by Perturbation Theory in Quantum Chromodynamics.*, *Sov. Phys. JETP* 46 (1977) 641–653.

[29] J. C. Collins, D. E. Soper and G. F. Sterman, *Factorization of Hard Processes in QCD*, *Adv. Ser. Direct High Energy Phys.* 5 (1988) 1–91, ARXIV: hep-ph/0409313 [hep-ph].

[30] B. Combridge, J. Kripfganz and J. Ranft, *Hadron production at large transverse momentum and QCD*, *Phys. Lett.* B70.2 (1977) 234 –238, ISSN: 0370-2693, DOI: http://dx.doi.org/10.1016/0370-2693(77)90528-7, URL: http://www.sciencedirect.com/science/article/pii/0370269377905287.

[31] B. Andersson et al., *Parton fragmentation and string dynamics*, *Phys. Rep.* 97.2–3 (1983) 31 – 145, ISSN: 0370-1573, DOI: 10.1016/0370-1573(83)90080-7, URL: http://www.sciencedirect.com/science/article/pii/0370157383900807.

[32] B. Webber, *A QCD Model for Jet Fragmentation Including Soft Gluon Interference*, *Nucl. Phys.* B238 (1984) 492, DOI: 10.1016/0550-3213(84)90333-X.

[33] D. Amati and G. Veneziano, *Preconfinement as a Property of Perturbative QCD*, *Phys. Lett.* B83 (1979) 87, DOI: 10.1016/0370-2693(79)90896-7.

[34] G. P. Salam, *Towards Jetography*, *Eur. Phys. J.* C67 (2010) 637–686, DOI: 10.1140/epjc/s10052-010-1314-6, ARXIV: 0906.1833 [hep-ph].

[35] M. Cacciari, G. Salam and G. Soyez, *The anti-k_t jet clustering algorithm*, *JHEP* 0804 (2008) 063, ARXIV: 0802.1189.

[36] T. Sjostrand, S. Mrenna and P. Skands, *PYTHIA 6.4 Physics and Manual*, *JHEP* 05 (2006) 026, ARXIV: hep-ph/0603175.

[37] G. Corcella et al., *HERWIG 6: An Event generator for hadron emission reactions with interfering gluons (including supersymmetric processes)*, *JHEP* 0101 (2001) 010, ARXIV: hep-ph/0011363 [hep-ph].

[38] R. Corke and T. Sjostrand, *Improved Parton Showers at Large Transverse Momenta*, *Eur. Phys. J.* C69 (2010) 1–18, DOI: 10.1140/epjc/s10052-010-1409-0, ARXIV: 1003.2384 [hep-ph].

[39] T. Sjostrand, S. Mrenna and P. Skands, *A brief introduction to PYTHIA 8.1*, *Comput. Phys. Commun.* 178.11 (2008) 852 –867, ISSN: 0010-4655, DOI: 10.1016/j.cpc.2008.01.036, ARXIV: 0710.3820 [hep-ph].

[40] S. Gieseke, P. Stephens and B. Webber, *New formalism for QCD parton showers*, *JHEP* 0312 (2003) 045, ARXIV: hep-ph/0310083 [hep-ph].

[41] J. Butterworth, J. R. Forshaw and M. Seymour, *Multiparton interactions in photoproduction at HERA*, *Z. Phys.* C72 (1996) 637–646, DOI: 10.1007/s002880050286, ARXIV: hep-ph/9601371 [hep-ph].

[42] M. Bahr et al., *Herwig++ Physics and Manual*, *Eur. Phys. J.* C58 (2008) 639–707, DOI: 10.1140/epjc/s10052-008-0798-9, ARXIV: 0803.0883 [hep-ph].

[43] M. Bahr, S. Gieseke and M. H. Seymour, *Simulation of multiple partonic interactions in Herwig++*, *JHEP* 0807 (2008) 076, DOI: 10.1088/1126-6708/2008/07/076, ARXIV: 0803.3633 [hep-ph].

[44] A. Sherstnev and R. Thorne, *Parton Distributions for LO Generators*, *Eur. Phys. J.* C55 (2008) 553–575, DOI: 10.1140/epjc/s10052-008-0610-x, ARXIV: 0711.2473 [hep-ph].

[45] A. D. Martin et al., *Parton distributions for the LHC*, *Eur. Phys. J.* C63 (2009) 189–285, DOI: 10.1140/epjc/s10052-009-1072-5, ARXIV: 0901.0002 [hep-ph].

[46] ATLAS Collaboration, *ATLAS tunes of PYTHIA 6 and PYTHIA 8 for MC11*, ATL-PHYS-PUB-2011-009, 2011, URL: http://cdsweb.cern.ch/record/1363300.

[47] H.-L. Lai et al., *New parton distributions for collider physics*, *Phys. Rev.* D82 (2010) 074024, DOI: 10.1103/PhysRevD.82.074024, ARXIV: 1007.2241 [hep-ph].

[48] R. D. Ball et al., *A first unbiased global NLO determination of parton distributions and their uncertainties*, *Nucl. Phys.* B838 (2010) 136–206, DOI: 10.1016/j.nuclphysb.2010.05.008, ARXIV: 1002.4407 [hep-ph].

[49] S. Forte et al., *Heavy quarks in deep-inelastic scattering*, *Nucl. Phys.* B834 (2010) 116–162, DOI: 10.1016/j.nuclphysb.2010.03.014, ARXIV: 1001.2312 [hep-ph].

[50] *HERAPDF 1.5*, URL: https://www.desy.de/h1zeus/combined_results/index.php?do=proton_structure.

[51] S. Alekhin, J. Blumlein and S. Moch, *Parton Distribution Functions and Benchmark Cross Sections at NNLO*, *Phys. Rev.* D86 (2012) 054009, DOI: 10.1103/PhysRevD.86.054009, ARXIV: 1202.2281 [hep-ph].

[52] J. C. Collins and W.-K. Tung, *Calculating Heavy Quark Distributions*, *Nucl. Phys.* B278 (1986) 934, DOI: 10.1016/0550-3213(86)90425-6.

[53] M. Aivazis et al., *Leptoproduction of heavy quarks. 2. A Unified QCD formulation of charged and neutral current processes from fixed target to collider energies*, *Phys. Rev.* D50 (1994) 3102–3118, DOI: 10.1103/PhysRevD.50.3102, ARXIV: hep-ph/9312319 [hep-ph].

[54] ATLAS Collaboration, *New ATLAS event generator tunes to 2010 data*, ATL-PHYS-PUB-2011-008, 2011, URL: http://cdsweb.cern.ch/record/1345343.

[55] P. Z. Skands, *Tuning Monte Carlo Generators: The Perugia Tunes*, *Phys. Rev.* D82 (2010) 074018, DOI: 10.1103/PhysRevD.82.074018, ARXIV: 1005.3457v4 [hep-ph].

[56] ATLAS Collaboration, *Charged particle multiplicities in pp interactions at* $\sqrt{s} = 900$ GeV *and* 7 TeV *in a diffractive limited phase-space measured with the ATLAS detector at the LHC and new PYTHIA6 tune*, ATLAS-CONF-2010-031, 2010, URL: https://atlas.web.cern.ch/Atlas/GROUPS/PHYSICS/CONFNOTES/ATLAS-CONF-2010-031/.

[57] ATLAS Collaboration, *The ATLAS Simulation Infrastructure*, *Eur. Phys. J.* C70 (2010) 823–874, ARXIV: 1005.4568 [physics.ins-det].

[58] S. Agostinelli et al., *GEANT4: A Simulation toolkit*, *Nucl. Instrum. Meth.* A506 (2003) 250–303.

[59] A. Ribon et al., *Status of GEANT4 hadronic physics for the simulation of LHC experiments at the start of LHC physics program*, CERN-LCGAPP-2010-01, Document available at http://lcgapp.cern.ch/project/docs/noteStatusHadronic2010.pdf, CERN, 2010, URL: http://sftweb.cern.ch/AAdocuments.

[60] A. E. Kiryunin et al., *GEANT4 physics evaluation with testbeam data of the ATLAS hadronic end-cap calorimeter*, *Journal of Physics: Conference Series* 160.1 (2009) 012075, URL: http://stacks.iop.org/1742-6596/160/i=1/a=012075.

[61] S. Catani and M. Seymour, *A General algorithm for calculating jet cross-sections in NLO QCD*, *Nucl. Phys.* B485 (1997) 291–419, DOI: 10.1016/S0550-3213(96)00589-5, ARXIV: hep-ph/9605323 [hep-ph].

[62] Z. Nagy, *Next-to-leading order calculation of three jet observables in hadron hadron collision*, *Phys. Rev.* D68 (2003) 094002, DOI: 10.1103/PhysRevD.68.094002, ARXIV: hep-ph/0307268.

[63] T. Carli et al., *A posteriori inclusion of parton density functions in NLO QCD final-state calculations at hadron colliders: The APPLGRID Project*, *Eur. Phys. J.* C66 (2010) 503–524, DOI: 10.1140/epjc/s10052-010-1255-0, ARXIV: 0911.2985 [hep-ph].

[64] T. Carli et al., *Measurement of the inclusive jet cross section in proton-proton collision data at* 2.76 TeV *centre-of-mass energy using the ATLAS detector*, ATL-COM-PHYS-2012-498, supporting document, CERN, 2012.

[65] M. Botje et al., *The PDF4LHC Working Group Interim Recommendations* (2011), ARXIV: 1101.0538 [hep-ph].

[66] H.-L. Lai et al., *Uncertainty induced by QCD coupling in the CTEQ global analysis of parton distributions*, *Phys. Rev.* D82 (2010) 054021, DOI: 10.1103/PhysRevD.82.054021, ARXIV: 1004.4624 [hep-ph].

[67] V. Sudakov, *Vertex parts at very high-energies in quantum electrodynamics*, *Sov. Phys. JETP* 3 (1956) 65–71.

[68] U. Baur, *Weak Boson Emission in Hadron Collider Processes*, *Phys. Rev.* D75 (2007) 013005, DOI: 10.1103/PhysRevD.75.013005, ARXIV: hep-ph/0611241 [hep-ph].

[69] K. Mishra et al., *Electroweak Corrections at High Energies* (2013), ARXIV: 1308.1430 [hep-ph].

[70] S. Dittmaier, A. Huss and C. Speckner, *Weak radiative corrections to dijet production at hadron colliders*, *JHEP* 1211 (2012) 095, DOI: 10.1007/JHEP11(2012)095, ARXIV: 1210.0438 [hep-ph].

[71] S. Frixione and B. R. Webber, *Matching NLO QCD computations and parton shower simulations*, *JHEP* 0206 (2002) 029, ARXIV: hep-ph/0204244 [hep-ph].

[72] P. Nason, *A New method for combining NLO QCD with shower Monte Carlo algorithms*, *JHEP* 0411 (2004) 040, DOI: 10.1088/1126-6708/2004/11/040, ARXIV: hep-ph/0409146 [hep-ph].

[73] M. Kramer, S. Mrenna and D. E. Soper, *Next-to-leading order QCD jet production with parton showers and hadronization*, *Phys. Rev.* D73 (2006) 014022, DOI: 10.1103/PhysRevD.73.014022, ARXIV: hep-ph/0509127 [hep-ph].

[74] S. Hoeche et al., *QCD matrix elements + parton showers: The NLO case*, *JHEP* 1304 (2013) 027, DOI: 10.1007/JHEP04(2013)027, ARXIV: 1207.5030 [hep-ph].

[75] E. Boos et al., *Generic user process interface for event generators* (2001), ARXIV: hep-ph/0109068 [hep-ph].

[76] S. Alioli et al., *A general framework for implementing NLO calculations in shower Monte Carlo programs: the POWHEG BOX*, *JHEP* 1006 (2010) 043, DOI: 10.1007/JHEP06(2010)043, ARXIV: 1002.2581 [hep-ph].

[77] P. Nason and C. Oleari, *Direct communication*.

[78] P. Jenni, *EAGLE : experiment for accurate gamma, lepton and energy measurements: Expression of interest* (1992).

[79] P. R. Norton, *The ASCOT detector at the LHC: Expression of Interest* (1992).

[80] Atlas Collaboration, *ATLAS: Detector and physics performance technical design report. Volume 1* (1999).

[81] Atlas Collaboration, *ATLAS: Detector and physics performance technical design report. Volume 2* (1999).

[82] J. Pequenao, *Computer generated image of the whole ATLAS detector*, 2008.

[83] J. Pequenao, *Computer generated image of the ATLAS inner detector*, 2008.

[84] ATLAS Collaboration, *Performance of primary vertex reconstruction in proton-proton collisions at* $\sqrt{s} = 7$ TeV *in the ATLAS experiment*, ATLAS-CONF-2010-069, CERN, 2010.

[85] ATLAS Collaboration, *The ATLAS Inner Detector commissioning and calibration*, *Eur. Phys. J.* C70 (2010) 787–821, DOI: 10.1140/epjc/s10052-010-1366-7, ARXIV: 1004.5293 [physics.ins-det].

[86] J. Pequenao, *Computer Generated image of the ATLAS calorimeter*, 2008.

[87] ATLAS Collaboration, *ATLAS Liquid Argon Calorimeter: Technical Design Report*, ATLAS technical design report, CERN, 1996, ISBN: 9789290830900, URL: http://books.google.de/books?id=Fp7FAQAACAAJ.

[88] ATLAS Collaboration, *The ATLAS Experiment at the CERN Large Hadron Collider*, *JINST* 3 (2008) S08003, DOI: 10.1088/1748-0221/3/08/S08003.

[89] M. Aharrouche et al., *Energy linearity and resolution of the ATLAS electromagnetic barrel calorimeter in an electron test-beam*, *Nucl. Instrum. Meth.* A568 (2006) 601–623, DOI: 10.1016/j.nima.2006.07.053, ARXIV: physics/0608012 [physics].

[90] ATLAS Collaboration, *ATLAS tile calorimeter: Technical Design Report*, Technical Design Report ATLAS, CERN, 1996.

[91] T. Davidek, *ATLAS tile calorimeter performance for single particles in beam tests*, *J. Phys. Conf. Ser.* 160 (2009) 012057, DOI: 10.1088/1742-6596/160/1/012057.

[92] B. Dowler et al., *Performance of the ATLAS hadronic end-cap calorimeter in beam tests*, *Nucl. Instrum. Meth.* A482 (2002) 94–124, DOI: 10.1016/S0168-9002(01)01338-9.

[93] J. Archambault et al., *Energy calibration of the ATLAS liquid argon forward calorimeter*, *JINST* 3 (2008) P02002, DOI: 10.1088/1748-0221/3/02/P02002.

[94] P. Jenni, M. Nessi and M. Nordberg, *Zero Degree Calorimeters for ATLAS*, LHCC-I-016. CERN-LHCC-2007-001, CERN, URL: http://cds.cern.ch/record/1009649.

[95] ATLAS Collaboration, *Charged-particle multiplicities in pp interactions at* $\sqrt{s} = 900$ GeV *measured with the ATLAS detector at the LHC*, *Phys. Lett.* B688 (2010) 21–42, DOI: 10.1016/j.physletb.2010.03.064, ARXIV: 1003.3124 [hep-ex].

[96] J. Pequenao, *Computer generated image of the ATLAS Muons subsystem*, 2008.

[97] A. Salvucci, *Measurement of muon momentum resolution of the ATLAS detector*, *EPJ Web Conf.* 28 (2012) 12039, DOI: 10.1051/epjconf/20122812039, ARXIV: 1201.4704 [physics.ins-det].

[98] V Cindro et al., *The ATLAS Beam Conditions Monitor*, *JINST* 3.02 (2008) P02004, URL: http://stacks.iop.org/1748-0221/3/i=02/a=P02004.

[99] S. van der Meer, *Calibration of the effective beam height in the ISR*, 1968.

[100] C. Rubbia, *Measurement of the luminosity of* $p\overline{p}$ *collider with a (generalized) Van der Meer Method*, CERN-pp-Note-38, CERN, 1977.

[101] *Improved Luminosity Determination in pp Collisions at* $\sqrt{s} = 7$ TeV *using the ATLAS Detector at the LHC*, ATLAS-CONF-2012-080, CERN, 2012.

[102] The Luminosity Group, *Preliminary Luminosity Determination in pp Collisions at* $\sqrt{s}$ = 8 TeV *using the ATLAS Detector in 2012*, ATL-COM-LUM-2012-013, CERN, 2012.

[103] ATLAS Collaboration, *Improved luminosity determination in pp collisions at* $\sqrt{s}$ = 7 TeV *using the ATLAS detector at the LHC*, *Eur. Phys. J.* C73 (2013) 2518, DOI: 10.1140/epjc/s10052-013-2518-3, ARXIV: 1302.4393 [hep-ex].

[104] C. Barschel et al., *Results of the LHC DCCT Calibration Studies*, 2012, URL: https://cds.cern.ch/record/1425904.

[105] A. Alici et al., *Study of the LHC ghost charge and satellite bunches for luminosity calibration.* 2012, URL: https://cds.cern.ch/record/1427728.

[106] G. Anders et al., *Study of the relative LHC bunch populations for luminosity calibration* (2012).

[107] A. Jeff et al., *Longitudinal density monitor for the LHC*, *Phys. Rev. ST Accel. Beams* 15 (3 2012) 032803, DOI: 10.1103/PhysRevSTAB.15.032803, URL: http://link.aps.org/doi/10.1103/PhysRevSTAB.15.032803.

[108] ATLAS Collaboration, *Updated Luminosity Determination in pp Collisions at* $\sqrt{s}$ = 7 TeV *using the ATLAS Detector*, ATLAS-CONF-2011-011, CERN, 2011.

[109] ATLAS Collaboration, *Jet energy measurement with the ATLAS detector in proton-proton collisions at* $\sqrt{s}$ = 7 TeV, *Eur. Phys. J.* C73 (2013) 2304, DOI: 10.1140/epjc/s10052-013-2304-2, ARXIV: 1112.6426 [hep-ex].

[110] S. Menke, *Topological Clustering*, 2008, URL: https://twiki.cern.ch/twiki/bin/viewauth/AtlasComputing/TopologicalClustering.

[111] W. Lampl et al., *Calorimeter clustering algorithms: Description and performance* (2008).

[112] M. Cacciari and G. P. Salam, *Dispelling the* N^3 *myth for the* k_t *jet-finder*, *Phys. Lett. B* 641.1 (2006) 57–61, ISSN: 0370-2693, DOI: 10.1016/j.physletb.2006.08.037.

[113] M. Cacciari, G. P. Salam and G. Soyez, URL: \href{http://fastjet.fr/}{http://fastjet.fr/}.

[114] ATLAS Collaboration, *Jet energy resolution in proton-proton collisions at* $\sqrt{s}$ = 7 TeV *recorded in 2010 with the ATLAS detector*, *Eur. Phys. J.* C73 (2013) 2306, DOI: 10.1140/epjc/s10052-013-2306-0, ARXIV: 1210.6210 [hep-ex].

[115] ATLAS Collaboration, *Single hadron response measurement and calorimeter jet energy scale uncertainty with the ATLAS detector at the LHC* (2012), Accepted by EPJC, ARXIV: 1203.1302 [hep-ex].

[116] E. Abat et al., *Study of energy response and resolution of the ATLAS barrel calorimeter to hadrons of energies from* 20 GeV *to* 350 GeV, *Nucl. Instrum. Meth.* A621 (2010) 134–150, DOI: 10.1016/j.nima.2010.04.054.

[117] P. Z. Skands, *Tuning Monte Carlo Generators: The Perugia Tunes*, *Phys. Rev.* D82 (2010) 074018, DOI: 10.1103/PhysRevD.82.074018, ARXIV: 1005.3457 [hep-ph].

[118] ATLAS Collaboration, *Study of Jet Shapes in Inclusive Jet Production in pp Collisions at* $\sqrt{s}$ = 7 TeV *using the ATLAS Detector*, *Phys. Rev.* D83 (2011) 052003, DOI: 10.1103/PhysRevD.83.052003, ARXIV: 1101.0070 [hep-ex].

[119] *Charged particle multiplicities in pp interactions for track* p_T > 100 MeV *at* $\sqrt{s}$ = 0.9 *and* 7 TeV *measured with the ATLAS detector at the LHC*, ATLAS-CONF-2010-046, CERN, 2010.

[120] ATLAS Collaboration, *In-situ pseudorapidity intercalibration for evaluation of jet energy scale uncertainty using dijet events in proton-proton collisions at* $\sqrt{s} = 7$ TeV, ATLAS-CONF-2011-014, CERN, 2011, URL: http://cdsweb.cern.ch/record/1334876.

[121] P. Bagnaia et al., *Measurement of Jet Production Properties at the CERN anti-p p Collider*, *Phys. Lett.* B144 (1984) 283, DOI: 10.1016/0370-2693(84)91822-7, URL: http://www.sciencedirect.com/science/article/pii/0370269384918227.

[122] S. Baker et al., *Measurement of inclusive jet and dijet cross sections in proton-proton collisions at* 7 TeV *centre-of-mass energy with the ATLAS detector (Supporting Documentation)*, ATL-COM-PHYS-2011-140, CERN, 2011, URL: https://cds.cern.ch/record/1328678.

[123] S. Baker et al., *Measurement of inclusive jet and dijet cross sections in proton-proton collision data at* 7 TeV *centre-of-mass energy using the ATLAS detector*, ATL-COM-PHYS-2011-738, internal supporting documentation, CERN, 2011.

[124] ATLAS Collaboration, *Jet energy measurement with the ATLAS detector in proton-proton collisions at* $\sqrt{s} = 7$ TeV (2011) 100, ARXIV: 1112.6426, URL: http://arxiv.org/abs/1112.6426.

[125] T. Carli, *How to clean jets in 2010 data*, 2011, URL: https://twiki.cern.ch/twiki/bin/viewauth/AtlasProtected/HowToCleanJets.

[126] ATLAS Collaboration, *Measurement of inclusive jet and dijet cross sections in proton-proton collisions at* 7 TeV *centre-of-mass energy with the ATLAS detector*, *Eur. Phys. J.* C71 (2011) 1512, DOI: 10.1140/epjc/s10052-010-1512-2, ARXIV: 1009.5908 [hep-ex].

[127] V. Lendermann et al., *Combining Triggers in HEP Data Analysis*, *Nucl. Instrum. Meth.* A604 (2009) 707–718, DOI: 10.1016/j.nima.2009.03.173, ARXIV: 0901.4118 [hep-ex].

[128] G. D'Agostini, *A Multidimensional unfolding method based on Bayes' theorem*, *Nucl. Instrum. Meth.* A362 (1995) 487–498, DOI: 10.1016/0168-9002(95)00274-X.

[129] M. Schmelling, *The method of reduced cross-entropy A general approach to unfold probability distributions*, *Nucl. Instrum. Meth.* A340.2 (1994) 400 –412, ISSN: 0168-9002, DOI: http://dx.doi.org/10.1016/0168-9002(94)90119-8, URL: http://www.sciencedirect.com/science/article/pii/0168900294901198.

[130] A. Hocker and V. Kartvelishvili, *SVD approach to data unfolding*, *Nucl. Instrum. Meth.* A372 (1996) 469–481, DOI: 10.1016/0168-9002(95)01478-0, ARXIV: hep-ph/9509307 [hep-ph].

[131] B. Malaescu, *An Iterative, dynamically stabilized method of data unfolding* (2009), ARXIV: 0907.3791 [physics.data-an], URL: http://arxiv.org/abs/0907.3791.

[132] Durham HepData Project, *Measurements of the electron and muon inclusive cross-sections in proton-proton collisions at* $\sqrt{s} = 7$ TeV *with the ATLAS detector*, URL: http://hepdata.cedar.ac.uk/view/ins926145.

[133] ATLAS Collaboration, *Observation of a Centrality-Dependent Dijet Asymmetry in Lead-Lead Collisions at* $\sqrt{s_{NN}} = 2.77$ *TeV with the ATLAS Detector at the LHC*, *Phys. Rev. Lett.* 105 (2010) 252303, DOI: 10.1103/PhysRevLett.105.252303, ARXIV: 1011.6182 [hep-ex].

[134] A. Abulencia et al., *Measurement of the inclusive jet cross section using the k(t) algorithm in p anti-p collisions at* $\sqrt{s} = 1.96$ TeV, *Phys. Rev. Lett.* 96 (2006) 122001, DOI: 10.1103/PhysRevLett.96.122001, ARXIV: hep-ex/0512062 [hep-ex].

[135] A. Abulencia et al., *Measurement of the inclusive jet cross section in* $p\bar{p}$ *interactions at* $\sqrt{s} = 1.96$ TeV *using a cone-based jet algorithm.*, *Phys. Rev.* D74 (2006) 071103, DOI: 10.1103/PhysRevD.74.071103, ARXIV: hep-ex/0512020 [hep-ex].

[136] A. Abulencia et al., *Measurement of the inclusive jet cross section using the k_T algorithm in $p\bar{p}$ collisions at $\sqrt{s}$ = 1.96 TeV with the CDF II detector*, *Phys. Rev.* D 75 (2007) 092006, DOI: 10.1103/PhysRevD.75.092006, ARXIV: hep-ex/0701051 [hep-ex].

[137] T. Aaltonen et al., *Measurement of the inclusive jet cross section at the Fermilab Tevatron $p\overline{p}$ collider using a cone-based jet algorithm*, *Phys. Rev. D* 78 (5 2008) 052006, DOI: 10.1103/PhysRevD.78.052006, URL: http://link.aps.org/doi/10.1103/PhysRevD.78.052006.

[138] V. M. Abazov et al., *Measurement of the Inclusive Jet Cross Section in $p\overline{p}$ Collisions at $\sqrt{s}$ = 1.96 TeV*, *Phys. Rev. Lett.* 101 (6 2008) 062001, DOI: 10.1103/PhysRevLett.101.062001, URL: http://link.aps.org/doi/10.1103/PhysRevLett.101.062001.

[139] V. M. Abazov et al., *Determination of the strong coupling constant from the inclusive jet cross section in $p\overline{p}$ collisions at $\sqrt{s}$ = 1.96 TeV*, *Phys. Rev.* D80 (2009) 111107, DOI: 10.1103/PhysRevD.80.111107, ARXIV: 0911.2710 [hep-ex].

[140] V. M. Abazov et al., *Measurement of the inclusive jet cross section in $p\bar{p}$ collisions at $\sqrt{s}$ = 1.96 TeV*, *Phys. Rev.* D85 (2012) 052006, DOI: 10.1103/PhysRevD.85.052006, ARXIV: 1110.3771 [hep-ex].

[141] Durham HepData Project, *Measurement of the inclusive jet cross section in pp collisions at $\sqrt{s}$ = 2.76 TeV and comparison to the inclusive jet cross section at $\sqrt{s}$ = 7 TeV using the ATLAS detector*, URL: http://hepdata.cedar.ac.uk/view/p8403.

[142] S. Chekanov et al., *Inclusive jet cross sections in the Breit frame in neutral current deep inelastic scattering at HERA and determination of α_s*, *Phys. Lett.* B547 (2002) 164–180, DOI: 10.1016/S0370-2693(02)02763-6, ARXIV: hep-ex/0208037.

[143] C. Adloff et al., *Measurement of inclusive jet cross-sections in deep inelastic ep scattering at HERA*, *Phys. Lett.* B542 (2002) 193–206, DOI: 10.1016/S0370-2693(02)02375-4, ARXIV: hep-ex/0206029 [hep-ex].

[144] C. Adloff et al., *Measurement of inclusive jet cross-sections in photoproduction at HERA*, *Eur. Phys. J.* C29 (2003) 497–513, DOI: 10.1140/epjc/s2003-01262-9, ARXIV: hep-ex/0302034 [hep-ex].

[145] S. Chekanov et al., *An NLO QCD analysis of inclusive cross-section and jet-production data from the ZEUS experiment*, *Eur. Phys. J.* C42 (2005) 1–16, DOI: 10.1140/epjc/s2005-02293-x, ARXIV: hep-ph/0503274.

[146] A. Aktas et al., *Measurement of inclusive jet production in deep-inelastic scattering at high Q^2 and determination of the strong coupling*, *Phys. Lett.* B653 (2007) 134–144, DOI: 10.1016/j.physletb.2007.07.050, ARXIV: 0706.3722 [hep-ex].

[147] F. D. Aaron et al., *Jet production in ep collisions at high Q^2 and determination of α_s*, *Eur. Phys. J.* C65 (2009), DESY-09-032, ARXIV: 0904.3870 [hep-ex].

[148] F. D. Aaron et al., *Jet Production in ep Collisions at Low Q^2 and Determination of α_s*, *Eur. Phys. J.* C67 (2010) 1–24, DOI: 10.1140/epjc/s10052-010-1282-x, ARXIV: 0911.5678 [hep-ex].

[149] H. Abramowicz et al., *Inclusive-jet cross sections in NC DIS at HERA and a comparison of the k_T, anti-k_T and SIScone jet algorithms*, *Phys. Lett.* B691 (2010) 127–137, DOI: 10.1016/j.physletb.2010.06.015, ARXIV: 1003.2923 [hep-ex].

[150] G. Arnison et al., *Inclusive jet production at $\sqrt{s}$ = 546 GeV*, 1985, URL: http://cds.cern.ch/record/161747.

[151] M. Banner et al., *Observation of very large transverse momentum jets at the CERN $p\overline{p}$ collider*, *Phys. Lett. B* 118.1–3 (1982) 203 –210, ISSN: 0370-2693, DOI: 10.1016/0370-2693(82)90629-3, URL: http://www.sciencedirect.com/science/article/pii/0370269382906293.

[152] J. Alitti et al., *Inclusive jet cross-section and a search for quark compositeness at the CERN $p\overline{p}$ Collider*, *Phys. Lett.* B257.1–2 (1991) 232 –240, DOI: 10.1016/0370-2693(91)90887-V, URL: http://www.sciencedirect.com/science/article/pii/037026939190887V.

[153] J. Appel et al., *Measurement of the s dependence of jet production at the CERN $p\overline{p}$ collider*, *Phys. Lett. B* 160.4–5 (1985) 349 –356, ISSN: 0370-2693, DOI: 10.1016/0370-2693(85)91341-3, URL: http://www.sciencedirect.com/science/article/pii/0370269385913413.

[154] G. Arnison et al., *Measurement of the inclusive jet cross section at the CERN $p\overline{p}$ collider*, *Phys. Lett.* B172.3–4 (1986) 461 –466, ISSN: 0370-2693, DOI: 10.1016/0370-2693(86)90290-X, URL: http://www.sciencedirect.com/science/article/pii/037026938690290X.

[155] F. Abe et al., *Inclusive jet cross-section in $\bar{p}p$ collisions at $\sqrt{s}$ = 1.8 TeV*, *Phys. Rev. Lett.* 68 (1992) 1104–1108, DOI: 10.1103/PhysRevLett.68.1104, URL: http://link.aps.org/doi/10.1103/PhysRevLett.68.1104.

[156] F. Abe et al., *Comparison of jet production in $p\overline{p}$ collisions at $\sqrt{s}$ = 546 and* 1800 GeV, *Phys. Rev. Lett.* 70 (10 1993) 1376–1380, DOI: 10.1103/PhysRevLett.70.1376, URL: http://link.aps.org/doi/10.1103/PhysRevLett.70.1376.

[157] F. Abe et al., *Inclusive jet cross section in $\bar{p}p$ collisions at $\sqrt{s}$ = 1.8 TeV*, *Phys. Rev. Lett.* 77 (1996) 438–443, DOI: 10.1103/PhysRevLett.77.438, ARXIV: hep-ex/9601008 [hep-ex].

[158] A. A. Bhatti, *Inclusive jet production at $\sqrt{s}$ = 630 GeV and a test of scaling at CDF*, *1996 Annual Divisional Meeting (DPF96) of the Division of Particles and Fields of the American Physical Society, Minneapolis, Minnesota, August 10-15*, 1996, URL: http://lss.fnal.gov/archive/1996/conf/Conf-96-352-E.pdf.

[159] B. Abbott et al., *The inclusive jet cross section in $\bar{p}p$ collisions at $\sqrt{s}$ = 1.8 TeV*, *Phys. Rev. Lett.* 82 (1999) 2451–2456, DOI: 10.1103/PhysRevLett.82.2451, ARXIV: hep-ex/9807018 [hep-ex].

[160] B. Abbott et al., *Inclusive jet production in $p\bar{p}$ collisions*, *Phys. Rev. Lett.* 86 (2001) 1707–1712, DOI: 10.1103/PhysRevLett.86.1707, ARXIV: hep-ex/0011036 [hep-ex].

[161] B. Abbott et al., *High-p_T jets in $\bar{p}p$ collisions at $\sqrt{s}$ = 630 GeV and* 1800 GeV, *Phys. Rev.* D64 (2001) 032003, DOI: 10.1103/PhysRevD.64.032003, ARXIV: hep-ex/0012046 [hep-ex].

[162] B. Abbott et al., *Ratio of Jet Cross Sections at $\sqrt{s}$ = 630 GeV and $\sqrt{s}$ = 1800 GeV*, *Phys. Rev. Lett.* 86.12 (2001) 2523–2528, ISSN: 0031-9007, DOI: 10.1103/PhysRevLett.86.2523, ARXIV: 0008072 [hep-ex], URL: http://arxiv.org/abs/hep-ex/0008072.

[163] T. Affolder et al., *Measurement of the strong coupling constant from inclusive jet production at the Tevatron $\bar{p}p$ collider*, *Phys. Rev. Lett.* 88 (2002) 042001, DOI: 10.1103/PhysRevLett.88.042001, ARXIV: hep-ex/0108034 [hep-ex].

[164] V. Abazov et al., *The inclusive jet cross-section in $p\bar{p}$ collisions at $\sqrt{s}$ = 1.8 TeV using the k_T algorithm*, *Phys. Lett.* B525 (2002) 211–218, DOI: 10.1016/S0370-2693(01)01441-1, ARXIV: hep-ex/0109041 [hep-ex].

[165] CMS Collaboration, *Measurement of the Inclusive Jet Cross Section in pp Collisions at $\sqrt{s}$ = 7 TeV*, *Phys. Rev. Lett.* 107 (2011) 132001, DOI: 10.1103/PhysRevLett.107.132001, ARXIV: 1106.0208 [hep-ex].

[166] CMS Collaboration, *Measurement of the inclusive production cross sections for forward jets and for dijet events with one forward and one central jet in pp collisions at* $\sqrt{s} = 7$ TeV, *JHEP* 1206 (2012) 036, DOI: 10.1007/JHEP06(2012)036, ARXIV: 1202.0704 [hep-ex].

[167] CMS Collaboration, *Measurements of differential jet cross sections in proton-proton collisions at* $\sqrt{s} = 7$ TeV *with the CMS detector*, *Phys. Rev.* D87 (2013) 112002, DOI: 10.1103/PhysRevD.87.112002, ARXIV: 1212.6660 [hep-ex].

[168] M. L. Mangano and J. Rojo, *Cross Section Ratios between different CM energies at the LHC: opportunities for precision measurements and BSM sensitivity* (2012), ARXIV: 1206.3557 [hep-ph].

[169] J. Wenninger, *Untitled Manuscript*, private communication, 2013.

[170] T. Akesson et al., *The jet cross-section in pp interactions at* $\sqrt{s} = 45$ GeV *and its* $\sqrt{s}$ *dependence*, *Phys. Lett.* B123 (1983) 133, DOI: 10.1016/0370-2693(83)90973-5.

[171] ATLAS Collaboration, *Measurement of the inclusive jet cross section in proton-proton collision data at* 2.76 TeV *centre-of-mass energy using the ATLAS detector*, auxiliar material, 2013, URL: https://atlas.web.cern.ch/Atlas/GROUPS/PHYSICS/PAPERS/STDM-2012-08/.

[172] ATLAS Collaboration, *Determination of the strange quark density of the proton from ATLAS measurements of the* $W \to l\nu$ *and* $Z \to ll$ *cross sections*, *Phys. Rev. Lett.* 109 (2012) 012001, ARXIV: 1203.4051 [hep-ex].

Acknowledgements

The past five years have been a truly exciting time in particle physics, and I am very happy that I could take my small part in it.

First of all, I would like to thank my thesis advisor, Prof. Dr. Hans-Christian Schultz-Coulon, for giving me the opportunity to perform my research in the ATLAS group at the Kirchhoff-Institute for Physics. I am deeply grateful for the trust and freedom that he showed me, as well as the encouragement to travel and present my work. He gave guidance and motivation when needed, and criticism when necessary.

I would also like to thank Prof. Dr. Norbert Herrmann, who kindly agreed in being the co-referee of this thesis.

Numerous people have contributed to the completion of this work. The most important one is my co-advisor Rainer, who always provided substantial feedback, and stood solid as a rock whenever I panicked. Shima, my co-worker at CERN, is the best colleague I could imagine to perform this measurement with, and I profited a lot from our close collaboration and the numerous discussions about the tiniest details of the analysis. Similarly, I would like to thank Tancredi, Sasha and Witek for providing valuable guidance and sharing their ideas and profound interest in physics. Coming to CERN was always productive, owing to the very friendly atmosphere in the jet community, the luminosity taskforce, and the L1Calo collaboration. In particular, I want to mention Pavel, Bogdan, Chris, Dennis, Brian and Witold. Besides, I want to thank Julia, Gabriel, Frederik and Taylor for showing me also the life outside of the CERN borders.

Nevertheless, it is the ATLAS and ILC group at Heidelberg that turned my PhD into a splendid time, be it in the daily work, or during the numerous activities beyond. Among all of my great colleagues, I want to mention Christoph, Micha, Thorsten, Sahill, Veit, Heiko and Julia, who also became close friends. Thanks for enduring my bad moods, in particular in the final stage of the writing, and all the help you provided. I hope I can make up for it at some point, and show that I still appreciate social activities.

Finally, I want to thank my friends and family for their understanding regarding my passion for physics, and for their endless, outright support over the years, even when I did not show up for weeks. I'm truly grateful to my parents, who made all this possible.

My very special thanks go to Theres, for her patience and her encouragement, and for bringing my attention to something much more important than physics. You kept me going!